Journal
International
of Modern
Engineering
IJME
WWW.IJME.US
Print ISSN: 2157-8052
Online ISSN: 1930-6628

INTERNATIONAL JOURNAL OF MODERN ENGINEERING

Fall / Winter 2013
Volume 14, Number 1

The Leading Journal of Engineering, Applied Science and Technology

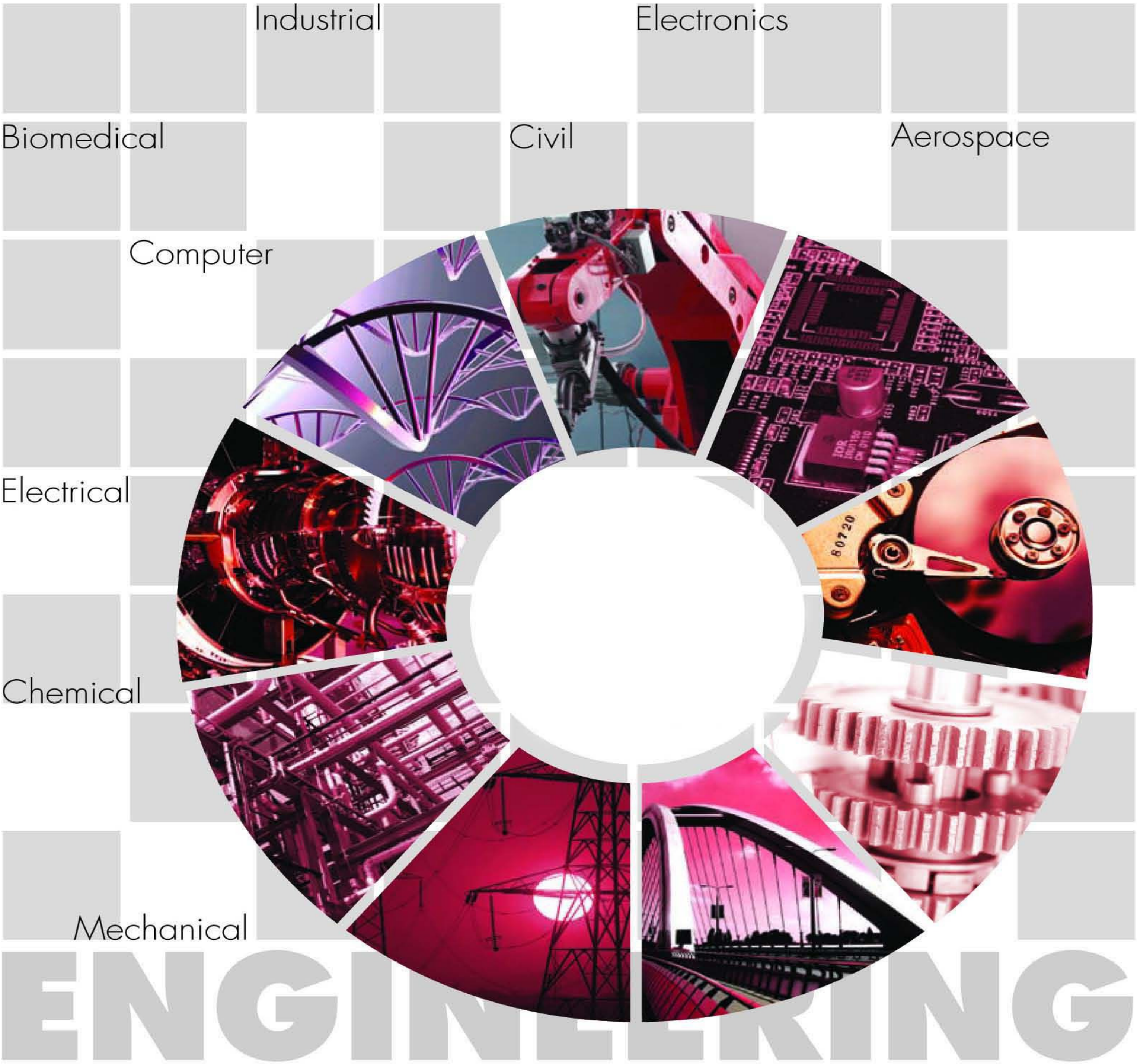

Published by the
International Association of Journals & Conferences

THE LEADING JOURNAL OF ENGINEERING, APPLIED SCIENCE, AND TECHNOLOGY

International Journal of Modern Engineering

www.ijme.us

Print ISSN: 2157-8052
Online ISSN: 1930-6628

International Association of Journals and Conferences

www.iajc.org

INTERNATIONAL JOURNAL OF MODERN ENGINEERING

ABOUT IJME:

- IJME was established in 2000 and is the first and official flagship journal of the International Association of Journal and Conferences (IAJC).
- IJME is a high-quality, independent journal steered by a distinguished board of directors and supported by an international review board representing many well-known universities, colleges and corporations in the U.S. and abroad.
- IJME has an impact factor of **3.00**, placing it among the top 100 engineering journals worldwide, and is the #1 visited engineering journal website (according to the National Science Digital Library).

OTHER IAJC JOURNALS:

- The International Journal of Engineering Research and Innovation (IJERI)
  For more information visit www.ijeri.org
- The Technology Interface International Journal (TIIJ).
  For more information visit www.tiij.org

IJME SUBMISSIONS:

- Manuscripts should be sent electronically to the manuscript editor, Dr. Philip Weinsier, at philipw@bgsu.edu.

  For submission guidelines visit www.ijme.us/submissions

TO JOIN THE REVIEW BOARD:

- Contact the chair of the International Review Board, Dr. Philip Weinsier, at philipw@bgsu.edu.

  For more information visit www.ijme.us/ijme_editorial.htm

INDEXING ORGANIZATIONS:

- IJME is currently indexed by 22 agencies. For a complete listing, please visit us at www.ijme.us.

Contact us:

Mark Rajai, Ph.D.

Editor-in-Chief
California State University-Northridge
College of Engineering and Computer Science
Room: JD 4510
Northridge, CA 91330
Office: (818) 677-5003
Email: mrajai@csun.edu

TIIJ International

www.tiij.org

International Journal of Engineering Research & Innovation IJERI

www.ijeri.org

INTERNATIONAL JOURNAL OF MODERN ENGINEERING

The INTERNATIONAL JOURNAL OF MODERN ENGINEERING (IJME) is an independent, not-for-profit publication, which aims to provide the engineering community with a resource and forum for scholarly expression and reflection.

IJME is published twice annually (Fall and Spring issues) and includes peer-reviewed articles, book and software reviews, editorials, and commentary that contribute to our understanding of the issues, problems, and research associated with engineering and related fields. The journal encourages the submission of manuscripts from private, public, and academic sectors. The views expressed are those of the authors and do not necessarily reflect the opinions of IJME or its editors.

EDITORIAL OFFICE:

Mark Rajai, Ph.D.
Editor-in-Chief
Office: (818) 677-2167
Email: ijmeeditor@iajc.org
Dept. of Manufacturing Systems
Engineering & Management
California State University-
Northridge
18111Nordhoff Street
Northridge, CA 91330-8332

THE INTERNATIONAL JOURNAL OF MODERN ENGINEERING EDITORS

TABLE OF CONTENTS

EDITOR'S NOTE

Philip Weinsier, IJME Manuscript Editor

The editors and staff at IAJC would like to thank you, our readers, for your continued support, and we look forward to seeing you at the upcoming IAJC conference. For this fourth IAJC conference, we will be partnering with the International Society of Agile Manufacturing (ISAM). This event will be held at the new Embassy Suites hotel in Orlando, FL, September 25-27, 2014, and is sponsored by IAJC, IEEE, ASEE, and the LEAN Institute.

The IAJC/ISAM Executive Board is pleased to invite faculty, students, researchers, engineers, and practitioners to present their latest accomplishments and innovations in all areas of engineering, engineering technology, math, science, and related technologies.

Selected papers from the conference will be published in the three IAJC-owned journals or 11 affiliate journals. Oftentimes, these papers, along with manuscripts submitted at-large, are reviewed and published in less than half the time of other journals. Publishing guidelines are available at www.iajc.org, where you can read any of our previously published journal issues, as well as obtain information on chapters, membership, and benefits.

I am pleased to report that, based on the latest impact factor (IF) calculations (Google Scholar method), IJME now has a remarkable IF = 3.0 and continues its march toward the top 20 engineering journals. IJME's sister journal, the International Journal of Engineering Research and Innovation (IJERI), also had a strong showing with an IF = 1.58, which is noteworthy as it is a relatively young journal (in publication since 2009). Any IF above 1 is considered high, based on the requirements of many top universities, and places the journals among an elite group.

Currently, there is no official ranking system for journals that publish areas of engineering the way that IJME and IJERI do. However, if IJME were placed with mechanical engineering journals, it would be ranked #5; or, #15 in chemical engineering (www.ijme.us/papers/Top%20journals.pdf). IEEE journals, where the journals publish papers in more than one category, use the same analogy to show the ranking of their journals in different categories. Highlights include:

- IJME is ranked among the top engineering journals that publish multiple-topic categories.
- Both IJME and IJERI now are indexed in most well-known indexing databases including DOAJ, which is the most prestigious and comprehensive database for open-access journals worldwide.
- Both journals now are indexed by hundreds of libraries worldwide, and in several states where there is near complete indexing across their university and college libraries.
- Both journals now are indexed in the libraries of all 10 campuses of the University of California system and the 23 campuses of the California State University system.

The biggest achievement, though, is that now both journals are also indexed by all of the top 10 universities in the world:

#1 California Institute of Technology
#2 Harvard
#3 Stanford
#4 University of Oxford
#5 Princeton University
#6 University of Cambridge
#7 Massachusetts Institute of Technology
#8 Imperial College London
#9 University of Chicago
#10 University of California, Berkeley

ISBN# 978-1-60643-379-9

Editorial Review Board Members

Listed here are the IAJC International Review Board members, who have devoted countless hours to the review of the many manuscripts that have been submitted for publication. Manuscript reviews require insight into the content, technical expertise related to the subject matter, and a familiarity with statistical tools and measures. Furthermore, revised manuscripts typically are returned for a second review to the same reviewers, as they already have an intimate knowledge of the work. So, as Manuscript Editor, I would like to take this opportunity to thank all of the members of the review board.

If you are interested in becoming a member of the IAJC International Review Board, send me (Philip Weinsier, IAJC/IRB Chair, philipw@bgsu.edu) an email to that effect. Review Board members review manuscripts in their areas of expertise for all three of our IAJC journals—IJME (the International Journal of Modern Engineering), IJERI (the International Journal of Engineering Research and Innovation), and TIIJ (the Technology Interface International Journal), as well as papers submitted to the IAJC conferences. Please watch for updates on our website (**www.IAJC.org**), and contact us anytime with comments, concerns, or suggestions.

Michelle Brodke	Bowling Green State U. Firelands (OH)
Jessica Buck	Jackson State University (MS)
Shaobiao Cai	Penn State University (PA)
Isaac Chang	Cal Poly State University SLO (CA)
Hans Chapman	Morehead State University (KY)
Rigoberto Chinchilla	Eastern Illinois University (IL)
Brad Deken	Southeast Missouri State U. (MO)
Z.T. Deng	Alabama A&M University (AL)
Mehran Elahi	Elizabeth City State University NC)
Rasoul Esfahani	DeVry University (OH)
Morteza Firouzi	University Technology (MALAYSIA)
Dave Hunter	Western Illinois University (IL)
Christian Hyeng	North Carolina A&T University (NC)
Pete Hylton	Indiana University Purdue (IN)
Ghassan Ibrahim	Bloomsburg University (PA)
John Irwin	Michigan Technological University (MI)
Sudershan Jetley	Bowling Green State University (OH)
Reza Karim	North Dakota State University (ND)
Tolga Kaya	Central Michigan University (MI)
Pete Klein	Ohio University (OH)
Ognjen Kuljaca	Brodarski Institute (Croatia)
Zaki Kuruppalil	Ohio University (OH)
Guoxiang Liu	University of North Dakota (ND)
G.H. Massiha	University of Louisiana (LA)
Sam Mryyan	Excelsior College (NY)
Arun Nambiar	California State University-Fresno (CA)
Jose Pena	Purdue University Calumet (IN)
Karl Perusich	Purdue University (IN)
Thongchai Phairoh	Virginia State University (VA)
Huyu Qu	Honeywell International, Inc.
Mulchand Rathod	Wayne State University (MI)
Sangram Redkar	Arizona State University-Poly (AZ)
Michael Reynolds	University of Arkansas Fort Smith (AR)
Marla Rogers	Wireless Systems Engineer
Anca Sala	Baker College (MI)
Ehsan Sheybani	Virginia State University (VA)
Siles Singh	St. Joseph U. (Tanzania, AFRICA)
Haoyu Wang	Central Connecticut State U. (CT)
Jonathan Williams	Bowling Green State U. Firelands (OH)
Alex Wong	Digilent Inc.
Pao-Chiang Yuan	Jackson State University (MS)
Chongming Zhang	Shanghai Normal University (CHINA)
Jinwen Zhu	Missouri Western State University (MO)

PERFORMANCE OF A REFERENCE IMPLEMENTATION OF A NOVEL TECHNICAL REFERENCE MODEL FOR WIRELESS SENSOR NETWORKS

Babak D. Beheshti, New York Institute of Technology; Howard Michel, University of Massachusetts, Dartmouth

Abstract

A Technical Reference Model (TRM) provides the definitions and formal structure for describing implicit and explicit concepts and operations. A TRM lays out the fundamental structure, inter-entity relations within a system, as well as external interfaces and expected scopes of functionality of each functional block in a generic system. None of the present-day wireless sensor architectures are generic enough to accommodate the functional decomposition of a broad spectrum of problems or for specifying the standards for all other aspects of the system, encompassing both information and control requirements, as well as inter- and intra-layer processes required to achieve a self-aware, self-healing, and adaptable system.

This study is based on a novel Integrated Technical Reference Model (I-TRM) and a multi-layered architecture for Wireless Sensor Networks (WSNs). The I-TRM combines an Information-Centric Technical Reference Model (IC-TRM), a Control Technical Reference Model (C-TRM), and a Behavioral (intelligence-based) Technical Reference Model (B-TRM) in order to provide a complete system technical reference model.

In this study, the authors present the overall structure of this TRM, the reusability and scalability of the I-TRM, and the capability that it provides in encapsulating module complexities by means of a set of Application Programmers' Interface (API) and data abstractions. In addition, the authors developed a reference implementation of this TRM. Simulation results of the I-TRM implementation and some key performance metrics of the implementation in order to draw some conclusions about scalability of this design in larger wireless sensor networks are also included here.

Introduction

Wireless Sensor Networks (WSNs) have evolved over the past decade to be an active area of research due to potentially large numbers of applications in which they can be used. WSNs have been used for many applications where sensing occurs in inaccessible, remote, and/or hostile environments. The work presented here is based on the foundations of the Integrated Technical Reference Model (I-TRM) for Wireless Sensor Networks (WSNs) by Michel and Fortier [1] and brings the existing foundations to a complete framework, along with a real system implementation of the framework. The authors developed the functional decomposition of each layer and the interlayer interaction. Based on previously published studies, an Application Programming Interface (API) for the layered I-TRM model was developed. Inner workings of each layer are sufficiently outlined. This API, while generic and expandable, contains a sufficient level of specification in order to make it directly implementable in a test platform.

The I-TRM by Michel and Fortier [1] defines the functional decomposition of the layers of the three faces of the model; however, the internal architecture of the model as well as practical interactions between these layers and faces were not identified. While it is a natural expectation of a reference model to be general enough to lend itself to a variety of scenarios within its space, a specific instantiation of the reference model can contribute significantly to a study and verification of overlaps of functionality or, conversely, gaps in areas of responsibility with respect to complete information, behavioral, and control management of a WSN.

It must be emphasized that the novel concept and the focus of this research is the complete and comprehensive development and definition of the I-TRM layers, their API, inter-plane and inter-layer messaging, and the associated reference message sequence charts.

Related Work

There have been numerous studies published on APIs that abstract various aspects of a WSNs programming. The API coverage in the literature is focused on one of two possible general directions [2], [3]:

1. Providing an API (in cooperation with a set of unifying functions, or middleware) to provide an abstraction of the underlying physical components and architectures, as well as the programming environment,

and provide a consistent interface across heterogeneous sensor nodes; and,
2. Providing in-field programmability for the sensor nodes.

There is also coverage of challenges associated with creation and deployment of APIs and middleware that is beyond the scope of this paper [4], [5]. In the following sections, a small sampling of the approaches taken to provide abstraction to WSN programming via APIs is presented.

The IEEE-1451 wireless standard is intended to integrate a wide range of sensors with a number of different wireless radio implementations utilizing standards-based protocols to communicate between the application and the sensor. The 1451 family of standards (IEEE Standard for a Smart Transducer Interface for Sensors and Actuators) includes:

- 1451.0-2007– Common Functions, Communication Protocols, and Transducer Electronic Data Sheet (TEDS) Formats
- 1451.1-1999 Network Capable Application Processor Information Model
- 1451.2-1997 Transducer to Microprocessor Communication Protocols & TEDS Formats
- 1451.3-2003 Digital Communication & TEDS Formats for Distributed Multi-drop Systems
- 1451.4-2004 Mixed-Mode Communication Protocols & TEDS Formats
- 1451.5-2007 Wireless Communication Protocols & Transducer Electronic Data Sheet (TEDS) Formats
- 1451.7-2010 Transducers to Radio Frequency Identification (RFID) Systems Communication Protocols and Transducer Electronic Data Sheet Formats

According to this architecture, IEEE 1451 defines a Transducer Interface Module (TIM) and Network Capable Application Processor (NCAP). The TIM can be a wired or wireless IEEE 1451.X module consisting up to 255 transducers, signal conversion and processing electronics, and Transducer Electronic Data Sheets (TEDS). One can think of TEDS as metadata associated with a sensor.

The IEEE 1451.0, approved as an IEEE standard on March 23, 2007, defines a set of common operations and TEDS for the IEEE 1451 family. This functionality is independent of the physical communications media. It includes the basic functions for the NCAP to read and write to each transducer and its TEDS, and to send configuration, control, and operation commands to the TIM. The IEEE 1451.5 standard is a wireless sensor interface standard, which defines a set of wireless communication specifications between the WTIM and NCAP. It adopts popular 802.11, Bluetooth, and ZigBee as its wireless communication protocols. There are three possible ways to access the sensors and actuators from:

1. IEEE 1451.1,
2. IEEE 1451.0 Hyper Text Transfer Protocol (HTTP),
3. Smart Transducer Web Services (STWS).

The NCAP can communicate wirelessly with WTIM through IEEE 1451.0 and 1451.5 protocols using the client-server and publisher/subscriber communication models. The client/server and publisher/subscriber communications between the two nodes can be implemented using Transmission Control Protocol/Internet Protocol (TCP/IP) and Transmission Control Protocol / User Datagram Protocol (TCP/UDP). As can be seen above, there are two major differences between the objectives of the I-TRM and the IEEE 1451 standards:

1. The IEEE 1451, while useful for individual sensor interfaces, is not suitable for a dynamically changing WSN. This standard also does not effectively address network-wide data access and aggregation issues. It is mainly intended to standardize transfer of information through known interfaces.
2. The IEEE 1451 relies on the TCP/IP protocol stack as its inherent network interface. This feature, while useful in implementation of an I-TRM, is NOT technology agnostic and, therefore, dictates a minimum processing and storage capability on the part of the sensor nodes. It is well known that to support the TCP/IP stack, a processor needs to have more than the minimal capabilities available in some small-sized sensor nodes.

Another example of abstraction via APIs is the TinyOS [6]. TinyOS is a free distribution environment that was designed especially for WSNs. One of the main characteristics of TinyOS is that it is written in NesC, which is a subset of C language that is optimized for limitations of memory and resources of sensor networks. Its functionality is defined through a set of tasks and processes that help each other, because its architecture is based on components, making it flexible when new hardware or software is developed and added. Moreover, it supports different kinds of sensor-node platforms for building applications. TinyOS was developed by a partnership formed by Berkeley University and Intel Research [7]. TinyOS has three elements within each process:

1. Events: Events are short-duration, time-critical entities that are caused by interrupts (e.g., from Timer, ADC, Sensors).

2. Commands: Commands are control services that provide sensor actuation and synchronous/asynchronous calls (split-phase with callback event).
3. Tasks: Tasks are time-flexible (delayed processing) entities that run sequentially by the operating system (TOS) Scheduler. They run to completion with respect to other tasks.

Another solution is “TinyDB” [8]. TinyDB is a distributed query processor that runs on each of the nodes in a sensor network. TinyDB has many of the features of a traditional query processor such as the ability to select, join, project, and aggregate data, as well as some additional power-saving capabilities. TinyDB is an application of TinyOS. It is designed specifically for the Mica2 platform; its more stable version is located at the TinyOS 1.x version. It consists of a front end that was developed in Java and is formed by three principal objects:

1. The TinyNetwork represents the network connection and activates the CmdFrame.
2. The CmdFrame represents sending processes on the network.
3. The QueryFrame represents design queries.

Among the TinyDB characteristics is the acquisition processing query of ACQP (Automatic Control for Quality and Production) whose goal is to reduce power consumption by making use of sensors that have control of where, how, and how often data are located. It then continuously samples and delivers results to database administrators.

The main drawback of systems such as TinyDB and other database query-based approaches is that they are limited to simple queries. While there is the possibility of extending the query capabilities by adding scripts, these extensions in turn bring about the additional storage, processing, and power consumption overhead associated with interpretation of scripting languages. I-TRM, on the other hand, is not intended to be only an abstraction of a distributed database system. It proposes to model the behavior of a WSN entirely in a layered manner. Had TinyDB’s implementation followed the layered architecture proposed in this research, one could consider TinyDB to be a possible instantiation of a subset of the functionalities defined by the I-TRM (i.e., parts of Control and Information faces), but still lacking the behavior face.

Finally, BNSF is another example of a layered reference architecture [9]. BNSF is a layered reference architecture that correctly argues that “Segregation of sensor networks into building blocks results in an architecture that permits the development of inter-changeable and compatible sensor, user and management elements.” Basis Sensor Network Framework or BNSF, uses graphical icons to represent various elements within a WSN, such as Sensors, Users, Managers, etc.

By interconnecting these icons, one specifies functional interfaces between various layers of BNSF. Each element type has its own layered plane in the BNSF. Networking of sensors is accomplished by a user element that acts as the network gateway of that sensor, called a Sensor Attached User (SA-U). There are models for user-plane data transfer; however, there is a clear absence of system-level modeling at the behavioral level at execution time. The authors propose that a working model of the GCL can be developed and serve as a basis for specification development.

Introduction to the I-TRM

The I-TRM illustrated in Figure 1 defines the functional decomposition of the layers of the three faces of the model. The Integrated Technical Reference Model (I-TRM) attempts to standardize the structure of applications running on a sensor network based on a layered model. This I-TRM for an autonomous Wireless Sensor Network is composed of three planes: the Information Plane, the Control Plane, and the Behavior Plane. This reference model lays out a detailed layered model with a functional description of each layer described in general terms.

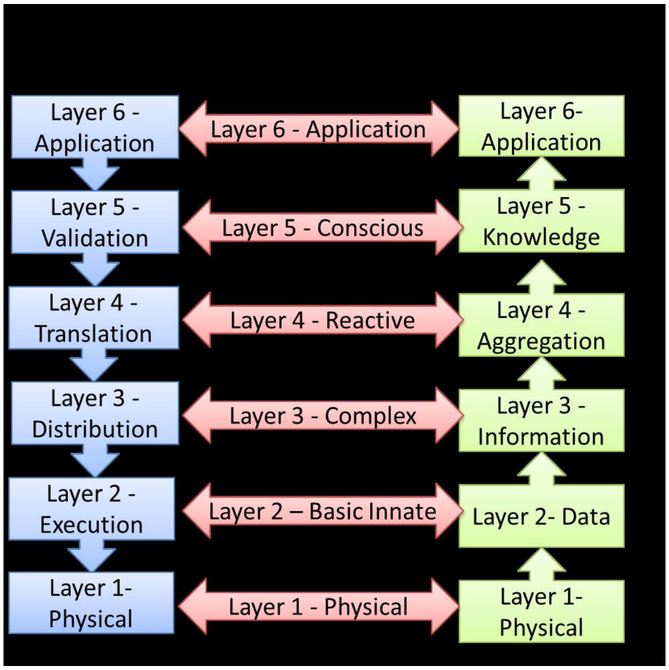

Figure 1. The I-TRM Layered Model

In this section the three planes (faces) of this model are introduced. As with any other layered model, the lower layers act as service providers to upper layers; and, as one goes up in layers, the scope of generality of the layer increases [10]. In this section, the function of each layer is described. It should be noted that these layers represent an abstraction of a system into functional compartments. An actual implementation may omit a layer or two, by the designers' decision to combine the functions of some layers into one. Also, the choice of where in the system each layer resides (i.e., in a node, or in the base station or sink) is entirely a design decision.

The Control Plane (C-TRM)

The Control Plane (as depicted in Figure 2) is responsible for the goal setting and control of the system [3]. The main focus is on the details about the control organization of the system including hierarchical control and task distribution. This closely follows the work done in the field of control architecture, authentication of the semantic correctness of the goal, and reduction of valid goals into functional tasks based on knowledge about the lower layers. The organization of system tasks for goal-achievement is in accordance with spatial and temporal information by reducing the task groups into sub-tasks and assigning priorities to them.

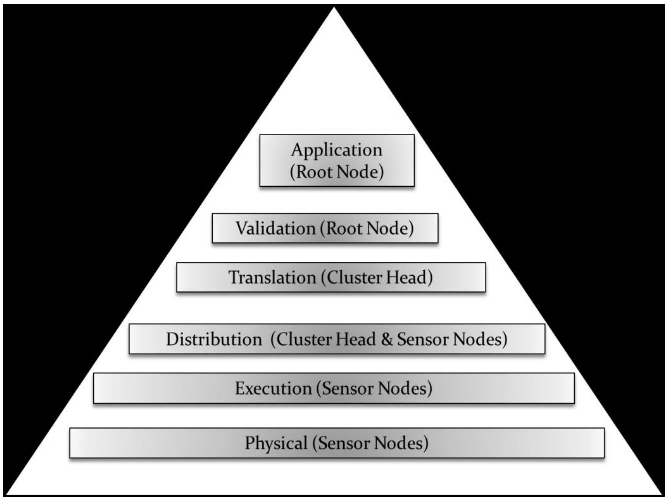

Figure 2. Control Face of the I-TRM

Application Layer (Layer 6): Layer 6 provides a means for the user to interact with the system in order to define mission goals. This layer will provide a universal and standard interface to all applications utilizing the I-TRM.

Validation Layer (Layer 5): Layer 5 authenticates the semantic correctness of the goal and determines whether the goal is accepted or not, based on intrinsic and extrinsic information and knowledge. It verifies the probability of accomplishing the goal with the resources available. As an example, metadata from the lower layers would be evaluated here to assess the readiness of the system to produce the family of engine performance curves requested. Are all of the required sensors in place, calibrated, and operating correctly? Is the software in place to create the required synthetic instruments? Are there other higher priority tasks causing conflicting demands on resources?

Translation Layer (Layer 4): Layer 4 reduces valid goals into functional tasks based on knowledge about the lower layers. This layer provides a mechanism for registering low-level system components and their physical capabilities (i.e., the system database). For example, it creates the need for synthetic instruments to produce synchronized temperature and pressure readings in the measurement zone, and synchronize them with corresponding readings for other required measurements from sensors measuring other phenomena. It then passes these requirements down to the Distribution Layer.

Distribution Layer (Layer 3): Layer 3 organizes system tasks for goal-achievement in accordance with spatial and temporal information by reducing the task groups into sub-tasks and assigning priorities to them. Software at this level might understand, for example, that there are four individual temperature sensors in the combustion chamber, and that if they all are reading within 50^{o}F of each other, then any one of them can be used to report the subject temperature. Furthermore, software at this level would understand that these temperature readings need to be closely synchronized with pressure and fuel-flow readings, but that because of physical characteristics, synchronization at the fraction-of-a-second level is sufficient, rather than at a microsecond level of synchronization. These commands are then passed down to the Execution Layer.

Execution Layer (Layer 2): Layer 2 receives directives from the distribution layer and transforms them into control signals for the physical layer. This layer implements basic error detection and correction in close cooperation with the physical layer. For example, the execution layer, based on its detailed understanding of the sensors involved, would issue a command to temperature sensor number XYZ to stream temperature data (assuming it has a stream mode) at 100 samples per second, using gain N starting at time T.

Physical Layer (Layer 1): Layer 1 constitutes sensors and mechanical units. It executes actions as directed by higher layers.

The Information Plane (IC-TRM)

This plane, as depicted in Figure 3, is responsible for the information processing side of the system [2]. The main focus is on data collection, information aggregation, knowledge generation, and presentation. It shows how data is transformed into knowledge. The lowest layer (physical layer) deals with the most concrete physical level of data acquisition, whereas layers above it deal with increasingly more complex issues in transforming data into information. In this section the function of each layer in the IC-TRM is described.

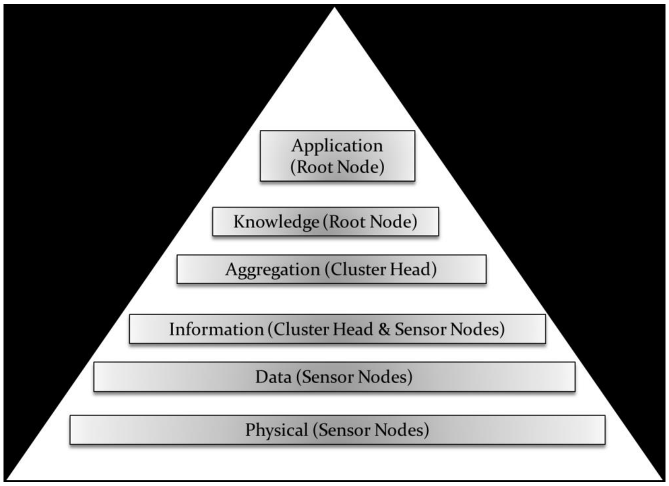

Figure 3. Information-Centric Face of the I-TRM

Physical Layer (Layer 1): This layer constitutes sensors and mechanical units. It gathers raw data in unformatted, unverified, and transitory format. It deals with the electrical, mechanical, and procedural characteristics. Metadata associated with the physical layer would be sensor type, serial number, location, and calibration status. This metadata would generally exist in a stable form as part of the physical sensor. For example, in a WSN, in order to minimized energy consumption due to over-the-air transmission, all metadata can be stored in a database in a remote location and the mapping of a sensor node's metadata to the data recorded in the database would be simply through use of a database key such as the sensor node number.

Data Layer (Layer 2): This layer extracts and transforms data into digital forms and checks the authenticity of the measurements. The voltage from the physical layer is transformed into a byte or a word using a proscribed (although possibly variable) process involving amplifiers, filters, and analog-to-digital converters. Variable parameters could include sampling rate, digitization accuracy, filter cutoff frequency, amplifier gain, etc.

Information Layer (Layer 3): The third layer correlates data with scaling, location, type of measurement, etc., in order to produce information about the system or environment. The data and metadata from the data layer would be combined to produce information that reports, for example, that the temperature at the 12 O'clock position in the combustion chamber of the number one engine was 1000 ^{o}F at T+1.0 seconds from test start, and that this measurement should be believed with a high efficiency.

Knowledge Layer (Layer 5): This later transforms aggregated information into knowledge by processing against intrinsic and extrinsic information and knowledge available. If the engine temperature approached or exceeded this value, warnings could be issued or commands could be issued to lower layers in the system in order to increase sampling rate or accuracy of the engine temperature sensors so that a more accurate post-test analysis could be conducted.

Application/Presentation Layer (Layer 6): The uppermost layer provides a means for the user to access and use information from the system in a consistent format. All event reports of layer 5 are made available to the applications via this layer. This layer will provide a universal and standard interface to all applications utilizing the I-TRM.

The Behavior Plane (B-TRM)

The behavior plane, as illustrated in Figure 4, at each level acts as a feedback path between the other two planes. Behavior is a mapping of sensory inputs to a pattern of motor/component actions, which then are used to achieve a task, the action or reaction of something under specified circumstances, and a series of events resulting from the execution of the operating rules of that system, as defined within rule-clusters.

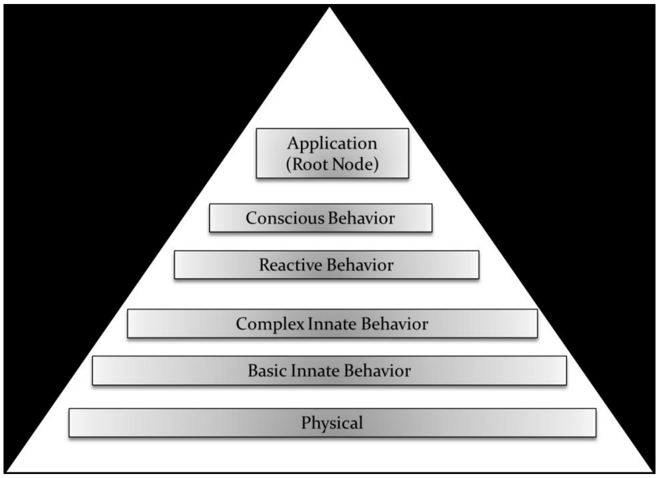

Figure 4. Behavior Face of the I-TRM

Physical Layer (Layer 1): This layer constitutes sensors and mechanical units. It is the same hardware as described in the IC-TRM and C-TRM.

Basic Innate Behavior Layer (Layer 2): This layer implements a stimulus-response behavior. It implements purely reflexive behavior, and combines the execution layer procedure-execution with the relevant data.

Complex Innate Behavior Layer (Layer 3): This layer is the highest reactive layer. It implements procedures which connect the information extracted from the data to task execution distribution. An example of a complex innate behavior might be to "continuously sample and stream data at a particular rate, gain setting, and filter characteristics." Another complex innate behavior might be a self-calibration mode.

Reactive Behavior Layer (Layer 4): This layer provides a mechanism for dealing with information collaboration from various modules into one structured data unit (local model). It provides procedures for translating goals into submodules in compliance with the state of the environment.

Conscious Behavior Layer (Layer 5): This layer takes care of deliberative actions for the systems. It provides schemas for checking the goals' validity and feasibility in the given situation, by checking goals against the intrinsic and extrinsic knowledge about the environment.

Application Layer (Layer 6): This layer is responsible for user interactions. It determines what information should be furnished and to whom, and which goal should be accepted. It either consumes knowledge passed up to it (as in the case of an intelligent program), or passes the knowledge to the user. It receives commands from the user-application interface.

API Definition and Inter-Layer and Inter-Plane Interfaces

The API definitions and inter-layer interactions are presented through Message Sequence Charts (MSCs) for all layers and all planes of the I-TRM. However, the volume of these specifications exceeds the scope of this paper. In the following section, a highlight of the specifications is presented.

There exist predefined API from the User Interface to layer 6 of each face, and correspondingly from every layer of each face to its neighboring layer. Two points are noteworthy: 1) there exist APIs that are defined across planes of the I-TRM in order to accommodate coordination of efforts and events across the three planes, 2) there exist cross-layer-mechanism an APIs within each I-TRM plane that allow for fast response of the system to parameter changes that need to be used to change some aspect of the WSN behavior. These cross-layer considerations are beyond the scope of this paper. For details on cross-layer considerations, please see Shakkottai et al. [11] and Beheshti and Michel [12].

Each API definition follows the following format.

Prototype:
int XXX_YYY__ZZZ_NAME_UUU (void *params)

Description: The user enters a goal for the entire system

where

- XXX is the name of the sender entity
- YYY is the name of the receiver entity
- ZZZ is the layer across which this API travels in a peer-layer communication
- NAME is the API's specific name
- UUU is the specific message indicator. Examples include REQ (for a request), IND (for an indicator of an event), CFM (for confirm), ACK (for acknowledgement), and REJ (for reject).
- params is a pointer to the data structure holding the parameters for this system).

For example, the API call C_UI_L6_SYSTEM_GOAL_SET_REQ, as its name implies is a message from the I-TRM (C) Control Face to the User Interface of the system (UI), operating at layer 6. The message is a request to the receiver to accept the system goal setting.

Example Use Case

Upon system initialization, the user via the User Interface (UI) sends a message to layer 6 of the C-TRM indicating the goals of the system run. The user can specify any arbitrary logical combination of individual goals as the overall system goal, in the form of a logical OR (or logical AND) or a combination of individual groupings of goals. Each individual grouping can be an AND or an OR combination. Each individual goal can be a statement such as "zone #12 temperature is greater than 120 ^{o}F", or "zone #35 slope of temperature is greater than 0.23 ^{o}/minute". Layer 6 of C-TRM sends this message to Layer 5, which is responsible for maintaining a repository of the system resources such as sensors available, location of the sensors, etc. Layer 5 can accept or reject this goal specification based on its assessment of available resources. For example, if there are no temperature sensors available in zone #12, then the request will be rejected. The MSC in Figure 5 demonstrates this use case where there are insufficient system resources available to validate the system goal. In this case, the system will not be operational.

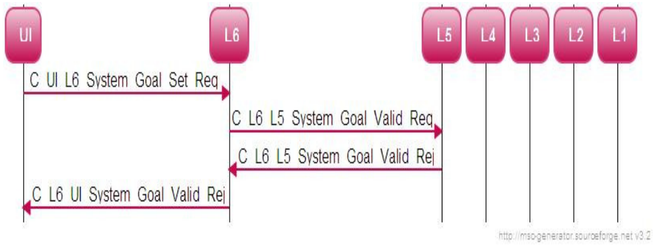

Figure 5. Failure Scenario L6 MSC for the Control Face

The actual API specifications for two messages are listed below.

C_L6_UI_System_Goal_Valid_Cfm

- From L6 of Control Face to UI
- Description: The system goals entered by the user are passed valid. The system can support the stated goal (s). The goals are application specific.
- Parameters:
  - Goal
- Prototype: int C_L6_UI_System_Goal_Valid_Cfm (void *params)

where params is a pointer to the data structure holding the parameters for this system.

C_L6_UI_System_Goal_Valid_Rej

- From L6 of Control Face to UI
- Description: The system goals entered by the user are not valid; the system resources are not sufficient to commit to these goals.
- Parameters:
  - Goal
- Prototype: int C_L6_UI_System_Goal_Valid_Rej (void *params)

where params is a pointer to the data structure holding the parameters for this system.

C_L6_UI_System_Goal_Invalid_Ind

- From L6 of Control Face to UI
- Description: The system goals entered by the user are no longer valid; the system resources are not sufficient any longer to commit to these goals.
- Parameters:
  - Goal
- Prototype: int C_L6_UI_System_Goal_Invalid_Ind (void *params)

where params is a pointer to the data structure holding the parameters for this system.

The text in Table 1 is a partial listing of the log file generated from this implementation that verifies the above message sequence chart.

Table 1. Partial Listing of the Log File

```
>>>>>>>>>>>>>>>>>Sun Aug 14 06:15:55 2011

API Msg Sent: From = UI_ID            To: CTRM_L6_ID Msg:
C_UI_L6_System_Goal_Valid_Req

>>>>>>>>>>>>>>>>>Sun Aug 14 06:15:56 2011
API Msg Sent: From = CTRM_L6_ID  To: CTRM_L5_ID Msg:
C_L6_L5_System_Goal_Valid_Req

>>>>>>>>>>>>>>>>>Sun Aug 14 06:15:57 2011
API Msg Sent: From = CTRM_L5_ID  To: CTRM_L6_ID Msg:
C_L5_L6_System_Goal_Valid_Rej
```

Software Implementation

In this section, the development of a complete end-to-end implementation of the software of a WSN based on the I-TRM API and inter-layer and inter-plane interfaces is presented. While the entire software system was written to validate the novel I-TRM API, the operating system and the packet communication infrastructure available in the hardware platform's tools was utilized.

The hardware platform used contains the well-known sensor nodes originally designed at UC Berkeley and generally used in the research community (see Figure 6). These low-cost nodes can be strewn, or carefully placed in a deployment zone, allowing for collection, aggregation, and communication of environmental data between themselves and ultimately to a user station.

Figure 6. The MicaZ Crossbow Berkeley Mote

This is a fully implemented design for the layered architecture of the proposed I-TRM layers—with a significant subset of the API being included in the implementation. The I-TRM was implemented in a logical tree-like hierarchical structure that is physically distributed. The layered approach that was followed here is a natural approach to capture the overall picture of a complex system. In general, the decomposition into levels of abstraction is the key for managing systems that encompass high-level and low-level issues. The approach presented here has been successfully adopted in areas such as networking and communication as part of the open-system interconnection initiative (OSI) [11] and more recently in particular software or large system design.

Also, experiments for the purposes of performance analysis of the I-TRM were designed. The definition of performance metrics, as well as design of experiments that would provide for a thorough analysis of the I-TRM, has been an integral part of this research. Since the value proposition of the I-TRM is its encapsulation of "intelligence" within a WSN, manifested by self-healing, self-reconfiguration, scalability, and ability to change behavior based on external stimuli, test cases for the implemented WSN were developed to exercise the WSNs performance with respect to the above criteria.

- The removal of sensor nodes during system operation. This mimics, for example, the failure of a sensor monitoring a patient in a healthcare facility.
- The addition of sensor nodes during system operation. This mimics, for example, the addition of a new patient admitted into a healthcare facility.
- Moving of sensor nodes within the WSN. Again, for example, this mimics the movement of patients within a healthcare facility.
- The creation of an event that would cause system behavior to change (e.g., increase sampling rate, change data aggregation mechanisms). As an example of this test case, this mimics the need to acquire additional and more frequent data from a patient being monitored in a healthcare facility once a sensor has detected an abnormality such as abnormal heart rate.

The implementation of this platform is based on a four-tiered software architecture (as illustrated in Figure 7):

- The sensor mote software: This tier of the software resides in the sensor nodes. This tier in itself is composed of two sub-tiers:
- Layers 1 and 2 that reside in the sensor motes. These nodes are the components responsible for ALL data collection in the WSN.
- Layers 3 and 4 that reside in Cluster Heads. Cluster Heads are essentially processors with additional computing and storage resources. In this implementation, the cluster head functions have been consolidated into the backend server functions in a portable/ embedded PC.

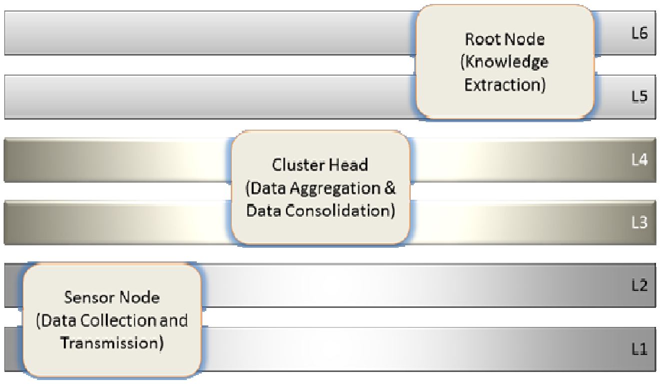

Figure 7. Location of Software Layers in the WSN

Software Modules

The implemented system is composed of several modules. The Backend Server software described in this section and the software embedded in the individual sensor nodes are the embodiment of the layers of the I-TRM as introduced in the previous sections. In particular, the left-hand side of Figure 10 illustrates the exact mapping of the proposed framework to the software implementation. A brief description of each software module and its functionality is provided below.

1. The Gateway: This tier runs as a Windows™-based application that provides gateway functionality between the wireless sensor nodes and a PC. This application is responsible for the following:
    a. Establishing a USB device driver interface to the sensor mote connected to the USB, and treating this USB connection as a serial COM port.
    b. Receiving packets from the base station mote and relaying them through a socket-based interface to the backend server.
    c. Receiving packets from the backend server (intended for individual sensor motes and sending them to the base station mote via the USB connection).
    d. Providing basic test features to allow the user to send test commands to the sensor nodes as well as sending test messages to the backend server.

This application is written in Microsoft Visual Basic™. Figure 8 depicts a screen shot of the gateway application.

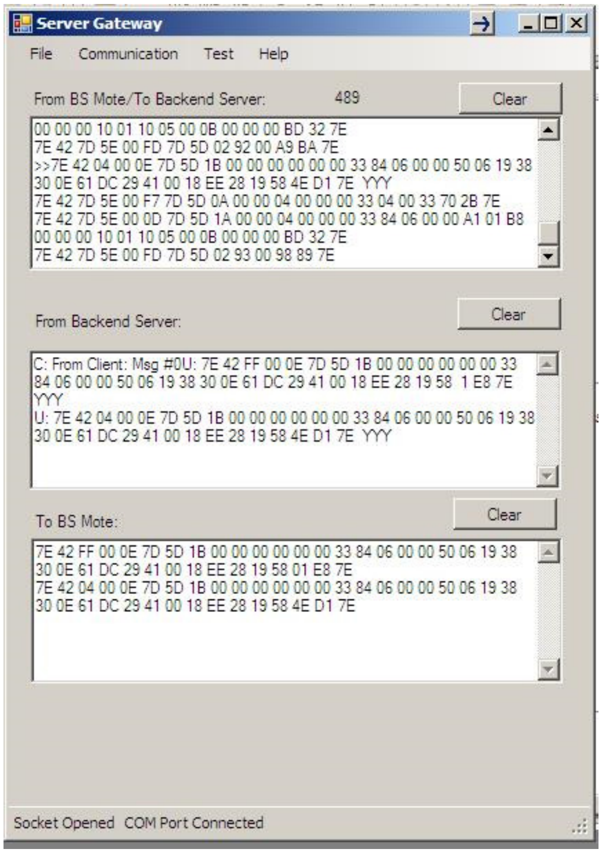

From BS Mote/To Backend Server: 489

```
00 00 00 10 01 10 05 00 0B 00 00 00 BD 32 7E
7E 42 7D 5E 00 FD 7D 5D 02 92 00 A9 BA 7E
>>7E 42 04 00 0E 7D 5D 1B 00 00 00 00 00 00 33 84 06 00 00 50 06 19 38
30 0E 61 DC 29 41 00 18 EE 28 19 58 4E D1 7E  YYY
7E 42 7D 5E 00 F7 7D 5D 0A 00 00 04 00 00 00 33 04 00 33 70 2B 7E
7E 42 7D 5E 00 0D 7D 5D 1A 00 00 04 00 00 00 33 84 06 00 00 A1 01 B8
00 00 00 10 01 10 05 00 0B 00 00 00 BD 32 7E
7E 42 7D 5E 00 FD 7D 5D 02 93 00 98 89 7E
```

From Backend Server:

```
C: From Client: Msg #0U: 7E 42 FF 00 0E 7D 5D 1B 00 00 00 00 00 00 33
84 06 00 00 50 06 19 38 30 0E 61 DC 29 41 00 18 EE 28 19 58  1 E8 7E
YYY
U: 7E 42 04 00 0E 7D 5D 1B 00 00 00 00 00 00 33 84 06 00 00 50 06 19 38
30 0E 61 DC 29 41 00 18 EE 28 19 58 4E D1 7E  YYY
```

To BS Mote:

```
7E 42 FF 00 0E 7D 5D 1B 00 00 00 00 00 00 33 84 06 00 00 50 06 19 38
30 0E 61 DC 29 41 00 18 EE 28 19 58 01 E8 7E
7E 42 04 00 0E 7D 5D 1B 00 00 00 00 00 00 33 84 06 00 00 50 06 19 38
30 0E 61 DC 29 41 00 18 EE 28 19 58 4E D1 7E
```

Figure 8. Gateway Application

This application is a multi-threaded application. The receive and transmit threads run concurrently with the display thread so that there would be no noticeable delays in the display of the data being transacted. This application is intended to stay out of the user's way and be operational in the background during normal operation of the system.

2. The user interface: This module runs as a Windows™-based application that provides the end-user visibility into the WSN information collection, and control of the WSNs behavior. Figure 9 illustrates a screen shot of the user interface written in Microsoft Visual Basic™ Express 2008. This tier communicates primarily to the backend server and obviously to the user through its menu and display interfaces. This tier does not contain any decision-making intelligence. It acts as a conduit and data format converter, gluing the field-deployed portions of the WSN to the user as well as the analysis engine together in a seamless interface to the end user.

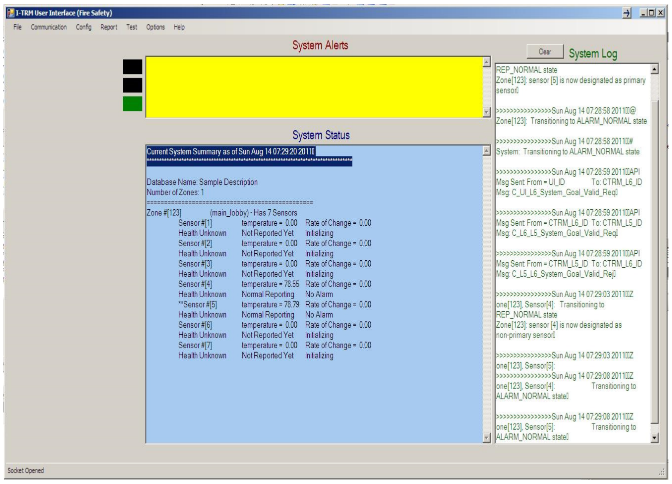

```
Current System Summary as of Sun Aug 14 07:29:20 2011▯
**********************************************************

Database Name: Sample Description
Number of Zones: 1
==================================================
Zone #[123]         (main_lobby) - Has 7 Sensors
          Sensor #[1]       temperature =  0.00   Rate of Change =  0.00
          Health Unknown    Not Reported Yet      Initializing
          Sensor #[2]       temperature =  0.00   Rate of Change =  0.00
          Health Unknown    Not Reported Yet      Initializing
          Sensor #[3]       temperature =  0.00   Rate of Change =  0.00
          Health Unknown    Not Reported Yet      Initializing
          Sensor #[4]       temperature = 78.55   Rate of Change =  0.00
          Health Unknown    Normal Reporting      No Alarm
          **Sensor #[5]     temperature = 78.79   Rate of Change =  0.00
          Health Unknown    Normal Reporting      No Alarm
          Sensor #[6]       temperature =  0.00   Rate of Change =  0.00
          Health Unknown    Not Reported Yet      Initializing
          Sensor #[7]       temperature =  0.00   Rate of Change =  0.00
          Health Unknown    Not Reported Yet      Initializing
```

```
REP_NORMAL state
Zone[123]: sensor [5] is now designated as primary
sensor▯

>>>>>>>>>>>>>>>>Sun Aug 14 07:28:58 2011▯▯@
Zone[123]:  Transitioning to ALARM_NORMAL state

>>>>>>>>>>>>>>>>Sun Aug 14 07:28:58 2011▯▯#
System:  Transitioning to ALARM_NORMAL state

>>>>>>>>>>>>>>>>Sun Aug 14 07:28:59 2011▯▯API
Msg Sent: From = UI_ID           To: CTRM_L6_ID
Msg: C_UI_L6_System_Goal_Valid_Req▯

>>>>>>>>>>>>>>>>Sun Aug 14 07:28:59 2011▯▯API
Msg Sent: From = CTRM_L6_ID  To: CTRM_L5_ID
Msg: C_L6_L5_System_Goal_Valid_Req▯

>>>>>>>>>>>>>>>>Sun Aug 14 07:28:59 2011▯▯API
Msg Sent: From = CTRM_L5_ID  To: CTRM_L6_ID
Msg: C_L5_L6_System_Goal_Valid_Rej▯

>>>>>>>>>>>>>>>>Sun Aug 14 07:29:03 2011▯▯Z
one[123], Sensor[4]:   Transitioning to
REP_NORMAL state
Zone[123]: sensor [4] is now designated as
non-primary sensor▯

>>>>>>>>>>>>>>>>Sun Aug 14 07:29:03 2011▯▯Z
one[123], Sensor[5]:
>>>>>>>>>>>>>>>>Sun Aug 14 07:29:08 2011▯▯Z
one[123], Sensor[4]:             Transitioning to
ALARM_NORMAL state▯

>>>>>>>>>>>>>>>>Sun Aug 14 07:29:08 2011▯▯Z
one[123], Sensor[5]:             Transitioning to
ALARM_NORMAL state▯
```

Figure 9. User Screen Capture of the Interface

This application is responsible for the following functions:

a. Providing the interfaces to allow the user to initialize the system configuration and establish system goals.
b. Displaying a running log of all significant events in the system, including state changes in the sensors as well as the system.
c. Establishing a socket-based interface to the backend server. All messaging between the user interface and the backend server is through this socket interface. In addition, provide for a flexible, expandable, and reliable communication protocol through this socket interface.
d. Providing a summary snapshot of the system in the "System Status" window.
e. Providing visual as well as audio alerts when the system enters an alarm state.
f. Providing test functions for the rudimentary system-level tests.

3. The backend server: This program contains layers 3 through 6 of all faces of the I-TRM (Control, Information, and Behavioral). Each layer of any face is implemented as a software thread communicating to other layers via inter-thread communication. It communicates to the user interface tier through a socket interface. This tier, therefore, can run remotely from the WSN deployment field, away from potential physical hazards.

This application is written in C, under the GNU Cygwin runtime environment. It is a multi-threaded program responsible for the implementation of the I-TRM functionality in the system. Figure 10 depicts the overall thread architecture of the backend server as well as its external interfaces.

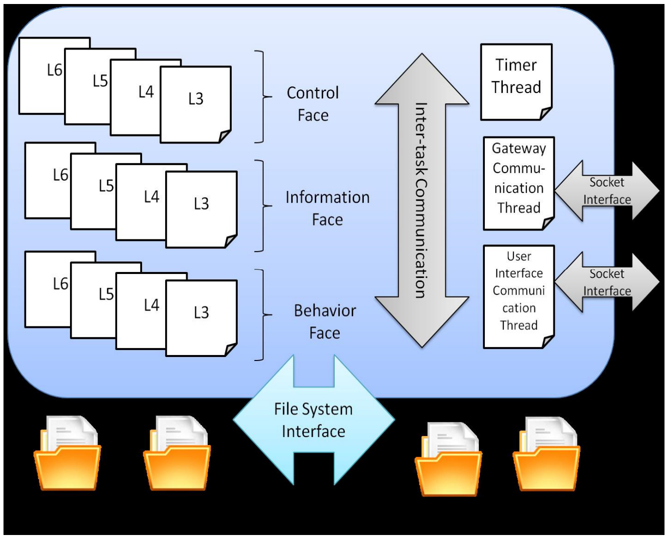

Figure 10. Backend Server Software Architecture

Simulation Results and Performance Data

Cold Startup Measurements: Latencies, Overhead, Message Count

In this set of system runs, starting with one sensor node in the WSN, each test case was executed by adding one sensor to the WSN and restarting the WSN from a cold start (i.e., resetting the base station node and all sensor nodes, thereby eliminating any history of a formed ad hoc network, as well as resetting the backend server containing the system-level database and the upper three layers' state machines). For each test case, various system performance metrics were collected until the WSN reached "steady state". In this study, steady state was defined as the state in which all nodes within the WSN have reported in, the layer 6 state machines indicate a fully operational WSN available, and all system resources to perform the stated system goals are present. These performance metrics are:

A. *Cold Startup Time*

Cold Startup Time is defined as the time required for the WSN to reach steady state, as defined above.

B. *Aggregate Number of Packets Transmitted until Steady Sate is Reached*

This is the total number packets transmitted in the WSN to set up the routing, establish an ad hoc network, set up "zones" within the WSN, assign primary sensors within each zone, and start reporting measured sensor values.

C. *Aggregate System-Wide Bit Rate until Steady Sate is Reached*

This is a derived value from "Aggregate Number of Packets Transmitted" defined above. It is calculated by multiplying the number of packets by the packet size, thereby obtaining the aggregate number of bits transmitted in the WSN, and subsequently dividing this number by the startup time duration to find an average startup and transient response bit rate.

The system runs completed were based on the presented design. Each test case was performed using one sensor. Then one sensor was added to the WSN and the test case was repeated. Each test case was, therefore, repeated for 1, 2… 10 sensors within the WSN. The following figures illustrate the measured performance metrics for cold startup time, Number of Packets Transmitted in the WSN from Cold Start to Steady State, and cold startup aggregate bit rate. The implementation specific parameters that governed this test set were:

- Sampling rate per sensor: once every 5 seconds
- Packet size = 39 bytes – 312 bits
- Network formation algorithm, Data Rate, MAC Layer Protocol, etc.

Figure 11 depicts the cold startup times on the I-TRM-based WSN for one through ten sensor nodes in the network. With such a large inter-sample period of seconds, the projected large startup time was expected. By reducing the inter-sample period, the large startup time of the WSN could be alleviated. However, it should be noted that inter-sample time is a design value that, once made smaller, will have an impact on the peak bit rate requirements in the WSN. Furthermore, the cold startup data presented above constitute a worst-case scenario for the network formation. Any partial network failure, resulting in a network recovery, would obviously constitute a time duration less than or equal to the times measured in this study.

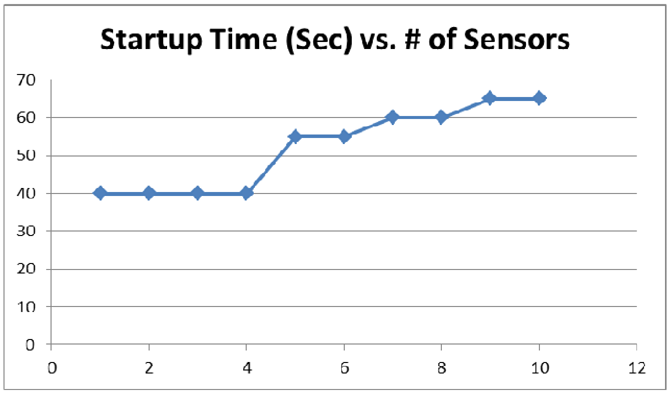

Figure 11. Cold Startup Time versus Number of Sensors

Figure 12 shows the results of experiments with respect to total number of packets transacted in the WSN versus the number of nodes in the network. These data can be used to provide for sufficient bandwidth for a deployed WSN. The count is simply the count of packets generated to implement the messaging required to start up the I-TRM-based WSN.

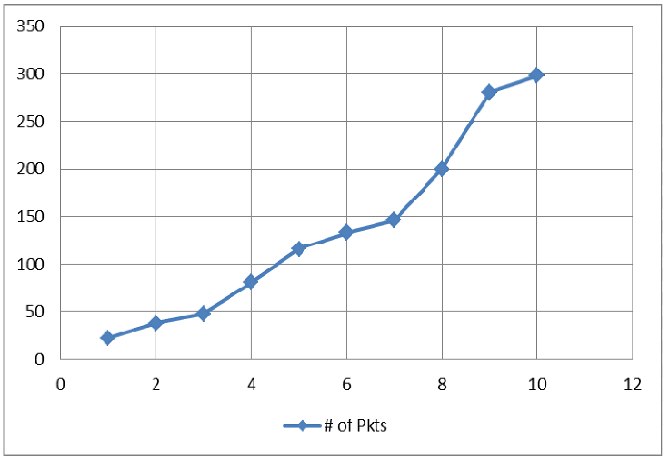

Figure 12. Number of Packets Transmitted in the WSN from Cold Start to Steady State versus Number of Sensors

Figure 13 illustrates the collected total bits transacted per second for the I-TRM-based WSN to go from initial power-up to steady state. Again, it is important to note that with 5-second inter-sample times, this system is well below its bandwidth capacity. The intent of these experiments was not to test the system for congestion-related issues, as I-TRM is indifferent to the underlying communication protocol used in the network. The data here are useful for establishing a baseline of the bit rate required as a function of sampling rate and network size.

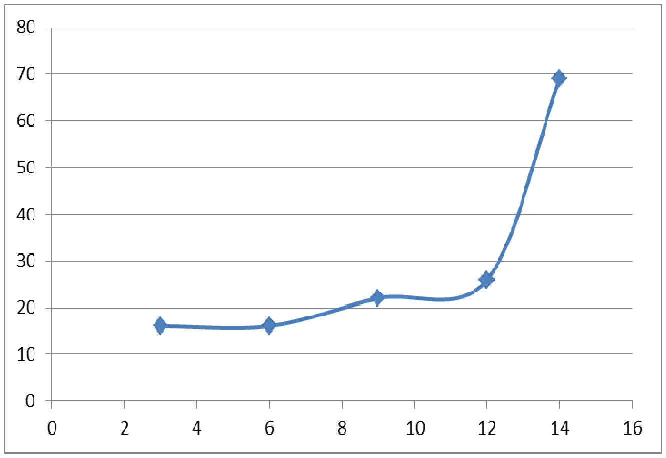

Figure 13. Cold Startup Aggregate Bit Rate (bps) versus Number of Sensors

Steady Measurements: Latencies, Overhead, Message Count, Scalability

In this set of system runs, starting with one sensor node in the WSN, each test case was executed by adding one sensor to the WSN and restarting the WSN from a cold start (i.e., resetting the base station node and all sensor nodes, thereby eliminating any history of a formed ad hoc network, as well as resetting the backend server containing the system-level database and the upper three layers' state machines). For each test case, the aggregate number of bits transmitted was collected until the WSN reached was well past the steady state, as defined above. This aggregate bit count was then divided by the total measurement duration in order to obtain an average aggregate steady-state bit rate. The typical test case duration was about 60 minutes.

Similar to the previous test set, the measured data for the number of sensors varying in the range of {3, 6, 9, 12, 14} are depicted in Figure 14.

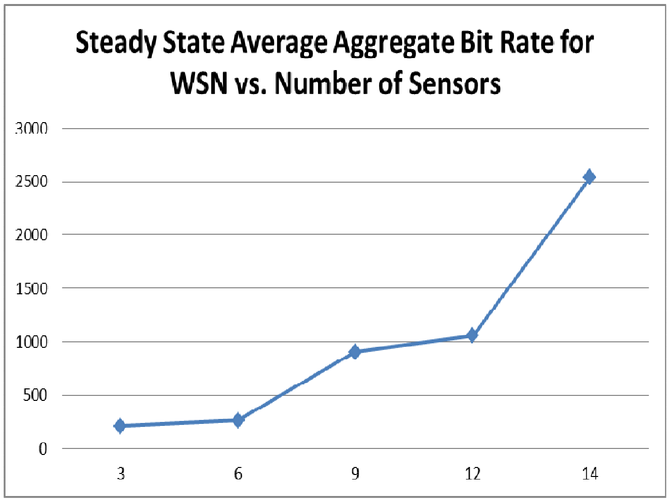

Figure 14. Steady-State Average Aggregate Bit Rate for the WSN versus Number of Sensors

One important point must be made with respect to the obtained results. An aggregate bit rate was chosen as a measure because even though it does not describe traffic requirements across individual links, it is very general in describing upper boundaries for a system bandwidth. Obviously, depending on the WSN configuration and routing patterns, multi-hop vs. broadcast, etc., traffic loads across different links in a WSN vary widely. In the absence of any such specific data, the average aggregate bit rate is a good performance metric.

Steady Measurements: Peak Bit Rate

While measurements in the section above provide valuable information about the average aggregate bit rate in the system, they provide no useful information on the instantaneous "peak" bit-rate requirements on the system. Such peak rates can, for example, be observed during the initial formation of the network, as well during a partial recovery from a node failure. The following set of data was also collected from the test set introduced in the previous section. The data presented in Figures 15 through 19 illustrate peak aggregate bit rates required in WSNs with increasing numbers of sensors within them.

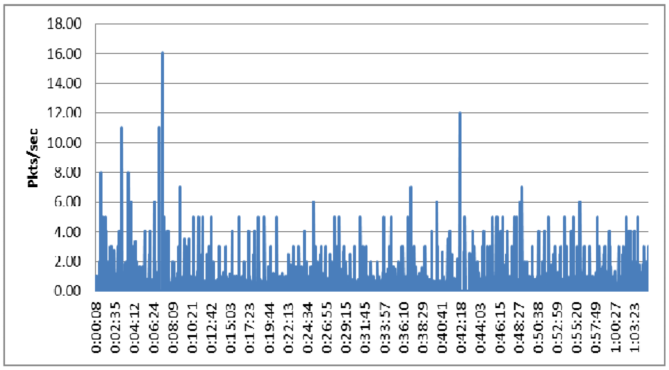

Figure 15. Peak Packet Rate for a WSN with 3 Sensors

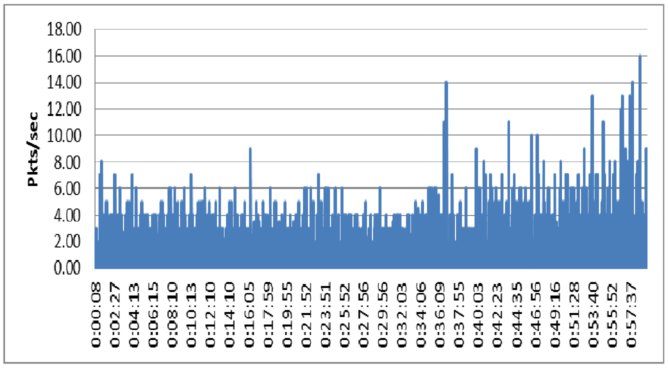

Figure 16. Peak Packet Rate for a WSN with 6 Sensors

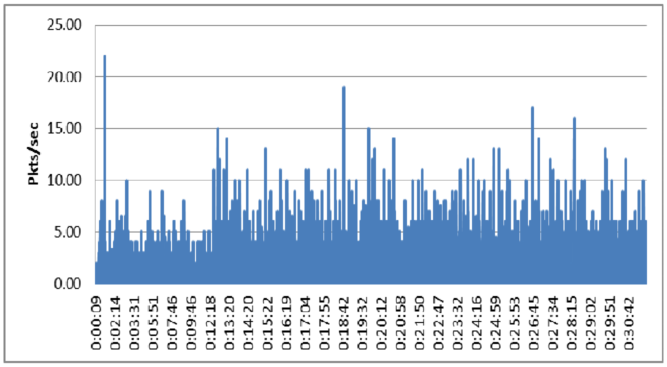

Figure 17. Peak Packet Rate for a WSN with 9 Sensors

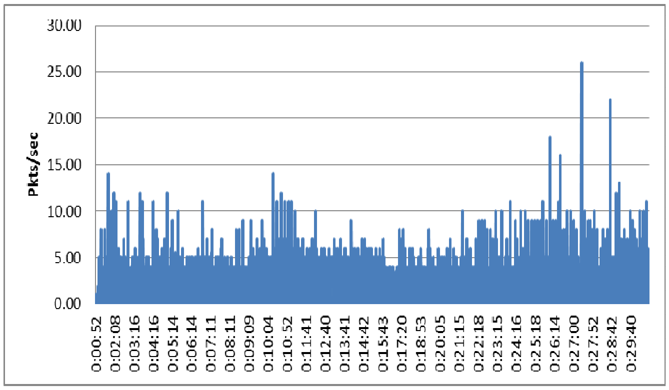

Figure 18. Peak Packet Rate for a WSN with 12 Sensors

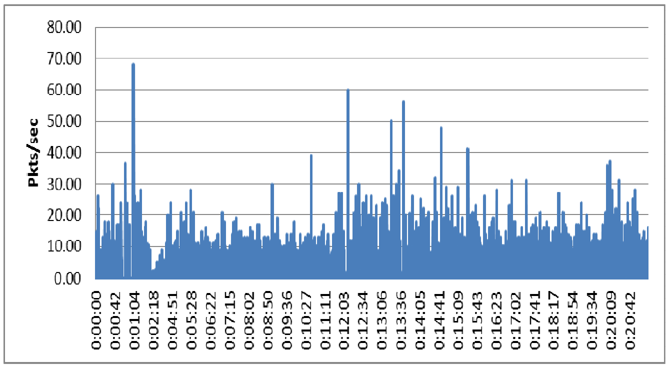

Figure 19. Peak Packet Rate for a WSN with 14 Sensors

As can be seen above, the peak demand of the WSN bit rate varies as the number of sensors is increased.

Conclusion

This study defined a novel framework for wireless sensor networks. A complete system framework, architecture, and implementation for a self-aware adaptable, distributed sensing and computing system capable of functioning in a broad array of environments was developed. The functional breakdown of each layer and the interlayer interaction was developed and specified, including models for data and metadata structures and generic behaviors. In order to validate the proposed API (in the context of the I-TRM), a full WSN system was developed, demonstrating a significant subset of the APIs offerings across three target problem spaces: 1) environmental safety, 2) embedded instrumentation, and 3) medical instrumentation and monitoring.

We hope and anticipate that the current platform implemented based on our proposed I-TRM can be used by researchers to develop not only robust real-time models of the algorithms listed above, but also novel algorithms to further expand on the ever-growing field of Wireless Sensor Networks.

References

[1] Joshi, H., & Michel, H. (2008). Integrated Technical Reference Model and Sensor Network Architecture. *International Conference on Wireless Networks.* Las Vegas, NV.

[2] Beheshti, B. D., & Michel, H. (2011). A Proposed API for the Information Plane of the WSN Integrated Technical Reference Model (I-TRM). *Proceedings of SDR'11 Wireless Innovation Conference and Exposition.* Washington DC.

[3] Beheshti, B. D., & Michel, H. (2011). A proposed API for the control plane of the WSN Integrated Technical Reference Model (I-TRM). *Emerging Technologies for a Smarter World (CEWIT).* (pp. 1-5).

[4] Hadim, S., & Mohamed, N. (2006). Middleware: middleware challenges and approaches for wireless sensor networks. *Distributed Systems Online, IEEE.*

[5] Romer, K., Kasten, O., & Mattern, F. (2002). Middleware challenges for wireless sensor networks. *ACM SIGMOBILE Mobile Communication and Communications Review*, *6*(2).

[6] UC Berkeley, TinyOS -- An open-source OS for sensor networks. *Fifth International TinyOS Technology Exchange (TTX5).* Berkeley, CA.

[7] Hill, J., Szewczyk, R., Woo, A., Hollar, S., Culler, D., & Pister, K. (2000). System Architecture Directions for Networked Sensors. *Proceedings of ASPLOS-IX.* Cambridge, MA, USA.

[8] Madden, S., Franklin, M. J., Hellerstein, J. M., & Hong, W. (2003). The Design of an Acquisitional Query Processor for Sensor Networks. *Proceedings of the 2003 ACM SIGMOD international conference on Management of data (SIGMOD '03).* ACM, New York, NY, USA, 491-502.

[9] Serri, J. A. (2004). Reference architectures and management model for ad hoc sensor networks. *Sensor and Ad Hoc Communications and Networks. IEEE SECON 2004. 2004 First Annual IEEE Communications Society Conference*, (pp. 592- 600).

[10] Zimmermann, H. (1980). OSI Reference Model--The ISO Model of Architecture for Open Systems Interconnection. *Communications, IEEE Transactions*, *28* (4), 425- 432.

[11] Shakkottai, S., & Rappaport, T. S., & Karlsson, P. C. (2003). Cross-Layer Design for Wireless Networks. *IEEE Commun. Mag., 41*(10), 74–80.

[12] Beheshti, B., & Michel, H. (2011). A Cross Layer, Adaptive Data Aggregation Algorithm Utilizing Spatial and Temporal Correlation for Fault Tolerant Wireless Sensor Networks. *Proceedings of 2012 IEEE Long Island Systems, Applications and Technology Conference (LISAT2011).* Farmingdale, New York.

Biographies

BABAK BEHESHTI is a Professor of Electrical And Computer Engineering Technology at the School of Engineering and Computing Sciences, New York Institute of Technology, Old Westbury, New York, where he has served since 1987. Babak received his BEEE and MSEE both in Electrical Engineering from State University of New York at Stony Brook, and PhD in Electrical Engineering from the University of Massachusetts Dartmouth. Babak is author of numerous articles and papers, and has presented in many conferences on topics ranging from engineering education to wireless systems. Babak is a recipient of the IEEE Millennium Medal, two IEEE Region 1 awards, three IEEE Long island Section awards and the Ellis College Excellence in Teaching Award. Babak is a member of Tau Beta Pi engineering honor society, and Eta Kappa Nu electrical engineering honor society. (email: bbehesht@nyit.edu)

HOWARD E. MICHEL is associate professor of electrical and computer engineering at the University of Massachusetts Dartmouth. He retired from the U.S. Air Force in 1994, having served as a pilot, satellite launch director, engineer and engineering manager. Other achievements include successfully launching seven satellites by directing launch-base test and integration involving booster, satellite, and range hardware; and developing Department of Defense engineering processes for mission-critical computer systems. Michel is currently a consultant for the U.S. Navy in the area of embedded instrumentation and architectures. (email: hmichel@umassd.edu)

A COST DATA STANDARD FOR DRINKING WATER PIPELINE INFRASTRUCTURE RENEWAL ENGINEERING

Stephen M. Welling, Virginia Tech; Sunil K. Sinha, Virginia Tech

Abstract

Cost data management methodologies are integral to buried water pipeline infrastructure asset management. This paper summarizes the development of a novel drinking water pipeline renewal engineering (RE) cost data and metadata collection and reporting methodology as part of the WATERiD project. The objective was to collect high-quality, standardized cost data in an efficient way; that is, leveraging the power of extract, transform, and load (ETL), a process for collecting, homogenizing, and storing data that is made possible through advanced computing and the World Wide Web. Cost data were gathered from over 30 drinking water utilities for nearly 200 pipeline RE applications in the U.S. Direct costs for popular methods of work were gathered along with supplemental direct costs such as traffic control and service reconnections. Societal costs for projects were also derived using previously developed methods. Results show factors driving the overall project cost such as distance to other critical infrastructure and number of valves and fittings, and further gives a monetary estimate of the societal burden involved in drinking water pipeline projects, for example when blocking traffic. This methodology for collecting and standardizing the costs of RE work for drinking water pipelines will be valuable to the industry because it addresses a far greater amount of cost drivers than previously considered by researchers, and was developed to work under the umbrella of a national database now commonly used by utilities.

Introduction

An understanding of informatics is critical to the successful development and sustainability of buried drinking water pipeline infrastructure. This includes real economic and societal solutions to contemporary issues driven by the collection of data and subsequent conversion to valuable knowledge. This knowledge then drives advanced asset management plans that delve into many areas including financial, social, and environmental aspects. While the direct costs of managing the assets can be readily found, often there are no clear patterns or trends on which to base future cost predictions due to disparate datasets and the lack of normalization. Further, it is difficult to understand “soft costs” such as the impacts on society due to commerce and transportation interference caused by pipeline construction projects. Researchers have sought to better understand the impacts of managing these assets by quantifying them in dollar amounts, yet no standard method exists for collecting and reporting these data on a grand scale to determine the true trends and drivers. Best practices in cost estimating and budgeting rely on industry experts from various disciplines, whether engineering, law, environmental, social, and so on. Effective measures require the use of informed judgment and intuition to estimate costs and provide for cost control in all circumstances built on previous experience [1].

The nature of informatics then guides the work towards a single platform for collecting, storing, and manipulating the cost data to societal needs and in a manner that reduces cost and societal impacts, as well as maximizing sustainability. The Water Infrastructure Database (WATERiD, http:// waterid.org) was developed as a central, Web-based interactive database for water infrastructure systems in order to provide a standard platform through which institutional knowledge on several fronts could be shared; it was funded by National Science Foundation (NSF), the United States Environmental Protection Agency (U.S. EPA), and the Water Environment Research Foundation (WERF). The intent of this centralized database is to provide a “one-stop-shop” for a utility researching the costs of technologies or products to apply to a specific project or to approve for use within their municipality. Information about pipeline renewal engineering (RE), condition assessment, subsurface utility engineering for locating pipelines, management practices, models and tools, costs, benchmarking, and product qualification is included.

Tools of the nature of WATERiD have been shown to be valuable in similar industries, such as transportation and energy, yet they have lagged behind in the drinking water industry. This has resulted in continued practices of low-cost pricing as opposed to lifecycle cost estimating, a failure to integrate all necessary disciplines into the planning process, and further a robust, sustainable means of data collection and full utilization of the data. A standard data methodology could prevent disparity in cost estimates and, hence, substantial errors in estimating, where over-estimations have resulted in an inefficient application of precious resources, and underestimation can escalate into expensive change orders or even cumbersome lawsuits. Lastly, managers have traditionally been hindered by having to rely on legacy information sources and heuristics. Coupled with the unseen nature of the pipelines, these dated, less-effective practices have in turn brought misallocation of funds and a buried pipeline infrastructure that might well deserve a rating of D by the American Society of Civil Engineers (ASCE) [2]. Further, is has been shown that financial costs, as a result of compiling and collecting pipeline data, can be too costly for some utilities that might greatly benefit from this type of tool [3].

Background

Previous researchers have sought to develop better estimating methods to meet modern industry needs. One such initiative [4] included the development of estimating models for water pipeline rehabilitation projects, yet only covered the direct costs of the work such as pipe material costs, appurtenances, earthwork, etc. The true costs of the project should include initiatory costs such as design and planning, as well as looking at societal burdens.

Researchers have done work that shows only the direct unit costs of various trenchless methods [5] or only looks at a few variables in order to understand cost drivers [6]. Other research has shown that increasing the number of examples used for cost model development provides more relevance to the industry as a whole [1]. This research transcends previous efforts by its foundational basis on larger datasets, the development of a data standard as a collaborative effort with an expert committee comprising utility directors and consultants with an average of 25 years of industry experience, and its nature as a “living” creature to be continuously upgraded and reviewed as part of the interactive WATERiD database.

USEPA has supported the need for studies similar to this to benefit the water industry in the U.S., where previous researchers determined that adequate amounts of comprehensive, pipeline RE costs are difficult to capture from industry, and a centralized cost database is necessary for utilities to better share, analyze, and utilize cost data in decision making [7], [8]. It was determined that the use of a web-accessible tool was useful to utilities in decision making for asset management and for calculating social costs to assess indirect costs and societal burden of utility construction projects [9], [10].

Interest in infrastructure asset management has been stimulated in recent years as many critical components of the built environment reach the end of their useful lives, often with catastrophic consequences. Utility managers are adopting asset management systems to effectively identify, track, and prioritize maintenance on their assets, particularly pipelines. The goal is to minimize the overall cost of owning the assets while maximizing their useful life [11]. Also, while life is lengthened and cost is reduced, the asset must maintain a required level of performance [12]. Key factors of a successful asset management plan include the effective management of asset design [11], maintenance, condition assessment, RE, and investment decisions.

The successful outcome of each of the parameters can be attributed to leveraging the right information about the system. This warrants the collection of substantial amounts of data from all departments of the utility that must be maintained and kept current indefinitely in order to discover long-term trends and perform enhanced analyses. Having a large arsenal of standardized data can empower utility managers to make better decisions regarding each key component of owning and maintaining this critical infrastructure [11]. A framework to best capture and manage these data from several sources is essential to mitigating unnecessary costs and risks, and enables better decisions [13].

Cost data for buried drinking water pipeline infrastructure is available in inconsistent formats and is collected and stored differently, even within the same utility. Consequently, the need for a cost data standard that can homogenize and sanitize data, and provide direct comparisons for trend and relationship analysis to drive decision making from project through managerial levels is apparent. The collection and conflation process is shown in Figure 1, demonstrating how the disparate cost data obtained from multiple utilities can be collected, standardized, and stored in an automated manner. These standards do not currently exist in an internationally recognized format, thereby limiting the ability of managers to extract much useful information in investment decision-making.

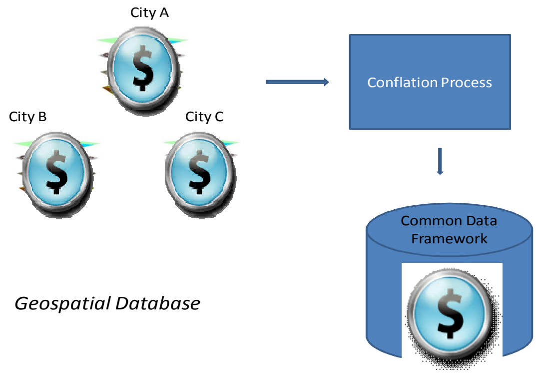

Figure 1. Conflation Process of Disparate Municipal Utility RE Cost Data

Goals

Researchers sought to address these drawbacks in current cost estimating practices in industry by developing a novel standard methodology for drinking water pipeline RE cost data and metadata collection as part of the WATERiD project. The overall goal was to collect high-quality, standardized cost data in an efficient way, i.e., leveraging the power of extract, transform, and load (ETL), a process for collecting, homogenizing, and storing data that is made possible through advanced computing power and the World Wide Web. ETL is an automated process that searches a web domain, recognizes and locates specific data, and pulls the data into a single database while altering it to meet the data model. An analysis of the data was then performed in order to determine apparent trends and cost drivers behind the various projects involved in the study. It also involved the utilization of Google Fusion Tables to query and display cost data on the WATERiD website. Case studies involving the total costs for specific projects were also developed. While this is a major advancement to current practices, data are still lacking to perform robust trend analyses. The cost data graphs shown in this study are a result of piloting the methodology, and they only give a high-level view of current project costs. Estimating practices can be strengthened with industry support of this methodology for data collection, as the power of collecting and standardizing data in an automated manner becomes apparent and creates a real benefit to industry on an international scale.

Research Objectives and Scope

The objective of this research was to enhance industry understanding of costs to support RE decisions for buried drinking water pipeline infrastructure by developing a framework for collecting and standardizing cost data in an automated manner. Further, it considered how RE cost information, when captured in a standard data structure, can produce better statistical analyses for trends and drivers, and also show the entire picture behind these types of projects in capturing standardized societal burden costs from a broad range of sources. The key objectives of the research were to:

- Analyze existing research on data management tools available in order to determine gaps and limitations.
- Develop a methodology for collecting and standardizing costs of RE work for drinking water pipelines that was performed as part of the WATERiD project.
- Collect data from drinking water utilities across the U.S. and conflate them to a standard.
- Analyze the collected data to uncover apparent cost trends and drivers in direct costs, and to determine the amount of societal burden accompanying various RE technologies.
- Develop a platform in WATERiD for utilities to access their data and graph them using Google Fusion Tables.
- Develop case studies on cost from various RE projects.

Project Costs

The total cost of water pipeline replacement is defined as the sum of the direct costs, and social and environmental costs. The direct costs are those related to the practices paid for directly by the utility. Social costs in this study included traffic delay and lost revenues due to business disruption. The environmental costs included only noise pollution in this study. Combined, social and environmental costs make up societal costs for this study.

Most direct and a few societal costs were considered for an analysis of the total cost of the RE work being performed by water utilities. The costs and technologies were selected based on their relatively abundant nature in industry and ease of access. As the data standard comes into more widespread use, other costs and technologies can be added and the data standard can be adjusted as industry directs. The purpose of this study was to show that RE project costs could be collected in a rapid, standardized method and used to find apparent cost drivers. Widespread participation would also demonstrate the benefit of such work so that utilities would be willing to take part for the benefit of industry overall.

Renewal Engineering

USEPA states that "System Renewal includes a wide range of Repair, Rehabilitation, and Replacement techniques that bring the pipeline system at acceptable levels of performance within budgets" [7]. The decision-making process for the proper balance of repair, rehabilitation, and replacement is a function of the condition of the pipe, the lifecycle cost of the various RE (repair/rehabilitation/replacement) options, and the related risk reductions. Renewal of pipeline systems is an engineering challenge when compared with infrastructure assets like bridges, dams, and buildings, because they are "out-of-sight" and "out-of-mind." Common issues that are addressed through renewal efforts include corrosion, joint dislocation, tuberculation, and ground settlement. Numerous materials, installation methods, diameters, and construction practices are also in use, creating a challenge for the utility and the designer in selecting the most appropriate one. Comprehensive system renewal is further complicated by variations in physical, chemical, geographical, technical, and condition of existing and renewed pipe. The determination of the cost of various technologies for renewal of these assets is complex, and further research is needed into the various methods. A few popular methods of renewal were chosen for analysis based on ease of access and collection. These methods are defined in the following sections.

Cured-in-Place Pipe Liners

Cured-in-place pipe (CIPP) liners are used to seal and/or structurally renew existing pipes without excavation of the pipe itself. The basic CIPP liner is a tube, impregnated with a liquid thermoset resin, inserted into a pipeline and cured. The major classes of CIPP liners are described in terms of tube construction, insertion method, the resins used, and the cure method. The tubes can be manufactured from felt or fiber-reinforced materials, and are woven, unwoven, or spirally wrapped.

Pipe Bursting

With pipe bursting (for brittle materials) and pipe splitting (for ductile materials), the old pipe is ruptured and pushed into the surrounding soil, while a new pipe follows the cone-ended bursting tool to replace the old pipe. A key advantage of pipe bursting is that it allows for the upsizing of the original pipe. Depth, soil conditions, peripheral utilities, and service connections will dictate whether pipe bursting is appropriate [14].

Horizontal Directional Drilling

Horizontal directional drilling (HDD) is a relatively new method for installing underground piping. It does not require an entire section of earth to be removed. Rather, pits are excavated on either end and a space is drilled through the soil for piping. Applications of this type have been dubbed as “trenchless” and are expanding the opportunities for piping installation and renewal across the globe. Many piping locations create extenuating circumstances for installation and maintenance, whether under a water body, a major highway, or a structure, wherein HDD can provide an excellent alternative to an open cut excavation. The amount of readily available HDD data made it a good choice for this study.

Open Cut Replacement

Open cut replacement consists of the traditional method of pipe installation, where an excavation crew typically performs surface removal first. The surface is then leveled, if necessary, and a trench dug using a track excavator or backhoe. The existing pipe can either be removed through direct excavation or abandoned in place. Open cut work is typically very disruptive to the adjacent area and requires a great deal of traffic control, is typically slower than trenchless methods, and is also more dangerous as both workers and residents risk cave-ins when in or near the trenches.

Methodology

A comprehensive research review was conducted to determine the published knowledge on the cost of drinking water pipeline RE technologies. The researchers performed data extraction by soliciting input through a standardized spreadsheet that could be placed on a utility’s own website and then accessed via WATERiD’s ETL tool, as outlined in Figure 2. WATERiD was designed to pull datasets into the database from federal sources and utilities, as shown. These data can then be queried and continuously enhanced and reviewed. Also, some data were gathered and entered into the database manually. Python script language was used to develop the ETL tool. WATERiD was written in Drupal, hence the graphs and tables produced from the data were embedded in Drupal pages. An example of this can be found on the Utility Hub Page, which will be discussed later.

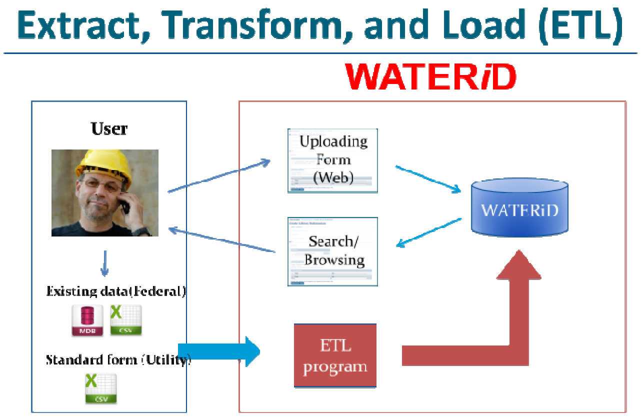

Figure 2. WATERiD ETL Data Collection and Storage Process

The process of translating data from utilities into the standard data model framework started with preparing a cost database. The process included creating data element mappings between the raw data and distinct data model. This initial step allowed for a wide variety of data integration tasks including data transformation between a data source and a destination. The tool allowed for the data from all the participating utilities to be extracted from the Excel spreadsheet into the standard data model and database. A conversion tool was designed to transform the utility cost data and insert them into a geodatabase to be used in future research involving ArcMap, which will allow utilities to query all the cost data collected by technology, date, pipeline attributes, etc., and to perform analyses for cost estimating purposes.

Often, key data were lacking in the spreadsheets that were filled out by the utilities, wherein utility personnel interviews and public utility records filled in the gaps. Additionally, an expert committee made up of utility managers and consultants each provided direction as to the development and implementation of the cost data collection and management methodology. Some limitations included not being able to capture every single type of cost, making some assumptions as to the similarity of projects in grouping them together, and finally assuming that the data received through the collection and interviews were indeed accurate. It is very difficult to collect all the data and deem them to be 100% accurate, hence the standardization can help to minimize errors in the process.

Standard Data Structure

The standard data structure was developed to help save time for utility personnel charged with collecting and reporting the data. The standard data structure was built to allow data to be aggregated and analyzed at different management levels for different output needs. Simplicity and efficiency were the drivers for the design of the standard data structure used in the collection of cost information. Table 1 shows the desired data in the left column and a description of the data in the right.

Usefulness of the Data

The standard data structure was intended to be useful at all hierarchical levels (maintenance, operational, tactical, strategic) within a utility for detecting broad cost trends. Maintenance activities involve routine work meant to sustain normal pipeline operation. Operational activities address the condition of the pipeline with respect to its level of operation. Tactical activities involve projects that help a utility meet its ultimate goals and plans. Strategic activities include those long-term goals and overarching objectives to be met. Data for maintenance and operational considerations will be of the most benefit to that utility itself. However, the data reported of a tactical and strategic nature will help a utility both internally and externally. As broad trends began to be found in the data, they could help drive better financial decision making in industrial utilities to see where the best value could be had. The utilities would then perform analysis and interpretation of the information and make more informed choices in technology. For example, a utility could look at trends in the “Technology Used” category and couple that with a look at the “On Budget” set of data in order to determine the frequency of a particular technology staying within budget. Further, geographical trends can be helpful to utilities in understanding how the cost of pipeline renewal engineering in their location is affected by their geographical region. Data capture and storage by utilities in this manner will allow for the extraction, transformation, and loading of the data into WATERiD. This can be done by the database automatically on a set schedule if the location of the data is known. As utilities adopt these practices, and large amounts of data are collected, robust trending analysis can take place.

Results

Data were received from several utilities participating in the WATERiD project. In all, data were gathered from over 30 utilities for a total of 190 cases. The data were collected into a database and then standardized. Graphs and tables are provided to show the story that the data is telling about the industry practice. All costs were converted to July, 2012, dollars using RS Means 2013 [15] and referenced from their respective areas to the average cost nationwide for heavy construction. Once the project characteristics and direct cost data were compiled, information was collected from the Internet concerning the average annual daily traffic (AADT), approximate number of surrounding businesses near a project that may have been affected by the work, and the average home price in the area.

These data were then used to estimate the societal costs of the project, as performed in previous research [16]. A good-faith attempt was made to determine a best estimate the AADT on the roadways from the DOT sites on the Internet containing historical counts for the specific roadways. If an exact street was not named by the utility, average AADTs, home prices, and the number of surrounding businesses were determined from a brief survey of the area in Google Maps and various real estate websites (e.g., Zillow, Trulia, etc.). In cases where information differed, values were chosen on the more costly side. The final results were compiled, averaged, and expressed.

Equations developed from this study can be found in the work by Jung and Sinha [16]. As an example, working days with traffic control for a typical open cut project might be 10 days, or 80 total hours using eight-hour workdays. If the project took place in a busy residential area, a typical AADT would be 3,000. The equations from the previous study would then become Equation (1) [16]:

Table 1. Standard Data Structure

Description of Data	Desired Data
Region	USEPA Regions 1-10
Utility	Utility
Project Name	Project Name/Phase
Project Location Zip	Location
Bid Date	Date work bid, MM/DD/YYYY
Work Start Date	Date work started, MM/DD/YYYY
Work End Date	Date work ended, MM/DD/YYYY
Item Duration	Hours
(LF/HR)	Production
Project Type	Condition Assessment (CA) or Renewal Engineering (RE)
Application Type	Continuous or Point Repair
Existing Pipeline Type	In-situ Pipeline Material
Existing Pipeline Size	Inner Diameter (inches)
New Pipeline Type	New Pipeline Material
New Pipeline Size	Inner Diameter (inches)
Pipeline Rating Class	Pressure Classification
Rating	Rating in PSI, Size-dimension ratio, Thickness (in, mm, etc.)
Depth	Depth
Age	Pipe Age
Technology Used	Type of Work (CIPP, Pipe Bursting, etc.)
Scope of Work	Continuous or Point Repair
Units	(Lineal Feet, Each, Hours, etc.)
Cost per Unit	Dollars
Item Total	Bid Item Total
Total Cost	Total Contract
Item Percent of Total	Percent
Planning, Design, or Training Costs: Description and Percentage of Total	Costs
Mobilization	Costs
Traffic Control	Costs
Temporary Main	Costs
Main Reconnection	Costs
Service Reconnection	Costs
Valves, Fittings, Cathodic Protection, Hydrants, etc.	Costs

Table 1 cont. Standard Data Structure

Description of Data	Desired Data
Earthwork	Costs
Testing/Inspection	Costs
Surface Restoration Costs:	Costs
Safety Costs (Shoring, etc.)	Costs
Runoff/SWPPP	Costs
Abandonment/Disposal Costs	Costs
Change Orders	Costs
Additional Costs due to Crossings: Description and cost	Costs
Traffic Disruption	Costs
Lost Revenue for Adjacent Businesses	Costs
Noise Pollution	Costs
Funding Source	(Internal Funds, Bonds, Grants, etc.)
Cost of Capital	% of Total Cost
Total Cost all inclusive	Total Cost
On Budget	(Yes/No)
On Schedule	(Yes/No)
Drivers	Primary Drivers for Project (Increased demand, Failure, New funding, etc.)
Circumstances	(Routine/Challenging/Difficult/Emergency)
Notes	Please provide guidance as to what made these costs differ from typical
Other Notes	Text
File path or web address	Information Link

$$\text{Log10 (Cost)} = 0.00022 \times 3000 + 3.5556 \quad (1)$$

or nearly $17,553.

The analysis tool developed for the loss of revenue for local businesses was based on a study conducted in 2004, the formula for which is shown in Equation (2) [17]:

$$\text{LOP}_1 = (\text{number of employees affected}) \times (\text{average hourly output, \$/h}) \times (\text{productivity reduction factor}) \times (\text{project duration; h}) \quad (2)$$

Previous researchers [16] also developed a method for calculating the environmental cost of noise pollution caused by pipeline construction. From this, a noise depreciation index (NDI) was developed to estimate the possible depreciation of property values based on the aversion to the increase in noise. The researchers then applied an equation using the NDI and the increase in noise for a given project; that equation is shown here as Equation (3):

$$0.0017 \times K\ (\text{additional dBAs of effective noise level}) \times \text{original housing price} = \$\ (\text{Noise Cost}) \quad (3)$$

The same researchers used an example of a 20-decibel increase brought about by an open cut excavation project to an area where the median home price was $118,900. The average noise cost for a year then becomes 0.0017 × 20 × 118,900 × 30 = $121,278. The article established the dBA increase for trenchless technologies such as pipe bursting as only 10, thereby only accounting for half the cost of traditional open cut projects.

CIPP

The CIPP work cost for water mains was first plotted by unit cost according to the pipeline diameter in Figure 3, which shows the unit cost per lineal foot (LF) for the various CIPP projects surveyed. The projects ranged from 6–14 inches in diameter, as shown, with the majority of the projects being 6 inches in size. The projects surveyed cost at a minimum of just under $100/LF, and at a maximum of just over $300/LF. A trend line was fit to the data of $y = 9.8231x + 76.503$ with an $R^2 = 0.1763$.

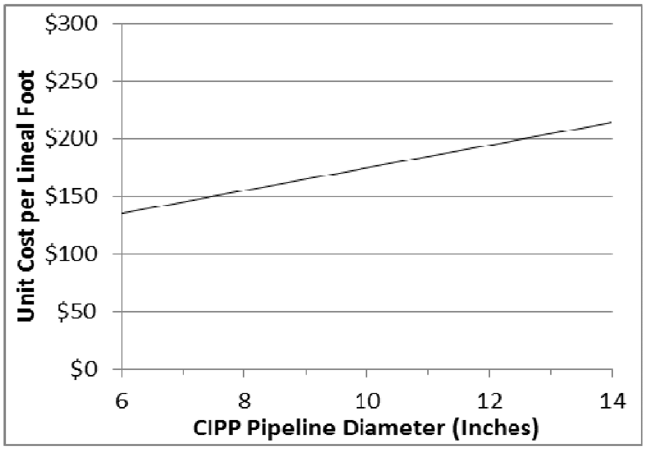

Figure 3. CIPP Unit Cost by Diameter

Following the study of the costs as driven by pipeline diameter, the costs were then plotted to see how project length affected the unit cost per foot (see Figure 4); this projection shows how the project length of CIPP work is affected by the length of the work performed for a particular application. The data seem to converge on an average cost around $125/LF after the length of the project reaches 1,200 LF. This is somewhat intuitive, though more data are necessary to begin to see any significant trends and/or potential cost drivers.

Lastly, the various supplemental direct and societal costs were broken out and plotted to see how they were driving the total project cost. Apparently, the only major contributors to the overall cost burden to society was the cost of traffic disruption, while the major components of project cost to the utilities were mobilization, testing and inspection, valves and fittings, and service reconnections. The various costs supplemental to CIPP work are shown by percentage of the total work, which shows that only five types of costs are adding to the cost of the projects in a significant way. Mobilization played the biggest role in the various supplemental costs beyond CIPP work, followed by testing and inspection, valves and fittings, and service reconnections. Safety measures were next in line in their influence on the overall project cost and consisted of items such as protective gear for workers entering manholes and trench protection. The provision of a temporary water main was the only other cost that is adding a noticeable amount to the total costs of the projects. The societal costs, however, are surprising in their overall effect.

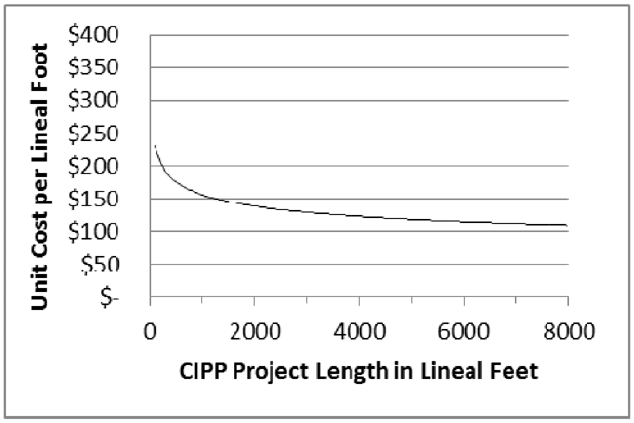

Figure 4. CIPP Unit Cost by Project Length

The excessive traffic costs were due to the project in New York City. The low environmental noise costs were caused by a few of the projects taking place: Joint Base Elmendorf-Richardson (JBER) and a U.S. Air Force base in Alaska. These costs are not shouldered by the utility or municipality directly, but by society as a whole. The largest of these, traffic disruption, would be the cost to society of the hindered lane of travel in roadways considered important to commerce. As will be seen in other technologies for pipeline renewal, this is rather low, showing that the trenchless nature of this work provides a large advantage in relieving the burden on society. The level of business disruption is often correlated with the level of influence of traffic disruption, quickly growing as the project site nears the city centers. Yet, again, CIPP work creates a far better alternative for local business than methods requiring trenching and removal of the majority of the street and even walkways. Finally, the noise pollution related to CIPP work is shown as negligible; this is due to the nature of the work and the lack of extensive earth-moving equipment inherent to other methods of pipeline construction. Figure 5 shows the differing costs as a percent of the total cost burden. In this graph and those like it throughout the paper, the direct costs paid by the utility are shown by the darker bars, with the lighter bars representing the burden on society.

HDD

Next, HDD projects were analyzed, first to see how the unit cost was affected by the pipeline diameter. The data more or less follow a linear trend as costs rise with the diameter of the pipeline in question. Projects that were more costly than others of a similar size were those involving river crossings, using a heavier-rated pipe than others, or had access issues that drove the cost higher. Contractors that were afforded plenty of work space and the ability to access the area of the bore were able to bid lower prices. When the project unit costs for HDD work were plotted as a function of pipeline diameter, it was apparent that the costs mostly followed a linear trend. Some projects costs were due more to the heavier nature of the pipe or the limited access or room for mistakes, as in river crossings. Beyond that, the projects were all of a similar nature and strong trends for cost drivers were not apparent from the project context. Figure 6 depicts the unit cost of HDD work for water line replacement as a function of pipeline diameter.

The data were then plotted to see cost as a function of project length in Figure 7. This figure shows the unit costs for HDD work as affected by the length of the work completed in the specific project. A trend line was fit to the data of y = 143.57x-0.218 with an $R^2 = 0.1084$. The data mostly followed a power trend line, except for the project involving a river crossing and another using heavy-duty pipe. The data all fell under 4000 lineal feet in project length. Again, projects costing more had access issues or were driven as a function of the pressure class of the pipeline installed. Also, it appeared that as the project length surpassed 1000 LF, most of the projects fell within a lower unit cost range.

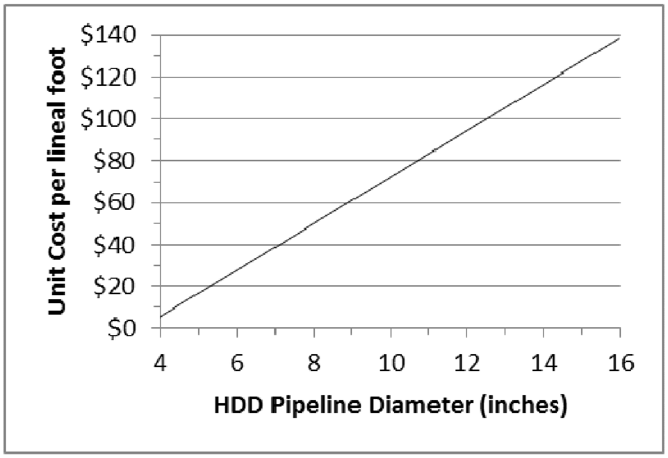

Figure 6. HDD Unit Cost by Diameter

Finally, the other direct and indirect costs were plotted as a percentage of the total cost of the project in Figure 8,

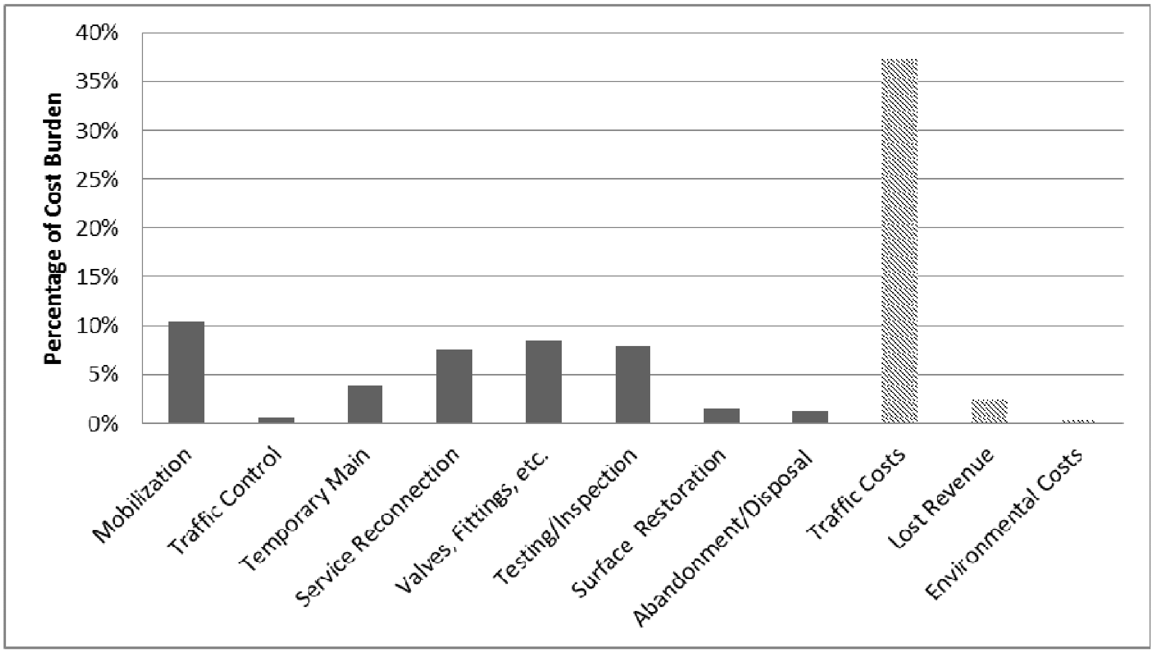

Figure 5. Supplemental Costs of CIPP Work by Percentage of Cost Burden

which shows that surface restoration and service reconnection accounted for the largest direct costs associated with the work. This was caused by work in city streets, where extensive excavation work was performed in order to accommodate the drilling pits and warranted extensive restoration efforts. Valve and fitting installation also accounted for large portions of the project costs. Traffic disruption and lost business revenues accounted for a substantial amount of burden to the community, while noise pollution was of a lesser nature at ~2% of the total cost.

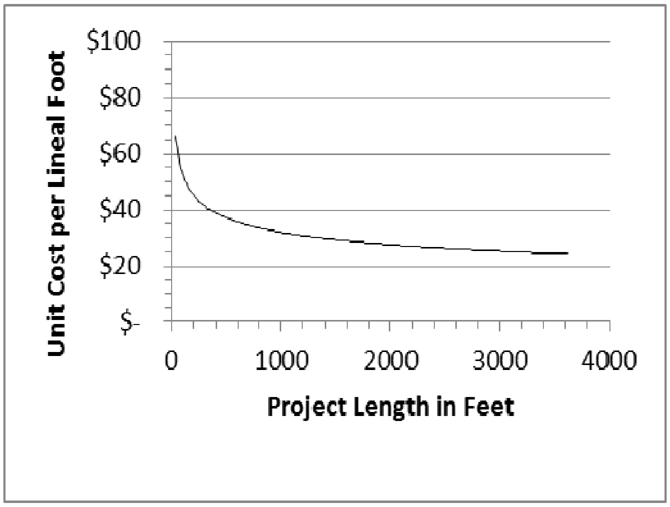

Figure 7. HDD Unit Costs by Length

Open Cut

Then, the cost data for open cut replacement was plotted. A trend line was fit to the data to show where the average cost was falling. Most of the smaller diameter projects were seeing costs in the $20–$100/LF range. The projects that appeared inordinately high were very short in length. The trend line was $y = 4.3885x + 22.482$ where $R^2 = 0.1813$. Projects that exceeded this mark were mostly of a shorter length and required immediate attention rather than being a part of a large routine project. It appeared that as utilities were thinking ahead and rehabilitating old lines rather than fixing them after they had become a problem were seeing a great deal of cost savings per LF. The unit cost by pipeline diameter can be seen in Figure 9, which shows the data for the open cut projects surveyed. The unit cost data were then plotted for open cut work by the length of the project, as shown in Figure 10.

The percentage of total project cost that various supplemental direct and societal costs comprised was then plotted, which shows the average of the contribution to the total cost of the work from each type of cost related to open cut work. The lower bars in Figure 11 represent the other direct costs of the work such as mobilization and service reconnections. Valves and fittings, user services, and surface restoration played major roles in supplemental costs and were actually lower in this case than trenchless methods as the ground was already open from the pipeline installation. The societal

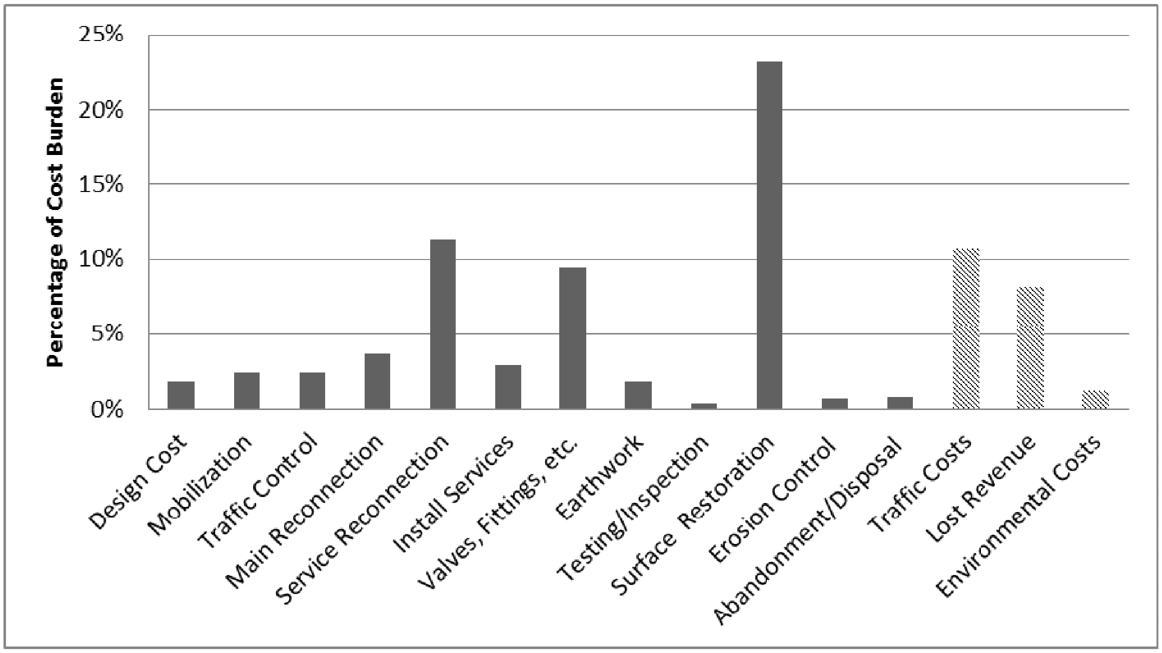

Figure 8. Supplemental Costs of HDD Work by Percentage of Cost Burden

costs are worth noting as they create a much, much larger burden on society than their trenchless counterparts. This is intuitive as it is commonly known that open cut work is far more obstructive to society with lane blockage, with entire road closings being the norm rather than the exception. Also, heavy excavators, dozers, frontend loaders, and so on create a great deal more noise than pipe lining, drilling, and bursting projects. This can be seen in Figure 11.

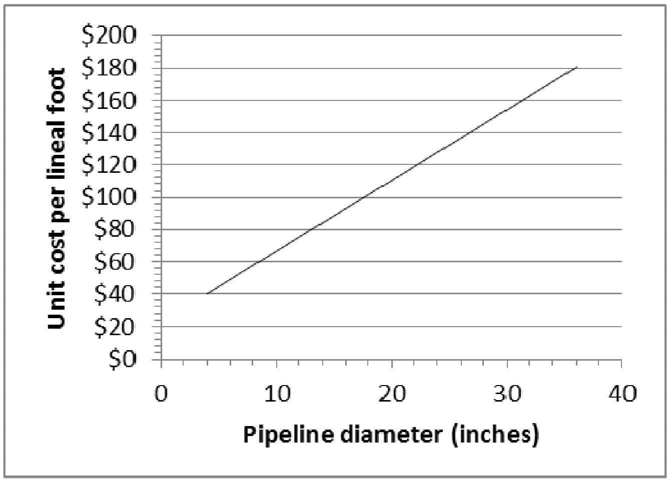

Figure 9. Open Cut Unit Cost by Diameter

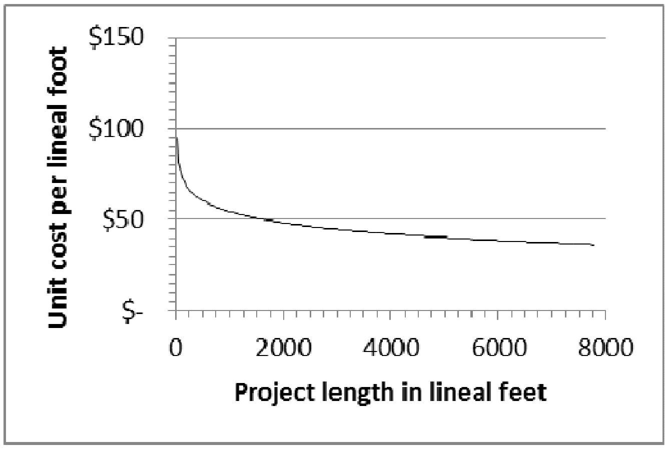

Figure 10. Open Cut Unit Costs by Length

Pipe Bursting

Pipe bursting in drinking water pipe renewal was first plotted by unit cost according to pipeline diameter in order to determine trends and drivers to show the unit cost of pipe bursting per LF and how it may change according to the inner diameter of the pipeline being renewed. Data were gathered in the range of 4 to 12 inches. Data were much more easily found in the 6- and 8-inch sizes. Projects with

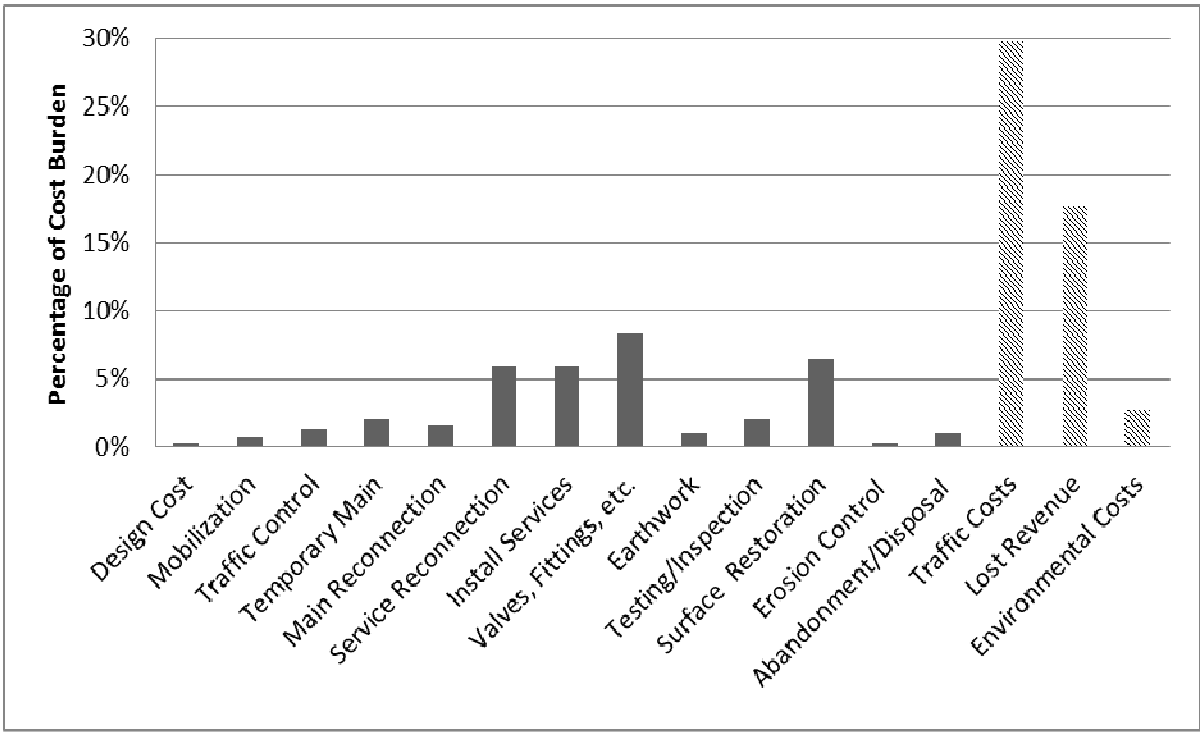

Figure 11. Supplemental Costs of Open Cut Work by Percentage of Cost Burden

more excessive costs were shorter and had limited access for entry and exit holes. Though a great deal of data are not available in this category, it is apparent that the majority of smaller-diameter projects would fall in the $30–$150/LF range. As the diameter increases, it appears likely that this trend will not continue. This is shown in Figure 12. Lastly, the other direct and indirect costs were graphed by percent of the total item cost, as shown in Figure 13.

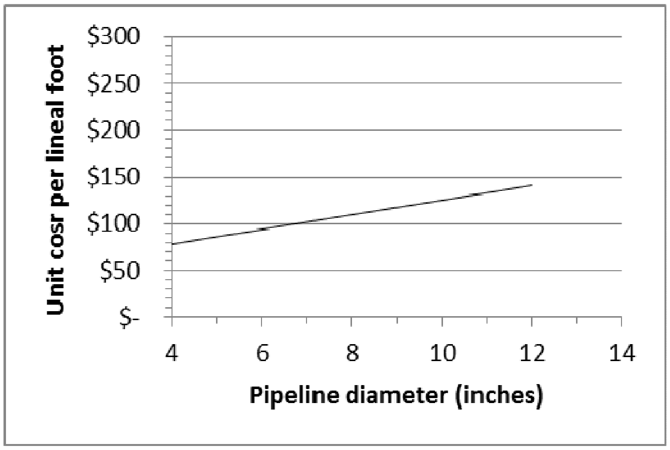

Figure 12. Pipe Bursting Work Unit Cost by Pipeline Diameter

The results of the cost breakdown were interesting in that the valves and fittings were so much of an influence on the total cost. This shows that pipe bursting a project in long runs without any branches or services can be very cost effective, yet, for every fitting, service, etc., that needs to be installed, this can heavily influence the overall cost of the work. Of the direct costs related to the work, valves and fittings accounted for the largest percentage of the cost. Service reconnections played the next biggest role in the various supplemental costs in addition to the pipe bursting work, followed by surface restoration, main reconnections, and old pipeline abandonment. Earthwork was next in line in its influence on the overall project cost and consisted of items such as test pits and the like. Mobilization (which frequently includes bonds and insurance, but is also often limited as a percentage of the total contract, for example, no more than 3%) did not significantly drive the cost in most cases, though they were often significant amounts of money. Utilities were able to take advantage of economies of scale and to absorb much of these costs into a great deal of rehabilitation work. The remaining categories of direct cost can be seen as not overly crucial in determining the overall cost of the project, each falling below 2.0% of the total cost. The societal costs were not significant in their overall effect. These costs are not shouldered by the utility or even the municipality directly, but to society as a whole. The largest of these, traffic disruption, added less than 5% of the total cost of the work to society.

Utility Hub Pages were created in the WATERiD website to provide information to users as to what technologies and practices were being employed with regards to managing

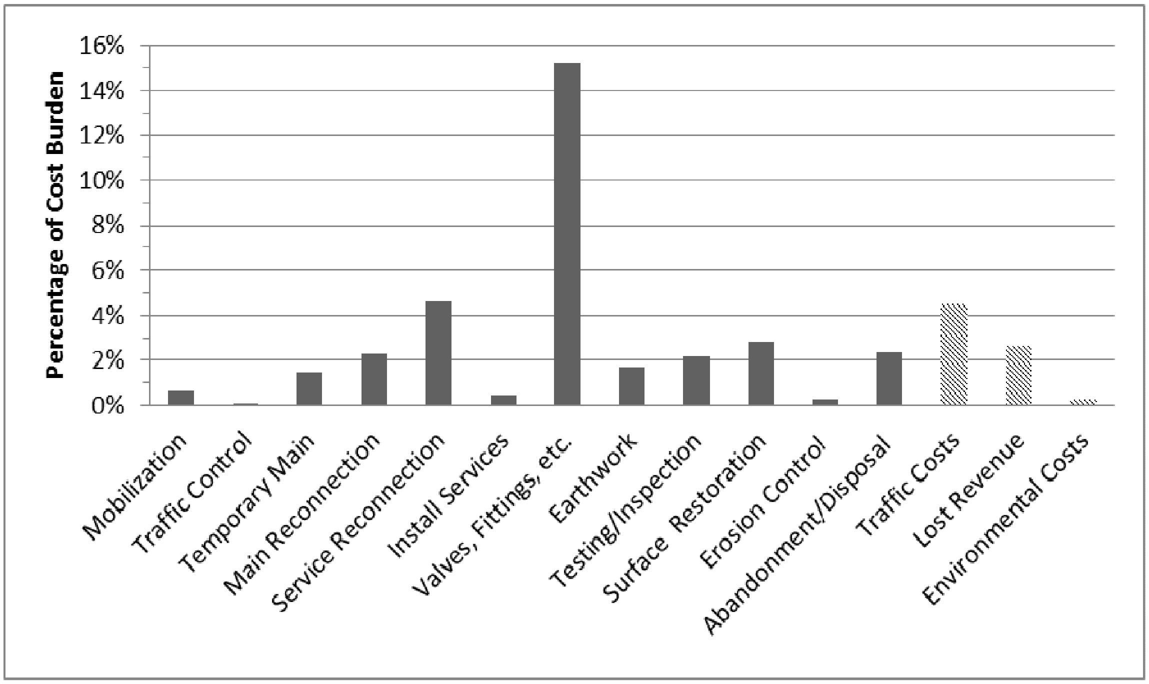

Figure 13. Supplemental Costs of Pipe Bursting Work by Percentage of Cost Burden

their buried pipeline assets. The Hub Pages were also found to be useful to the utilities themselves as they could access their own data in a simple, single location. The hub page for the Town of Blacksburg, Virginia, is shown in Figure 14.

Town of Blacksburg Utility Hub Page

The Town of Blacksburg provides water, sewer and refuse services. The Town is a member of the Blacksburg-Christiansburg-VPI Water Authority, which delivers and sells wholesale water to the Town. The Water Authority currently has the capacity to supply 12.4 million gallons per day. Average daily consumption is approximately 7.0 million gallons for the system, and the Town's daily consumption is 3.3 million gallons. Blacksburg has 164 miles of water mains, four pump stations and five water tanks, with a total capacity of 5.5 million gallons.

Related Case Study

- TOWN OF BLACKSBURG GIS DATA MANAGEMENT
- Application of Virginia Underground Utility Marking Standards
- APPLICATION OF RFID MARKERS AND GPS TECHNOLOGY FOR SUE
- SewerCAD Model for Capacity Assessment at Town of Blacksburg (TB)
- Successful Sewer System Evaluation Survey Practices in the Town of Blacksburg, VA

Figure 14. Hub Page for the Town of Blacksburg, Virginia, as Found on the WATERiD Website

While data were collected on many facets from these utilities in concert with the objectives of the WATERiD project, the goal of this study was to demonstrate the functionality of the site with regards to the cost data. Sample graphs were created from the data to show how it can be used, as shown in Figure 15. These graphs were not created to show comprehensive trends or drivers, but to provide an example of what can be done with the standardized data. The users themselves can come to the site and create any plot they desire from the data, only limited by the options within Google's Fusion Tables. Several participants found this to be a useful tool with great possibilities going forward.

Under development!

Figure 15. Sample Graphs Related to Cost in the Hub Page

Conclusions and Recommendations

This paper summarized the development of a novel drinking water pipeline RE cost data and metadata collection and reporting methodology as part of the WATERiD project. The authors employed an ETL tool for collecting cost data from nearly 200 RE applications from over 30 drinking water utilities in the U.S. While this is a major advancement to current practices, the data are still lacking in order to be able to perform robust trend analyses. The cost data graphs shown in this paper were a result of piloting the methodology, which can only give a high-level view of current industry practices. Once industry professionals begin to adopt this process, it will drive best practices in infrastructure cost management to unsurpassed levels, and greatly benefit the global drinking water industry.

The RE techniques analyzed here included open cut replacement, cured-in-place pipe lining, horizontal directional drilling, and pipe bursting. Of the direct costs involved, it appeared that valves and fittings, service reconnections, and surface restoration accounted for the majority of the additional costs respective to the work. Of the indirect costs, traffic disruption appeared to be the greatest social cost to the consumer. It was also found that utilities do not collect all the useful cost information in pipeline management, and that a standardized data capture and reporting methodology would be of great value to industry. More importantly, it was shown that utilities were willing participants in this study, evidence that they saw great value in this type of work concerning the creation and implementation of a central cost data standard and database, by which data could be collected, analyzed and shared. Cost data management is an important aspect of any infrastructure management system. While the most commonly used level of data storage and management involves the use of a computerized database system not created specifically for capturing and leveraging condition assessment and RE cost data, greater sophistication in data management is required in order to more effectively create a basis upon which management decisions can be made with respect to initiating RE work for drinking water pipelines. Armed with standardized, quality data, utility managers can defend budget requests and more effectively manage their water pipeline infrastructure.

Acknowledgements

Special thanks to NSF, USEPA, and WERF, and all of the individuals that were integral to this study. Any opinions, findings, and conclusions or recommendations expressed in this material are those of the authors and do not necessarily reflect the views of the NSF, USEPA, and WERF.

References

[1] Mahfouz, T., Jones, J., & Kollwitz, S. (2013). An Ordered Probability Framework For Assessing Markup Values for the Construction Industry. *International Journal of Engineering Research & Innovation, 5*(1), 53-61.

[2] ASCE (2013). 2013 Report Card for America's Infrastructure. Retrieved May 5, 2013from http://www.infrastructurereportcard.org/drinking-water

[3] Angkasuwansiri, T., & Sinha, S. (2013). Comprehensive List of Parameters Affecting Wastewater Pipe Performance. *Technology Interface International Journal, 13*(2), 68-79.

[4] Clark, R., Sivaganesan, M., Selvakumar, A., & Sethi, V. (2002) Cost models for water supply distribution systems. *Journal of Water Resources Planning and Management, 128*(5), 312–321.

[5] Selvakumar, A., Clark, R., & Sivaganesan, M. (2002). Cost for water supply distribution system rehabilitation. *Journal of Water Resources Planning and Management*, *128*(4), 303–306.

[6] Yang, M., & Su, T. (2007). An optimization model of sewage rehabilitation. *Journal of the Chinese Institute of Chemical Engineers, 30*(4), 651–659.

[7] USEPA. (2010). State of Technology for Rehabilitation of Wastewater Collection Systems. (Contract No. EP-C-05-057. Task Order No. 58): U.S. Environmental Protection Agency.

[8] USEPA. (2010). Report on Condition Assessment of Drinking water Collection Systems (No. EPA/600/R-10/101): United States Environmental Protection Agency.

[9] Matthews, J., & Allouche, E. (2009) *TTWorld: A Web-Portal For Assessing The Suitability Of Trenchless Construction Methods For Utility Projects And Associated Social Cost Savings*. Paper Presented at ASCE Pipelines Specialty Conference, 2009.

[10] Matthews, J., & Allouche, E. (2010) *A Social Cost Calculator For Utility Construction Projects*. Paper presented at No Dig Conference, 2010.

[11] McKibben, J., & Davis, D. (2002). Integration GIS, Computerized Maintenance Management Systems (CMMS) and Asset Management. *Proceedings of the 22nd Annual ESRI International User Conference*, San Diego, CA, USA, July 8-12, (http://gis.esri.com/library/userconf/proc02/pap0554 /p0554.htm).

[12] Harlow, K. (2000). Part 1: Asset Management: A Key Competitive Strategy. Retrieved January 12, 2012, from (http://www.publicworks.com/content/news/article.asp?docid={187e5ca1-8fc5-11d4-8c63-009027de0829})

[13] Faculty of Information Studies. (2007). Information Management FAQ. University of Toronto, ON, Canada, (http://choo.fis.utoronto.ca/ IMfaq) Accessed May 4, 2012.

[14] FHWA. (1995). Culvert Repair Practices Manual. Volume 1, Chapter 7.

[15] RS Means. 2013. RSMeans Construction Cost Indexes, July 2013.

[16] Jung, Y., & Sinha, S. (2007). Evaluation of Trenchless Technology Methods for Municipal Infrastructure System. *Journal of Infrastructure Systems*, *13* (2), 144-156

[17] Gilchrist, A., & Allouche, E. (2005). Quantification of social costs associated with construction projects: state-of-the-art review, *Tunnelling and Underground Space Technology*, *20*(1), 89-104.

Biographies

STEPHEN M. WELLING is a Graduate Research Assistant in Civil Engineering at Virginia Tech. He earned his B.S. degree from Utah State University (Civil Engineering, 2005). Mr. Welling is currently a Ph.D. Student at Virginia Tech. His interests are in cost and risk management of water pipeline infrastructure systems. Mr. Welling may be reached at stevo82@vt.edu.

SUNIL K. SINHA is an Associate Professor of Civil Engineering at Virginia Tech. He earned his B.S. degree from Birla Institute of Technology, MS and Ph.D. (Civil and System Design Engineering, 2000) from the University of Waterloo, Canada. Dr. Sinha is currently teaching at the Virginia Tech. His interests are in asset management, pipe infrastructure systems, and decision-making methodologies for the rehabilitation of civil infrastructure systems. Dr. Sinha may be reached at ssinha@vt.edu.

A SCHMITT-TRIGGER AND TRANSISTOR-SIZING-BASED OPTIMIZATION TECHNIQUE FOR DYNAMIC CMOS CIRCUITS

Kumar Yelamarthi, Central Michigan University

Abstract

One of the most widely used styles of circuit used in high-performance VLSI systems is dynamic CMOS. With its principal advantage of being able to implement evaluation logic only in a pull-down network, it offers a significant performance boost when compared to its static CMOS counterpart. However, the rising magnitude of circuits implemented on a chip, along with shrinking device size and process variations, has increased the complexity of implementing dynamic CMOS circuit efficiently. Answering this challenge, the author proposes a Schmitt-trigger and transistor-sizing-based optimization technique for dynamic CMOS circuits. This method operates by i) identifying the significance of each timing path, and updating the size of each transistor in the path; ii) running the evaluation network and feedback keeper at lower supply voltages in order to reduce charging and discharging at dynamic nodes; and, iii) using a Schmitt trigger to restore the low-voltage swing at the dynamic node to normal levels at the design output. When tested through implementation on a IBM 90nm CMOS process, the proposed method has shown an improvement in worst-case delay by 40.64%, delay uncertainty by 49%, delay sensitivity by 28%, power consumption by 36%, and energy-delay-product by 77% when compared to their initial performances.

Introduction

Traditionally, the goal of CMOS circuit designers has been to obtain the best trade-off between delay and power consumption. As CMOS technology continues to scale towards the nanometer regime, millions of transistors are densely packed to increase system functionality. Such advancements of dense packaging and shrinking device sizes led to the advent of further challenges in power density, leakage power, parametric yield, and process parameter variations [1]. Furthermore, performance degradation of circuits occurred due to leakage, poor noise margins, dense packaging results in design performance variability, and loss of parametric yield [2], [3]. The ratio of this performance variability to nominal values has been increasing with shrinking device sizes towards 32nm [3]. At the same time, process parameter variations have a strong impact on circuit performance in terms of speed, dynamic power, leakage power, and even possibly causing functional failure [4], [5].

Of the many challenges in the timing optimization of dynamic CMOS circuits, variation in delay (uncertainty) due to process variations is the most prominent due to parameter variations within and across dies. Tschanz et al. [6] showed that circuits implemented using 180 nm CMOS technology have shown about 30% variation in timing performance, and a 20x variation in leakage current. Along with shrinking CMOS device sizes, the magnitude of these performance variations is predicted to increase significantly [7-10].

Typically, microprocessors and digital signal processors are designed using dynamic CMOS circuits due to their speed and compactness in designs with wide fan-in [11]. However, dynamic CMOS circuits suffer from dynamic leakage power and sub-threshold leakage current, thereby limiting overall design performance. Identifying this challenge, numerous methods were proposed in the recent years. While many of these methods increase system performance in one factor, it is often at the expense of others. Transistor sizing is one efficient method that allows designers to move away from the conventional method of minimizing a single factor, instead focusing on optimizing several factors concurrently. For instance, through transistor sizing: a) several sources of leakage current and power consumption due to glitches can be minimized; b) propagation delay due to device parasitic capacitances can be reduced; and, c) sufficient noise margins can be maintained. Addressing these challenges, and based on previous work by the author [12], [13], a Schmitt-trigger and transistor-sizing-based optimization method for dynamic CMOS circuits is presented here, while accounting for process variation and parametric yield.

Delay Uncertainty due to Process Variations

Process variations are categorized into two types: die-to-die variations and within-die variations. Within-die variations influence the mean of delay distribution, while die-to-die variations influence the variance, which is also an important factor in performance optimization [14]. Consider the situation presented in Figure 1, where curve "A" denotes the delay distribution of a pre-optimized circuit. When the circuit is optimized only for mean delay, delay distribution curve "B" is formed, where a significant portion of the circuits operate fast, but with higher leakage current. On the other hand, when the circuit is optimized only for delay variance, delay distribution curve "C" is formed, which has lower delay variance but no positive impact on mean delay.

As the objective of circuit optimization is reducing both circuit delay and leakage current, accounting for a linear combination of mean and standard deviation ($\mu+\sigma$) improves overall performance, resulting in curve "D", where μ is the mean delay, and σ is the standard deviation of delay distribution. Other parameters to be considered during performance optimization are delay uncertainty ($\Delta = T_{max} - T_{min}$) and delay sensitivity ($\delta = \sigma/\mu$), where T_{min} and T_{max} are the minimum and maximum delays due to process variations.

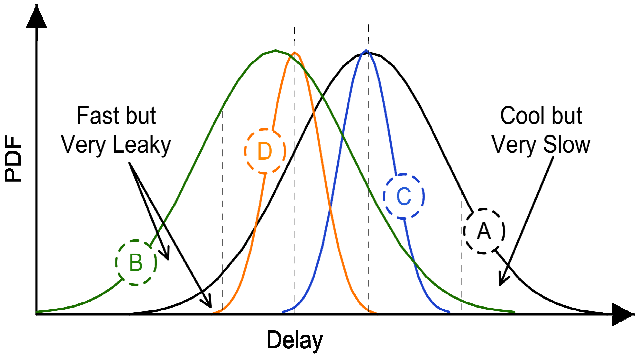

Figure 1. Delay Distribution Profiles with Different Optimization Parameters

While significant research was performed in order to identify and reduce the impact of process variations, the majority either deal with statistical variation—and thus are not optimal for circuits with large numbers of process variations—or require these variations to be correlated, which is often not the case in CMOS circuits [15]. With the rising number and magnitude of process variations, along with limited simulation time available, the ideal solution is to pick a set of parameters, find the worst-case path in each case, and take a combination of these paths to obtain the performance characteristics (μ, σ, Δ, δ). Some parameters that are to be considered during this process include junction capacitance, overlap capacitance, gate length and width, threshold voltage, gate oxide thickness, and mobility [16].

Previous Work

Due to the significance of timing optimization in high-performance circuits, numerous methods utilizing transistor sizing have been proposed [15], [17-20], but are primarily targeted towards static CMOS and transistors with multiple threshold voltages. One of these prominent works is the TImed LOgic Synthesizer (TILOS) [17] that sizes transistors iteratively based on the significance of the timing path at the cost of larger device sizes, and higher power consumption. MINFLOTRANSIT, proposed by Sundararajan et al. [18], operates based on the iterative generation of directed acyclic graphs at every step of the timing optimization process. One of the other predominately used transistor sizing methods is *Logical Effort* [15], which requires computation of every input capacitance, a cumbersome task for circuits with interconnected timing paths; this method also operates at the expense of increased area [15]. One of the other recently proposed works is the simple exact algorithm [20] that operates by grouping series and parallel transistors for iterative parametric sweep analyses. While this method works for dynamic CMOS circuits, it does not always converge to an optimal solution. Also, the simulation time increases at a quadratic rate in proportion to size of the design. Most importantly, none of these algorithms account for process variations.

On the other hand, numerous methods [6], [8], [21-24] have been proposed to limit the impact of process variations on CMOS circuits. The Adaptive Body Biasing (ABB) method presented by Tschanz et al. [6] and Borkar et al. [23] operates by computing bias voltages specific to a die, thus reducing the variation in frequency. However, this method suffers from the limitation of not addressing the intra-die variations, and increased leakage power due to reduction in threshold voltages. While programmable keepers proposed by Kim et al. [24] address impacts from both intra-die and inter-die variations, its significance is limited by additional keeper hardware, and noise imposed on dynamic nodes through coupling capacitances [21].

Schmitt-Trigger-Based Pseudo-pMOS Feedback Keeper

Power consumption, an important metric to evaluate circuit performance, is represented in Equation (1), where f is the clock frequency, C_L is the average switched capacitance per clock cycle, V_{dd} is the supply voltage, I_{short} is the short-circuit current, and I_{leak} is the leakage current. While minimizing V_{dd} reduces power consumption, it is typically at the expense of higher worst-case delay (τ) as in Equation (2), where, V_T, β, and α are threshold voltage, gate transconductance, and velocity saturation index, respectively.

$$P = f\,C_L V_{dd}^2 + f\,I_{short} V_{dd} + I_{leak} V_{dd} \tag{1}$$

$$\tau = C_L V_{dd} \Big/ \beta \left(V_{dd} - V_T\right)^{\alpha} \tag{2}$$

Addressing this challenge, Figure 2 shows a new architecture using a Schmitt-trigger-based pseudo-pMOS feedback keeper for simultaneous optimization of delay and power consumption. This technique operates on two basic principles: (i) the evaluation of network and feedback keeper are operated at a reduced supply voltage, ΦV_{dd} (Φ is a technology dependent factor in the range of 0.6-0.8), to lower the amount of charging and discharging of each dynamic node, thus reducing power consumption, and (ii) the use of a Schmitt trigger to restore the logic levels from ΦV_{dd} to V_{dd} for a smooth operation with other designs on the system chip. During the pre-charge phase, the dynamic node *'D'* is charged to a logic-high voltage of ΦV_{dd} rather than V_{dd}. Then, during the evaluation phase, voltage at this dynamic node will either be retained at ΦV_{dd} or decreased to *0*, depending on the state of the inputs. When the dynamic node is at its logic-high, ΦV_{dd}, the Schmitt trigger will discharge the gate output *'Q'* to *0*, and when the dynamic node is at its logic-low, *0*, it will charge the gate output *'Q'* to V_{dd}. Accordingly, this method will reduce circuit delay and power consumption as charging the dynamic node from *0* to ΦV_{dd} is much faster and consumes less power than charging it from *0* to V_{dd}.

Pseudo-pMOS Feedback Keeper

As dynamic circuits suffer from charge leakage on the dynamic node (*D*), and the proposed architecture operates on dual supply voltages, an efficient keeper design is necessary to ensure optimal design performance. A simple feedback keeper transistor is easy to implement, thus the fundamental challenge is choosing the optimal transistor size in order to obtain a balance between power consumption and signal contention. Figure 2 shows a Pseudo-pMOS inverter feedback keeper [25] with a weak CMOS inverter employed to generate the feedback signal. This keeper at the dynamic node (*D*) has at least two advantages: (i) faster feedback response time that is independent of external gate load, and (ii) autonomy to independently optimize the feedback keeper. However, the keeper *I-V* characteristics are susceptible to slight changes in transistor parameter variations. As the keeper current quickly drops with the voltage level at the dynamic node *D*, the most important parameter is the size ratio of pull-up and pull-down transistors (K_1 and K_2).

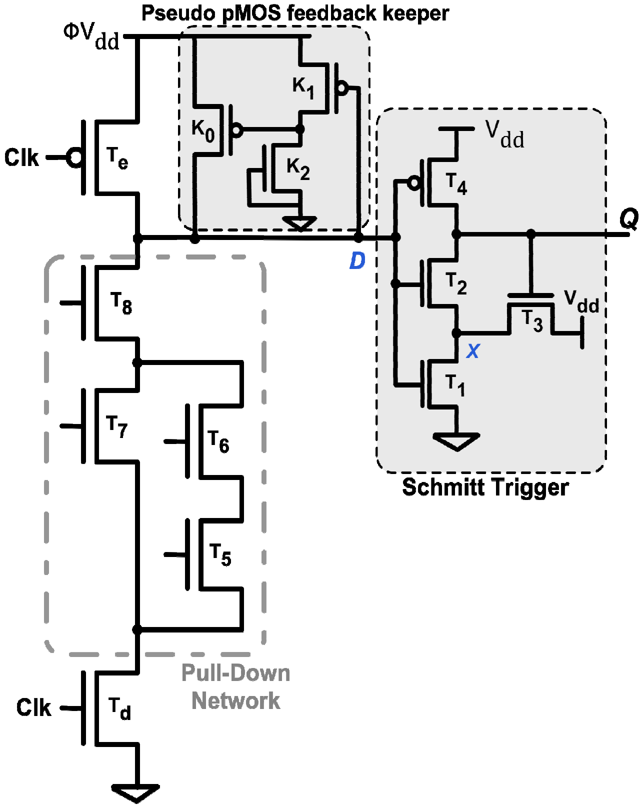

Figure 2. Dynamic Logic Gate with Schmitt-Trigger-Based Pseudo-pMOS Feedback Keeper

Schmitt Trigger

Consider that gate output *'Q'* is high (V_{dd}) and the dynamic node *'D'* is low (0). As transistors T_1 and T_2 are off and T_3 is on, the source of T_3 will float to V_{dd}–V_{TH3}. As long as $V_D < V_{TH1}$, V_X remains at V_{dd}–V_{TH3}. When the voltage at dynamic node *'D'* increases, T_1 begins to turn on and voltage V_X starts to decrease. This high switching point voltage is defined when Equation (3) is satisfied or when T_2 starts to turn on. When T_2 turns on, output *'Q'* will start to decrease towards ground, causing T_3 to start turning off. This, in turn, causes V_X to decrease, turning T_2 on even more. This continues until T_3 is totally off, and T_1 and T_2 are on. Accordingly, when Equation (3) is valid, current in T_1 and T_3 is essentially the same as in Equation (4).

$$V_D = V_{TH2} + V_X = \Phi V_{dd} \tag{3}$$

$$\frac{\beta_1}{2}\left(V_{SPH} - V_{TH1}\right)^2 = \frac{\beta_3}{2}\left(V_{dd} - V_X - V_{TH3}\right)^2 \tag{4}$$

As the sources of T_2 and T_3 are connected together, $V_{TH2}=V_{TH3}$, and the increase in threshold voltages from the body effect is the same for both transistors. Combining Equations (3) and (4) yields Equation (5), where, *S* and *L* are the transistor size width and length, respectively. With equal minimum gate lengths, Equation (5) can be simplified to Equation (6) in order to find the size of T_1 and T_3. Based on Equation (6) and the general design rule [26], the size of T_3 and T_4 can be found from Equations (7) and (8), respectively.

$$\frac{\beta_1}{\beta_3} = \frac{S_1 L_3}{L_1 S_3} = \left[\frac{V_{dd} - \Phi V_{dd}}{\Phi V_{dd} - V_{TH1}}\right]^2 \tag{5}$$

$$\frac{S_1}{S_3} = \left[\frac{V_{dd} - \Phi V_{dd}}{\Phi V_{dd} - V_{TH1}}\right]^2 \tag{6}$$

$$S_2 \geq S_1 \text{ } or \text{ } S_3 \tag{7}$$

$$S_4 = \frac{\mu_n}{\mu_p} \times S_2 \tag{8}$$

Transistor Sizing

The initial step in keeper optimization is identifying the unique timing discharge paths ($p_1 = \{T_i, T_{i+1},..\}$) in the evaluation network. The timing discharge paths in Figure2 are p_2 = {T_5, T_6, and T_8} and p_3 = {T_7, T_8}. Later, each transistor in the design is assigned a weight (*w*) in the range of 0.05-0.5 based on its distance from the dynamic output node (*D*). For example, the circuit in Figure 2 is comprised of three transistor stacks based on their distance from the output. Stack-1, closest to the dynamic output, includes T_8; Stack-2 includes T_6 and T_7; and, Stack-3 includes T_5. Accordingly, transistors in these stacks are assigned weights of 0.1, 0.2, and 0.4, respectively. Next, the keeper sizing factor, *Mp*, for each path-p is found through Equation (9), where S_i and w_i are size and weight of each transistor in a timing path, respectively. Later, the widths of keeper transistors K_0, K_1, and K_2 are found using Equations (10) and (11), where *f* is a technology dependent initial sizing factor between 1.1 and 1.5.

$$M_p = \max\left(S_i \times w_i, S_{i+1} \times w_{i+1}, \ldots\right) \tag{9}$$

$$K_1 = \sum\nolimits_{i=1}^{p} M_p \tag{10}$$

$$K_2 = K_0 = f \times K_1 \tag{11}$$

LBMP for Timing, Power, and Parametric Yield

Delay, the performance metric of a circuit, depends on the size and number of transistors in the evaluation network. While increasing the size of transistors in one path might reduce its path delay, it might advertently increase the delay of its neighboring path due to capacitive load from the channel-connected transistors. To demonstrate this optimization complexity further, a 2-b Weighted Binary-to-Thermometric Converter (WBTC) as used in high-performance binary adders is presented in Figure 3, and a Load Balancing of Multiple Paths (LBMP) optimization algorithm is presented in Figure 4.

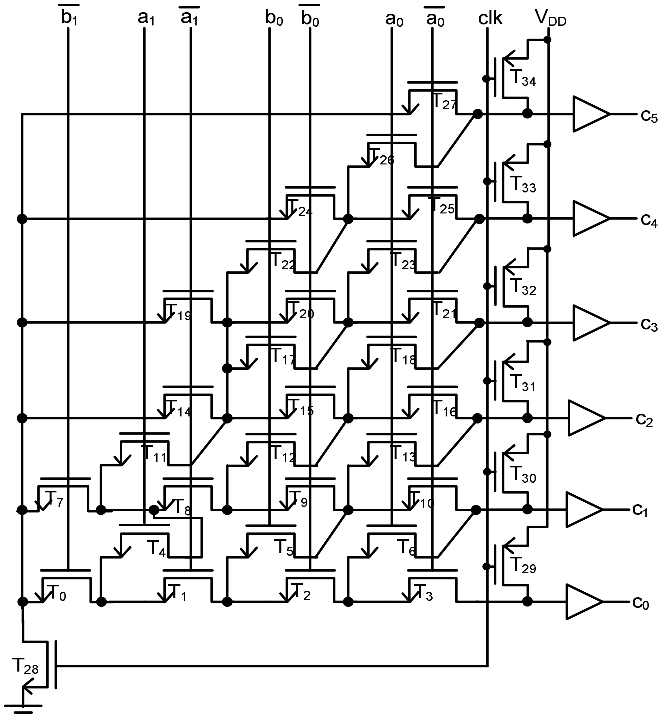

Figure 3. 2-b Weighted Binary-to-Thermometric Converter

Two neighboring timing paths, {T_{28}, T_7, T_8, T_{12}, T_{18}} and {T_{28}, T_0, T_4, T_{11}, T_{15}, T_{16}}, are shown in Figure 3, where the first path has a much higher delay compared to the second. To reduce its delay, the sizes of all transistors in the path are slightly increased. While doing so reduced the delay of the first path, it significantly increased the delay of the second path, due to capacitive load from channel-connected transistors. In this case, {T_4, T_{11}}, {T_{15}, T_{16}} in the second path are channel-connected to {T_7, T_8}, {T_{15}, T_{16}} in the first path, respectively. Increasing sizes of transistors in the first path increased the capacitive load on the second path and, thus, its delay. Accordingly, astute care must be taken in choosing the sizing factor of every transistor in a design with multiple channel-connected transistors and timing paths.

As leakage charge and power consumption decrease overall design performance, the first step in the proposed optimization algorithm is inserting the pseudo-pMOS feedback keeper and Schmitt trigger at each of the dynamic output nodes, and sizing their respective transistors per Equations (7) and (8). Later, each transistor in the design is assigned a weight (*w*) in the range of 0.05–0.5 based on its distance from the dynamic output node, similar to the method presented in the previous section. The next step in the optimization algorithm is identifying the significance of each transistor in the circuit based on the number of timing paths in which it is present, and denoting this number as it repeats (*r*). Once the repeat and weight profiles are obtained, all transistor widths (*S*) are initially sized with $S_i = S_{\min} \times f^{\psi}$ for faster optimization convergence, where *f* is a technology dependent initial sizing factor between 1.1 and 1.5, and ψ is the relative position of the transistor from the output.

Later, process variations are induced in the circuit design with updated transistor sizes to obtain a delay distribution of all timing paths. From these delay profiles, all transistors in the top 20% of the critical paths are clustered to *set-c*, and the respective widths are updated by Equation (12), where r_j and w_j are repeat and weight of transistor-*j*. Next, to limit the impact of the capacitive load from the channel-connected transistors, all first-order connections to the transistors in *set-c* are identified and clustered to *set-d*, and their respective widths are updated by Equation (13), where r_k and w_k are repeated along with the weight of transistor *k*. Next, sizes of transistors in the pseudo-pMOS feedback keeper are updated using Equations (10) and (11), and the footer size is updated using Equation (14).

$$S_{new} = S_{old}\left(1 + \left(r_j w_j / \left(1 + r_j\right)\right)\right) \tag{12}$$

$$S_{new} = S_{old}\left(1 - \left(r_k w_k / \left(1 + r_k\right)\right)\right) \tag{13}$$

$$S_f = \sum_{l=1}^{n} S_l \times w_l \tag{14}$$

The next step in the optimization algorithm is sizing the evaluation network footer transistor, T_f. All first-order connections to T_f are identified and its size, S_f, is updated using Equation (14). Later, process variations are induced in order to obtain new delay profiles for further timing optimization and the algorithm is repeated for further delay convergence.

Performance Optimization from the LBMP Algorithm

Performance optimization of the proposed LBMP optimization algorithm is demonstrated through a 2-b WBTC, as shown in Figure 3. With its complex 34 timing paths and channel loading on neighboring paths, this 2-b WBTC as used in high-performance adders is an ideal circuit to test the effectiveness of an optimization algorithm. Through initial simulations, the initial worst-case delay of the circuit was found to be 550 ps from path-1. Per the LBMP algorithm presented in Figure 4, a Schmitt-trigger-based Pseudo -pMOS feedback keeper was inserted at each of the dynamic CMOS output nodes, and the supply voltage was changed from V_{dd} to ΦV_{dd}. Later, based on technology parameters and Equations (6)-(8), sizes of transistors (T_1, T_2, T_3, and T_4) in the Schmitt Trigger were changed from 120 nm (minimum size) to 157 nm, 120 nm, 120 nm, and 480 nm, respectively.

The next step in the algorithm is updating the evaluation network transistor sizes. In order to do this, transistors in the top 20% critical paths from initial simulations were found, and their initial sizes were increased by a ration, S_i. For instance, the sizes of transistors T_{22}, T_{11}, T_4, and T_0 in path-1 were updated from 120 nm to $120 \times 1.1^1 = 132$ nm, $120 \times 1.1^2 = 145$ nm, $120 \times 1.1^3 = 160$ nm, and $120 \times 1.1^4 = 176$ nm, respectively. Similarly, the sizes of transistors in all of the remaining 20% critical paths were updated, and process variations were induced to obtain updated delay distribution profiles. In a similar manner, through further updates of transistor sizes per the proposed LBMP optimization algorithm, the worst-case delay of 2-b WBTC was reduced to 322 ps, accounting for an improvement of 41.48%.

To demonstrate the effectiveness of the proposed LBMP algorithm, further analysis was performed using multiple performance metrics. As reducing the standard deviation, σ, in the delay distribution is equally important compared to mean, μ, Figure 5 shows a comparison of delay distribution of a pre- and post-optimized 2-b WBTC with low supply voltage, where the worst-case delay ($\mu + \sigma$), and delay uncertainty (Δ) were reduced from 550 ps to 322 ps, and from 210 ps to 65 ps, an improvement of 41.48% and 70%, respectively. Furthermore, the deterministic nature of the LBMP optimization algorithm is demonstrated in Figure 6, where worst-case delay ($\mu + \sigma$), delay uncertainty (Δ), and delay sensitivity (δ), always converged towards an optimum value. As power consumption optimization is equally, if not more important, Figure 7 shows the optimization efficiency of the proposed algorithm, where the average power was reduced from 28.3 µW to 22.02 µW, accounting for an improvement of 22.2%.

Table 1. Delay Improvements in Benchmark Circuits

Design	Pre-opt Delay (ps)	Post-opt Delay (ps)	Delay Improvement (%)	Area Increase (%)	Uncertainty Improvement (%)	Sensitivity Improvement (%)
2-b WBTC	550.6	322.2	41.4	60.2	69.1	63.0
74181-ALU	351.1	207.0	41.0	53.1	47.7	18.6
c2670-CLA	369.3	266.4	27.8	58.3	33.5	17.7
c3540-CC5	247.2	152.0	38.5	36.2	31.7	14.2
c3540-CC8	724.3	348.2	51.9	53.8	42.8	17.8
c3540-CC9	316.1	243.2	23.0	45.1	44.6	12.5
c5315-CalP2	312.2	201.6	35.4	36.5	37.4	13.5
c5315-GLC4_2	788.2	303.0	61.5	31.2	60.6	47.7
c5315-CB4	476.6	282.0	40.8	61.1	71.1	52.8
c7552-CGC34_4	620.8	388.0	37.5	66.3	46.5	17.9
c7552-CGC17	228.3	119.0	47.8	48.7	57.2	22.1
c7552-GLC5_1	476.3	282.0	40.7	60.8	71.1	52.8
c7552-CGC20	249.2	148.0	40.6	35.2	31.5	14.6
Average	40.6	49.7	49.6	28.1		

Table 2. Power Consumption Improvements in Benchmark Circuits

Design	Pre-Opt Power (uW)	Post-Opt Power (uW)	Improvement (%)
2-b WBTC	28.30	22.02	22.19
74181-ALU	16.70	10.52	37.00
c2670-CLA	17.30	8.63	50.11
c3540-CC5	3.04	1.91	37.17
c3540-CC8	38.19	24.12	36.84
c3540-CC9	37.65	25.26	32.90
c5315-CalP2	7.12	4.88	31.46
c5315-GLC4_2	5.36	3.06	42.91
c5315-CB4	5.30	3.02	43.01
c7552-CGC34_4	9.12	6.77	25.76
c7552-CGC17	2.99	1.97	34.11
c7552-GLC5_1	5.30	3.02	43.01
c7552-CGC20	3.04	1.91	37.17
Average			**36.43**

Additionally, the proposed LBMP optimization algorithm was applied to several ISCAS benchmark circuits [23] and results showed an average improvement in delay and power consumption by 40.64% and 36.43%, respectively, as presented in Table 1. In addition to optimization of worst-case delay (see Figure 8), the algorithm also demonstrated an optimization in delay uncertainty and delay sensitivity by 49.64% and 28.12%, respectively, (see Figures 9 and 10). Furthermore, the proposed algorithm has reduced the average power consumption by 36.43% without any penalty in delay (see Table 2).

While power-delay-product is an oft-used performance metric, considering it to assess design performance is questionable as energy can be reduced by operating the designs slowly at a lower supply voltage [15]. The energy- delay product, however, is less prone to such inconsistencies [27]. Accordingly, the energy-delay products in pre- and post-optimized designs are computed—normalized data are presented in Figure 11—which demonstrate an improvement of 77%. Moreover, parametric yield of the benchmark circuits at different supply voltages was studied with simulation results (obtained from Cadence Spectre) presented in Table 3. When the supply voltage in the pre-optimized designs was reduced from 1.2 V to 0.8 V (minimum supply voltage per the 90nm CMOS technology library used), the measured parametric yield in the 2-b WBTC quickly decreased to 54%. However, the same circuits, when optimized using the LBMP algorithm, showed an improvement in parametric yield up to 100%.

```
Given: Dynamic CMOS circuit with 'm' transistors and 'n
    timing paths
Inputs:  1) List of timing paths
    2) Supply voltage levels ($V_{dd}$, $\Phi V_{dd}$)
Objective: Minimize path-delay distributions
    $max(d_1, d_2, d_3, .... Dn)$
        subject to: $S_{min} \le S_i \le S_{max}$ for i = $\{1,2,3,...,m\}$
Output: Optimized transistor sizes $\{S_1, S_2, ....., S_m\}$
========================================
Compute repeat $(r_i)$ and weight $(w_i)$ for all transistors
    $i=\{1,2,3,....m\}$
Insert a Pseudo-pMOS feedback keeper and Schmitt
    trigger at each of the dynamic CMOS output node
Change the supply voltage for entire circuit, except
    the Schmitt trigger, from $V_{dd}$ to $\Phi V_{dd}$
Compute the sizes of transistors in the Schmitt trigger
    for switching of supply levels through
    $S_1/S_3 = [(V_{dd} - \Phi V_{dd})/(\Phi V_{dd} - V_{TH1})]^2$
    $S_2 \ge S_1 or S_3$
    $S_4 = (\mu_n/\mu_p) \times S_2$
Initialize all transistor sizes in evaluation network with
    $S_i = S_{min}\, x\, f^{\alpha}$
do {
Induce process variations & obtain path-delay
    distribution $(d_1,d_2,d_3,....,d_n)$ of all paths
Sort and rank all paths based on their delay $(\mu_i + \sigma_i)$
List set-c $=\{T_1,T_2,T_3,....,T_x\}$ transistors from top 20%
    paths
for $j \leftarrow 1$ to c
    $S_j = S_j\left(1+\left(r_j w_j/(1+r_j)\right)\right)$
end for
Identify $1_{st}$ order connection transistors 'set-
    d=$\{T_1,T_2,...,T_y\}$' to set-x transistors
Exclude set-x transistors from set-y if any
for $k \leftarrow 1$ to d
    $S_k = S_k\left(1-\left(r_k w_k/(1+r_k)\right)\right)$
end for
For all unaltered transistors, $S_{new} = S_{old}$
For all dynamic output nodes, update the pseudo-
    pMOS feedback keeper transistor sizes
    $M_P = max(S_i \times w_i, S_{i+1} \times w_{i+1},\ldots)$
    $K_1 = \sum_{i=1}^{p} M_p$
    $K_2 = K_0 = f \times K_1$
update the size $(S_f)$ of footer transistor $T_f$ using
    $S_f = \sum_{l=1}^{n} S_l \times w_l$
} while // delay converges to an acceptable value
```

Figure 4. LBMP Optimization Algorithm

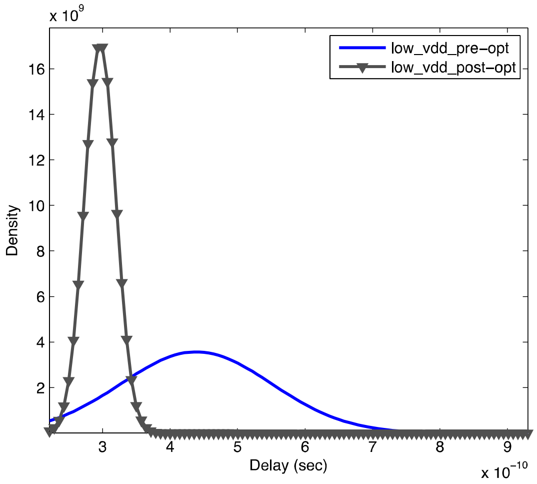

Figure 5. Delay Distribution Comparison in 2-b WBTC

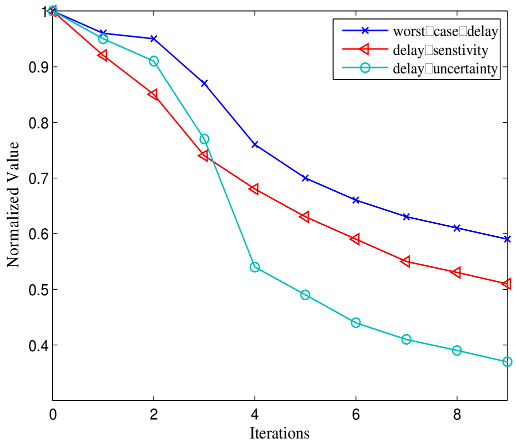

Figure 6. Timing Performance Convergence of 2-b WBTC

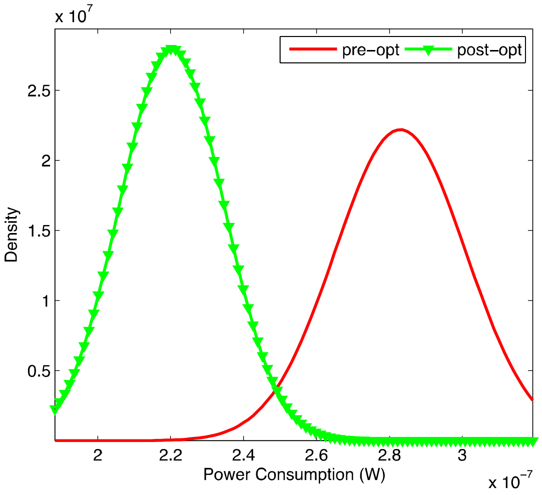

Figure 7. Pre- and Post-Optimized Power Distribution Comparison of 2-b WBTC

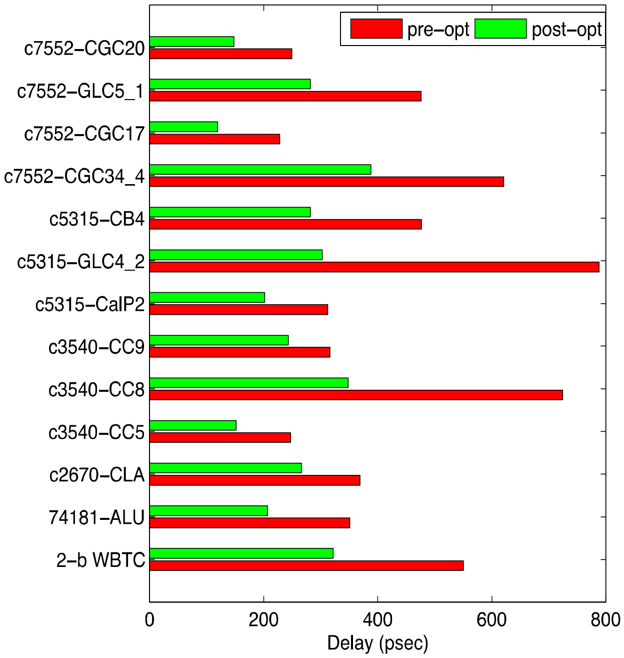

Figure 8. Worst-Case Delay Optimization

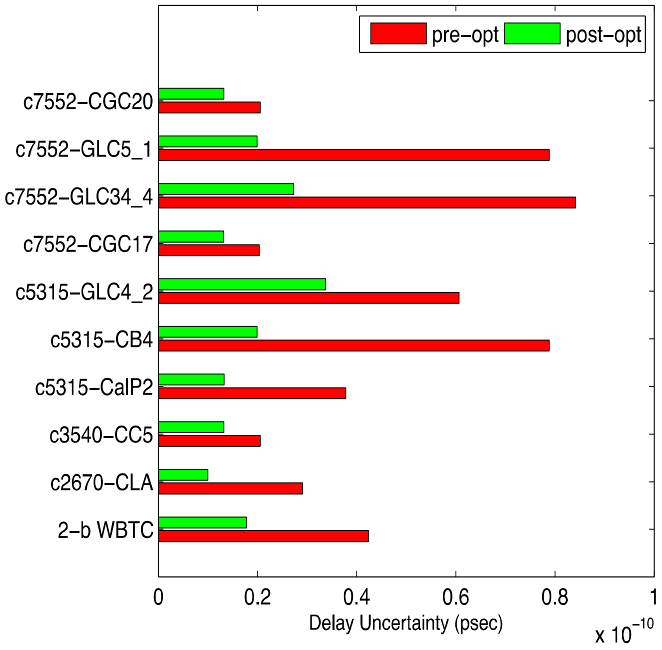

Figure 10. Delay Sensitivity Improvement

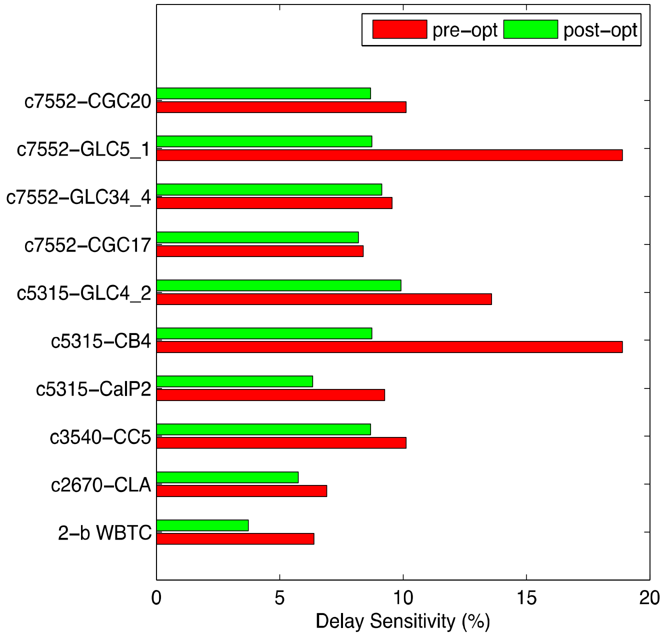

Figure 9. Delay Uncertainty Improvement

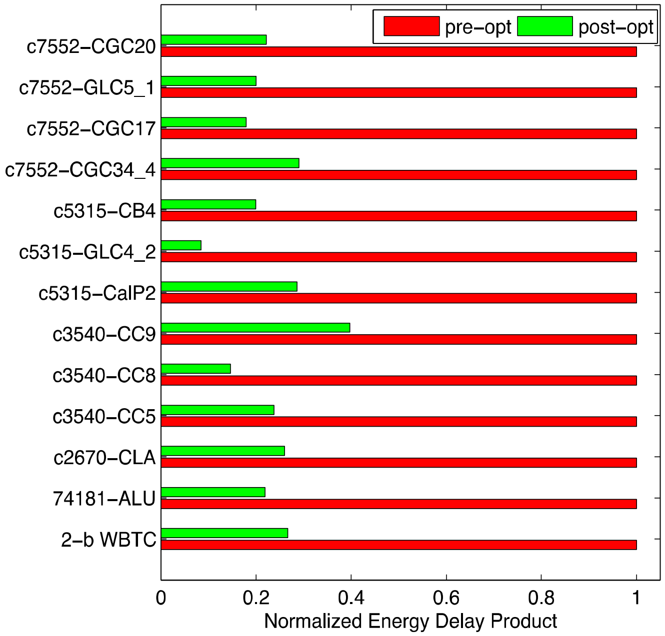

Figure 11. Energy-Delay Product Comparison

Table 3: Parametric Yield Optimization at Different Supply Voltages

Design	Pre-/Post-Opt Yield (%)				
	Vdd=1.2	Vdd=1.1	Vdd=1.0	Vdd=0.9	Vdd=0.8
2-b WBTC	100/100	100/100	98/100	82/100	55/100
74181-ALU	100/100	100/100	95/100	86/100	60/100
c2670-CLA	100/100	100/100	96/100	65/100	32/100
c3540-CC5	100/100	100/100	97/100	76/100	65/100
c3540-CC8	100/100	100/100	95/100	78/100	60/100
c3540-CC9	100/100	100/100	97/100	81/100	55/100
c5315-CalP2	100/100	100/100	97/100	73/100	41/100
c5315-GLC4_2	100/100	100/100	94/100	85/100	76/100
c5315-CB4	100/100	100/100	90/100	69/100	52/100
c7552-CGC34_4	100/100	100/100	92/100	52/100	30/100
c7552-CGC17	100/100	100/100	94/100	83/100	69/100
c7552-GLC5_1	100/100	100/100	90/100	69/100	52/100
c7552-CGC20	100/100	100/100	97/100	76/100	65/100
Average	100/100	100/100	95/100	75/100	54/100

Conclusion

In this paper, an LBMP optimization algorithm was proposed for performance improvement in timing, power, and parametric yield. The efficiency of the proposed algorithm was demonstrated through three key features: (i) proficiently balancing the capacitive load on critical paths from neighboring timing paths; (ii) implementing the updated evaluation network at reduced supply voltage to lower the charging and discharging; and, (iii) using a Schmitt trigger to restore the reduced voltage swing to normal levels at the design output.

Previous work in timing optimization focused on reducing delay and the effects of process variations by sacrificing power consumption. This current study suggests that by employing Schmitt-trigger-based pseudo-pMOS feedback keeper and operating the evaluation network at a lower supply voltage leads to faster circuits, while at the same time results in energy savings with a moderate increase in circuit area. To demonstrate the efficiency of the proposed algorithm, numerous benchmark circuits were tested in order to obtain an average improvement in worst-case delay by 40.64%, delay uncertainty by 49%, delay sensitivity by 28%, power consumption by 36%, and energy-delay-product by 77%.

References

[1] Li, C., & Soares, A. (2011). Measuring Clock Jitter, *Technology Interface International Journal*, *11*(2), 10-15.

[2] Pavlov, A., & Sachdev, M. (2008). *CMOS SRAM Circuit Design and Parametric Test in Nanoscaled Technologies*. Springer, New York.

[3] Mohanty, S. P., Singh, J., Kougianos, E., & Pradhan, D. K. (2012). Statistical DOE-ILP based power-performance-process (P3) optimization of nano-CMOS SRAM. *Integration, the VLSI Journal*, *45*(1), 33-45.

[4] Zhang, L. (2005). Statistical Timing Analysis for Digital Circuit Design," Unpublished doctoral dissertation, University of Wisconsin, Madison.

[5] Sylvester, D., Agarwal, K., & Shah, S. (2008). Variability in nanometer CMOS: Impact, analysis, and minimization. *Integration, the VLSI Journal*, *41*(3), 319-339.

[6] Tschanz, J., Bowman, K., & De, V. (2005). Variation-tolerant circuits: circuit solutions and techniques. *Design Automation Conference*, (pp. 762-763), Anaheim, CA.

[7] Bhardwaj, S., & Vrudhula, S. (2008). Leakage Minimization of Digital Circuits using Gate Sizing in the

Presence of Process Variations. *IEEE. Trans on CAD Design of Integrated Circuits and Systems*, *27*(3), 445 -455.

[8] Zuchowski, P. S., Habitz, P. A., Hayes, J.., & Oppold, J. H. (2004). Process and Environmental Variation Impacts on ASIC Timing. *IEEE/ACM International Conference on Computer Aided Design,* (pp.336-342).

[9] Sahafi, A., & Navi. K. (2012). A Novel Five-Input Configurable Cell Based on Single Electron Transistor Minority Gates. *International Journal of Engineering Research and Innovation, 4*(1), 30-33.

[10] Olasupo, K. R., Nkansah, F. D., Sadiku, M., & Dunkley, R. K. (2012). The Impact of Channel Doping Density on Nano-Scaled MOS Devices. *International Journal of Engineering Research and Innovation, 4*(2), 34-37.

[11] Frustaci, F., Corsonello, P., Perri, S., & Cocorullo, G. (2008). High-performance noise-tolerant circuit techniques for CMOS dynamic logic. *IET Journal of Circuits, Devices, Syst.*, *2*(6), 537 - 548.

[12] Yelamarthi, K., & Chen, C-I. H. (2009). Process Variation-Aware Timing Optimization for Dynamic and Mixed-Static-Dynamic CMOS Logic. *IEEE Transactions on Semiconductor Manufacturing*, *22*(1), 31-39.

[13] Yelamarthi, K., & Chen, C-I. H. (2012). Timing Optimization and Noise Tolerance for Dynamic CMOS Susceptible to Process Variations. *IEEE Transactions on Semiconductor Manufacturing*, *25*(2), 255-265.

[14] Bowman, K. A., Duvall, S. G., & Meindl, J. D. (2002). Impact of die-to-die and within-die parameter fluctuations on the maximum clock frequency distribution for gigascale integration. *IEEE Journal of Solid-State Circuits, 37*(2), 183-190.

[15] Weste, N., & Harris, D. (2004). *CMOS VLSI Design: A Circuits and Systems Perspective*. (3rd ed.). Addison Wesley.

[16] Samaan, S. (2004). Impact of Device Parameter Variations on the Frequency and Performance of VLSI Chips. *International Conference on Computer-Aided Design, (*pp 343-346).

[17] Fishburn, J. P., & Dunlop, A. E. (1985). TILOS: A Posynomial Programming Approach to Transistor Sizing. *International Conf. Computer Aided Design*, (pp. 326-328).

[18] Sundararajan, V., Sapatnekar, S. S., & Parhi, K. K. (2002). Fast and Exact Transistor Sizing Based on Iterative Relaxation. *IEEE Trans. Computer Aided Design*, *21*(5), 568-581.

[19] Sutherland, I., Sproull, B., & Harris, D. (1999). *Logical Effort: Designing Fast CMOS Circuits*. Morgan Kaufmann Publishers.

[20] Nikoubin, T., Bahrebar, P., Pouri, S., Navi, K., & Iravani, V. (2010). Simple Exact Algorithm (SEA) for Transistor Sizing of Low-Power-High-Speed Arithmetic Circuits. *VLSI Design*, doi: 264390.

[21] Dadgour, H. F., & Banerjee, K. (2010). A Novel Variation-Tolerant Keeper Architecture for High-Performance Low-Power Wide Fan-In Dynamic OR Gates. *IEEE Tran. Very Large Scale Integr. (VLSI) Syst*ems, *18*(11), 1567-1577.

[22] Scheffer, L. (2004). The Count of Monte Carlo, *ACM/IEEE TAU Workshop*.

[23] Borkar, S., Karnik, T., Narendra, S., Tschanz, J., Keshavarzi, A., & De, V. (2003). Parameter Variations and Impact on Circuits and Microarchitecture. *IEEE/ACM Design Automation Conference*, (pp. 338-342), Anaheim, CA.

[24] Kim, C. H., Roy, K., Hsu, S., Krishnamurthy, R., & Borkar, S. (2006). A process variation compensating technique with an on-die leakage current sensor for nanometer scale dynamic circuits. *IEEE Tran. Very Large Scale Integr. (VLSI) Systems, 14*(6), 646-649.

[25] Ding, L., & Mazumder, P. (2004). On Circuit Techniques to Improve Noise Immunity of CMOS Dynamic Logic. *IEEE Tran. Very Large Scale Integr. (VLSI) Systems*, *12*(9), 910-925.

[26] Baker, R. J. (2010). *CMOS Circuit Design, Layout, and Simulation*. (3rd ed.). Wiley-IEEE.

[27] Hansen, M., Yalcin, H., & Hayes, J. P. (1999). Unveiling the ISCAS-85 Benchmarks: A Case Study in Reverse Engineering. *IEEE Design and Test*, *16*(3), 72-80.

Biographies

KUMAR YELAMARTHI received his Ph.D. degree from Wright State University in 2008. He is currently an Assistant Professor of Electrical Engineering at Central Michigan University, Mt Pleasant, MI. His research interest is in the area of RFID, embedded systems, robotics, integrated circuit optimization, and engineering education. Dr. Yelamarthi has served as a technical reviewer for several IEEE/ASME/ASEE international conferences and journals, and has published over 75 articles in archival journals and conference proceedings. Dr. Yelamarthi is a member of Tau Beta Pi engineering honor society, and Omicron Delta Kappa national leadership honor society, and a senior member of IEEE. Dr. Yelamarthi may be reached at kumar.yelamarthi@cmich.edu

SOME THEORETICAL RESULTS IN THE PERSPECTIVE ANALYSIS OF IMAGES

Hongyu Guo, University of Houston – Victoria

Abstract

The perspective rectification of images using projective transformations has become common practice in photo editing, image processing, architectural design, civil engineering, photogrammetric engineering, and machine vision. Although the principles of projective transformations from one projective plane to another is well understood, when it comes to 3-D scenes, it has not been investigated. The relationship between images of the same scene, 2-D or 3-D, captured from different angles and from different distances were examined in this study. Perspective depth inference from a single image was also investigated. Compared with other research efforts in depth inference from a single image, this effort intended to calculate the depth of a few points of interest, instead of all the pixels in an image. It relies on partial prior knowledge of the 3-D scene and object recognition by human intelligence. The consequence of this approach is the reliability of the depth calculations, which is critical in photo forensic analysis, architectural design, image understanding, and machine vision.

Introduction

Many image editing software packages, like Adobe Photoshop, provide a projective transformation tool. Perspective rectification of images has already become a common practice of digital light rooms, architectural design and computer aided design, civil engineering and photogrammetric engineering [1-3]. That is, to use software to change the view angle of the camera after the photograph has been taken. For example, the camera was pointing upward when the photograph in Figure 1(a) was taken. This is often the case when the camera is too close to the building but the photographer still wants the entire building to be contained in the photograph. The buildings have a feeling of being tilted, or falling down. A one-point perspective or two-point perspective is often considered more aesthetic and desirable, with the camera pointing horizontally, as in the pictures in coffee table magazines. The fundamental theorem of projective geometry states that a projective transformation from a projective plane to another projective plane (or itself) is uniquely determined by the images of four points in general position [4]. The term "in general position" means that no three points in the set are collinear (on the same line). In Adobe Photoshop, one can select four points in general position, most often the four corners of the photograph, and drag them to the desired new positions, and the projective transformation of the image can be performed instantly with the aid of the software, as shown in Figure 1(b). Projective transformations have the property of mapping straight lines to straight lines.

Projective transformations are also used in many other virtual reality applications, from the old-time Apple QuickTime VR movies to Google Earth and Google Street View. Virtual reality applications are used by many universities as well as the real estate industry to show virtual tours of university campuses or real estate properties.

In most 3-D computer graphics applications, including animations and 3-D games, 3-D models are built and stored in the computer. The computer graphics applications make use of a virtual camera. The virtue camera is defined by the coordinates of the center of the camera, the direction of the axis and the position of the image plane (view distance). No physical implementation is necessary. The viewing of the 3-D scene from any angle and position is just a matter of mathematical manipulation of central projection, utilizing the fast matrix crunching power of the GPU. Comparing Google Street View with computer graphics applications, it is still too early for the current technology to build and store 3-D models for each street in thousands of the cities. Google Street View relies on 2-D images, and the viewing from different angles is accomplished by 2-D–to–2-D transformations. These transformations are projective transformations in nature. When a sequence of 2-D images is stitched to make a 360° panorama, nonlinear distortion is unavoidable. Circular fisheye images can also be used to stitch spherical panoramas. The projection model can be nonlinear also, like cylindrical projection or spherical projection in those panoramas. However, locally, the change of view angle by a small amount is still an approximation of a projective transformation. To the human eye, the projective transformation of an image represents the image of the same 3-D scene viewed from a different angle. However, is there a theoretical base for this phenomenon and this practice? In projective geometry, the projective transformation is defined from one projective plane to another projective plane. This applies easily when the image, say a framed photograph or painting hanging on the wall, is viewed from different angles. However, in the aforementioned perspective rectification practice, or the panorama view applications, the scene that is being viewed from different angles is a 3-D scene. Are the images of 3-D scenes viewed from different angles also related by a projective transformation?

(a) Original image

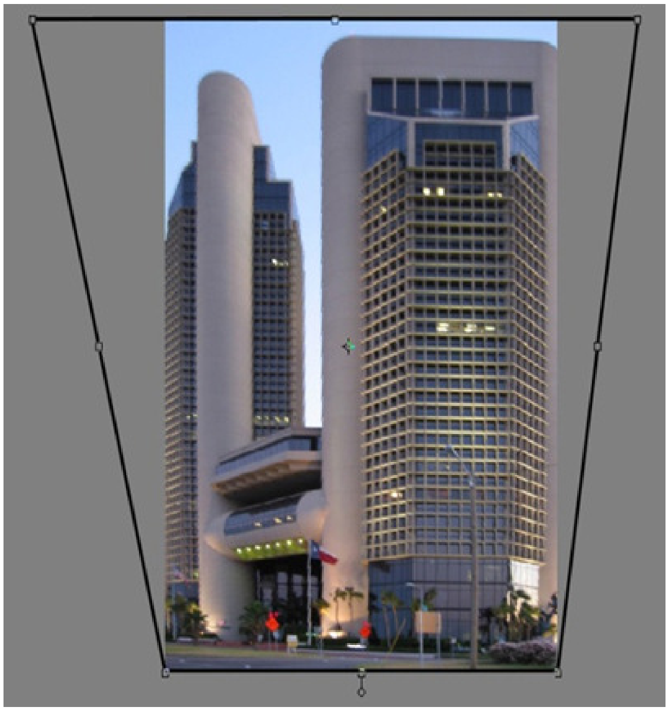

(b) After a projective transformation

Figure 1. Perspective Rectification of an Image

Figures 2(a) and 2(b) are photographs of the same scene taken from different distances, one with a wide-angle lens and the other with a telephoto lens. In Figure 2(a), the background building looks further away from the foreground pavilion, while in Figure 2(b), the same background building looks much closer. This phenomenon gives an illusion and a misconception that a wide-angle lens stretches distance and a telephoto lens compresses distance. There have been explanations by some photographers to clarify and correct this misconception. Most recently, Guo [5] gave a quantitative analysis of perspective distortions by defining a perspective diminution factor and a perspective foreshortening factor. Are the two images in Figures 2(a) and 2(b) related by a projective transformation?

(a) Short-Distance Shot **(b) Long-Distance Shot**

Figure 2. Perspective Distortion

Figures 3(a) and 3(b) are two portraits of the same model, with the same position and same pose. Figure 3(a) was shot with a 24 mm wide-angle lens (35 mm film equivalent) from a close-up distance of one foot, while Figure 3(b) was shot with a 100 mm telephoto lens (35 mm film equivalent) from a longer distance. Apparently, the image in Figure 3(a) suffers from distortion. This type of face distortion is very common in face images in front of Webcams or the built-in cameras of cellphones during a video call. Are those two images in Figures 3(a) and 3(b) related by a projective transformation? If so, then it implies that the distorted image can be rectified with a projective transformation.

If the answers to the above questions are yes, they need to be justified. If no, an explanation is necessary to determine why the practice of perspective rectification works well for certain situations, but not for others. Another natural question to ask is: Under what conditions is the projective transformation a good approximation. This study investigated these problems and attempted to answer these questions. In the following sections, the images of 3-D scenes from different angles are shown not to be related by a projective transformation; and under certain conditions, the relationship is shown to be approximated by a projective transformation.


(a) Close-up Shot **(b) Long-Distance Shot**

Figure 3. Perspective Distortion

A related topic is depth inference. Photographs, such as those in Figures 2(a) and 2(b), may deceive the eyes about distance in space. Is there a way to calculate the true 3-D distance by performing some measurements on the 2-D image? The answer to this question in the general context is "no". This is due to the depth ambiguity of central projection. That is, an entire line in 3-D space is projected on a single point in the image plane under central projection. The depth information is lost after this central projection. However, the depth inference from a single image becomes a meaningful problem if partial prior knowledge—depth cues of the 3-D scene—is known. Depth inference from images is essential to machine vision, unmanned vehicles [6-8] and robotics [9]. Recently, there has been a new interest in depth inference from single images [10-16]. Without exception, all of these efforts assume partial prior knowledge of the 3-D scene, but most of them are not based on object recognition. Saxena et al. [14] use supervised learning methods for depth inference. The effort tries to infer depth for each pixel in the image. Object recognition is not conducted. Large numbers of training images of the same or similar scenes are needed. The error rate is still high. Yu et al. [16] use limited image understanding by first detecting edges that are straight lines. In this study, object recognition and partial prior knowledge of the 3-D scene from the human was assumed. Depth information, such as how far away the camera was from the scene when the image was taken, and distances between objects in the depth direction was calculated with measurements on the 2-D image.

Projective Model of the Camera and Coordinates

The projective model of the camera was used in the following discussion [5]. A coordinate system (x,y,z) was set up with the origin O at the center of projection (COP). The image plane was parallel to the x-y plane with an image distance f. In casual use of terminology in photography, or even in computer graphics, this image distance f is often called focal length of the camera. Precisely, the image distance is different from the optical local length of the lens. In practice, the image distance in a camera is close to the focal length, especially when scene objects are far away. This does not cause confusion when the projective model of the camera is used and optics is not concerned. In the following discussion, focal length simply means image distance f. The image plane is placed in front of COP instead of behind it. This is different from real cameras. It makes no difference in theory, but it gives more convenience because the image of the scene in this virtual camera is upright, like the picture on an artist's canvas, rather than upside down, as on real cameras' sensors.

Imagine a person looking through this virtual camera. It is customary for the viewer to set the positive x to the right direction, the positive y to the upward direction, and z to the forward direction in depth. This way, all of the scene points that a viewer can see have positive z values, and z increases when a points moves "forward" from the viewer's perspective. This convention of coordinate setup results in a left-handed coordinate system. In computer graphics applications, Microsoft DirectX adopts this left-handed coordinate system as its default for this viewer's convention.

On the image plane, an X-Y coordinate system is used with the origin at C, where C is the principal vanishing point, which is the intersection of the image plane and the z-axis. X is parallel to x, and Y is parallel to y. With this coordinate system setup, for any scene point (x,y,z) in 3-D space, the coordinates of the image point (X,Y) in the image plane are

$$\begin{aligned} X &= f\,\frac{x}{z} \\ Y &= f\,\frac{y}{z} \end{aligned} \tag{1}$$

In the following section, 2-D scenes and 3-D scenes are investigated as separate cases because there are essential differences in these cases. Some clarification of the terms is needed. A 2-D scene is taken to mean that all of the scene points lie in a 2-D plane. The scene plane may or may not be parallel to the image plane of the camera. An alternative to the term 2-D scene is “planar scene”, which is more accurate. Whenever the term 2-D scene is used, it should be understood as “planar scene”. Similarly, the more accurate term for “3-D scene” is “non-planar” scene, which means that all of the scene points do not lie in a single plane.

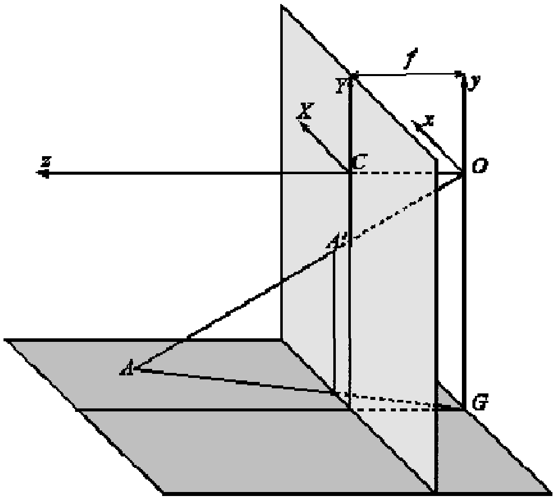

Figure 4. Camera Coordinate System

Relationship between Images Captured from Different Angles

2-D Scenes

Suppose the scene is 2-D. That is, the scene points are on the same plane. The scene plane is not necessarily parallel to the image plane. This is the case when the scene is a framed photograph or art painting hanging on the wall. In Figure 5, let π_0 be the scene plane (art painting hanging on the wall). Suppose a photograph of this scene is taken, with O_1 being the COP and π_1 being the image plane (image sensor).

Now suppose another photograph of the same scene, π_0, is taken from a different angle and camera position, O_2, with the image plane, π_2. Suppose that the scene plane, π_0, does not pass through either O_1 or O_2 .

Result 1. *When the scene is 2-D, as shown in Figure 5, the two images of the same scene shot from different angles are related by a projective transformation.*

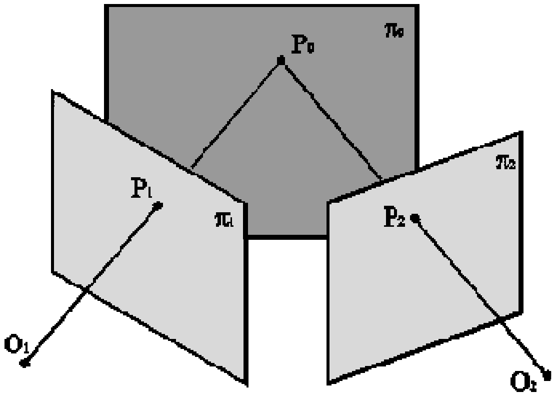

Figure 5. A 2-D Scene

This result is not new and it has been well understood in projective geometry [17]. It is listed here for the purpose of completeness of all situations and for comparison. The two photographs are related by a projective transformation, which is the product (composition) of two perspective transformations. The transformation is described by the following formula:

$$X' = \frac{a_{11}X + a_{12}Y + a_{13}}{a_{31}X + a_{32}Y + a_{33}}$$

$$Y' = \frac{a_{21}X + a_{22}Y + a_{23}}{a_{31}X + a_{32}Y + a_{33}} \qquad (2)$$

Where (X,Y) are the nonhomogeneous coordinates of a point on the image plane π_1, (X',Y') are the nonhomogeneous coordinates of the corresponding point on the image plane π_2, a_{ij} are constant parameters determined by the positions of O_1 and O_2 and the positions of π_0, π_1, and π_2.

3-D Scenes

Result 2. *When the scene is 3-D in space, as shown in Figure 6, the two images of the same scene shot from different angles are not related by a projective transformation. In fact, there is not even a well-defined mapping between the two images.*

Proof. Assume two photographs of the same 3-D scene are taken from different angles, as in Figure 6. Only one counterexample suffices to show this. Let x,y,z be the coordinate system attached to the first camera with its origin at O_1. Suppose further that there is a circle in the scene shown in Figure 7, which is described by

$$y^2 + (z-a)^2 = b^2, x = 0, b > 0, a > f + b \qquad (3)$$

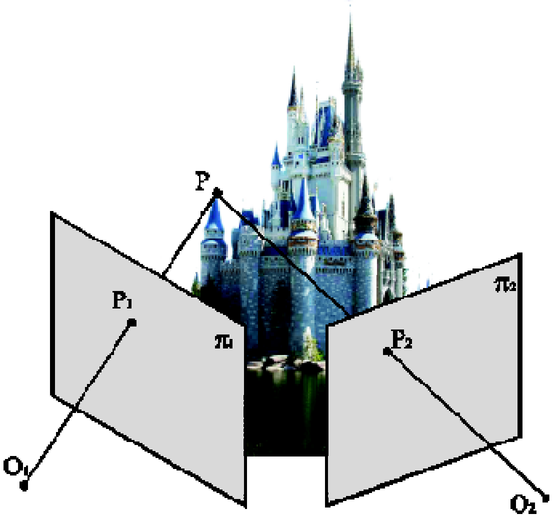

Figure 6. A 3-D Scene

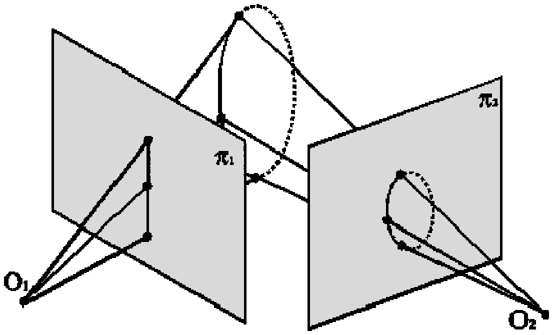

Figure 7. Part of a 3-D Scene: One Image is a Straight Line while the other is a Curve

The image of this circle on the photograph taken with the first camera is a straight line because the plane $x = 0$ passes through O_1. It is obvious that the image of the same circle is a curve on the second photograph taken by the second camera, provided that O_1 and O_2 are different and the axes z and z' (optical axis of the second camera) do not coincide. Because projective transformations always map straight lines to straight lines, the correspondence from image points (X,Y) to image points (X',Y') cannot be a projective transformation. In fact, in the general situation, the correspondence from one photograph to another is not even a well-defined mapping. This fact is evident in epipolar geometry, where a single point in one image corresponds to one entire epipolar line in the other image. ■

Figure 8 illustrates another counterexample in art. It is a sculpture by the Swiss artist Markus Raetz. From one angle, Figure 8(a), it looks like “YES”, while from a perpendicular angle, Figure 8(d), the word reads “NO”.

However, as discussed in the introduction with the example in Figures 2(a) and 2(b), given an image of a building, after a projective transformation performed in the image plane, it does look like another image of the same scene from a different angle. Does this contradict Result 2? In fact, this is an approximation. The conditions for this approximation to work are as follows:

Result 3. *When the scene is 3-D in space, the relationship between the two images of the same scene can be approximated by a projective transformation, under the following conditions:*

(1) The depth of the scene (the maximum difference in depth between any two points in the scene) is small compared with the subject distance (from the COP to the front of the scene).

(2) The difference between the two viewing angles is small.

(3) There are no occlusions (there are no points showing on one image but not on the other).

This explains why the perspective rectification works for the example in Figures 2(a) and 2(b). It also explains why the projective approximation fails in the case of Figure 8. In this case, the two viewing angles differ by 90° and there are

(a) Front View **(b) Oblique View** **(c) Oblique View** **(d) Side View**

Figure 8. Same 3-D Scene Viewed from Different Angles [Markus Raetz "Zeichnungen" © 2013 Artists Rights Society (ARS), New York / ProLitteris, Zurich. Reproduced by Permission.]

severe occlusions from these two viewing angles. If the difference in viewing angles is small and there are no occlusions, the projective approximation should also work for the images of this sculpture, like the two views in Figures 8(b) and 8(c).

Relationship between Images Captured from Different Distances

The next situation that needs to be analyzed is when the two images of the same scene are shot from the same angle but different distances. The axes of the two cameras coincide and the image planes of the two cameras are parallel to each other. The scene can be either 2-D or 3-D. This is really a special case of the situation that was analyzed in the last section, so the results in the last section apply here also. However, because this situation is encountered so frequently in practical situations, it deserves special attention and treatment. The analysis of this situation is also related to depth inference; that is, to infer how far away the camera was from the scene when the photograph was shot, and the relative distances between objects in 3-D, by measurements on the image.

2-D Scenes

First assume the scene is 2-D. In Figure 9, camera one has COP O_1 and camera two has COP O_2, and the axes (z-axes) of the two cameras coincide. The image planes π_1 and π_2 are parallel, and both are perpendicular to the line O_1O_2 . The scene plane, π_0, is not necessarily parallel to π_1 or π_2. The following is really a corollary of Result 1; a special case of the situation in the last section with 2-D scenes.

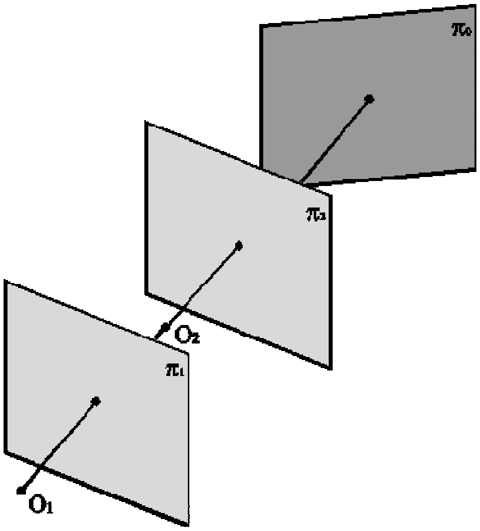

Figure 9. A 2-D Scene at an Oblique Angle

Result 4. *In the setting described in Figure 9, the two images on π_1 and π_2 of the same planar scene, π_0, are related by a projective transformation.*

As a special case of Result 4, if the scene plane, π_0, is also parallel to π_1 and π_1, as shown in Figure 10, the projective transformation becomes a similar transformation. This is the case when a photograph of a framed painting on the wall is shot from different distances. If the camera is leveled, the images from different distances are related by a scaling factor. By merely looking and measuring on the photograph, there is no way to infer how far away the camera was from the wall when the photograph was shot.

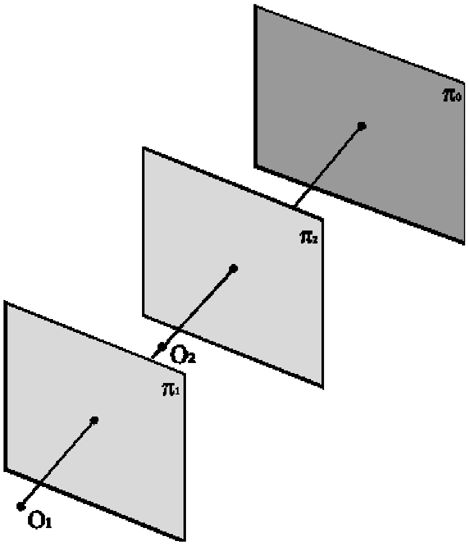

Figure 10. A 2-D Scene Parallel to the Image Planes

Result 5. *In the setting described in Figure 10, when the scene plane is parallel to the image planes, the two images on π_1 and π_2 of the same scene, π_0, are related by a similar transformation.*

Proof. The proof is straightforward. Suppose two cameras have focal lengths f and f'. The subject distance for camera one is z and that for camera two is z'. Because the scene is 2-D and parallel to π_1 and π_2, z and z' are constants for all the scene points. In the coordinate systems for the two cameras, x and x' coincide, and y and y' coincide as well. On the first image,

$$\begin{aligned} X &= \frac{fx}{z} \\ Y &= \frac{fy}{z} \end{aligned} \tag{4}$$

The same scene point has the same x and y coordinates in the second camera coordinate system but a different z' coordinate. On the second image,

$$\begin{aligned} X' &= \frac{f'x}{z'} \\ Y' &= \frac{f'y}{z'} \end{aligned} \tag{5}$$

The two images are then related by

$$\begin{bmatrix} X' \\ Y' \end{bmatrix} = \frac{f'z}{fz'} \begin{bmatrix} X \\ Y \end{bmatrix} \tag{6}$$

This is a similar transformation because z and z' are constants for all the scene points. ■

3-D Scenes

When the scene is 3-D, the situation is more complex, but there is a simple case in which the two cameras are positioned at the same point and same direction. The two cameras, though, may have different focal lengths. In that case, the two images are related by a similar transformation (scaling).

Result 6. *Suppose the scene is 3-D in the setting described in Figure 11, and the two cameras are located at the same position (O_1 and O_2 coincide). The two cameras are shooting in the same direction (z and z' coincide). The two cameras may have different focal lengths, f and f'. Then the two images on π_1 and π_2 are related by a similar transformation.*

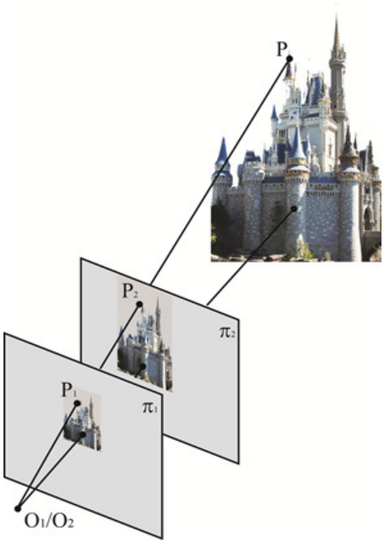

Figure 11. 3-D Scene with Two Cameras at the Same Position

Proof. The proof is trivial. While in real situations, it is the case that the two pictures are taken at different times, geometry does not deal with time. The two image planes, π_1 and π_2, of the two cameras can be placed side by side such that they would be parallel to each other according to the assumption. The scene point P, the image point P_2 on π_2, the image point P_1 on π_1, and the COP O_1/O_2 all lie on the same line. The image on π_2 and the image on π_1 are related by a similar transformation with f'/f being the scaling factor. ■

The same conclusion can be reached using coordinates. The coordinates (X',Y') of the image point P_2 on π_2 and coordinates (X,Y) of the image point P_1 on π_1 are related by

$$\begin{bmatrix} X' \\ Y' \end{bmatrix} = \frac{f'}{f} \begin{bmatrix} X \\ Y \end{bmatrix} \tag{7}$$

This clarifies the misconception in photography that wide-angle and telephoto lenses may cause perspective distortions. What causes the perspective distortion is not the focal length of the camera, but rather the subject distance. This has been known to some photographers. Guo [5] gives a quantitative analysis of perspective distortion by defining a perspective diminution factor and a foreshortening factor. The perception of perspective distortion is caused by the shooting distance and also by resizing the image. This is because when the shooting distance is different, the depth of the same scene point is different in two camera coordinate systems, and both the perspective diminution factor and foreshortening factor are functions of depth.

As an example, Figures 12(a) and 12(b) are two photographs of the same scene taken at the same position, with one wide-angle lens and one telephoto lens. If the center part in the rectangle frame of Figure 12(a) is cropped and enlarged, it is identical to Figure 12(b).

Now suppose that two photographs of the same 3-D scene are taken from different distances, as shown in Figure 13. Figure 13 looks similar to Figure 11, but note that there is a big difference. In Figure 11, the two cameras are located at the same position: O_1 and O_2 are the same point. In Figure 13, the two cameras are located at two different locations, O_1 and O_2. Let the distance $O_1O_2 = s$. The two cameras may have different focal lengths f and f'.

Result 7. *When the scene is 3-D in space, the two images of the same scene shot from different distances are not related by a projective transformation. In fact, there is not even a well-defined mapping between the two images.*

(a) Wide-Angle Lens, from a Distance of 12 Meters

(b) Telephoto Lens, from a Distance of 12 Meters

Figure 12. Same Scene Shot with a Wide-Angle Lens and a Telephoto Lens from the Same Distance

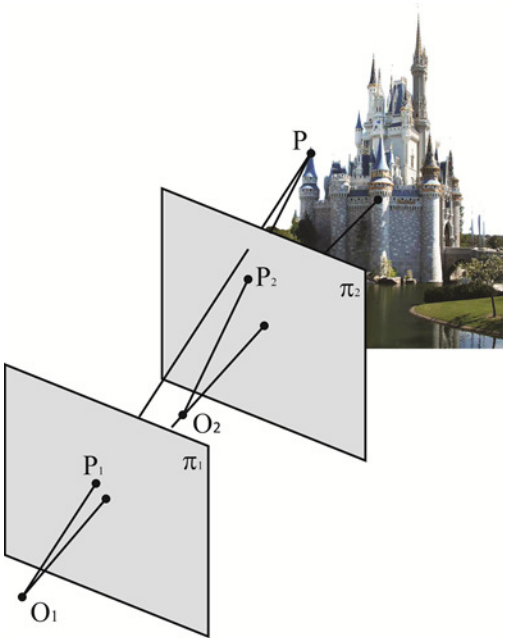

Figure 13. 3-D Scene with Two Cameras from Different Distances

The same scene point *P* has coordinates (*x*,*y*,*z*) and (*x*′,*y*′,*z*′) in the two camera coordinate systems and they are related by

$$\begin{aligned} x' &= x \\ y' &= y \\ z' &= z - s \end{aligned} \tag{8}$$

For the scene point *P* in space, its image point $P_1 = (X,Y)$ in photograph π_1 is

$$\begin{aligned} X &= f\,\frac{x}{z} \\ Y &= f\,\frac{y}{z} \end{aligned} \tag{9}$$

The image point $P_2 = (X',Y')$ in photograph π_2 of the same scene point *P* is

$$\begin{aligned} X' &= f'\,\frac{x}{z-s} \\ Y' &= f'\,\frac{y}{z-s} \end{aligned} \tag{10}$$

The same scene point *P* in 3-D space is projected in photograph π_1 as point $P_1 = (X,Y)$, but is projected in photograph π_2 as point $P_2 = (X',Y')$. This induces a correspondence from $P_1 = (X,Y)$ in π_1 to $P_2 = (X',Y')$ in π_2. When O_1 and O_2 are different and $s \neq 0$, the correspondence from (X,Y) to (X',Y') is not a similarity transformation. It is not a projective transformation either. In fact, this correspondence from (X,Y) to (X',Y') is not even a well-defined mapping. From Equations (2) and (3),

$$\begin{aligned} X' &= \frac{f'z}{f(z-s)}X \\ Y' &= \frac{f'y}{f(z-s)}Y \end{aligned} \tag{11}$$

Notice that coordinates (X',Y') are not uniquely determined by (X,Y). They are also affected by the depth, z, of the scene point. The 3-D position (x,y,z) of the scene point P could be altered so that z is changed but (X,Y) remain the same. But (X',Y') will change because z changes, even if (X,Y) are kept the same.

Figures 14(a) and 14(b) are two photographs of the same 3-D scene. Figure 14(a) was shot from a closer distance (4 m) with a wide-angle lens, while Figure 14(b) was shot from a further distance (12 m) with a telephoto lens. Since the image planes of the two cameras are parallel and the z axes coincide, if the two images are related by a projective transformation, it must be a similar transformation. It is easy to see that these two images are not related by a similar transformation, because when the front arch in the two photographs are registered (aligned), the images of the background arch are not aligned (one is bigger than the other).

Figures 3(a) and 3(b) are two portraits of the same person. Figure 3(a) was shot with a 24 mm lens (35 mm film equivalent) from a subject distance of one foot, while Figure 3(b) was shot with a 100 mm telephoto lens (35 mm film equivalent) from a much longer subject distance. In general, close subject distances introduce more distortions. Note that big eyes do not always make the subject more attractive if the face is distorted. This type of perspective distortion exists in most of the self-portraits shot by Webcams and cell phones due to close subject distances. Many factors may contribute to the distortions in the left portrait in Figure 3(a). With very short focal length wide-angle lenses, barrel distortions also exist, which is one type of aberration of the lenses, known as curvature of field. Curvature of field is not due to perspective. It is a nonlinear aberration of the lens which makes a lens deviate from a linear optical system. The image of a straight line becomes a curve if curvature of field exists with the lens. The discussion here is limited to perspective distortions. Even if the distortion of the portrait in Figure 3(a) is purely perspective, it could be the combined effect of a tilted viewing angle and short subject distance. The tilted view angle can be rectified by a projective transformation with the help of software tools. A projective transformation may slightly enhance it, but it is not possible to transform the portrait in Figure 3(a) to exact the one in Figure 3(b) because of the deformation caused by depth difference in the scene. Without the depth information of each point in Figure 3(a), the image cannot be rectified through a simple transformation. It is the common wisdom in portrait photography that longer focal lengths produce more pleasing, attractive portraits and wide-angle lenses and short subject distances should be avoided to reduce perspective distortion.

Bryan et al. [18] performed surveys of people's perceptions of face portraits shot from close-up distances and longer distances, and reported that close-up portraits are perceived less attractive, less trustworthy, and less competent. Those factors involve psychological and social issues and are difficult to be rigorously defined. Result 7 offers a quantitative analysis and explanation of this phenomenon. That is, the two images shot from different distances of the 3-D scene are not related by a similar transformation. This results in the perspective distortion when the subject distance is extremely short. Furthermore, this perspective distortion cannot be rectified with a simple projective transformation. It is commonly felt that a portrait shot from a very close

(a) Wide-Angle Lens: Shot from a Short Distance (4 Meters) **(b) Telephoto Lens: Shot from a Long Distance (12 Meters)**

Figure 14. Same Scene Shot with a Wide-Angle Lens and a Telephoto Lens from Different Distances

distance like that in Figure 3(a) is less aesthetic. In practical situations, one's eyes usually do not have a lot of experience staring at a person's face at such a close distance (say, one foot), as the camera in Figure 3(a) does.

There is also a common misconception about close-up photographs. It is the principle of perspective that for the same object, when the distance is bigger, the image is smaller. When the distance is closer, the image is larger. So, people tend to associate large images of a small part of an object to a close viewing distance. However, one factor that is often overlooked is that the images can be artificially enlarged. Many such "close-up" photographs are artificially enlarged images (either by a telephoto lens when the image was shot, or by image editing after the image was shot). Enlarging an image with image editing software is so easy to do, when high resolution imaging becomes a practical standard with the improvement of the resolution of image sensors of digital cameras. Cropped and enlarged images can give a "close-up" impression because a small part of the object may look very big, but they may not be images shot with really close distances and they do not have severe distortions.

Perspective Depth Inference in a Single Image

It must be made clear that no inference of the depth of the 3-D scene can be made from a single image, unless additional prior knowledge about the 3-D scene is available. This is because the depth ambiguity is caused by central projection from 3-D space to the 2-D image plane. With this central projection, an entire line is projected to a single point in the image plane, thereby losing the depth information. Just by examining a photograph of a castle, there is no way to tell whether this is a photograph of a real 3-D castle or a photograph of a framed photograph of a castle hanging on the wall. In the former case, the scene points of the real castle have various depths, while in the latter case all of the scene points in the framed art have the same depth.

In many common 3-D scenes, like buildings on a street, there are naturally three families of parallel lines. The three families of lines are usually the length, width, and depth directions of the buildings. They are perpendicular to each other and a Cartesian coordinate system $(\tilde{x}, \tilde{y}, \tilde{z})$ can be established along these directions, which shall be called the world coordinate system. The relative orientation of the camera coordinate system (x,y,z) and the world coordinate system $(\tilde{x}, \tilde{y}, \tilde{z})$ determine whether the image is a one-point perspective, two-point perspective, or three-point perspective. The first two cases are discussed next.

One-Point Perspective

In a one-point perspective image, there is one vanishing point. The world coordinate lines $(\tilde{x}, \tilde{y}, \tilde{z})$ are parallel to the camera coordinate lines (x,y,z), respectively. The image of the lines parallel to the z direction converge to the principle vanishing point, C.

Figures 2(a) and 2(b) are one-point perspective images. Figure 2(a) is duplicated, with points labeled in Figure 15. Let A_1 and A_2 be two points at the feet of the two columns in the front, and B_1 and B_2 be two points at the feet of the two columns in the back of the pavilion. D_1D_2 is the end line of the pool on the far side. Assume that partial knowledge of the objects in the image is available; that is, the ground plane and objects on the ground plane can be recognized, like the concrete tiles under the pavilion and the pool are in the ground plane. It can be assumed that the image plane is vertical, which is perpendicular to the ground plane when the image was taken. If the image has not been cropped, and the ground plane is exactly horizontal and the image plane is exactly vertical, then the center of the image is the vanishing point. These conditions cannot always be exactly guaranteed when the image is taken, so it is safer not to make all of these assumptions. Some lines on the ground, perpendicular to the image plane, can be recognized; for example, the two long edges of the pool. The intersection of these lines is vanishing point C, which is also the coordinate origin in the image plane. Through C, draw a line perpendicular to A_1A_2, B_1B_2 , and D_1D_2, meeting them at A, B, and D, respectively. CA is along the Y-axis in the image plane. The same coordinate system as in Figure 4 is used. Let O be the COP, and $OG = h$ and f be the focal length of the camera.

For any point P on the ground plane, it has coordinates $(x,-h,z)$ and, according to the camera projection formula in Equation (1), its image (X,Y) in the image plane has

$$Y = -\frac{fh}{z} \tag{12}$$

The depth, z, can be obtained by

$$z = -\frac{fh}{Y} \tag{13}$$

In this section, only the depth of the objects in the ground plane is concerned. The depth of the vertical objects can be found from the depth of their feet on the ground. In this coordinate system, $Y < 0$ for all the objects on the ground. For convenience, the absolute value $|Y|$ is used. That is,

$$z = \frac{fh}{|Y|} \tag{14}$$

where, f and h are intrinsic and extrinsic parameters of the camera.

Figure 15. Depth Inference on a One-Point Perspective Image

In machine vision applications, as well as in photogrammetry, the camera can be fully calibrated with all of the intrinsic and extrinsic parameters calculated. In everyday, casual photography, this is not possible. However, it is not necessary to know the focal length of the camera and the height of the camera, h, when the photograph was taken. If the product fh is known, the depth information, z, can be inferred through the measurement of distance $|Y|$ on the image. Most of the time, the image is scaled (enlarged). The size of the image in print or on the computer screen is not the same as that on the image sensor of the camera, the distance $|Y|$ is relative and fh is relative also, up to a scaling factor. The distance of some line segment along the depth direction needs to be known in order to calibrate Equation (4) to find the parameter fh. In this example, assume some prior knowledge about the pavilion is available: the pavilion is a square shape with a side length of about $d_{AB} = z_B - z_A = 3.0$ meters. The measurements on the image will use centimeters, so all distances are converted to centimeters, with $d_{AB} = 300$ cm. Hence,

$$\begin{gathered} z_A = \frac{fh}{|Y_A|} \\ z_A + d_{AB} = \frac{fh}{|Y_B|} \end{gathered} \tag{15}$$

With measurements on the image, the following values were obtained: $|Y_A| = 2.40$ cm, $|Y_B| = 1.70$ cm, and

$$fh = \frac{Y_A Y_B}{|Y_A - Y_B|} d_{AB} = 1748.6 \tag{16}$$

hence,

$$z = \frac{1748.6}{|Y|} \tag{17}$$

and $z_A = 7.29$ cm. That is, the camera was 7.3 m away from the pavilion when the image was shot. It, too, was calculated: $z_B = 10.3$ m. With the measurement $|Y_B| = 0.25$ cm, it was also found that $z_D = 69.9$ m. The distance from the background building to the front pavilion $BD = z_D - z_B$ was about 60 m.

The same process of depth inference can be applied to the image in Figure 2(b). Figure 2(b) was duplicated, with points labeled in Figure 16. The same labels were used from Figure 15. The coordinate system (x,y,z) used for the image in Figure 16 was different from that for Figure 15 because the origin was different now and z, for the same scene point, was different. The focal length of the camera, f', was different also. The camera height, h', may be different as well. In this image, $|Y_A| = 2.20$ cm, $|Y_B| = 1.88$ cm, and $|Y_D| = 0.48$ cm. It can be found that

$$z = \frac{3877.5}{|Y|} \tag{18}$$

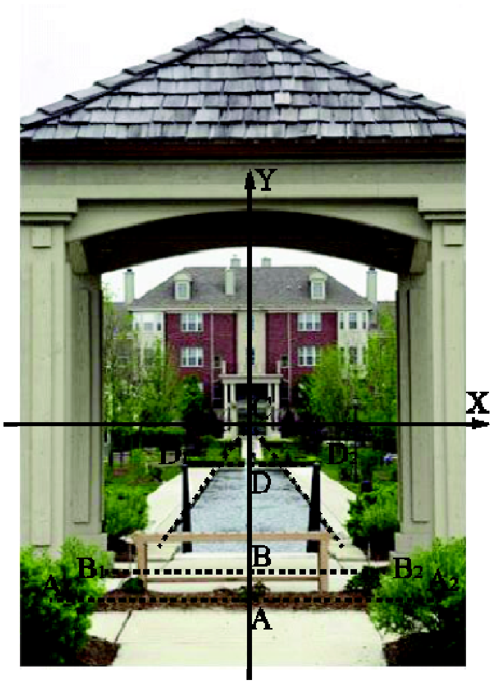

Figure 16. Depth Inference on a One-Point Perspective Image

The calculation reveals that z_A = 17.7 m. This means that the camera was 17.7 m away from the pavilion with a telephoto lens when this image was shot. This verifies that the camera was really further away when this image was shot, compared with the image in Figure 15, which was shot from a distance of 7.3 m, with a wide-angle lens. The distance between the background building and the front pavilion is $z_D - z_B$ = 60.2 m. This corroborates the depth inference made from the image in Figure 15.

Two-Point Perspective

It is often the case that the image is a two-point perspective instead of a one-point perspective. In such cases, the depth inference techniques for a one-point perspective discussed in the last section can be adapted to two-point perspectives as well. In a two-point perspective image, there are two vanishing points.

Figure 17 is a drawing in two-point perspective. The world coordinate line is parallel to the camera coordinate line y, but $(\tilde{x}, \tilde{z})$ are at oblique angles with x and z (see Figure 18). In Figure 17, the two vanishing points on the image plane are V_1 and V_2 . The line V_1 V_2 is the horizon line. The same coordinate system, X, Y, can be used in the image plane. Perspective depth inference can work with two -point perspectives as well.

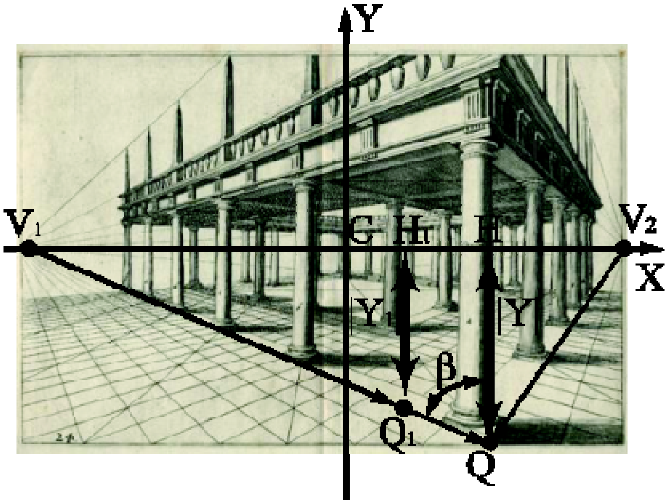

Figure 17. Depth Inference on a Two-Point Perspective Image

Figure 18 shows the ground plane. Point G is the station point, which is the perpendicular foot of COP O on the ground, as in Figure 4. Axes $(\tilde{x}, \tilde{z})$ form an angle α with axes x and z. Then,

$$\tilde{z} = \frac{z}{\cos\alpha} \tag{19}$$

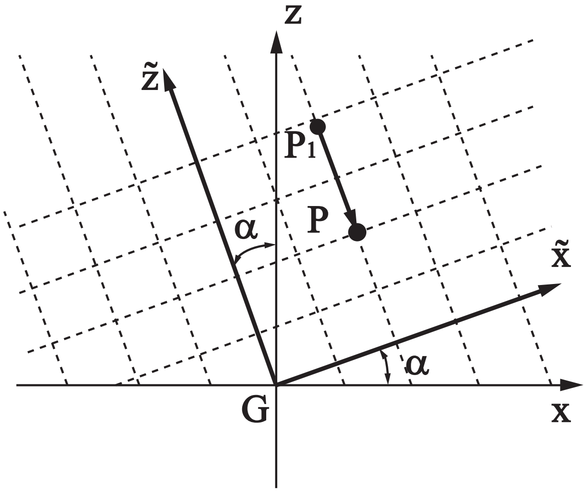

Figure 18. The Ground Plane in the Scene of Figure 17

Let P and P_1 be two points in the ground plane along the $\tilde{z}$ direction. Their images are Q and Q_1 in the image plane (see Figure 17). The distances Q and Q_1 to the horizon line V_1 V_2 are $|Y|$ and $|Y_1|$. Suppose V_1Q forms an angle β with the vertical line in the image; then,

$$\overline{V_1Q} = \frac{|Y|}{\cos\beta} \tag{20}$$

The measurement on the image can use the vertical distance $|Y|$ to the horizon line, or the distance $\overline{V_1Q}$ to the vanishing point V_1, since they only differ by a constant factor. By Equation (1),

$$|Y| = \frac{fh}{\tilde{z}\cos\alpha} \tag{21}$$

If distance $\overline{P_1P_2}$ between two points P_1 and P_2 along the $\tilde{z}$ direction is known, it can be used to calibrate the parameter $fh/\cos\alpha$, and the depth along $\tilde{z}$ the direction can be calculated by

$$\tilde{z} = \frac{|Y_1||Y_2|}{|Y_2 - Y_1|}\frac{\overline{P_1P_2}}{|Y|} \tag{22}$$

The depth inference along the $\tilde{x}$ direction can be accomplished similarly because $\tilde{x}$ is also proportional to z, with a simple relationship

$$\tilde{x} = \frac{z}{\sin\alpha} \tag{23}$$

When the 3-D scene has three orthogonal families of parallel lines, the image can take the form of a one-point perspective, two-point perspective, or three-point perspective, with the first two being the most common. The depth inference in a two-point perspective image is a little more completed than a one-point perspective. In a two-point perspective image, depth inference can be conducted along the z direction, $\tilde{z}$ direction, or $\tilde{x}$ direction. With the analysis above, the depth inference in either of these directions is the same as the depth inference in a one-point perspective image.

Conclusions

The relationship between images of the same scene shot from different angles and from different distances was investigated. Results are shown for 2-D scenes and 3-D scenes. For the 2-D scenes, the images are related by projective transformations and, in special cases, similar transformations. For 3-D scenes, the images are not related by a projective transformation. Even further, the relationship is not even a well-defined mapping because of the depth ambiguity in central projection from 3-D space to the 2-D plane. The conditions are given when the relationship between images of 3-D scenes can be approximated by a projective transformation and, hence, when perspective rectification applies. Depth inference from a single image is also explored with the assumption of partial knowledge of the 3-D scene and human recognition of objects. A special example of two images of the same scene was used to illustrate this process. The distance from the camera to the scene was recovered. It was inferred that one image was shot from a closer distance of 7.3 m with a wide-angle lens, while the other was shot from a longer distance of 17.7 m with a telephoto lens. The background building looks closer to the front pavilion in one image than in the other. Although cameras may cheat the eyes, with the demonstrated calculations in perspective analysis on two quite different looking images, a consistent conclusion about the depth of the background building is determined from both images.

Image Credits

The author would like to thank Rosh Sillars for permission to use two images, which appear in Figures 2(a) and 2 (b), Figures 15 and 16. The drawing in Figure 17 is from Jan Vredeman De Vries (1604) [19], which is in the public domain. The remaining photographs in this article were taken by the author.

References

[1] Roncella, R., & Forlani, G. (2003). Image-to-Image Perspective Rectification. *The International Archives of the Photogrammetry, Remote Sensing and Spatial Information Sciences, 34*(5/W12), 289-293.

[2] Fryer, J. G., & Brown, D. C. (1986). Lens distortion for Close-Range Photogrammetry. *Photogrammetric Engineering & Remote Sensing*, *52*(4), 51-58.

[3] Clark, P., & Mirmehdi, M. (2003). Rectifying Perspective Views of Text in 3D Scenes Using Vanishing Points. *Pattern Recognition, 36*(11), 2673–2686.

[4] Veblen, O., & Young, J. W. A. (1938). *Projective geometry*. Ginn & Co.

[5] Guo, H. (2013). Definitions of Perspective Diminution Factor and Foreshortening Factor: Applications in the Analysis of Perspective Distortion. *International Journal of Modern Engineering*, *13*(2), 78-87.

[6] Thamma, R., Kesireddy, L. M., & Wang, H. (2012). Centralized Vision-Based Controller for Unmanned Guided Vehicle Detection. *International Journal of Modern Engineering*, *12*(2), 58-65.

[7] Vargas-Clara, A., & Redkar, S. (2011). Dynamics of a Vertical Takeoff and Landing (VTOL) Unmanned Aerial Vehicle (UAV). *International Journal of Engineering Research Innovation*, *3*(1), 52-58.

[8] Eydgahi, A., Godaliyadda, D., & Falase, S. (2007). A Simulation Software for Autonomous Navigation of Unmanned Surface Vehicles Using MATLAB Environment. *International Journal of Modern Engineering*, *7*(2).

[9] Zhang, B., & Skaar, S. B. (2010). Laser-Assisted Uncalibrated Vision Guide Robotic De-palletizing. *International Journal of Engineering Research Innovation*, *2*(2), 17-24.

[10] Cao, Y., Xia, Y., & Wang, Z. (2010). A Close-Form Iterative Algorithm for Depth Inferring from a Single Image. *Proc. Perspectives in Neural Computing*, 729 -742.

[11] Wu, B., Ooi, T. L., & He, Z. J. (2004). Perceiving Distance Accurately by a Directional Process of Integrating Ground Information. *Nature*, *428*(6978), 73-77.

[12] Gao, X., Hou, X., Tang J., & Cheng, H. (2003). Complete Solution Classification for the Perspective-Three-Point Problem. *IEEE Trans PAMI*, *25*(8):930-943.

[13] Saxena, A., Chung, S. H., & Ng, A. Y. (2005). Learning Depth from Single Monocular Images. *Neural Information Processing System*, *18*.

[14] Saxena, A., Sun, M., & Mg, A. Y. (2008). Make3d: Learning 3-d Scene Structure from a Single Still Image. *IEEE Tran. PAMI*, *31*, 824-840.

[15] Saxena, A, Schulte, J., & Mg, A. Y. (2007). Depth Estimation Using Monocular and Stereo Cues. *International Joint Conference on Artificial Intelligence*.

[16] Yu, S. X., Zhang H., & Malik, J. (2008). Inferring Spatial Layout form a Single Image via Depth-ordered Grouping. *Workshop on Perceptual Organization in Computer Vision*.

[17] Coxeter, H. S. M. (2008). *The Real Projective Plane*. 3rd ed., Springer.

[18] Bryan, R., Perona, P., & Adolphs, R. (2012). Perspective Distortion from Interpersonal Distance Is an Implicit Visual Cue for Social Judgments of Faces. *PLoS ONE*, *7*(9), e45301.

[19] Jan Vredeman de Vries, (1968). *Perspective*. Dover Publications.

Biography

HONGYU GUO is an Assistant Professor of Computer Science at the University of Houston – Victoria. He received his Ph.D. degree in Computer Science from the University of Florida. His research interests are in computer graphics, computer vision, image processing and artificial intelligence. He can be reached at guoh@uhv.edu.

THE INFLUENCE OF LIQUID COOLANT FLOW REGIMES ON THE QUALITY OF INJECTION MOLDED PLASTIC PARTS

Rex Kanu, Ball State University; Nathan Marsh, Ball State University

Abstract

The injection molding of plastic parts is comprised sequential interconnected events, which include closing of the mold, injecting of molten plastic into the closed mold, forming of the molten plastic into a desired shape, cooling of the shaped molten plastic, and opening of the mold and ejecting the sufficiently cooled and shaped plastic parts. Of these events, the cooling of the shaped molten plastic plays an important role in obtaining good and acceptable quality parts. For this reason, this study was undertaken to elucidate the cooling process and its impact on plastic molded parts. While there are many factors that affect cooling in injection molding, such as the layout of the cooling channels and the materials used in building the mold, the authors chose to study the influence of coolant flow regimes on molding cooling. The findings of this work suggest that coolant flow regimes and coolant temperatures affect the heat-transfer coefficient of the coolant and, consequently, the mold cooling efficiency. Furthermore, it was found that inefficient molding cooling can result in a rather large temperature difference between the coolant inlet and outlet temperatures, which in turn can result in substantial plastic part warpage. Based on the authors' findings, it is suggested that coolant flow rate for efficient mold cooling should be determined for individual plastic materials since it does not appear that one coolant flow rate is suitable for all plastic materials.

Introduction

The injection molding of plastic parts consists of a sequence of interconnected events, and the time required to complete these events is known as the cycle time of the process. These events include closing the mold, injecting molten plastic into the closed mold, cooling the molten plastic, and opening the mold and ejecting the sufficiently cooled plastic parts. Among this series of events, the cooling process appears to play a crucial role in a successful injection molding process because it alone generally accounts for about 75% of the cycle time [1]. Furthermore, the cooling process has a large influence on plastic part quality [2].

Separately, the cooling process is comprised of three major components: 1) cooling of the molten plastic, 2) conduction of heat from the molten plastic to the cooling channels in the mold, and 3) convection cooling by liquid coolant in the cooling channels [3]. Of these three major components, the first two components are usually determined during the design stage of an injection molding project, while the third component is implemented during the processing of plastic parts. Since the authors were interested in the effect of liquid coolant flow regimes on plastic parts quality, an existing injection machine and mold were used to examine the effects of convection cooling on physical properties and tensile properties of injection molded parts. To achieve these goals, the authors employed the relationship between the convection heat-transfer coefficient of the cooling process and the flow regimes of the liquid coolant. This relationship is captured by the Colburn [4] equation (Equation 1), which shows how the coolant flow regime, described by its Reynolds number, N_{RE} (Equation 2), is related to the individual (inside of cooling channel) convection heat-transfer coefficient, h_i, for forced convection in turbulent flow (N_{RE} greater than 6,000) for Newtonian liquids.

$$\frac{h_i}{c_p G}\left(\frac{c_p \mu}{k}\right)^{2/3}\left(\frac{\mu_w}{\mu}\right)^{0.14} = \frac{0.023}{\left(D G \big/ \mu\right)^{0.2}} \tag{1}$$

where,

c_p = specific heat capacity at constant pressure, J/g-ºC or Btu/lb-ºF
D = diameter, m or ft
G = mass velocity, kg/m^2-s or lb/ft^2-s ($G = V\rho$)
h_i = individual heat-transfer coefficient, W/m^2-ºC or Btu/ft^2-h-ºF
k = thermal conductivity, W/m-ºC or Btu/ft-h-ºF
V = average velocity, m/s or ft/s
ρ = density, kg/m^3 or lb/ft^3
μ = viscosity, kg/m-s or lb/ft-s, μ_w = value at wall temperature

$$N_{RE} = \frac{DV\rho}{\mu} \tag{2}$$

Equation 3 is used for laminar flows (N_{RE} less than 2,100), while a graphical solution [5] is used for transition flows (N_{RE} between 2,100 and 6,000):

$$\frac{h_i}{c_p G}\left(\frac{c_p \mu}{k}\right)^{2/3}\left(\frac{\mu_w}{\mu}\right)^{0.14} = 1.86\left(\frac{D}{L}\right)^{1/3}\left(\frac{DG}{\mu}\right)^{-2/3} \tag{3}$$

where,

L = length of the cooling channels (tubes) in the mold, m or ft.

The overall heat-transfer coefficient, U , for the cooling process is expressed by Equation 4 [6], where K is the thermal conductivity of mold material [7] and S is the conduction shape factor of the cooling channels. In this study, K and S were considered constant since their values were set when the mold was built. Values of h_i were estimated from Equations 2, 3 and a graphical solution [6].

$$\frac{1}{U} = \frac{1}{KS} + \frac{1}{\pi D h_i} \tag{4}$$

The ultimate goal of this study was to determine optimal coolant flow rates in gallons per minute (gpm) in the efficient production of good quality injection molded parts based on the coolant flow regimes and heat-transfer coefficients.

Experimental Setup

Materials

Table 1 contains the plastic materials used in this study. These materials were selected because they were readily available.

Table 1. Plastic materials and some of their properties

Information	Polycarbonate (PC)	Polypropylene (PP)
Trade Name	Lexan® 940A	CP PRYME® PPH200-20M
Supplier	SABIC Innovative Plastics	Chase Plastics
Processing Grade	Injection Molding	Injection Molding
Melt Mass-Flow Rate	10g/10 min	12g/10 min
Nature of Solid	Amorphous	Semi-Crystalline

Equipment

A Sandretto 60-ton injection molding machine was used. A Conair Mold Temperature Controller (MTC), model TCI-DI, shown in Figure 1, was used to supply coolant to the mold and also control the mold temperature. The MTC displayed the coolant flow pressure, and the inlet and outlet temperature of the coolant.

Figure 1. Conair Mold Temperature Controller (MTC) and its Control Panel on the Right

A two-part cold mold made by Master Unit Die Products, Inc., shown in Figure 2(a), was used in the study to produce tensile and impact test specimens. The mold material was Stainless Steel 420 (420 SS). In Figure 2(a), the blue tube represents the coolant inlet to the mold while the red tube was the coolant outlet from the mold. The coolant flow rate in each part of mold halves was controlled with two ball valves attached to two Omega flow meters, model FL-2300ABR, shown in Figure 2(b). Figure 3 shows a schematic diagram showing the layout of the cooling channels of the two-part mold shown in Figure 2(a).

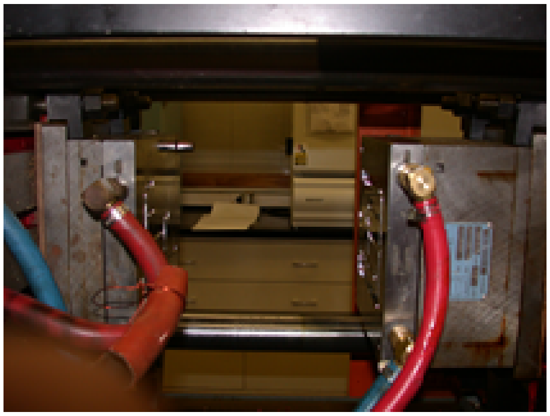

(a) A Two-Part Injection Mold

(b) Omega Flow Meters and Ball Valves

Figure 2. Injection Mold, Flow Meters, and Ball Valves

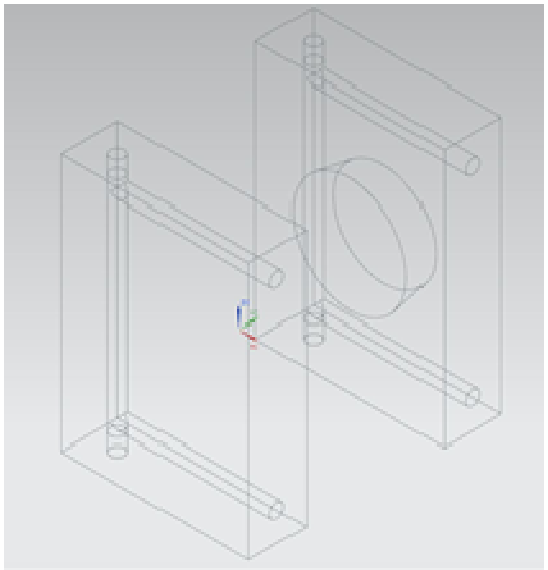

Figure 3. Schematic Diagrams of the Two-Part Cold Mold

Procedure

Before injection molding the plastic parts, PC and PP were dried for 3.5 hours at 250 ºF and for 1.5 hours at 190 ºF, respectively, with a Conair CD30 dehumidifying dryer. During the injection molding process, samples were not collected until the difference between the coolant inlet and outlet temperatures had reached a steady state; that is, $\Delta T = (T_{\text{out}} - T_{in}) =$ constant. After several trial runs, Table 2 shows the processing variables used to establish the baseline for this study. The baseline samples were regarded as the "perfect" plastic parts; the parts had no flash, short shot, sink marks, voids, or any visible defects.

Table 2. Injection Molding Process Variables

Processing Variable	Polycarbonate (PC)	Polypropylene (PP)
Melt Temperature	535 ºF	400 ºF
Mold Temperature	190 ºF	75 ºF
Injection Screw Speed	60 rpm	60 rpm
Back Pressure	100 psi	200 psi
Cooling Time	10 seconds	15 seconds
Coolant Flow rate	1.5 gpm	1.5 gpm

Having established the baseline processing variables, the effect of coolant flow regimes on the parts quality was examined by varying the coolant flow rates while keeping other variables constant. For any given coolant flow rate, 10 samples of PC and PP were collected after the system had attained a steady-state condition, that is, ΔT ($=T_{\text{out}} - T_{\text{in}}$) of coolant = constant. The coolant flow rates were randomly changed to prevent any systematic errors in the data collection process.

After a 40-hour wait period following the injection molding of the parts, five samples of PC and PP were randomly selected for testing for each coolant flow rate. The following tests were performed on the PC and PP samples.

- Gloss test with a Horiba Gloss Checker IG-320
- Warpage test with a bench steel block from Smith Tool and Engineering Company
- Tensile strength at yield and tensile strain at yield test using Instron® Universal Testing Instrument, Model 1011

Results and Discussion

Figure 4 shows the effect of the coolant temperature on coolant flow regimes, as indicated by its Reynolds Number, N_{RE}. With regard to the mold, all processing variables were the same except for the coolant inlet temperature (T_{in}), which was 75 ºF for PP and 190 ºF for PC. From Equation 1, it appears that coolant viscosity and density were highly impacted by the "average" coolant temperature:

$$\left[T_{average} = \frac{T_{out} - T_{in}}{2}\right] \qquad (5)$$

The effect of temperature of these fluid properties explains the large difference between the N_{RE} for PP and PC. This is so because the higher the average coolant temperature, the lower the coolant viscosity and density. Since the viscosity of water seems to be more sensitive to temperature changes than the density of water, the increase in coolant temperatures resulted in substantial increases in N_{RE}, according to Equation 1, with other variables held constant. The data showed that the coolant attained turbulent flow, $N_{RE} > 6000$, at 0.3 gpm for PC, and 0.7 gpm for PP.

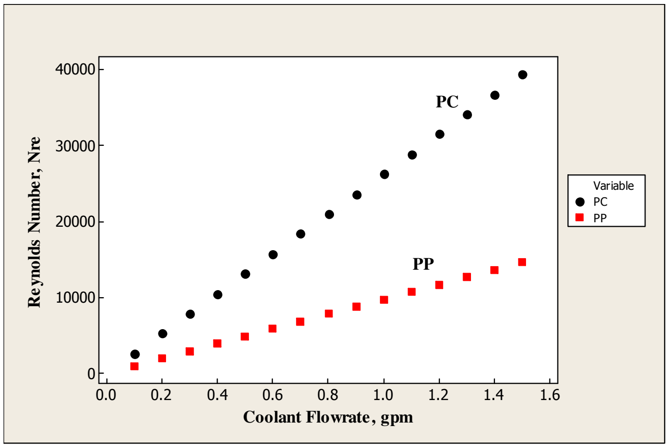

Figure 4. Coolant Reynolds Number for PC and PP

Figure 5 shows the influence of the coolant flow regimes on the individual (inside the tube) heat transfer coefficient of the coolant for PC and PP. The breaks in the plots show the effect of transitioning from laminar and transition flows to turbulent flow on the heat-transfer coefficient of the coolant for PC and PP. Combining the results of Figures 4 and 5, it is apparent that coolant regimes contributed to the differences in the heat-transfer coefficient of the coolant for PC and PP.

Figure 6 shows the temperature difference (ΔT) between the coolant inlet and outlet temperatures. The temperature readings were read off the mold temperature controller with a unit digit resolution. The low resolution in temperature readouts may be responsible for the shape of the plots in the figure. For example, the temperature readouts could be either 78 ºF or 79 ºF, but not 78.6 ºF. Despite this drawback, the figure shows a larger ΔT for PP than for PC at all coolant flow rates. Also, the difference appeared larger at lower flow rates (laminar and transitions flow) than at higher flow rates (turbulent flow). The significance of ΔT on part quality was noted by Rees [8] and Dym [9]. Rees [8] suggested that a large ΔT could result in "uneven molding cooling and longer molding cycles." He suggested that for some molding applications, ΔT should be between 1 – 2 ºC (2 – 4 ºF), while Dym [9] suggested a ΔT of 10 ºF for simple moldings and 5 ºF for complex moldings. Choosing a ΔT of 5 ºF for this study resulted in a recommendation that a coolant flow rate greater than 0.4 gpm would suffice for PC, while a coolant flow rate greater than 1.4 gpm would work for PP. These coolant flow rates correspond to an N_{RE} of 10,500 and 13,500 for PC and PP, respectively.

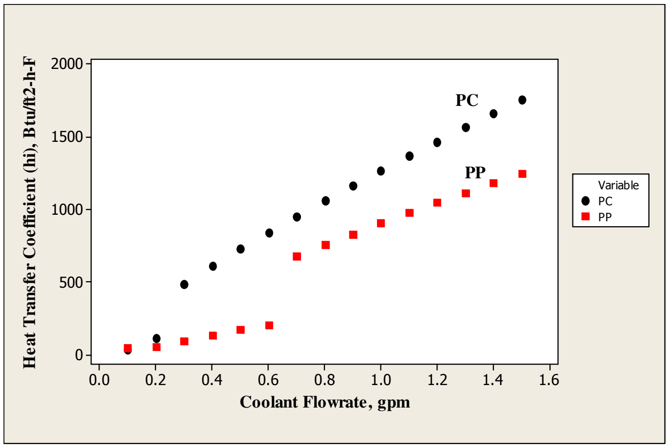

Figure 5. Heat Transfer Coefficient of Coolant for PC and PP

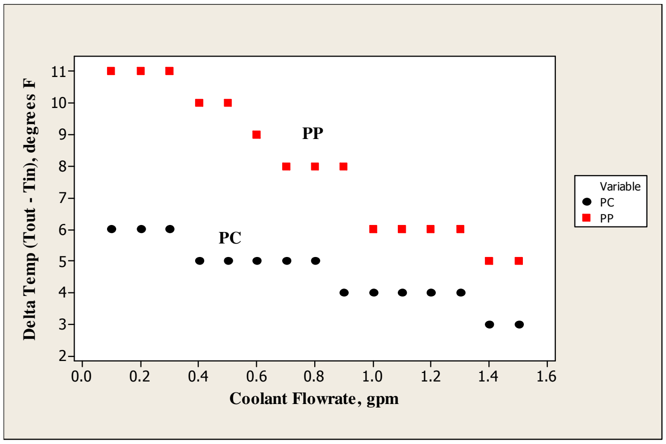

Figure 6. Difference, ΔT, in the Coolant Inlet and Outlet Temperatures

In Figure 7, the authors examined the influence of the coolant flow regimes on the tensile strength at yield of PC and PP, and it did not seem that coolant flow regimes had any significant effect on this property. Zhu et al. [10] also found in their work that the cooling process had a significant effect on the tensile strength of injection molded parts. As in Figure 7, Figure 8 shows that coolant flow regimes had no effect on tensile strain at yield of PC and PP, thus indicating negligible or no occurrence of brittleness due to thermal degradation, particularly in PP.

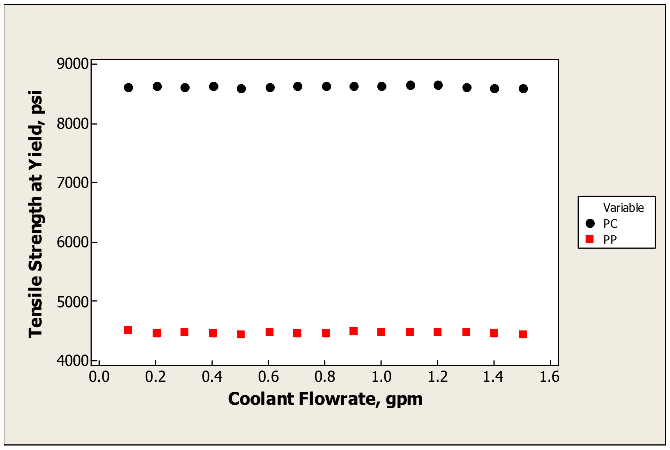

Figure 7. Tensile Strength at Yield of PC and PP

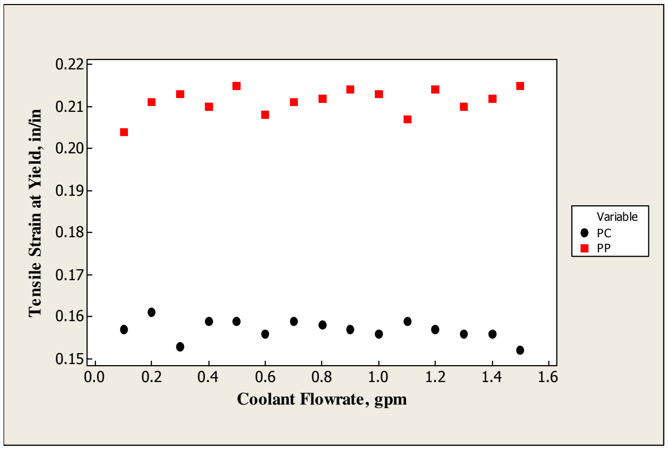

Figure 8. Tensile Strain at Yield of PC and PP

Rees [11] suggested that gloss of molded products could be a problem if the mold was cooled too fast. In this study, the authors did not observe any effect of the coolant flow regimes on the gloss of PC and PP, as Figure 9 shows. Perhaps the authors did not use very high coolant flow rates, hence the absence of any measureable effect of the coolant flow regimes on the gloss of PC and PP.

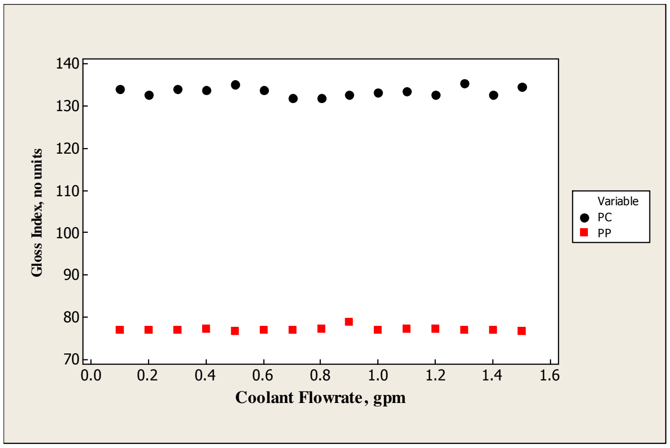

Figure 9. Gloss Index for PC and PP

Figure 10 shows that significant warpage was not found in PP parts when the coolant flow rate was greater than 0.8 gpm, while it was present in the PP parts for all coolant flow rates used in the study. Both plots of PP and PC showed negative slopes of -0.957 and -0.400, respectively. These results further suggest that coolant flow regimes and mold temperature can significantly affect part quality. Figure 11 (a) shows the ASTM test specimens (i.e., plastic parts) produced in this study. Figures 11(b) and 11(c) show how part warpage was estimated using the bench steel block from Smith Tool and Engineering Company.

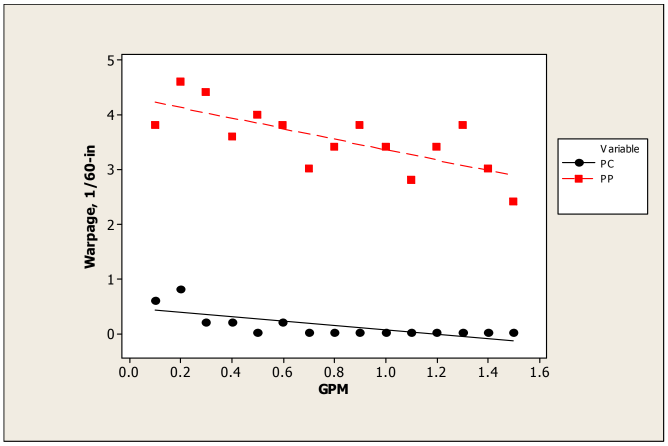

Figure 10. Warpage of PC and PP

Conclusion

This study has shown that coolant flow regimes do influence the cooling process of injection molding through the individual heat-transfer coefficient, h_i, of the cooling channels: a higher value of h_i results in a better cooling process. This was evidenced by the occurrence of warpage in PP plastic at coolant flow rates less than 1.4 gpm. Given the processing conditions used in this study, it is suggested that for the materials studied, for an efficient cooling process to take place, a minimum coolant flow rate of 1.4 gpm and 0.8 gpm has to be attained for PP and PC, respectively. Furthermore, this study revealed that each plastic material was unique and may require a minimum coolant flowrate for efficient mold cooling; in other words, one minimum coolant flow rate may not “fit” all plastic materials [12]. The authors did not find any effect of coolant flow regimes on the tensile strength at yield or the tensile strain at yield of PC and PP, suggesting that the parts did not become brittle because of inefficient cooling, particularly for the PP parts. Similarly, no effect of coolant flow regimes on gloss of PC and PP were found.

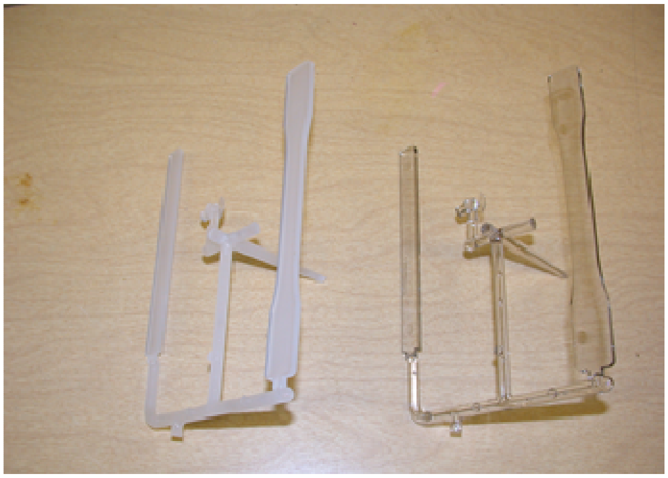

(a) Injection Molded PP and PC ASTM Test Specimens

(b) Warpage Absent in Sample

(c) Warpage Present in Sample

Figure 11. Test Specimens and Warpage

The authors would like state that the findings of this study are limited to the plastic materials, the coolant flow rate range of 0.1 gpm to 1.5 gpm, the coolant temperatures, and the coolant (water) used in this study.

References

[1] Kimerling, T. (2002). *Injection Molding Cooling Time Reduction and Thermal Stress Analysis*. Retrieved from http://www.ecs.umass.edu/mie/labs/mda/fea/fealib/Tom%20Kimerling/TKimerling_injection _modling_pdf.

[2] Rannar, I. E. (2008). *On Optimization of Injection Molding Cooling*. (p. 7). Norway: Department of Engineering Design and Materials, Norwegian University of Science and Technology.

[3] Rosato, D. V., Rosato, D. V., & Rosato, M. G. (2000). *Injection Molding Handbook*. The Netherlands: Kluwer Academic Publications.

[4] McCabe, W. I., Smith, J. C., & Harriott, P. (1993). *Unit Operations of Chemical Engineering*. New York, USA: McGraw-Hill, Inc.

[5] McCabe, W. I., Smith, J. C., & Harriott, P. (1993). *Unit Operations of Chemical Engineering*. New York, USA: McGraw-Hill, Inc.

[6] Rosato, D. V., Rosato, D. V., & Rosato, M. G. (2000). *Injection Molding Handbook*. The Netherlands: Kluwer Academic Publications.

[7] Meckley, J. (2007). A Study of the Thermal Characteristics of P20 Steel and S4 Rapid Tooling Material with Conventional and Conformal Cooling Channels. *The Technology Interface International Journal*, *8* (1).

[8] Rees, H. (1995). *Mold Engineering*. Cincinnati: Hanser-Gardner Publications.

[9] Dym, J. B. (1987). *Injection Molds and Molding*. London, Great Britain: Chapman and Hall.

[10] Zhu, J., Chen, J. C., & Kirby, E. D. (2004). Tensile Strength and Optimization of Injection Molding Processing Parameters Using the Taguchi Method. *International Journal of Modern Engineering*, *4*(2), 1-12.

[11] Rees, H. (1995). *Mold Engineering*. Cincinnati: Hanser-Gardner Publications.

[12] Technik, J. (2010). Injection Mold Cooling Configuration. Retrieved from http://acta.fihupt.ro/pdf/2010-1/ACTA-2010-1-12.pdf

Biographies

REX KANU is an Assistant Professor in the Department of Technology at Ball State University. He is currently the Coordinator of the Manufacturing Engineering Technology program. He has a B.S. and an M.S. in Chemical Engineering, an S.M. in Management Science, and a Ph.D. in Polymer Science.

NATHAN MARSH graduated from Ball State University in May 2009 and he is currently employed with the Chrysler Corporation.

EIGENVALUE-BASED DEFECT RECOGNITION METHOD FOR BRIDGE COATING ASSESSMENT

Sangwook Lee, Texas Tech University

Abstract

As existing infrastructure systems are aging and deteriorating rapidly, state agencies have started searching for more advanced ways to maintain their valuable assets at acceptable levels. One way is the application of digital image processing. Recently, in the civil engineering domain, digital image processing methods have been developed to assess pavement conditions, underground pipeline inspection, and steel bridge coatings. In this paper, the author deals with the application of a digital image processing method for the evaluation of steel bridge coating conditions. Most inspection work in the field is still performed visually by human eyes. With this conventional method, it is difficult to avoid limitations, such as widely varying inspection results between inspectors. Machine vision-dependent inspections could overcome the shortcomings of this conventional method and provide more consistent results. A novel approach to recognizing the existence of bridge coating rust defects and develops a decision-making tool to determine whether a given digitized image contains defects is also presented. The developed method was shown to be effective through the validation process.

Introduction

As existing infrastructure systems are aging and deteriorating rapidly, state agencies have started searching for more advanced ways to maintain their valuable assets at acceptable levels. One way is the application of digital image processing. This technology has been applied to various engineering/technology areas such as paper bag stacking and unstacking, automatic facial expression recognition, control of unmanned guided vehicles, replication of historical artifacts, fruit defect recognition, and identification of bone fragments [1-6]. Recently, in the civil engineering domain, digital image processing methods have been developed in the areas of pavement conditions, underground pipeline inspection, and steel bridge coating assessment [7-10]. The main reasons for choosing this advanced technology are its advantages in accuracy, objectivity, speed, and consistency. These distinct advantages have caught the attention of state agencies seeking to minimize the shortcomings of existing inspection practices.

The condition of painted steel bridge surfaces can be evaluated accurately and quickly by applying digital image processing. Machine vision-dependent inspections can also provide more consistent inspection results than human visual inspections. Because conventional inspections rely heavily on individual abilities, inspection results are error-prone and may vary widely between inspectors. The results can be different depending on personal preferences, work experiences, and the workload of the inspectors. It is important to develop reliable infrastructure condition assessment for better maintenance of public assets. In the case of bridge coating conditions, bridge managers can more realistically develop long-term, cost-effective maintenance programs if they have dependable coating condition data. This information can aid decisions as to whether a bridge shall be painted again immediately or later. Efficient coating condition assessment is also essential for the successful implementation of steel bridge coating warranty contracting. Under warranty contracting, an owner and a contractor inspect steel bridge coating conditions on a regular basis and decide whether additional maintenance actions are needed. However, it is extremely difficult to determine if a bridge contains more defects than an allowable level with the naked eye. For instance, the Indiana Department of Transportation (INDOT) has tentatively set up the maximum level of rust percentage at 0.3% within 5 years. However, it is quite challenging to determine if rust defects are over 0.3% [9]. If an owner and a contractor are in conflict, they may have to go through a lengthy process to reach an agreement.

This paper focuses on rust defects on highway steel bridges. Rust defects are one of the most commonly observed defects on coating surfaces and must be taken care of appropriately since they can severely affect the structural integrity of bridges and present an unpleasant appearance to passing drivers. A rust defect assessment method must be developed to maintain good quality steel bridge painting. For more objective rust defect recognition, digital image recognition methods have been developed in the past few years and are expected to replace or complement conventional painting inspection methods.

Described first is a digital image processing method for assessing steel bridge coating surfaces. The image processing method was developed based on eigenvalues and can be used to recognize the existence of bridge coating rust defects. An automated defect recognition method can make a decision whether a given digitized image contains defects. Later, the current conditions of infrastructure systems are presented while focusing on bridges and a step-by-step procedure for the development of an automated defect recognition method.

Deteriorated Bridge Infrastructure Conditions

The report cards published by the American Society of Civil Engineers (ASCE) are important indicators for understanding the current conditions of major civil infrastructure systems in the U.S. A wide range of civil facilities are included for evaluation such as bridges, roads, dams, schools, transit, energy, and so on, and graded on an A to F grading scale [11]. Many leading civil engineers are involved in preparing the report card and in the analyses of reports, studies, and other sources. Unfortunately, the overall American infrastructure has received a failing grade since the beginning of report card studies. The overall grades in 1998, 2001, 2005, and 2009 were D, D+, D, and D, respectively. Also, the report cards indicate the estimated investment needs for the next 5 years to recover infrastructure systems to the acceptable level. The dollar amount needed has been increasing. The 2001 ASCE study indicated that the estimated cost for infrastructure renewal was $1.3 trillion dollars or $260 billion annually. But, the 2005 study estimated that the cost of renewal would be $1.6 trillion, and the 2009 study reached an even higher point, $2.2 trillion dollars. As existing infrastructure systems are aging rapidly, more and more investment funding becomes necessary to eliminate deficiencies. However, the available funding amount is much less than required and is typically limited. Thus, it is very important to set up an efficient management plan on how to expend limited resources each year. In the case of bridges, the GPAs in 1998, 2001, 2005, and 2009 were C-, C, C, and C, respectively. The grades are a little bit higher than for other infrastructure facilities, but still are not satisfactory.

NACE International (2009) proved that the corrosion of metallic structures has had a significant impact on every industrial sector in this country [12]. A study to estimate the total economic impact of metallic corrosion in the United States was performed from 1999 to 2001 by CC Technologies Laboratories, Inc. with support from the Federal Highway Administration (FHWA) and National Association of Corrosion Engineers (NACE). The results of the study estimated the total annual direct cost of corrosion in this country to be $276 billion; that is equivalent to 3.1% of the nation's Gross Domestic Product (GDP). This number did not take into consideration indirect or user costs incurred by owners and operators of structures, manufacturers of products, and suppliers of services. Indirect costs include such factors as lost productivity due to outages, delays, failures, and litigation. The study roughly estimated the indirect cost to be equal to the direct cost. Then, the total costs due to corrosion become $552 billion, representing 6% of the GDP. The study divided the U.S. economy into five major sector categories to analyze the direct cost of corrosion: infrastructure, utilities, transportation, production and manufacturing, and government. The biggest portion came from utilities, which accounted for 34.7% of the total direct cost, with transportation as the second largest category, 21.5%. Infrastructure takes third place at 16.4%. Under the category of infrastructure, there are four subcategories: highway bridges, hazardous materials storage, gas and liquid transmission pipelines, and waterways and ports. Among these four, highway bridges takes first place and annual direct costs are estimated to be $8.3 billion to replace deficient bridges, repair concrete bridge decks and substructures, and maintain bridge paint. The study concluded that corrosion is a natural phenomenon commonly found in the metal-based structures and develops continuously through reaction with the environment. However, it is controllable and preventable by inventing corrosion-resistive materials and improving corrosion maintenance practices. The study suggested that the U.S. must find ways to implement better corrosion control and prevention practices and effectively manage existing corroded structures.

Automated Defect Recognition Method

The development of a defect recognition method can be divided into three stages: (I) image acquisition, (II) image processing, and (III) data analysis and results. Detailed descriptions of each stage are given as follows.

Image Acquisition

In the image acquisition stage, the first step is to take images of steel bridge coatings. All of the digital images for this study were acquired by visiting highway steel bridges on Interstate Highway 65 in Indiana. The color of the coating was blue, which is one of the most commonly used painting colors. During the data acquisition phase, bridge coating images were taken at a distance of around 3 feet (0.92 m) from the steel beam surfaces to acquire clear coating images with a digital camera. From the acquired digital images, image data sets were prepared for further analysis. Two kinds of testing sets were created: a group with defects and a group without defects. Digital images in the defect-free group contained no observable rust defects. And, imag-

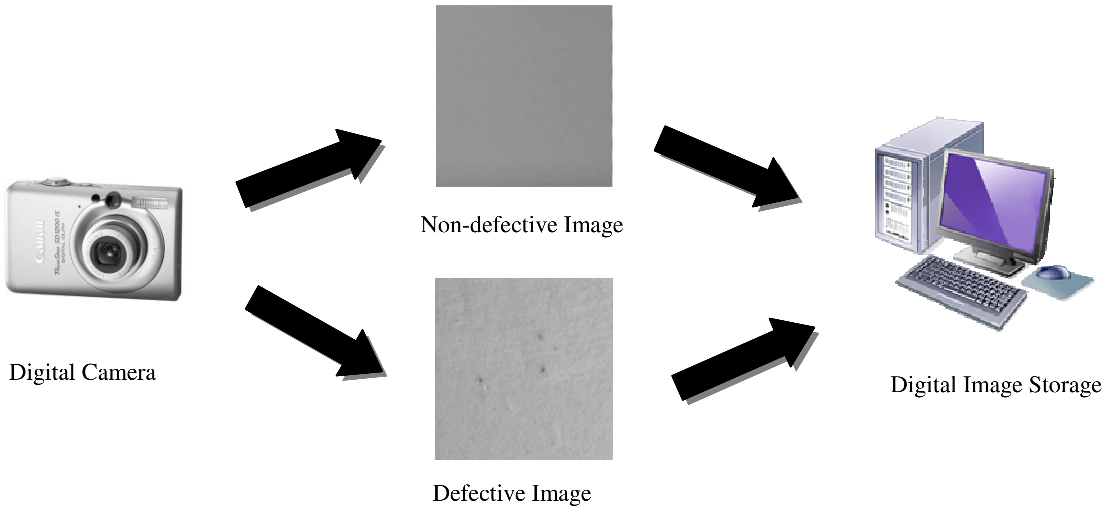

Figure 1. Bridge Coating Image Acquisition

es in the group containing defects enclosed small- to medium-level rust defects. Figure 1 illustrates the image acquisition process and sample testing images.

Image Processing

In the image processing stage, original color images were converted to gray-scale images. A color image is composed of three primary colors: red, green, and blue. A color can be generated by numerical proportion of the three components. Each primary color axis has 256 (2^8) levels of color shade, which means a total of 2^{24} colors can be generated technically from the color space. The origin of the cube corresponds to black and can be designated as (0, 0, 0). The point with (1, 1, 1) indicates white [13]. The three primary colors of red, green, and blue are located on each primary axis. If an image has a combination value of (255, 0, 0), it will be pure red.

Gray-level images are represented by only 8 bits. A value is assigned to each pixel according to light intensities ranging from 0 to 255. The value of 0 means black and the value of 1 means white. There are many of sophisticated gray levels between white and black. Therefore, image sizes can be significantly reduced by converting to grayscale images, while improving computing efficiency. Eigenvalues can be obtained by making a pair-wise comparison between digital images; for example, a defect image and another defect image or a defect image and a non-defect image. The similarity or dissimilarity of eigenvalues from two different group comparisons must be examined. A differentiating power will be increased as resulting values show a large difference in the pair-wise comparison. For this process, 15 bridge coating images were prepared for a defect group and the same number of images were prepared for a non-defective group. Thus, a total of 105 data points can be created from a pair-wise comparison between a non-defective image and another non-defective image. And, a total of 225 data points can be achieved from a pair-wise comparison between a defective image and a non-defective image.

The procedure to calculate eigenvalues is as follows. A digital image can be expressed in two-dimensional spatial coordinates, $f(x, y)$, with size $m{\times}n$. Then, the value of f at any point (x, y) is proportional to the brightness of the image at that point. Brighter pixels are assigned higher values and darker pixels are assigned lower values. By adding one more reference image, $w(x, y)$, with the same size of $f(x, y)$, the covariance matrix of C (2×2) can be calculated by Equation (1) [14].

$$C = \begin{bmatrix} c_{11} & c_{12} \\ c_{21} & c_{22} \end{bmatrix} \tag{1}$$

where,

$$c_{11} = \left[\frac{1}{m \times n} \sum_{x=0}^{m-1} \sum_{y=0}^{n-1} f^2(x, y) \right] - (\overline{f})^2$$

$$c_{22} = \left[\frac{1}{m \times n} \sum_{x=0}^{m-1} \sum_{y=0}^{n-1} w^2(x, y) \right] - (\overline{w})^2$$

$$c_{12} = c_{21} = \left[\frac{1}{m \times n} \sum_{x=0}^{m-1} \sum_{y=0}^{n-1} f(x, y) \bullet w(x, y) \right] - (\overline{f} \bullet \overline{w})$$

$\overline{f}$ and $\overline{w}$ are the mean gray values of $f(x,y)$ and $w(x,y)$, respectively.

The covariance matrix is symmetrical and square. In the matrix, diagonal components, c_{11} and c_{22} indicate the variance between one variable and itself. The other two components indicate the nature of the association between two random variables [15]. There are two eigenvalues obtained from the symmetrical matrix, C. A larger value is denoted as λ_L and a smaller one is denoted as λ_S. The equations to compute the values are as follows.

$$\lambda_L = \frac{1}{2}\left[c_{11} + c_{22} + \sqrt{(c_{11} - c_{22})^2 + 4c^2{}_{12}}\right] \quad (2)$$

$$\lambda_S = \frac{1}{2}\left[c_{11} + c_{22} - \sqrt{(c_{11} - c_{22})^2 + 4c^2{}_{12}}\right] \quad (3)$$

where, $\lambda_L \geq \lambda_S$.

The eigenvalues of matrix C can be used to extract shape information about the gray-level distribution in the pair-wise comparison. The larger eigenvalue, λ_L, represents the variance of data along the major axis of the distribution shape, and the smaller eigenvalue, λ_S, represents the variance of data along the minor axis of the shape in the two-dimensional distribution map. For example, Figure 2(a) shows the results of mapping a gray-level distribution of a coating image to the image itself. A 45° diagonal line was obtained in the resulting gray-level distribution map. Pixel values were placed along the positive diagonal direction. In this case, a larger eigenvalue shows the variance of the diagonal (or major) direction. But, this curve does not have a variance in the orthogonal direction, with a small eigenvalue of zero, since two identical images were compared. Figure 2 (b) is a typical gray-level distribution that can be observed in a pair-wise comparison.

Data Analysis and Results

In this stage, bridge coating images were processed to generate eigenvalues. Two kinds of pair-wise comparisons were performed: two defect-free images and a defect-free image and an image containing defects. From the comparison, 105 data points were obtained of two defect-free images (Group A). Also, 225 data points were achieved from the comparison of a defect-free image and an image containing defects (Group B). Figure 3 shows the gray-level distribution of Group A, and Table 1 presents descriptive statistics based on the figure. Five values (minimum, maximum, average, standard deviation, and variance) were calculated to a small eigenvalue and a large eigenvalue. Figure 4 shows the gray-level distribution of Group B, and Table 2 presents descriptive statistics of five values based on the figure.

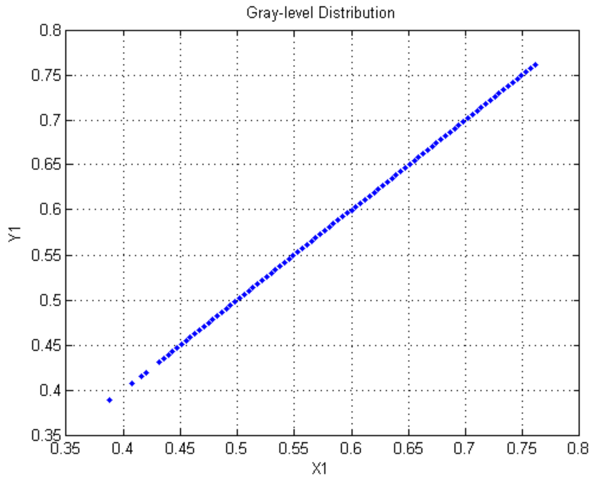

(a) Gray-Level Distribution with One Coating Image

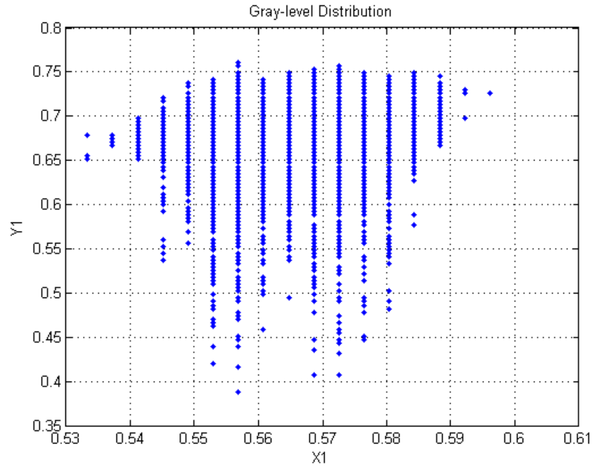

(b) Gray-Level Distribution with Two Coating Images

Figure 2. Gray-Level Distribution in the Pairwise Comparison

Table 1. Resulting Statistics of Eigenvalues in Group A

λ	Minimum	Maximum	Average	Stdev	Variance
λ_S	0.0121	0.1948	0.0686	0.0432	0.0019
λ_L	0.0546	0.5063	0.2395	0.0972	0.0094
Note: Stdev is a standard deviation.					

Table 2. Resulting Statistics of Eigenvalues in Group B

λ	Minimum	Maximum	Average	Stdev	Variance
λ_S	0.0322	0.3428	0.1308	0.0719	0.0052
λ_L	0.2667	3.7773	1.0005	0.8360	0.6989
Note: Stdev is a standard deviation.					

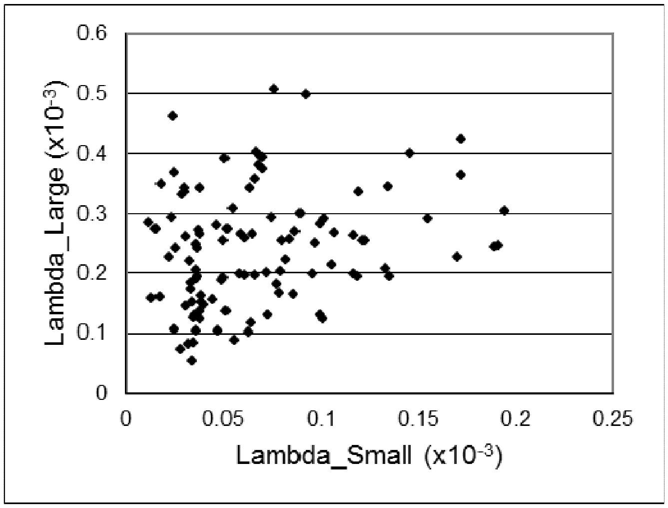

Figure 3. Eigenvalue Distribution of Group A

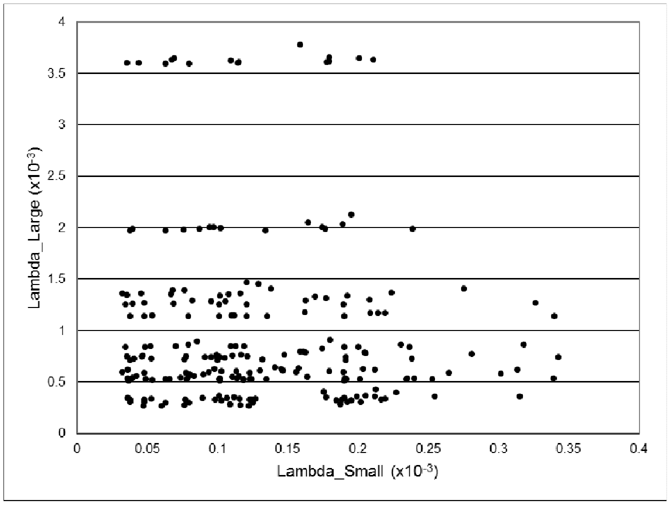

Figure 4. Eigenvalue Distribution of Group B

Discussion

Data results from image processing and resulting two-dimensional distribution maps yielded the following important findings.

- The distribution patterns from Figures 3 and 4 must be compared to each other. Figure 3 shows that most data points are close to each other and are strongly clustered together within a small region when processing two different non-defective images. However, data points become widely scattered in vertical and horizontal axes, and are dispersed over a large area when processing a defect-free image and an image containing defects at the same time. The degree of spread becomes greater when it comes to a large eigenvalue, rather than a smaller one.

- To identify the range of data points, minimum and maximum values were acquired from both groups. Small eigenvalues ranged from 0.0121 to 0.1948, and large eigenvalues ranged from 0.0546 to 0.5063 in Group A. In Group B, small eigenvalues ranged from 0.0322 to 0.3428, and large eigenvalues ranged from 0.2667 to 3.7773, while showing much wider distribution in both eigenvalues.

- Resulting statistics revealed that large eigenvalues are superior to small eigenvalues in detecting bridge coating defects using gray-scale image processing. This outcome can be explained by comparing data ranges of large and small eigenvalues. Also, it can be demonstrated by looking at average values in both groups. The average values of small eigenvalues were 0.0686 and 0.1308 in Group A and B, respectively. However, the average values of large eigenvalues were 0.2395 and 1.0005 in each group, while showing a wider difference between two groups.

- In summary, experimental results demonstrated that it seems effective to distinguish images showing defects from defect-free images by developing an eigenvalue-based defect recognition method. Two groups, A and B, showed different distribution patterns and dissimilar data ranges, while some data points overlapped between the two groups. Large eigenvalues have a greater differentiation capability than small eigenvalues, based on the experimental analysis. Most large eigenvalues were distributed below 0.4 in Group A. On the other hand, the eigenvalues were placed above 0.5 in Group B.

Testing and Validation

In this stage, the defect recognition method developed for the study was tested and validated by using other coating images to test the model efficiency. Ten coating images were used for this process among which five included defects and five were defect-free. Each testing image went through pair-wise comparisons with defect-free images used for a model development in order to generate eigenvalues. Then, average eigenvalues were compared with group average eigenvalues listed in Tables 1 and 2. Average eigenvalues for Group A were (λ_S, λ_L) = (0.0686, 0.2395). Average eigenvalues for Group B were (λ_S, λ_L) = (0.1308, 1.0005). A testing image was classified into the group with or without defects based on the Euclidean distance. The Euclidean distance between points ***p*** and ***q*** can be defined as follows.

$$D(p,q)=\sqrt{\sum_{i=1}^{n}(p_i-q_i)^2)} \qquad (4)$$

where, $\boldsymbol{p} = (p_1, p_2, \ldots, p_n)$ and $\boldsymbol{q} = (q_1, q_2, \ldots, q_n)$ in a n-dimensional space.

If the distance of a given image is closer to the average point of Group A than Group B, the image will be classified as defect-free. Otherwise, the image will be classified as defective. Table 3 presents the testing results. These testing results indicate that an eigenvalue-based defect recognition method is functional and effective. All defect-free images were categorized as defect-free correctly, and four of five images containing defects were correctly categorized as containing defects. Overall, the accuracy of image recognition was high (90%). This validation test was also performed using a large eigenvalue only, since the large value was found to have great differentiation capability during model development. It should be noted that nine out of ten test images were classified accurately, while showing the same performance in Table 3.

Table 3. Validation Results

Group		Predicted		Accuracy (%)
		Containing Defects	Defect-free	
Actual	Containing Defects	4	1	80
	Defect-free	0	5	100

Conclusion

This paper presented a novel approach for recognizing the existence of bridge coating rust defects by utilizing digital image processing to better assess bridge coating surfaces. The image defect recognition method was developed by making pair-wise comparisons and calculating eigenvalues which were chosen as a key feature for distinguishing images containing defects from defect-free images.

The rust defect recognition method was realized by taking the following three stages: image acquisition, image processing, and data analysis. In the image acquisition stage, bridge painting digital images were acquired and prepared in order to generate two types of data sets: a group with defects and a group without defects. In the image processing stage, a pair-wise comparison was performed to generate eigenvalues. The first comparison was performed between two different defect-free images, where a total of 105 data points were generated. The other comparison was carried out between a defect-free image and an image containing defects, where a total of 225 data points were generated. Large and small eigenvalues were generated and distributed on a two-dimensional distribution map. And, five statistical values were calculated and presented in tables.

The results from this experimental study were described in detail in the discussion section. Experimental results demonstrated that an eigenvalue-based defect recognition method is highly effective in distinguishing defective images from non-defective images. Some limitations of this study need to be addressed. Digital image processing is an effective tool for assessing external conditions of a facility. However, there is a limitation to examining internal conditions. When internal conditions of a structure are in question, additional methods such as infrared technology should be considered.

References

[1] Zhang, B., & Skaar, S. B. (2010). Laser-Assisted Uncalibrated Vision Guided Robotic De-palletizing. *International Journal of Engineering Research & Innovation*, *2*(2), 17-24.

[2] Li, C., & Soares, A. (2011). Automatic Facial Expression Recognition Using 3D Faces. *International Journal of Engineering Research & Innovation*, *3*(1), 30-34.

[3] Thamma, R., Kesireddy, L. M., & Wang, H. (2012). Centralized Vision-Based Controller for Unmanned Guided Vehicle Detection. *International Journal of Modern Engineering*, *12*(2), 58-65.

[4] Sirinterlikci, A., Uslu, O., Behanna, N., & Tiryakioglu, M. (2010). Preserving Historical Artifacts through Digitization and Indirect Rapid Tooling. *International Journal of Modern Engineering*, *10*(2), 42-48.

[5] Tao, Y., & Wen, Z. (1999). An Adaptive Spherical Image Transform for High-Speed Fruit Defect Detection. *Transactions of the ASAE*, *42*(1), 241-246.

[6] Tao, Y., & Ibarra, J. G. (2000). Thickness-Compensated X-ray Imaging Detection of Bone Fragments in Debonded Poultry-Model Analysis. *Transactions of the ASAE*, *43*(2), 453-459.

[7] Cheng, H. D., Chen, J., Glazier, C., & Hu, Y. G. (1999). Novel Approach to Pavement Cracking Detection based on Fuzzy Set Theory. *Journal of Computing in Civil Engineering*, *13*(4), 270-280.

[8] Sinha, S. K., Fieguth, P. W., & Polak, M. A. (2003). Computer Vision Techniques for Automatic Structural Assessment of Underground Pipes. *Computer-Aided Civil and Infrastructure Engineering*, *18*(2), 95 -112.

[9] Lee, S., Chang, L. M., & Chen, P. H. (2005). Performance Comparison of Bridge Coating Defect Recognition Methods. *Corrosion*, *61*(1), 12-20.

[10] Lee, S., Ghanta, S., & Karp, T. (2012). Comparative Study of Retrospective Methods to Reduce Non-uniform Illumination Effects to Bridge Coating. *Automation in Construction*, *22*, 537-544.

[11] ASCE Report Card. (n.d.). Retrieved September 14, 2009, from http://www.infrastructurereportcard.org.

[12] NACE International. (n.d.). Retrieved September 14, 2009, from http://events.nace.org/publicaffairs/images_cocorr/ccsupp.pdf.

[13] Plataniotis, K. N., & Venetsanopoulos, A. N. (2000). *Color Image Processing and Applications*. Springer-Verlag Berlin Heidelberg, Germany.

[14] Strang, G. (1988). *Linear Algebra and Its Applications*. Harcourt Brace Jovanovich, Orlando, Florida.

[15] Devore, J. (2011). *Probability and Statistics for Engineering and the Sciences*. Cengage Learning (8th Ed.).

Biographies

SANGWOOK LEE is an Assistant Professor of Construction Engineering and Engineering Technology at Texas Tech University. He earned his B.S. degree from Chung-Ang University, Seoul, South Korea, MS (Civil Engineering, 2000) from Purdue University, West Lafayette, Indiana, and Ph.D. (Civil Engineering, 2005) from Purdue University, West Lafayette, Indiana. Dr. Lee is currently working at Texas Tech University. His research interests are in infrastructure management and inspections and green construction. Dr. Lee may be reached at sang.lee@ttu.edu.

OPTIMAL TUNING OF PID CONTROLLERS SUBJECT TO PROCESS CONSTRAINTS

Constantine Tzouanas, Clear Lake High School; Vassilios Tzouanas, University of Houston–Downtown

Abstract

In this paper, the authors propose a method for tuning proportional-integral-derivative (PID) controllers by optimizing a performance criterion (integral square error or integral absolute error) that is subject to constraints such as controlled variables, manipulated variables, and rate-of-change constraints. The tuning method is applicable to open-loop-stable or unstable processes, is independent of the PID controller type, and can accommodate controllers with proportional and/or derivative action on the error or process variable. It further accounts for robustness in response to modeling errors by including constraints on the maximum sensitivity function. Implementation of the proposed method does not require elaborate optimization techniques and computing platforms. Microsoft Excel and its Solver function were used in this study. The performance of the proposed method was demonstrated using simulation examples and compared to that of classical tuning methods.

Introduction

In today's business environment, companies must achieve and sustain operational excellence in order to remain competitive. This implies that they must operate safely and in an environmentally friendly manner with improved equipment reliability and reduced maintenance costs, while simultaneously producing quality products, improving operational efficiency, and responding promptly to changing market conditions.

Process automation is of paramount importance for achieving operational excellence. A number of technologies can be combined together in a hierarchical manner (see Figure 1) to help achieve operational excellence (OE). If any of these automation layers does not function properly, then the entire pyramid will collapse. The lower automation levels are of paramount importance in achieving OE. In one of these layers, the Distributed Control Systems (DCS) layer, resides a number of regulatory and advanced regulatory control structures.

Indeed, at the DCS level, the predominantly used control algorithm is of the PID type [1]. Thus, it is of interest to develop efficient tuning methodologies for PID controllers.

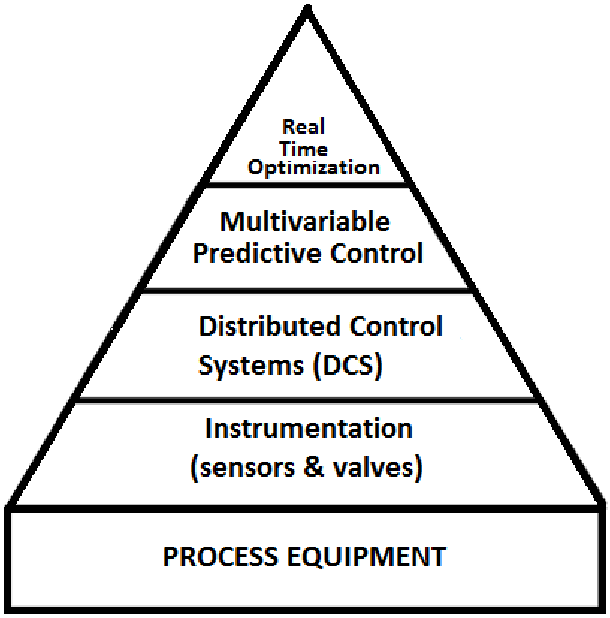

Figure 1. Process Automation Hierarchy

A great deal of research has been devoted to this subject [2]-[5]. An extensive list of PI and PID tuning methods can also be found [6]. The famous Ziegler-Nichols tuning method [2] was developed more than 70 years ago and is still widely used. However, over the years, new methods have been proposed which result in better control performance and improved robustness [7], [8]. Among others, techniques based on gain margin, phase margin, log modulus, and IMC tuning criteria have been proposed. Simple and easy-to-remember tuning rules have been proposed for a wide range of processes [7]. Most of these techniques are analytical in nature and, using a process model, they indeed provide an insight into the tuning issue [8].

In addition, a number of methods have been proposed on how to tune a PID controller such that a performance criterion is optimized [9]-[16]. Almost exclusively, such methods are concerned with optimizing a performance criterion and the efficiency of the optimization method. However, from a practical point of view, it is also desirable to optimize the tuning of PID controllers subject to operating constraints. Using constraints on both the manipulated and controlled variables and the rate of change for manipulated variables helps take into account process limitations and also brings a balance between speed of response and control performance. A number of multivariable controllers can easily account for this balance. Thus, it makes sense to tune PID controllers from this point of view. The search space for optimum tuning parameters could be defined using results obtained from analytical, model-based tuning methods. So, optimization could also include constraints for the range of the controller's tuning parameters.

Other important considerations in PID control include the type of the controller (e.g., ideal, cascade, parallel) and whether the proportional and derivative actions use the control error or the process variable. Typically, tuning rules refer to a particular type of controller. The user needs to be aware of it and convert the tuning parameters to the type of PID under consideration. With few exceptions, such a conversion is not a significant issue. However, it is of practical importance whether the proportional and/or derivative actions act on the control error or the process variable. Almost exclusively, suggested tuning guidelines assume that all modes of the controller act on the control error. In practice, most commercial PID algorithms allow the user to choose whether the P and/or D actions are based on the control error or the process variable. If the choice is made to use P and/or D actions on the process variable, then the controller must be retuned. In the absence of tuning guidelines, this is typically done by trial and error.

In this paper, the authors present a method for tuning PID controllers, while an optimization function is minimized subject to a number of constraints including, controlled variables, manipulated variables, rate-of-change and tuning parameters constraints. The method is applicable to different types of PID controllers and can handle P and/or D actions on the process variable or the control error. Furthermore, the method can be used to achieve a balance between setpoint response and disturbance rejection. To account for robustness, optimization is performed subject to a maximum sensitivity function constraint [9]. From an implementation viewpoint, the proposed method was programmed using Microsoft Excel and its Solver function, a widely used and inexpensive computing platform.

The Tuning Method

Block Diagram Representation

Consider a process under feedback control as shown in Figure 2.

where (in the Laplace domain),

$G_p(s)$	is the process model
$G_c(s)$	is the controller transfer function
$G_d(s)$	is the model of the disturbance
$m(s)$	is the manipulated variable
$y(s)$	is the controlled variable
$y_{sp}(s)$	is the controlled variable setpoint
$d(s)$	is the disturbance (or load)

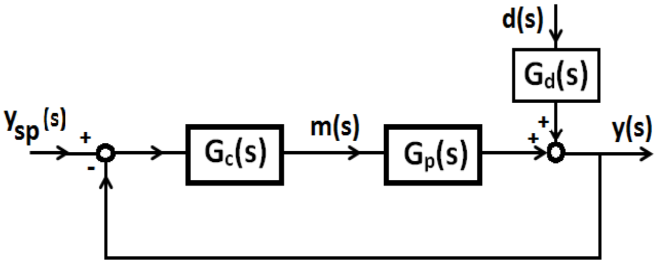

Figure 2. Schematic of a Feedback Control Loop

At the heart of the proposed method lies the process model. Most industrial processes, at least in the petrochemicals and refining sectors, can be described by a first- or second-order plus time delay model. On the other hand, a number of model reduction techniques, such as the "half rule", could be used to reduce the process model to a first-order plus dead time model (FOPDT) [7].So, without loss of generality, it can be assumed that the process is represented by a FOPDT model of the form given by Equation (1):

$$G_p(s) = \frac{K_p \cdot e^{-\theta \cdot s}}{\tau_p \cdot s + 1} \tag{1}$$

where,

K_p	is the process gain
τ_p	is the time constant
θ	is the dead time (or time delay)

Modeling

Different approaches could be taken to derive such a process model. For instance, detailed mathematical models based on first principles could be the starting point. Depending on the linear or non-linear nature of the equations, linearization and then Laplace transformations could yield the linear dynamic models. Again, if necessary, the "half rule" could be used to derive the FOPDT model. However, a more practical approach is based on step testing the process and fitting an empirical FOPDT model to the process response. Classical textbooks in process control describe this method [17], [18].

For our purposes, the different parameters of the FOPDT model are shown in Figure 3.

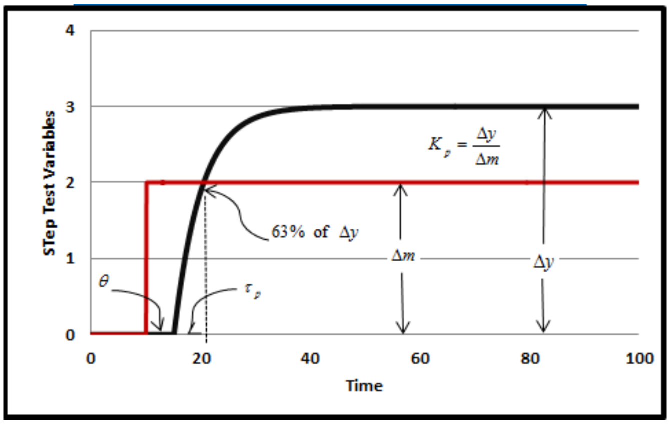

Figure 3. Generic Step Test with FOPDT Model Variables

PID Algorithms

There are different types of PID controllers. Some of the most common ones are: ideal, cascade, or parallel types. In the case of PI control, there is no difference between the ideal and cascade algorithms. The transfer functions of these types of PID controllers are as follows:

Ideal:

$$\frac{m(s)}{e(s)} = K_c \cdot \left[1 + \frac{1}{\tau_i \cdot s} + \tau_d \cdot s\right] \qquad (2)$$

Cascade (series, interacting):

$$\frac{m(s)}{e(s)} = K_c \cdot \left[1 + \frac{1}{\tau_i \cdot s}\right] \cdot (1 + \tau_d \cdot s) \qquad (3)$$

Parallel:

$$\frac{m(s)}{e(s)} = K_c + K_i \cdot \frac{1}{s} + K_d \cdot s \qquad (4)$$

where,

K_c is the proportional gain
τ_i is the integral time, time per repeat
τ_d is the derivative time
K_i is the integral gain
K_d is the derivative gain

For computer-based control, the controllers are discretized and programmed in the velocity form. For example, in the case of the ideal PID controller, when P and D act on the control error, Equation (5) is used.

$$\begin{aligned} m(k) = m(k-1) + K_c \cdot [(e(k) - e(k-1) + \frac{\tau_s}{\tau_i} \cdot e(k) + \\ + \frac{\tau_d}{\tau_s} \cdot (e(k) - 2e(k-1) + e(k-2))] \end{aligned} \qquad (5)$$

When P and D act on the process variable, Equation (6) is used.

$$\begin{aligned} m(k) = m(k-1) + K_c \cdot [(y(k-1) - y(k) + \frac{\tau_s}{\tau_i} \cdot e(k) + \\ + \frac{\tau_d}{\tau_s} \cdot (2y(k-1) - y(k) - y(k-2))] \end{aligned} \qquad (6)$$

In Equations (5) and (6), t_s is the controller's execution period. The method proposed in this study is independent of the controller form and, for the sake of brevity, will be demonstrated for the case of the ideal form.

PID Controller Tuning

In this section, the proposed tuning method is presented. The objective is not to replace but rather to complement previously proposed analytical tuning approaches by directly considering important process constraints such as manipulated variable size and rate-of-change constraints, as well as constraints on the controlled variables and the tuning parameters. Manipulated variable constraints are meant to reflect the inherent capacity of the process to cause and/or reject change in the case of setpoint response or load disturbances, respectively. Controlled variable constraints are meant to meet desired objectives such as product quality constraints. Constraints on the tuning parameters are meant to limit the search space by utilizing experiential knowledge or analytical knowledge.

Estimation of the tuning parameters is based on optimizing a performance criterion. In this study, and without loss of generality, the integral absolute error and integral square error criteria were considered. Specifically, the integral absolute error was:

$$IAE = \sum_{j=0}^{k} \left|e(j)\right| \qquad (7)$$

while the integral square error was:

$$ISE = \sum_{j=0}^{k} e(j)^{2} \qquad (8)$$

The objective was to minimize Equations (7) or (8), subject to the following constraints:

Manipulated Variable Constraints

$$m_{LL} \leq m(t) \leq m_{UL} \tag{9}$$

$$\Delta m_{LL} \leq \Delta m(t) \leq \Delta m_{UL} \tag{10}$$

Controlled Variable Constraints

$$y_{LL} \leq y(t) \leq y_{UL} \tag{11}$$

Tuning Parameter Constraints

$$K_{c,LL} \leq K_c \leq K_{c,UL} \tag{12}$$

$$\tau_{i,LL} \leq \tau_i \leq \tau_{i,UL} \tag{13}$$

$$\tau_{d,LL} \leq \tau_d \leq \tau_{d,UL} \tag{14}$$

where the subscripts $_{LL}$ and $_{UL}$ refer to the lower limit and upper limit of a variable.

Implementation of the PID Tuning Method

For the purposes of this study, optimization of the performance objectives in Equations (7) or (8), subject to Equations (9) through (11), was carried out in Microsoft Excel where the dynamic model is solved using the Euler method. While other computing platforms could have been chosen, Excel was chosen because of its widespread use in both academia and industry and its low cost.

A snapshot of the Excel implementation is shown in Figure 4. All cells with a green background are user-specified inputs (e.g., upper/lower limits for manipulated variables or tuning parameters, size of setpoint change, what modes of PID will be active, whether P and/or D act on error, or process variables). In this simplistic user interface, closed-loop system performance can be evaluated for setpoint and/or load changes. For comparison purposes, closed-loop performance using the AMIGO [8], classical IMC [5], and Simple IMC [7] tuning methods can also be calculated. The exact equations of these tuning methods are shown in Appendix 1.

The proposed method was programmed in Microsoft Excel using the Solver function, as shown in Figure 5. Here, the user specifies the cell location that holds the value of the variable to be optimized (i.e., set objective) and the cells' location, which will be changed (i.e., by changing variable cells) such that the objective is achieved. Optimization is done subject to a number of constraints, which are specified in the "Subject to the Constraints" section of Figure 5. Also, the user can specify the Solving method which, for this study, was the GRG nonlinear method.

Simulation Results

In this section, a number of simulation examples are used to illustrate the proposed method. Its performance is tested for setpoint changes and disturbance rejection. The effect of P and/or D acting on the control error or the process variable is demonstrated. Tuning parameters, subject to performance criteria, are estimated for PI and PID controllers. Control performance is compared to that obtained using different analytical methods [5], [7], [8]. Since relative time delay is an important parameter in the control of a process [8], simulation examples cover lag-dominant, delay-

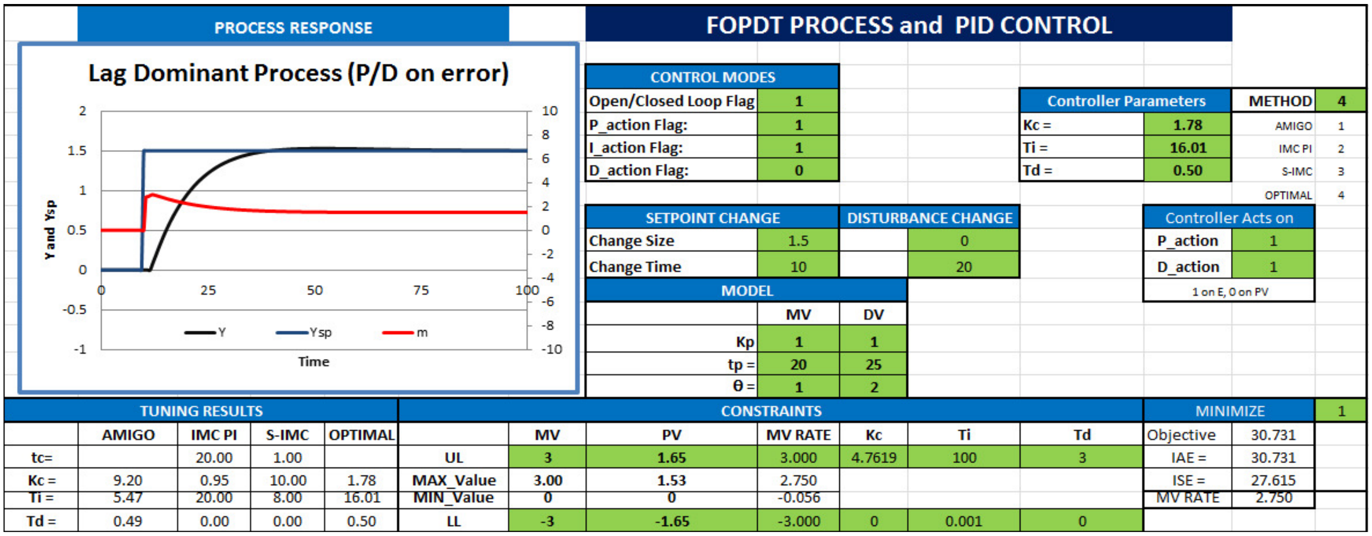

FOPDT PROCESS and PID CONTROL

CONTROL MODES	
Open/Closed Loop Flag	1
P_action Flag:	1
I_action Flag:	1
D_action Flag:	0

Controller Parameters	
Kc =	1.78
Ti =	16.01
Td =	0.50

METHOD	4
AMIGO	1
IMC PI	2
S-IMC	3
OPTIMAL	4

	SETPOINT CHANGE	DISTURBANCE CHANGE
Change Size	1.5	0
Change Time	10	20

Controller Acts on	
P_action	1
D_action	1
1 on E, 0 on PV	

MODEL	MV	DV
Kp	1	1
tp =	20	25
θ =	1	2

TUNING RESULTS	AMIGO	IMC PI	S-IMC	OPTIMAL
tc=		20.00	1.00	
Kc =	9.20	0.95	10.00	1.78
Ti =	5.47	20.00	8.00	16.01
Td =	0.49	0.00	0.00	0.50

CONSTRAINTS	MV	PV	MV RATE	Kc	Ti	Td
UL	3	1.65	3.000	4.7619	100	3
MAX_Value	3.00	1.53	2.750			
MIN_Value	0	0	-0.056			
LL	-3	-1.65	-3.000	0	0.001	0

MINIMIZE	1
Objective	30.731
IAE =	30.731
ISE =	27.615
MV RATE	2.750

Figure 4. Microsoft Excel User Interface

dominant, and lag/delay-balanced processes. In all cases, the controller execution period is set to 0.5 units of time and equals the integration step of the Euler method.

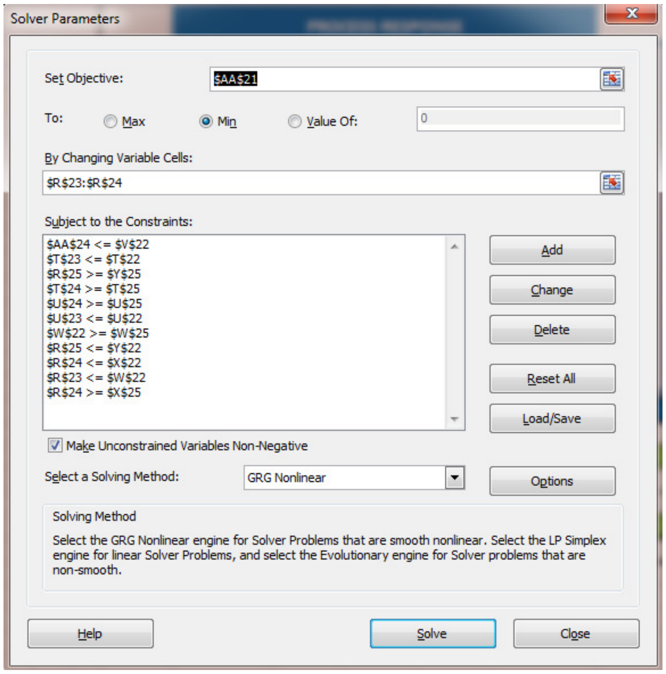

Set Objective: $AA$21

To: ○ Max ● Min ○ Value Of: 0

By Changing Variable Cells: $R$23:$R$24

Subject to the Constraints:

```
$AA$24 <= $V$22
$T$23 <= $T$22
$R$25 >= $Y$25
$T$24 >= $T$25
$U$24 >= $U$25
$U$23 <= $U$22
$W$22 >= $W$25
$R$25 <= $Y$22
$R$24 <= $X$22
$R$23 <= $W$22
$R$24 >= $X$25
```

☑ Make Unconstrained Variables Non-Negative

Select a Solving Method: GRG Nonlinear

Solving Method

Select the GRG Nonlinear engine for Solver Problems that are smooth nonlinear. Select the LP Simplex engine for linear Solver Problems, and select the Evolutionary engine for Solver problems that are non-smooth.

Figure 5. Microsoft Excel Solver Setup

Example 1 (Lag Dominant Process)

This process is lag dominant, the model for which is given by Equation (15):

$$G_{p2}(s) = \frac{1 \cdot e^{-1s}}{20s+1} \qquad (15)$$

The relative time delay, τ, is:

$$\tau = \frac{\theta}{\theta + \tau_p} = \frac{1}{1+20} = 0.0476 \qquad (16)$$

Controller tuning using the proposed optimization method was done subject to the constraints summarized in Table 1. The min/max limits are based on process limitations. The max limit for τ_i was set as a multiple of max(τ_p, 8 θ) in a way that mimics the τ_i= min(τ_p, 8 θ) [7]. The upper limit for the derivative time was set to 1/5 of τ_i.

Table 1. Tuning Constraints for Example 1

	min	max
Max/Min MV Change (%)	-3	3
Max/Min MV Rate of Change (%/min)	-3	3
CV Setpoint Change	1.5	1.5
Max/Min CV Change	10% under shoot	10% over shoot
Proportional Gain, K_C	0	$5K_{C\_IMC}$
Integral Time, t_i	0.001	2 max(t_p, 8 q)
Derivative Time, t_d	0	t_i /5

The tuning parameters and corresponding IAE values for the different methods are shown in Table 2. Two cases were considered: one when the P and/or D contributions were estimated using the control error and another when the process variable was used. For the IMC tuning method, the filter time constant was set equal to the process time constant. For the S-IMC method, the filter time constant was set equal to the process time delay.

Figure 6 shows the closed-loop performance of a PI controller when it is tuned using the different methods under consideration. In Figure 6, two sets of plots are considered: one for the case when the control error is used to calculate the P/D contribution and another when the process variable is used.

Table 2. Tuning Results for Example 1

	Controller acts on error				Controller acts on PV			
	AMIGO	IMC PI	S-IMC	OPTIMAL	AMIGO	IMC PI	S-IMC	OPTIMAL
t_c=		20	1			20.00	1.00	
K_c =	9.20	0.95	10.00	1.78	9.20	0.95	10.00	4.03
t_i =	5.47	20.00	8.00	15.86	5.47	20.00	8.00	8.34
IAE	18.75	63.00	16.85	30.73	18.20	122.99	26.40	31.47

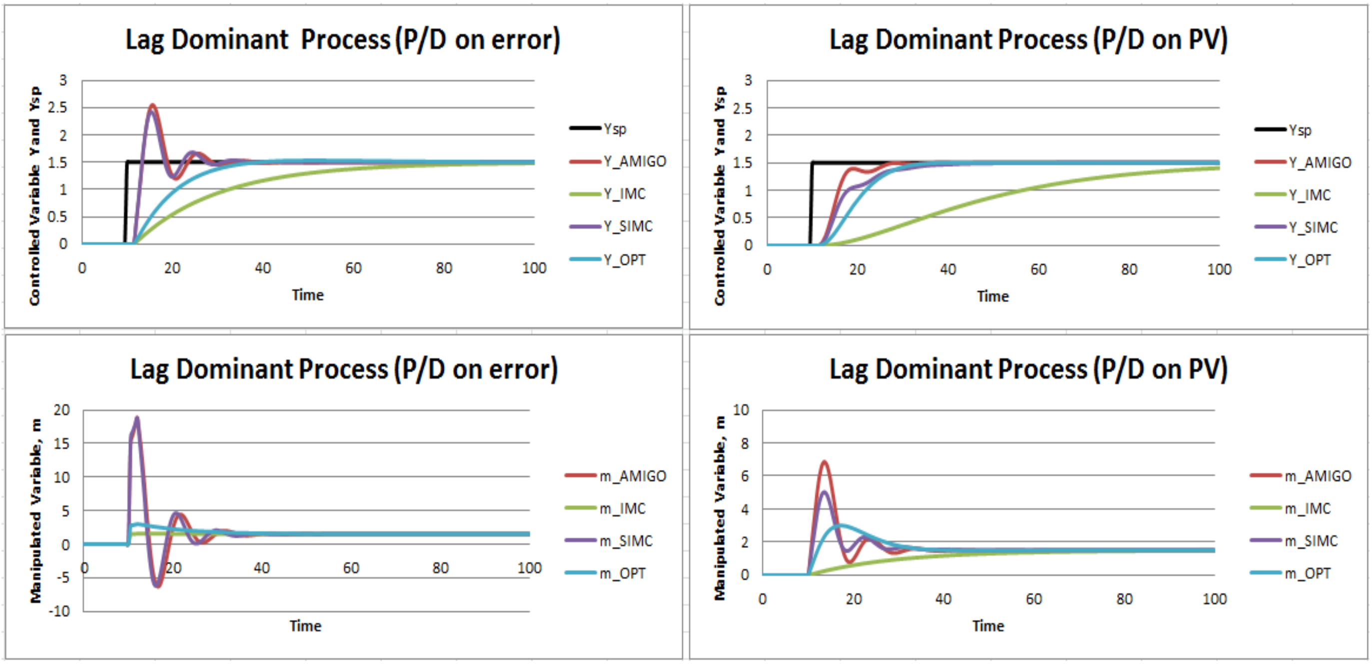
Lag Dominant Process (P/D on error)

Lag Dominant Process (P/D on PV)

Lag Dominant Process (P/D on error)

Lag Dominant Process (P/D on PV)

Figure 6. Setpoint Response for a Lag-Dominant Process

From a performance viewpoint, the AMIGO and S-IMC methods yield a more aggressive response than the other two methods (IMC and OPT). The classical IMC method yields the slowest response. The proposed method, OPTimal, brings a balance between speed of response and excessive manipulated variable movement. In the case of the Optimal method, more aggressive tuning was limited because the maximum manipulated variable constraint became active.

Considering the IAE, the AMIGO and S-IMC methods yield the least IAE but at the expense of excessive manipulated variable movement which, in many cases, may not be feasible or practical. In contrast, the proposed method observes manipulated variable movement constraints.

In many cases, in order to minimize sudden moves to the manipulated variable following a setpoint change, most practitioners apply the proportional and derivative actions of the controller on the controlled process variable (PV). Analytic tuning methods yield parameters which are not directly applicable to this scenario. So, manual retuning of the controller is required if the controller acts on the process variable. However, this is not an issue when the controller is tuned using the proposed method. Table 2 lists tuning results when the controller acts on the PV. Compared to the case when the controller acts on the error, the tuning using the proposed method is now more aggressive (higher proportional gain and smaller integral time).

Considering the performance of the PI controller using the AMIGO and S-IMC methods, when the controller acts on the process variable, it is more sluggish than when it acts on the control error. For the proposed method, because of the new tuning parameters, the control performance is almost unchanged (IAE is now 31.47 versus 30.73 in the previous case). Again, in this scenario, tuning was done subject to maximum manipulated variable value constraint.

Example 2 (Time-Constant / Delay-Balanced Process)

This is a balanced process from a lag- and time-delay viewpoint. The process transfer function model is given in Equation (17). Its relative time delay, τ, was 0.33.

$$G_{p2}(s)=\frac{1\cdot e^{-5s}}{10s+1} \qquad (17)$$

The tuning results for the cases when the controller's proportional action is based on the error or the process variable are given in Table 3. The closed-loop system performance for the different tuning methods is shown in Figure 7.

From an IAE error viewpoint, the proposed method yields the best performance. Compared to the process of Example 1, the AMIGO and S-IMC methods would require less aggressive movement in the manipulated variable.

Table 3. Tuning Results for Example 2 (Time-Constant / Delay-Balanced Process)

	Controller Acts on Error				**Controller Acts on PV**			
	AMIGO	IMC	S-IMC	OPTIMAL	AMIGO	IMC	S-IMC	OPTIMAL
t_c =		10	5			10.00	5.00	
K_c =	1.10	0.67	1.00	1.15	1.10	0.67	1.00	1.45
t_i =	8.33	10.00	10.00	11.56	8.33	10.00	10.00	8.81
IAE	39.98	45.00	35.52	34.60	49.58	75.00	60.00	47.39

Example 3 (Time-Delay-Dominant Process)

This is a time-delay-dominant process. The process transfer function model is given by Equation (18). Its relative time delay, τ, was 0.91. The tuning results for the cases when the controller acts on the error or the process variable are given in Table 4. The closed-loop system performance for the different tuning methods is shown in Figure 8.

$$G_{p3}(s) = \frac{1 \cdot e^{-10s}}{s+1} \tag{18}$$

In all cases, the setpoint response of the system using the tuning parameters obtained via the proposed method yielded the least IAE.

Balancing Setpoint Response and Disturbance Rejection

Using the proposed tuning method, controller parameters can easily be obtained in such a way that a balance between setpoint response and disturbance rejection is achieved. Considering the process of Example 1 and introducing a disturbance, the closed-loop system performance is shown in Figure 9. In this particular case, the disturbance was introduced at a time equal to 125 (units of time). The setpoint and disturbance rejection were considered to be of equal importance. While calculating the new tuning parameters, the maximum manipulated variable value and maximum process variable overshoot constraints were activated. The tuning parameters were then K_c = 1.67 and τ_i =10.22, compared with K_c = 1.78 and τ_i = 15.86 when only the setpoint response was considered.

Robustness Measures

Thus far, various types of constraints on controlled variables, manipulated variables, and tuning parameters have been considered. Also, it has been shown that the proposed method can help achieve a desired balance between setpoint response and disturbance rejection. In practice, robustness in response to modeling errors is of significant importance. The sensitivity function is a good measure for assessing closed-loop system robustness [9]. The sensitivity function, M_s, is given by:

$$M_s = \left| \frac{1}{1 + G_p(i\omega) \cdot G_c(i\omega)} \right| \tag{19}$$

Such a measure can easily be incorporated as part of the proposed method, as an additional constraint. Considering the process of Example 2 and tuning for a maximum M_s of 1.65, the new tuning parameters for a PI controller were K_c = 1.05 and τ_i = 10.89, as opposed to K_c = 1.15 and τ_i = 11.56 when the sensitivity function was not considered.

Table 4. Tuning Results for Example 3 (Time-Delay-Dominant Process)

	Controller acts on error				**Controller acts on PV**			
	AMIGO	IMC	S-IMC	OPTIMAL	AMIGO	IMC	S-IMC	OPTIMAL
t_c =		1	10			1.00	10.00	
K_c =	0.25	0.09	0.05	0.33	0.25	0.09	0.05	0.38
t_i =	4.75	1.00	1.00	5.00	4.75	1.00	1.00	5.00
IAE	58.19	82.21	66.07	46.794	72.45	84.52	69.01	56.92

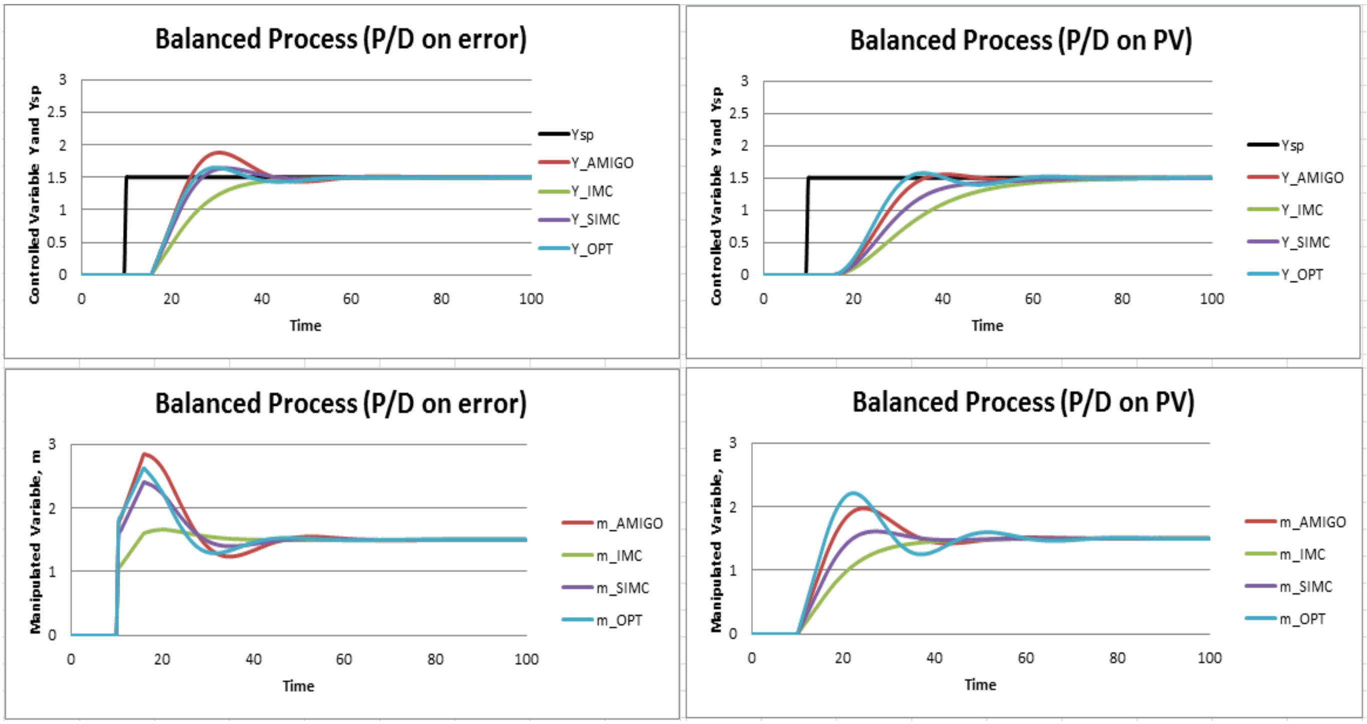

Figure 7. Setpoint Response for a Time-Constant / Delay-Balanced Process

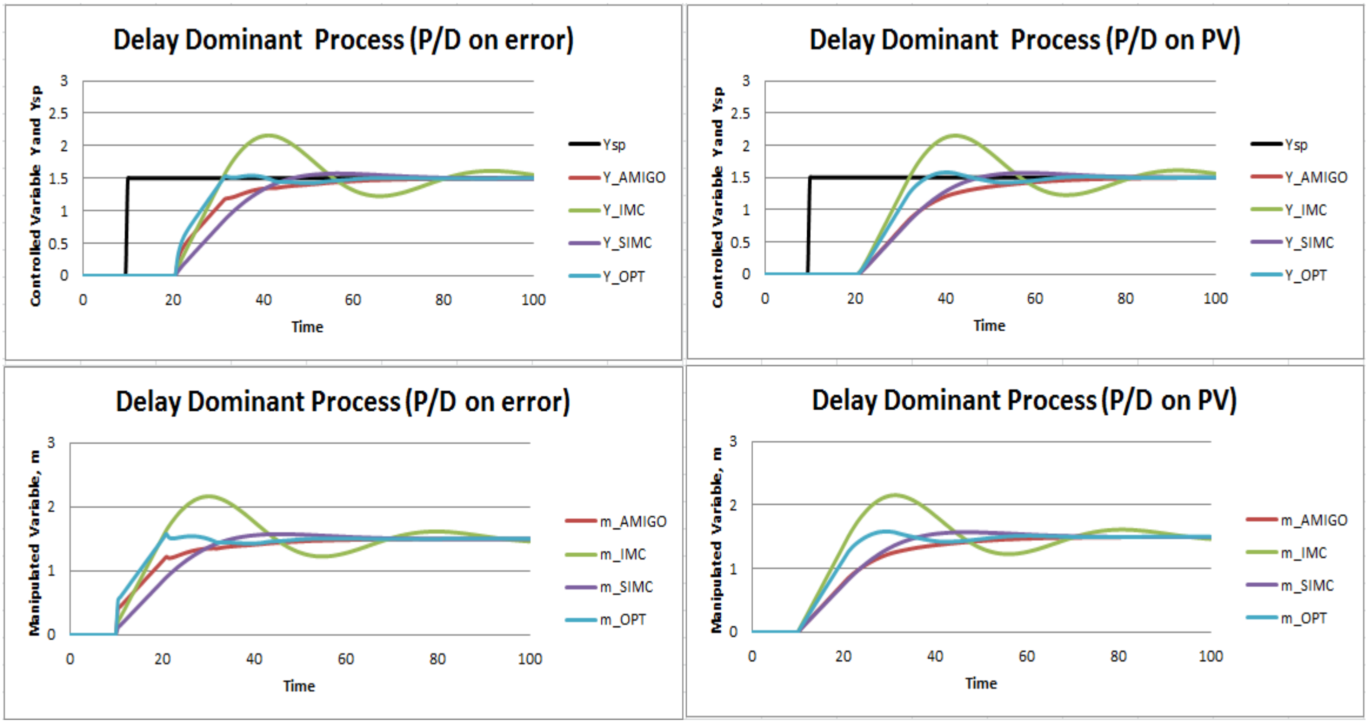

Figure 8. Setpoint Response for a Delay-Dominant Process

Example 4 (Open-Loop-Unstable Processes)

Thus far, all discussion has centered around open-loop-stable processes covering a wide range of relative time delays. The new tuning method was demonstrated using such processes to facilitate comparison with classical tuning methods for open-loop-stable processes. However, from an implementation point of view, the proposed method does not depend on whether the process is first order or second order or even if it is open-loop stable. The requirement is that a process model exists. That model could very well be non-linear.

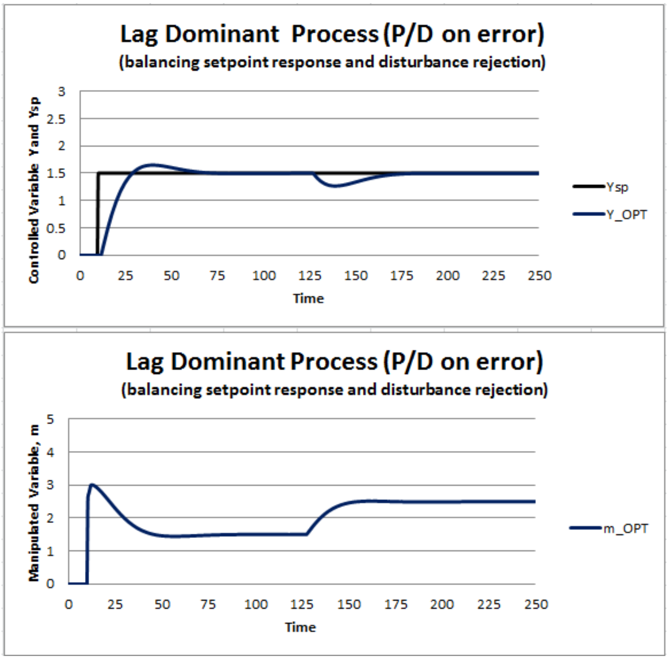

Figure 9. Balancing Setpoint Response and Disturbance Rejection

For demonstration purposes, the unstable processes considered are given by Equations (20) and (21):

$$G_{p4a}(s) = \frac{1 \cdot e^{-1s}}{20s - 1} \quad (20)$$

$$G_{p4b}(s) = \frac{1 \cdot e^{-5s}}{10s - 1} \quad (21)$$

To improve closed-loop system stability, a PID controller was used with its proportional and derivative modes acting on the process variable. The tuning parameters for the Gp4a process were $K_c = 6.77$, $\tau_i = 9.23$ and $\tau_d = 6.00$, while for the Gp4b process they were $K_c = 2.3$, $\tau_i = 24.59$ and $\tau_d = 11.53$. Figures 10 and 11 show the closed system performance for a setpoint change from 0 to 1.5 at time 10.

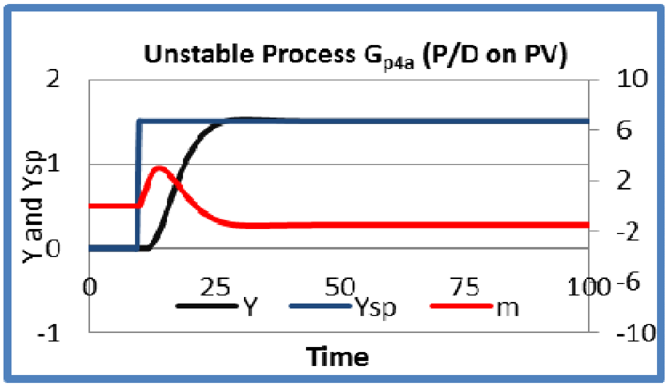

Figure 10. Setpoint Response Unstable Process G_{p4a}

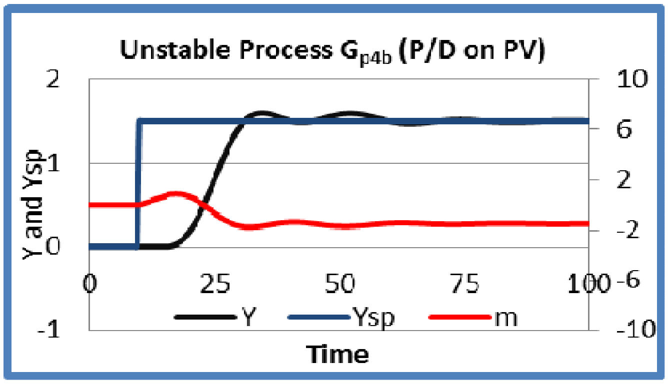

Figure 11. Setpoint Response Unstable Process G_{p4b}

Conclusions

In this paper, the authors proposed a method for the tuning of PID controllers subject to constraints. The optimization criteria were the integral square error or integral absolute error. The method is independent of the controller type and accommodates controllers with proportional and/or derivative action on the error or process variable. It was shown that the proposed method can be applied to open-loop-stable or unstable processes. Robustness in response to modeling errors was accounted for by implementing constraints on the maximum sensitivity function. The performance of the proposed method was demonstrated using simulation examples which covered a wide range of processes. Such performance was favorably compared to that of classical tuning methods. A widely used and inexpensive computer platform was used for programming purposes, thus making this method easily accessible for classroom teaching as well as for use in the field by the process control practitioner.

Appendix 1

This Appendix summarizes the equations for the different tuning methods as implemented in this study. It is assumed that the process model is of the form:

$$G_p(s) = \frac{K_p \cdot e^{-\theta \cdot s}}{\tau_p \cdot s + 1} \tag{A.1}$$

IMC Method [5]

$$K_c = \frac{1}{K_p} \cdot \frac{\tau_p}{\tau_c + \theta} \tag{A.2}$$

$$\tau_i = \tau_p \tag{A.3}$$

Simplified IMC Method [7]

$$K_c = \frac{0.5}{K_p} \cdot \frac{\tau_p}{\theta} \tag{A.4}$$

$$\tau_i = \min(\tau_p,\ 8\theta) \tag{A.5}$$

AMIGO Method [8]

$$K_c = \frac{1}{K_p} \cdot (0.2 + \frac{0.45\tau_p}{\theta}) \tag{A.6}$$

$$\tau_i = (\frac{0.4\theta + 0.8\tau_p}{\theta + 0.1\tau_p}) \cdot \theta \tag{A.7}$$

$$\tau_p = \frac{0.5 \cdot \tau_p \cdot \theta}{0.3\theta + \tau_p} \tag{A.8}$$

References

[1] Desbourough, L., & Miller, R. (2002). Increasing customer value of industrial control performance monitoring - Honeywell's experience. *Sixth International Conference on Chemical Process Control, AIChE Symposium Series*, *326*(98), 172-192.

[2] Ziegler, J. G., & Nichols, N. B. (1942). Optimum settings for automatic controllers. *Trans. ASME, 64*, 759–768.

[3] Cohen, G. H., & Coon, G. A. (1953). Theoretical consideration of retarded control. *Trans. ASME*, *75*, 827–834.

[4] Tyreus, B. D., & Luyben, W. L. (1992). Tuning PI controllers for integrator/dead time processes. *Industrial & Engineering Chemistry Research*, *31*, 2625-2628.

[5] Rivera, D. E., Morari, M., & Skogestad, S. (1986). Internal model control 4.PID controller design. *Industrial & Engineering Chemistry Process Design and Development, 25*, 252–265.

[6] O'Dwyer, A. (2003). *Handbook of Controller Tuning Rules*. Imperial College Press, London.

[7] Skogestad, S. (2003). Simple analytic rules for model reduction and PID controller tuning. *Journal of Process Control, 13*(4), 291–309.

[8] Astrom, K. J., & Hagglund, T. (2004). Revisiting the Ziegler–Nichols step response method for PID control. *Journal of Process Control, 14*(6), 635-650.

[9] Astrom, K. J., Panagopoulos, H., & Hagglund, T. (1998). Design of PI controllers based on non-convex optimization. *Automatica, 34*(5), 585–601.

[10] Panagopoulos, H., Astrom, K. J., & Hagglund, T. (2002). Design of PID controllers based on constrained optimization. *IEE Proceedings - Control Theory and Applications, 149*(1), 32–40.

[11] Tavakoli, S., & Tavakoli, M. (2003). Optimal Tuning of PID Controllers for First Order Plus Time Delay Models Using Dimensional Analysis. *The Fourth International Conference on Control and Automation (ICCA'03)*, Montreal, Canada.

[12] Madhuranthakam, C. R., Elkamel, A., & Budman, H. (2008). Optimal tuning of PID controllers for FOPTD, SOPTD and SOPTD with lead processes. *Chemical Engineering and Processing*, *47*, 251–264.

[13] Martins, F. (2005). Tuning PID Controllers Using the ITAE Criterion. *International Journal of Engineering Ed*ucation, *21*(5), 867-873.

[14] Kookos, I. K., Arvanitis, K. G., & Kalogeropoulos, G. (1999). PI Controller Tuning via Multiobjective Optimization. *Proceedings of the 7th Mediterranean Conference on Control and Automation (MED99),* Haifa, Israel.

[15] Romero, J. A., Sanchis, R., & Balaguer, P. (2011). PI and PID auto-tuning procedure based on simplified single parameter optimization. *Journal of Process Control, 21*, 840–851.

[16] Sanchis, R., Romero, J. R., & Balaguer, P. (2010). Tuning of PID Controllers based on simplified single parameter optimization. *Int. Journal of Control*, *83* (9), 1785-1798.

[17] Marlin, T. E. (2000*). Process Control.* (2nd ed.). McGraw-Hill.

[18] Seborg, D. E., Edgar, T. F., & Mellichamp, D.A. (2004). *Process Dynamics and Control.* (2nd ed.). Wiley.

Biographies

CONSTANTINE TZOUANAS is currently a Junior at Clear Lake High School, Houston, TX. His interests focus on economics and engineering.

VASSILIOS TZOUANAS is an Assistant Professor of Control and Instrumentation at the University of Houston – Downtown. Dr. Tzouanas earned a Diploma in Chemical Engineering from Aristotle University, the Master of Science degree in Chemical Engineering/Process Control from the University of Alberta, and the Doctor of Philosophy degree in Chemical Engineering/Process Control from Lehigh University. His professional experience includes technical and management positions with major operating companies. His research interests focus on process control systems, process modeling and simulation. He is a member of AIChE and ASEE. Dr. Tzouanas can be reached at tzouanasv@uhd.edu.

FIELD PROCEDURE FOR ESTIMATING THE MEASUREMENT AREA OF NON-CONTACT TEMPERATURE SENSORS

M. Khanal, Boise State University; R. Davidson, Ambient Sensors, LLC

Abstract

Transportation departments across the United States have installed sensors mounted on towers by the roadside to measure road surface temperatures. Since no guidelines exist for verifying the accuracy of such measurements, agencies are forced to accept claims made by vendors. To correct this situation, the Idaho Transportation Department (ITD) contracted with Boise State University (BSU) to test the accuracy of the non-contact, infrared temperature sensors installed throughout Idaho. Before collecting independent temperature data, BSU devised an easy-to-use procedure for determining the effective area viewed by the infrared sensors. According to ITD, the vendor claimed that at a distance of 10 m between the sensor and the road surface, the diameter of the effective area viewed by the sensor would be 80 cm. BSU's field experiment revealed that the sensor's viewing area was much larger than that claimed by the vendor. The discrepancy suggests that other claims made by the vendor regarding the accuracy and precision of their measurements cannot be relied upon and transportation departments will need to conduct independent tests to verify such claims.

Introduction

Background

Many state departments of transportation have installed non-contact temperature sensors as a part of their Road Weather Information Systems (RWIS). Many of these sensors are based on infrared technology and measure roadway temperatures by processing infrared signals emitted by the road surface. Vendor documents describe the accuracy and precision of these sensors, but there are no independent guidelines available to transportation departments to verify the claims made by vendors. Consequently, the Idaho Transportation Department (ITD) contracted with Boise State University (BSU) to verify the accuracy of the temperature sensors installed at RWIS stations in the state. A literature search revealed that there is very little documentation on field testing of non-contact pavement temperature sensors.

A National Cooperative Highway Research Program (NCHRP) report on test methods for evaluating field performance of RWIS sensors has a section on field testing procedures for pavement sensors. Five different field tests are listed for the "complete" testing of sensors for varying conditions, but the tests all pertain to sensors that are installed in the pavement, as opposed to those mounted on poles away from the carriage way [1]. Similarly, Rajabipour et al. [2] used a temperature sensor along with three electrical sensors to develop a material sensing and health monitoring system for concrete materials; the temperature sensor was embedded in the concrete. Other examples of sensors embedded in the pavement for measuring pavement temperatures or detecting ice formation on the road surface include Troiano et al. [3] and Sherif and Hassan [4].

The Battelle [5] corporation has evaluated ITD's RWIS, but their work was related to the integration of RWIS data with non-transportation weather data. The integration project was intended to solve various problems faced by ITD, but did not address potential inaccuracies in the data collected by the RWIS sensors.

Bogren et al. [6] quantified the effect of shading on pavement surface temperatures and present a formula to calculate the difference in pavement surface temperatures between areas exposed to and shaded from the sun as a function of solar elevation. They present the following formula to calculate the road surface temperature difference (RST_{diff}) as a function of solar elevation, β:

$$RST_{diff} = -2.7 + 0.46 \cdot \beta \quad in\ °C$$

This formula was used to compute the difference in temperatures due to shading at the Horseshoe Bend Hill RWIS site on State Highway 55 in Idaho. The solar elevation at this location (43° 54' 53" N – 116° 11' 52" W) on May 20, 2010, at 10:30am, was 43.81°. With β equal to 43.81, RST_{diff} was calculated to be 17.45° C. Based on this information, the authors of this study ensured that there was no shading of the pavement during data collection.

Bättig [7], in an article presented at the combined Fourth National Conference on Surface Transportation Weather and the Seventh International Symposium on Snow Removal and Ice Control Technology in June, 2008, reported on an expert system for winter maintenance that forecasts the road conditions for the next 24 hours. Temperatures used in Bättig's study were measured at a depth of 0.7 m under the road surface.

Need for Study

Since the literature does not describe how non-contact pavement temperature sensors can be tested, a new procedure had to be defined. But before collecting temperature data using alternative devices, the extent of the area viewed by the infrared sensor had to be determined. Literature describing such a procedure was also found to be lacking. For example, Jonsson and Riehm [8] reported results from their temperature measurement tests at an RWIS site in Sweden. They used temperature probes installed at depths of 2 mm and 0.3 mm as well as an IR camera and an IR thermometer mounted on a mast at different heights on the roadside. The diameter of the measurement spot side of the IR thermometer was given without any explanation. In contrast to the work presented by Jonsson and Riehm [8], this paper describes how the measurement area of remote, infrared temperature sensors can be estimated.

Infrared Signal Processing

An infrared sensor receives signals from a large area of the pavement around the point where the line of sight of the sensor lens hits the ground. Signals received from areas away from this center point will have a decreasing effect on the calculated value of the temperature. It was postulated that an area can be defined such that measurements from locations outside the area will have a minimal effect on the average temperature calculated from a particular set of measurements. Determination of the extent of such an area is useful to agencies that wish to verify the accuracy of their RWIS sensors: Any desired temperature measurement using an alternative device can be limited to this area. This note describes a process that transportation departments can use to rapidly determine the measurement footprint of infrared temperature sensors. The procedure involves estimation of the full width at half maximum of the Gaussian response function of the sensor.

Full Width at Half Maximum (FWHM)

It was assumed that an infrared sensor makes use of a Gaussian spatial response function in order to estimate the temperature of the measured area. Sensors that depend on infrared radiation, process signals received from an area defined by the full-width-at-half-maximum (FWHM) of a Gaussian function to estimate the average response. In signal processing, FWHM is defined as the frequency range where the power is half the maximum. For example, Keranen et al. [9] report that the field of view (FOV) of the sensor they used in their study was approximately 10° based on the FWHM of the sensor. The FWHM varies with distance from the sensor lens, as depicted in Figure 1.

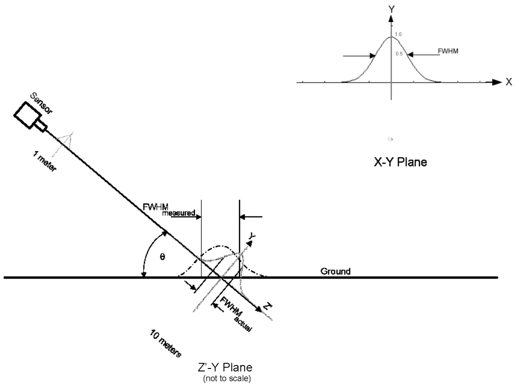

Figure 1. Measured Versus Actual FWHM

This function is symmetric with respect to the x and y axes and grows with the distance from the sensor as measured along the third axis, Z. The symmetry of the function results in $\sigma = \sigma_x = \sigma_y$. The standard deviation, σ, is dependent on z, the distance from the sensor. That is, $\sigma = \sigma(z)$.

Because the sensor is mounted on a pole on the side of road, the road surface is not perpendicular to its line of sight. Figure 1 shows the projection of the response function on the ground. The projection creates a situation where $\sigma_x \neq \sigma_y$; the projection of the Gaussian response function on the floor is elliptical. To measure the FWHM along the ground, a geometric correction must be applied. The correction depends on the angle between the camera's Z axis and the ground, according to the geometry shown in Figure 1.

Modeling Procedure

The response of the sensor was measured by sliding an object along the ground into the view of the sensor, as shown in Figure 2. The object shown in the figure is a polystyrene foam board but, in general, could be substituted by a variety of other materials. What is essential is the use of an object that will provide a thermal contrast between the road pavement and the surface of the object. Initially the sensor "sees" just the ground at ambient temperature. As the board is translated into view of the sensor, it measures the temperature of the combined view, the ambient ground temperature and the temperature of the board, which can be quite different in temperature. When the board is fully translated into the view of the sensor, the sensor will only detect the board at its temperature, T_{Board}.

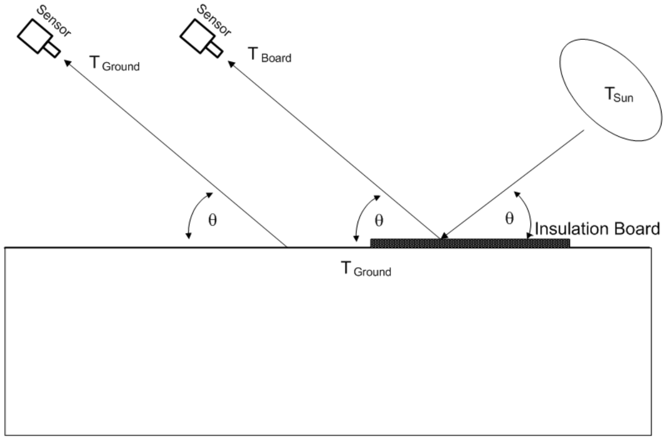

Figure 2. Temperature of the Board versus Temperature of the Ground

A key point is that the emissivity and reflectivity of the ground (asphalt pavement) and the sliding object (insulation board) will be different and as such, the temperatures of the two surfaces will be different. For example, the ground temperature, T_{Ground}, could be 10° C and T_{Board} could be 20° C. The emissivity of the asphalt road surface can be between 0.8 and 0.99 [8] and reflectivity around 0.08 [10]. The insulation board also has high emissivity and low reflectivity, but its values will be different from that of the road surface; hence, a thermal contrast between the two surfaces will be created. Additionally, the board with its top surface painted black will absorb more sunlight and will be at a higher temperature than the pavement surface. Further, as noted by Kranen et al. [9], the traditional optomechanical design of IR temperature measuring systems is optimized for situations in which the device is thermally stable and the measured targets are significantly warmer than the device. These conditions were ensured during the lab and field tests reported in this paper. Figure 3 depicts the field setup using a plywood sheet, one side of which was painted black. Plywood was later replaced by a 2.54 cm thick polystyrene foam board for the field test reported in this note.

Figure 4 depicts how the sensor measures different temperatures for the two surface types that appear in its field of view as the board is slid forward. Let *T*2*(z,x)* be the temperature of the surface of the insulation board and *T*1*(z,x)* be the temperature of the road surface.

Figure 3. Insulation Board for Temperature Measurement in the Field

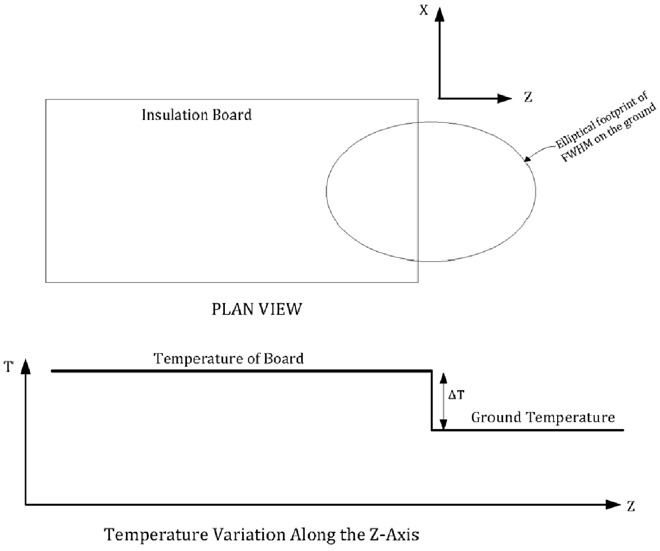

Figure 4. Sliding the Board into the Sensor's Field of View

The temperature, when the forward edge of the board is at location *z*, *T(z)*, is given by Equation (1). This location was measured with reference to a point in the ground immediately below the sensor. The temperature at each point *T(z,x)* was multiplied by a Gaussian weighting function to calculate *T*.

$$T(z)=\int_{-\infty}^{+\infty}\int_{-\infty}^{+\infty}T(\alpha,\beta)\cdot e^{-\left(\frac{\alpha^2}{2\sigma_\alpha^2}+\frac{\beta^2}{2\sigma_\beta^2}\right)}d\alpha d\beta=\int_{-\infty}^{z}\int_{-\infty}^{+\infty}T2(\alpha,\beta)\cdot e^{-\left(\frac{\alpha^2}{2\sigma_\alpha^2}+\frac{\beta^2}{2\sigma_\beta^2}\right)}d\alpha d\beta$$

$$+\int_{z}^{+\infty}\int_{-\infty}^{+\infty}T1(\alpha,\beta)\cdot e^{-\left(\frac{\alpha^2}{2\sigma_\alpha^2}+\frac{\beta^2}{2\sigma_\beta^2}\right)}d\alpha d\beta \qquad (1)$$

To simplify the model, it was assumed that $T2(\alpha,\beta)$ was constant on the top of the board and $T1(\alpha,\beta)$ was also constant on the road. Since the goal was to compute the difference in temperatures between the two surfaces, ΔT, it was further assumed that $T1(\alpha,\beta) = 0$. With these assumptions, Equation (2) was obtained to measure the difference in temperature.

$$\Delta T(z) = \int_{-\infty}^{z}\int_{-\infty}^{+\infty} A e^{-\left(\frac{\alpha^2}{2\sigma_\alpha^2}+\frac{\beta^2}{2\sigma_\beta^2}\right)} d\alpha d\beta = A\int_{-\infty}^{+\infty} e^{-\frac{\beta^2}{2\sigma_\beta^2}} d\beta \int_{-\infty}^{z} e^{-\frac{\alpha^2}{2\sigma_\alpha^2}} d\alpha$$

$$= B\int_{-\infty}^{z} e^{-\frac{\alpha^2}{2\sigma_\alpha^2}} d\alpha = \frac{\sqrt{\pi}}{2} B \cdot erf\left(\frac{z}{\sqrt{2}\sigma_x}\right) = K \cdot erf\left(\frac{z}{z_0}\right) \tag{2}$$

where,

DT is the difference in temperature between the two surfaces,

$$K = \frac{\sqrt{\pi}}{2} B$$

and A and B are constants.

$$z_0 = \sqrt{2}\sigma_z$$

The variable z_0 can be used to estimate the FWHM of the Gaussian function used by the sensor, but this FWHM will be with respect to the ground. Since this was what was actually measured in this experiment, it is denoted as $FWHM_{measured}$. The FWHM actually used by the sensor was along the longitudinal axis of the sensor, and is denoted by $FWHM_{actual}$. The measured FWHM value needed to be corrected to get the value corresponding to the longitudinal axis of the sensor lens. Equations used to compute these quantities are shown in Equation (3).

$$FWHM_{measured} = 2\times\sqrt{2\times\ln(2)}\sigma_z = 2.35\sigma_z = 2.35\frac{z_0}{\sqrt{2}}$$

$$FWHM_{actual} = \sin\theta \cdot FWHM_{measured} \tag{3}$$

where,

q is the angle between the line-of-sight of the lens and the ground.

In the above formulation, the constant temperature on the insulation board is denoted by A, and the temperature on the ground is also constant. The change in temperatures computed by Equation (2) is relative to the temperature on the ground. The goal of the modeling effort was to estimate z_o from Equation (2). But Equation (2) had to be modified before it could be fitted to the temperature data collected by sliding the board into the field of view.

The plot of the temperature data was expected to start from a low point corresponding to the bottom left leg of the Gaussian curve and increase to a maximum point corresponding to the top of the Gaussian curve. Midway between these low and high points, an inflection point was expected in the temperature plot. Equation (2) was modified to measure the temperature at fixed distances away from this midpoint. The modified formula is Equation (4). In the modified equation, the variable z is the distance between the subject location and the location of the mid-temperature value. Furthermore, since the actual location of the center point viewed by the sensor may be different from the one marked in the field, an offset correction needed to be introduced in the formulation. Equation (4) incorporates all of these changes.

$$T(z) = K \cdot erf\left(\frac{abs(z - offset)}{z_0}\right) + T_{midpt.} \tag{4}$$

There are four parameters in Equation (4): K, z_0, $offset$, and T_{midpt}. A least squares fitting of Equation (4) was performed in order to fit a Gaussian response model to the observed temperature data that were collected using a sensor in a lab and on the outside pavement. The square root of the sum of squared deviations between the estimated and observed values was minimized using the EXCEL Solver function. Values of the four unknown parameters were varied when computing the minimum.

Data Collection in a Lab

Before going out to the field, the suggested procedure was tested inside a lab in the Micron Engineering Center building at BSU. The distance between the sensor and the object was kept at 1 m. The sensor was set up on a table such that the z-axis was orthogonal to a room wall. A thin aluminum sheet was leaned against the wall. For purposes of this lab experiment, this sheet was considered to be the ground. A Masonite board was then slid over the aluminum sheet in 15 cm increments from right to left. A heater was also placed behind the aluminum sheet to create a temperature differential between the aluminum sheet and the Masonite board. The experimental setup is depicted in Figure 5.

Results from the Lab Experiment

Since there was no inclination between the sensor's z axis and the "ground", no correction for the angle of inclination was needed when using Equation (3) to calculate FWHM. That is, $FWHM_{ground} = FWHM_{longitudinal}$, in this case. The fitting of Equation (4) to the data collected in the lab is depicted in Figure 6. The optimized values of parameters, K, z_0, *offset,* and T_{midpt} were 12, 6.1, 3.3, and 36, respectively. The value of z_0 yielded 10.1 cm as the FWHM. The vendor-suggested value at a distance of 1 m between the sensor and the ground is 8 cm. The model estimated value of 10.1 cm was close to the suggested value.

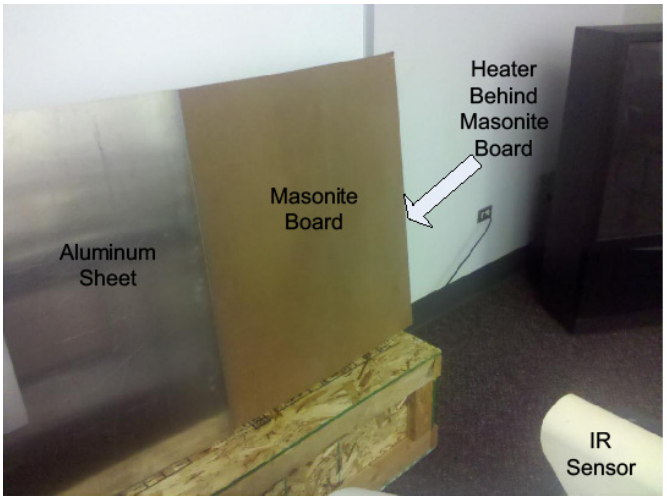

Figure 5. Laboratory Experimental Setup

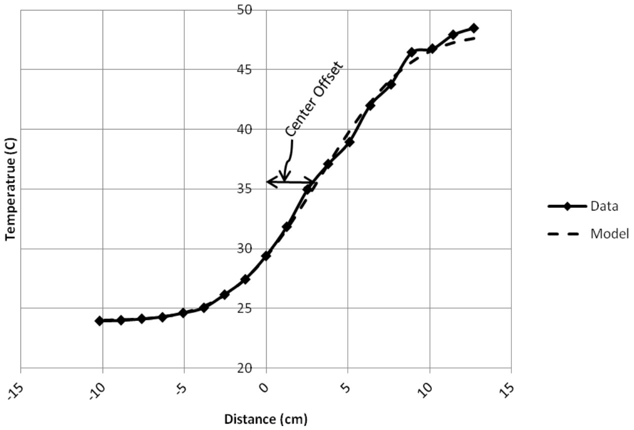

Figure 6. Modeling of the Lab Data

The "Center Offset" in Figure 6 is a measure of the inaccuracy in locating the center point of the field of view of the infrared sensor using the laser pointing device. As the figure shows, T_{midpt} was not observed at a distance of 0 cm but rather at an offset of 3.3 cm to the right of the presumed center point. The center offset is a measure of the error in using the laser pointing device to find the center point of the field of view; it does not, however, affect the estimation of the FWHM.

Data Collection in the Field

The observed data for the modeling exercise was obtained from the experiment performed on April 1, 2011. During the experiment, the center point of the area viewed by the sensor was located first. A laser pointing device mounted on the sensor lens was used to locate the center point. The insulation board was approximately 122 cm wide, 244 cm long, and 2.5 cm thick. One side of the board was painted black and the experiment was conducted on a clear, sunny day to ensure no confounding effects due to cloud cover. First, a straight line was drawn by joining the center point with another point directly below the sensor. This line was extended beyond the center point and marked at 30.5 cm intervals between -183 cm and +183 cm relative to the center point. The top edge of the board was then placed at the -183 cm mark, and temperature measured by the sensor was recorded. The procedure was repeated by moving the top edge of the board to other marks until the +183 cm mark on the line. The temperature data were then plotted and a model fitted. The results are shown in Figure 7.

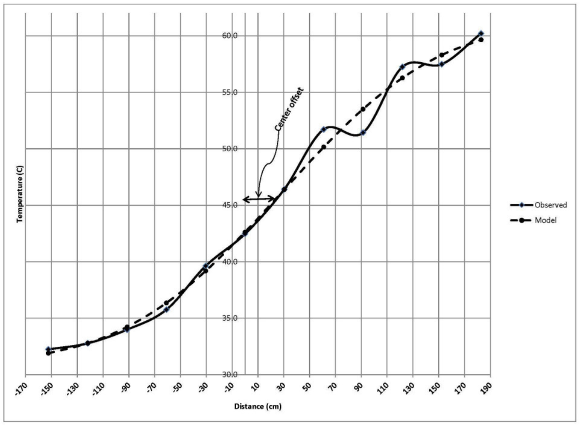

Figure 7. Modeling of the Field Data

Field Data Results

The figure only shows the data between -152 cm and -183 cm since the lowest and highest temperatures were recorded at these points. It can be seen from Figure 7 that the observed data in the lower half of the curve exhibit the expected trend and fit the model well. Data on the upper half are not as well behaved as in the lower half. The center offset of 28.5 cm indicates that the actual center point of the field of view was 28.5 cm away from the sensor relative to the presumed center point of the sensor's field of view, as estimated by the laser pointing device.

The values for K, z_0, *offset,* and T_{midpt} that resulted in the best fit were 27.3, 136.5, 28.5, and 46.1, respectively. This value of z_0 gives 226.8 cm as the FWHM on the ground. With 35.51° as the angle q in this experiment, the resulting $\text{FWHM}_{\text{transverse}}$ was 131.7 cm. The distance between the ground and the sensor was 7.22 m. According to the vendor's rule of a diameter of 80 cm at a distance of 10 m, the expected measurement area diameter should have been close to 58 cm. The model estimated value is, thus, more than double the suggested value.

Conclusions and Recommendations

Currently, state transportation departments have no guidelines to verify the accuracy of infrared temperature measuring devices that are part of road weather information systems (RWIS) installed in many states in the U.S. If a transportation department wants to use an alternative device to record temperatures, it will be difficult to make such measurements such that the two sets of measurements are comparable. As a result, transportation departments have to fully rely on statements made by their vendors.

The Idaho Transportation Department has many RWIS stations across the state. According to the vendor of the infrared temperature sensors installed at these stations, the measurement area of the sensor has an approximate diameter of 80 cm at a distance of 10 m and the diameter changes proportionately by distance. The experiment reported in this paper was designed to test that assertion. Based on the results reported here, the vendor's suggestion of an 80 cm diameter for a distance 10 m was somewhat accurate in a lab setting but grossly inaccurate in the field. The size of the area that the sensor detects in the field was found to be more than double that suggested by the vendor. Therefore, it is recommended that independent verifications of such vendor statements be made.

As noted during a Transportation Research Board conference [11], there is a need to think strategically about the development of remote sensing in transportation. The recommendations made at the conference with respect to wide-area remote sensing regarding the adoption of a model similar to the Intelligent Transportation Systems model of national protocols, architecture, and standards, are also applicable to RWIS systems. Therefore, it is recommended that departments of transportation at the state and federal levels should take steps towards standardizing field and test procedures for RWIS sensors.

Before such standardized procedures are developed, it is recommended that state departments of transportation follow the field procedure described in this paper to estimate the footprint of road temperature sensors prior to using alternative means of temperature measurements to verify the accuracy of their sensors.

Acknowledgement

This work was funded by the Idaho Transportation Department.

References

[1] Fleege, E. J., Scott, B., Minge, E., Gallagher, M., Sabie, J., Petersen, S., et al. (2006). *Test Methods for Evaluating Field Performance of RWIS Sensors.* Transportation Research Board, NCHRP Web-Only Document 87 (Project 6-15): Contractor's Final Report and Field Manual, Washington, D.C.

[2] Rajabipour, F., Sant, G., & Weiss, J. (2007). Development of Electrical Conductivity-Based Sensors for Health Monitoring of Concrete Material. *Annual Meeting CD-ROM*, Transportation Research Board, Washington, D.C.

[3] Troiano, A., Pasero, E., & Mesin, L. (2011). New System for Detecting Road Ice Formation. *IEEE Transaction on Instrumentation and Measurement, 60*(3), 1091–1101. Doi: 10.1109/TIM.2010.2064910.

[4] Sherif, A., & Hassan, Y. (2004). Modelling pavement temperature for winter maintenance operations. *Canadian Journal of Civil Engineering*, *31*, 367–378.

[5] Battelle. (2006). *Evaluation of the Idaho Transportation Department Integrated Road-Weather Information System.* U.S. Department of Transportation, ITS Joint Program Office: Final Evaluation Report, Contract Number: DTFH61-96-C-00077, Task Number: BA7730, Washington, D.C.

[6] Bogren, J., Gustavsson, T., Karlsson, M., & Postgard, U. (2000). The impact of screening on road surface temperature. *Meteorological Applications*, *7*, 1–8.

[7] Bättig, D. (2008). *The Road Temperature Forecast Tool.* Transportation Research Board, Transportation Research Circular E-C 126, Modeling and Forecasting Temperatures in Surface Transportation, Washington, D.C., (pp. 49–56).

[8] Jonsson, P. and Riehm, M. (2012). Infrared Thermometry in Winter Road Maintenance. *Journal of Atmospheric and Oceanic Technology, 29*, 846–856. Doi: 10.1175/JTECH-D-11-00071.1.

[9] Keranen, K., Makinen, J.-T., Korhonen, P., Juntunen, E., Heikkinen, V., & Makely, J. (2010). Infrared temperature sensor system for mobile devices. *Sensors and Actuator A: Physical, 158*, 161–167. Doi:10.1016/j.sna.2009.12.023.

[10] Li, H., Harvey, J., & Kendall, A. (2013). Field Measurement of Albedo for Different Land Cover Materials and Effects on Thermal Performance. *Building and Environment, 59*, 536-546.
[11] Transportation Research Board. (2003). *Remote Sensing for Transportation Products and Results: Foundations for the Future*. Conference Proceedings 29, The Transportation Research Board of the National Academies, Washington, D.C.

Biographies

MANDAR KHANAL is an Associate Professor of Civil Engineering at Boise State University in Boise, Idaho. Dr. Khanal received a Master of Science degree in Transportation Engineering from Northwestern University, Evanston, Illinois, and a Doctor of Philosophy degree in Civil Engineering from the University of California at Irvine, California, USA. At Boise State University, Dr. Khanal teaches various courses and conducts research related to transportation engineering and planning. Dr. Khanal also serves on the Editorial Board of the Journal of Civil and Environmental Engineering and has reviewed papers for various journals in his field. Dr. Khanal may be reached at mkhanal@boisestate.edu

ROBERT DAVIDSON is the President of Ambient Sensors LLC, located in Boise, Idaho; an Adjunct Professor in Mathematics; and a Research Professor in Electrical and Computer Engineering at Boise State University. Dr. Davidson received his BS from Washington State, an MS from Johns Hopkins, and a PhD from Carnegie Mellon University. Dr. Davidson may be reached at Robert.davidson@ambientsensors.com.

THE DEPENDENCE OF NON-LINEAR COUPLING ON LOADING FORCE ON ULTRASOUND TRANSDUCERS IN SONIC INFRARED IMAGING

Yuyang Song, Toyota Research Institute of North America; Xiaoyan Han, Wayne State University

Abstract

The Sonic Infrared (IR) imaging technique is a promising, nondestructive evaluation (NDE) technology for finding cracks through thermal imaging of vibration-induced crack heating. In Sonic IR, coupling materials are usually engaged between the ultrasound transducer and the sample so that it can play an important role in crack detection. In this study, the effect of loading force between the transducer and the coupling material on the nonlinear coupling effect was studied. A correlation analysis between the "acoustic energy" and the "thermal energy" in the crack will be discussed in this paper as well.

Introduction

Sonic Infrared (IR) Imaging, also referred as vibrothermography, is a novel NDE technology for finding cracks through thermal imaging of vibration-induced crack heating [1-5]. Over the past several years, the technique has proven to be a powerful tool for detecting surface and subsurface cracks, delaminations, and disbonds in metallic and composite materials [6-8]. The basic principle is to use ultrasonic excitation to induce frictional heating in the defects within an object. The frictional heating is then detected by an infrared camera via mapping surface temperature, which is the result of heat diffusion from the defects [9-11]. Coupling materials, usually a thin layer materials, which were originally used to prevent marking samples in experiments by the ultrasound transducer, were found important in the course of the development of Sonic IR technology [12], [13]. In addition, due to the nonlinear material properties of the coupling media, the loading force between transducer tip and coupling material become another important role for the input of the ultrasound excitation. In the community of NDE, however, there are no other research activities or related projects focused on this nonlinear coupling effect. Han et al. [14], [15] presented some preliminary results using only two loading forces to show this effect. Aside from that, there are no systematic and quantitative data and analyses showing the nonlinear effect [16], [17]. In this study, quantitative relationships between the vibrational "acoustic energy" and "thermal energy" in the crack for different loading forces on the ultrasound transducer were tested with one coupling material.

Experimental Setup

The experimental setup is shown in Figure 1.

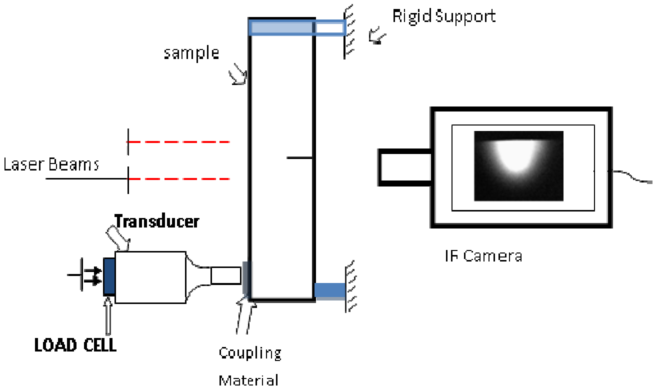

Figure 1. Schematic Drawing of Experimental Settings

The sample used to conduct all of the experiments was an aluminum (Al) bar with an edge-through crack. The dimension of the sample was 230 mm * 40 mm * 2.4 mm, with a crack length of 10 mm, which was created by an MTS machine. In order to effectively measure the heat generated from the crack through the IR camera and the vibration on both sides of the crack without worrying about the signal-to-noise ratio being too low, the size of the crack was intentionally made large. The infrared camera had a focal plane with a 640 x 512 pixel array. One end of the Al bar was clamped tightly to a rigid back in the post, while the other end was pushed by the transducer, also which had a rigid backing post. A Branson 900MA 20 kHz ultrasound system was used as an excitation source to inject ultrasound pulses into the sample. The power supply had a maximum power of 1000 watts, and the transducer tip had a diameter of 19.05 mm. Two laser Doppler vibrometers (OFV 511) were pointed and focused at two points across the crack to measure the relative vibration of the crack, as shown in Figure 1, and a close-up drawing, as shown in Figure 2. The data acquisition sampling rate was set as 512 kHz for the laser vibrometers. A coupling material was always placed between the ultrasound transducer tip and the sample. Typically, the coupling material used in a Sonic IR experiment is 25 mm * 25 * mm * 0.60 mm. The brand of coupling material was Nashua 357 premium grade duct tape, which has a high tensile strength (800Kg/m) and is very durable. Two layers of the tape was folded to make such a coupling material (2LayerDT). A photo of the materials is shown in Figure 3.

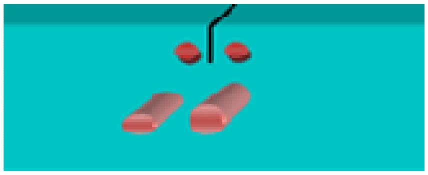

Figure 2. Close-up View of the Laser Beam locations

Figure 3. Coupling Material (2LayerDT) Used in the Experiment

The thickness of the coupling material was measured using Mitutoyo calipers on the effective contact area pushed by the transducer. The initial velocity input from the ultrasound transducer tip is shown in Figure 4.

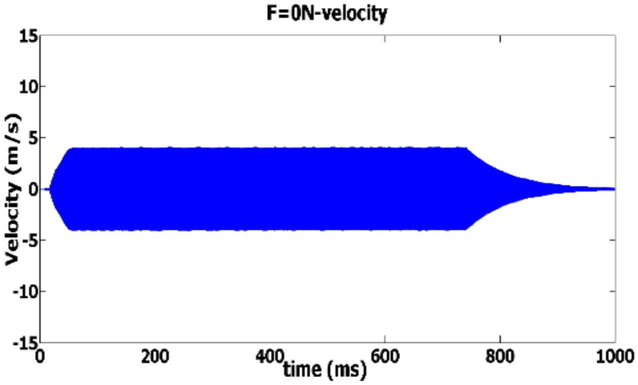

Figure 4. Velocity of the Ultrasound Transducer Tip When Free in the Air

The loading force was measured with a load cell, as shown in Figure 1, and the range for this study was from 48 Newtons to 216 Newtons, or up to the load when the ultrasound welder system automatically stops. The same experiments were repeated for each loading force used in this study. Between each individual experiment, there was at least a ten-minute cool-down time for the crack so that the test sample could reach the same equilibrium temperature. The duration of the input ultrasound pulse was also set to 800 ms, and the ultrasound transducer was placed at the same spot on the sample with a coupling material in between; the camera position was kept the same.

Experimental Results and Discussion

Quantitative Characterization of the Coupling Material

In order to quantitatively characterize the experimental results, some energy calculation algorithms were developed from the crack [18], [19], such as "thermal energy" and "acoustic energy". These numerical quantities do not have any inherent physical meaning. Neither "energy" is strictly energy; they are just a quantitative index. The "thermal energy" was calculated by

$$\sum_i \sum_j P(i,j,t) - \sum_i \sum_j B(i,j,t_{0^-}) \qquad (1)$$

Here, (i, j) was the pixel at the i^{th} row and j^{th} column; the variable t was time; P(i,j,t) was the pixel value at time t; B (i, j, t_0^-) was the pixel value before the ultrasound excitation pulse was turned on the background thermal radiation from the scene. The total thermal energy with the background subtracted can be obtained by summing the above quantity in Equation (1) over the time during which the IR image sequence was acquired. Details about the algorithm can be found in previous studies [18].

The "acoustic energy" of the crack at one spot was calculated according to the following Equation [2]:

$$E = \int |S(t)|^2 \, dt \qquad (2)$$

where S(t) was the relative velocity of two points across the crack with respect to time. The square of the relative velocity was used as a reference to the acoustic power. The result of integration over the excitation period was used as a measure of the "acoustic energy" at the particular spot where the vibrations were measured.

Preliminary results on the relationship between "thermal energy" and "acoustic energy" was studied and presented previously [12]. The efficiency of a coupling material is defined as the ratio of "thermal energy" to "acoustic energy", in order to express how efficiently the vibration converts into crack heating, which is represented by Equation (3).

$$TA = \left[\frac{ThermalEnergy}{AcousticEnergy} \right] \quad (3)$$

Using the same camera at the same room temperature, the camera was calibrated with the same parameter settings used in all of the experiments. By using a black body, the correlation between pixel values and temperature change can be provided. Under the corresponding camera settings in these experiments, the relationship between the pixel value and the temperature change was:

$$T = pixelvalue \times 4.19 \times 10^{-3}(1 \pm 1.35\%) \quad (4)$$

After each experiment, the thermal image of the crack area was saved and, by using in-house imaging processing software, the pixel value was automatically acquired at the point of interest. In each case, the temperature increase at the crack tip was converted using this formula.

Acoustic Energy on Loading Force Dependence

Figure 5 shows the result of “acoustic energy” calculated using Equation (2) at one spot on the crack with 2LayerDT as the coupling material at loading forces of 48N, 72N, 96N, 120N, 144N, 168N, 192N, 198N, 204N, and 216N. From this figure, the “acoustic energy” from the crack shows the trend as increasing when the loading force increases, except when an overload occurred at 198N.

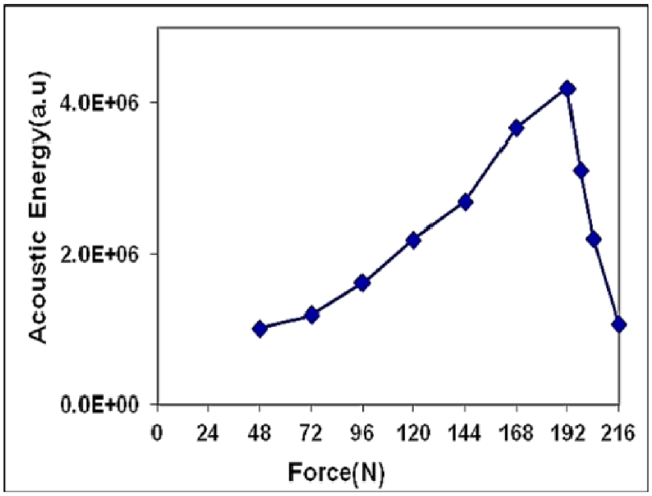

Figure 5. “Acoustic Energy” Calculated at One Spot on the Crack at Different Loading Forces

From Figures 6 (following page) and 7, the amplitude of the vibration waveform had the same trend as the “acoustic energy” from the lowest to the highest, except the overloading when pushing the transducer harder onto the coupling material. From the data, one can see that, when the loading force increases, the relative motion between the cracks’ faces increases before overloading occurs. In these situations, the ultrasound pulse length was not full length of 800ms. Therefore, with the much-shortened ultrasound pulse, the “acoustic energy” calculated at the crack spot, plotted in Figure 5, had a sharp drop from 192N to 198N.

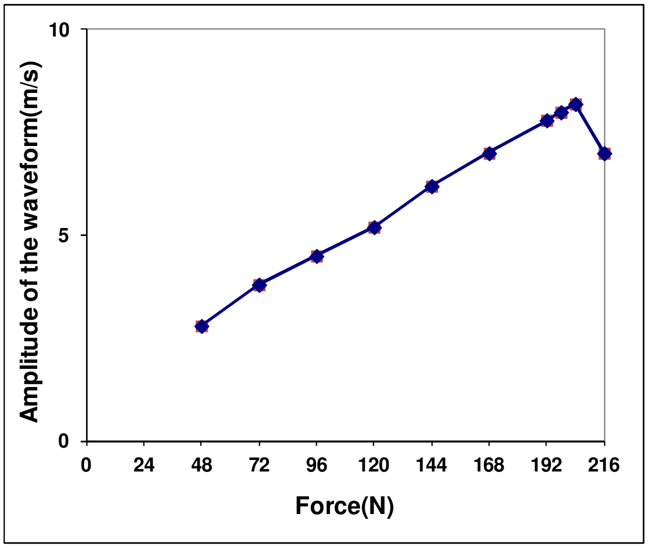

Figure 7. Relationship Between the Amplitude of the Waveforms and the Loading Forces

Thermal Energy on Loading Force Dependence

Figure 8 shows the calculated “thermal energy” based on Equation (1) using the pixel values of IR images at different loading forces at the same point of interest over the size of 150 * 150 pixels. It is clear that this curve has the same trend as the “acoustic energy” curve in Figure 5. The “thermal energy” increases when the loading force increases, until overloading happens at 198N. Figure 9 shows the corresponding IR images taken at times when the temperature of the crack reaches its highest point for each of these loading forces. All of these images were applied with the same contrast for display and visual comparison. When the loading force was 198N, overloading occurred in the system, where the pulse input to the sample was not the full length of the pulse setting as is shown in the vibration in Figure 6(g). Correspondingly, this short period of vibration only generates a small amount of the heat on the crack area, compared with the full length of the vibration process. Therefore, its IR signal level was lower when compared with the other situations.

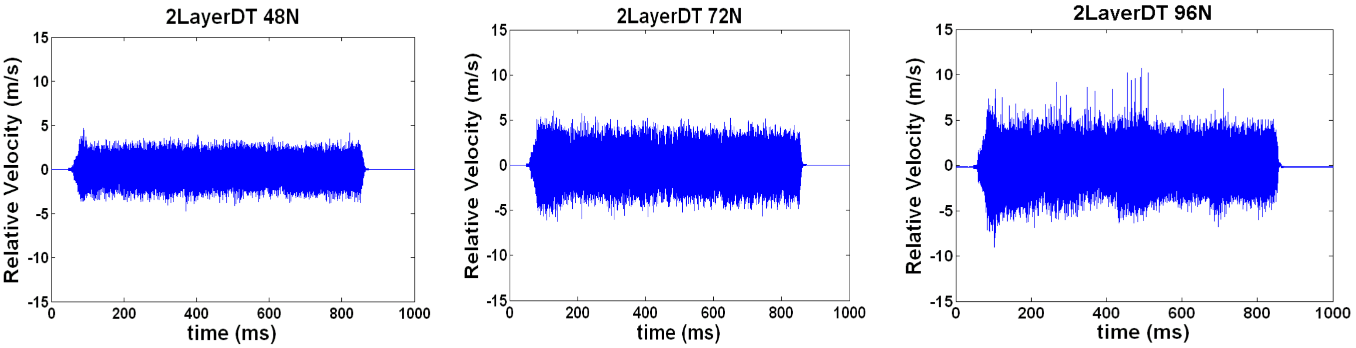

(a) Loading Force of 48N

(b) Loading Force of 72N

(c) Loading Force of 96N

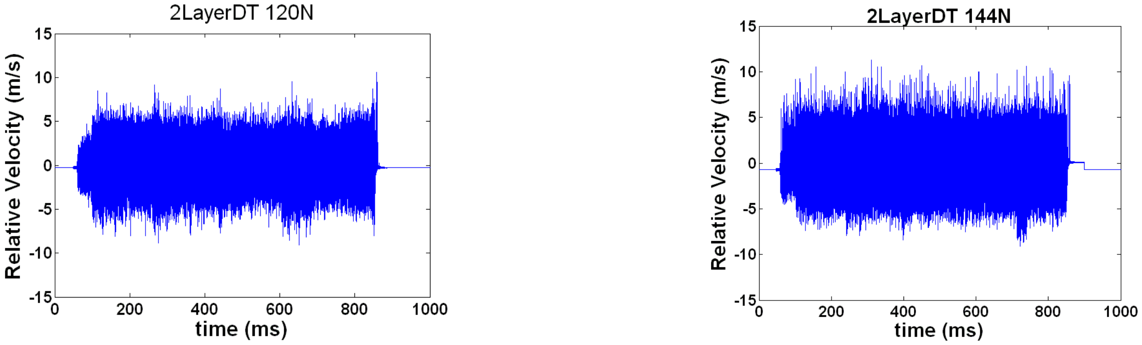

(d) Loading Force of 120N

(e) Loading Force of 144N

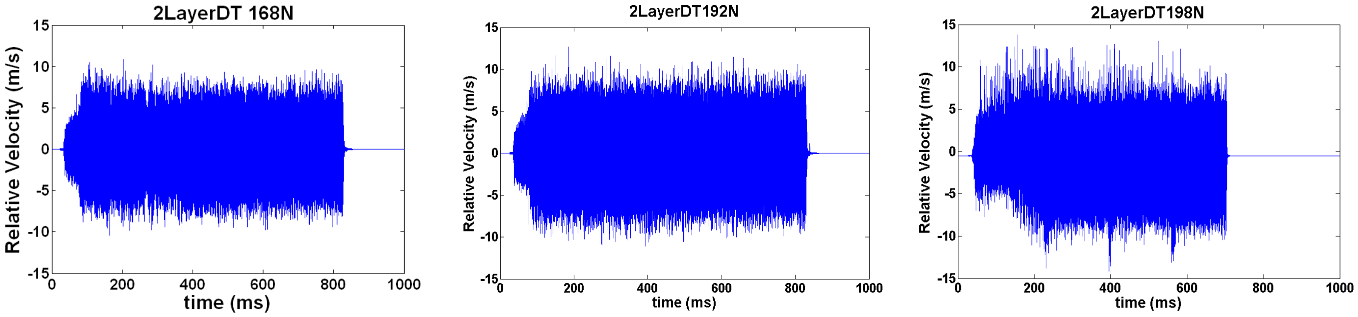

(f) Loading Force of 168N

(g) Loading Force of 192N

(h) Loading Force 198N

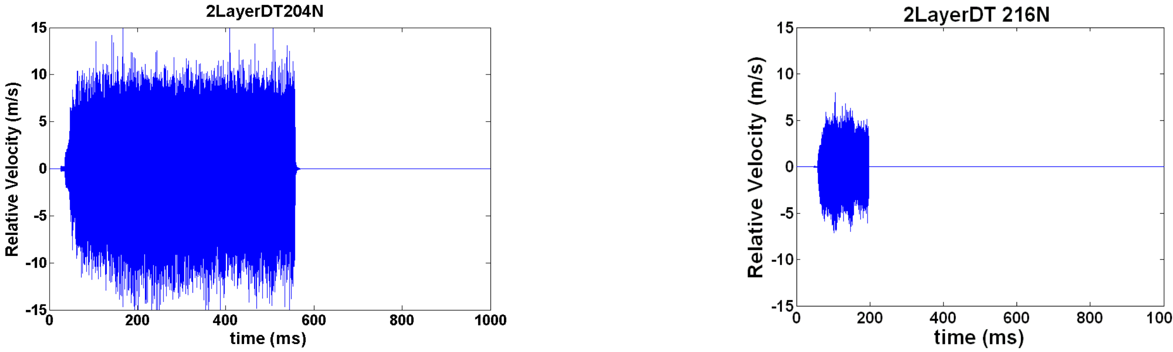

(i) Loading Force of 204N

(j) Loading Force of 216N

Figure 6. Relative Vibration Waveform at Different Loading Forces

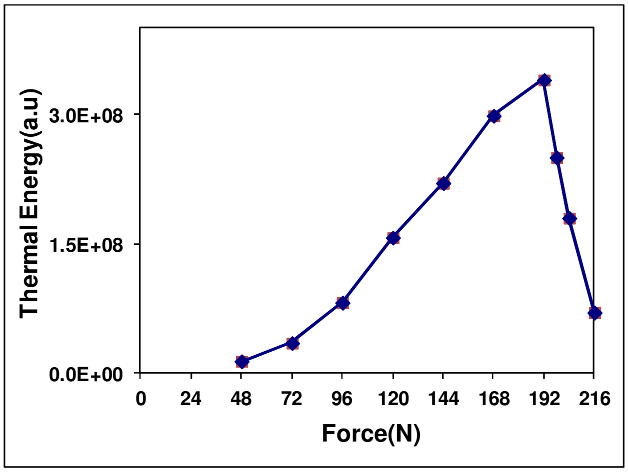

Figure 8. "Thermal Energy" Calculated at Point of Interest from Crack Area at Different Loading Forces

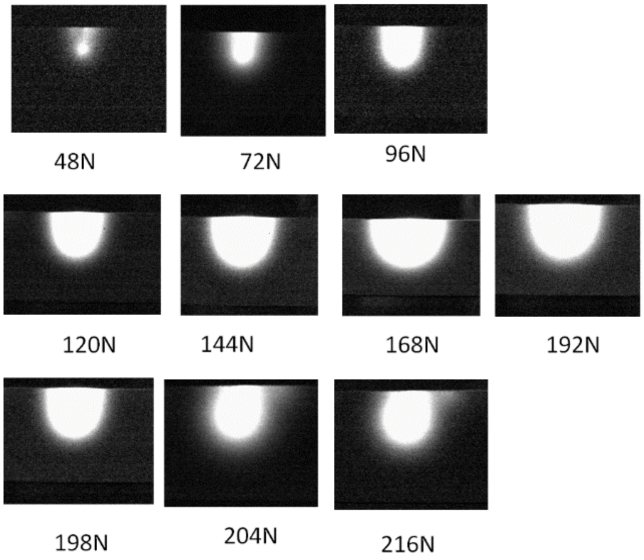
48N

72N

96N

120N

144N

168N

192N

198N

204N

216N

Figure 9. IR Images of the Crack Taken with Different Loading Forces

Figure 10 shows the maximum temperature increase at the crack with different loading forces. The temperature increased at different loading forces, which also show the same trend as the "acoustic energy".

At the same time, the area under the temperature time curve for different loading force was estimated, as shown in Figure 11. It was numerically calculated by integration of the curve from 0-1000ms. The difference of the area for different loading forces was plotted in Figure 12, which also shows the same trend as "thermal energy" and "acoustic energy". As the force increased, the area increased, while after the overload, it decreased as the maximum temperature decreased.

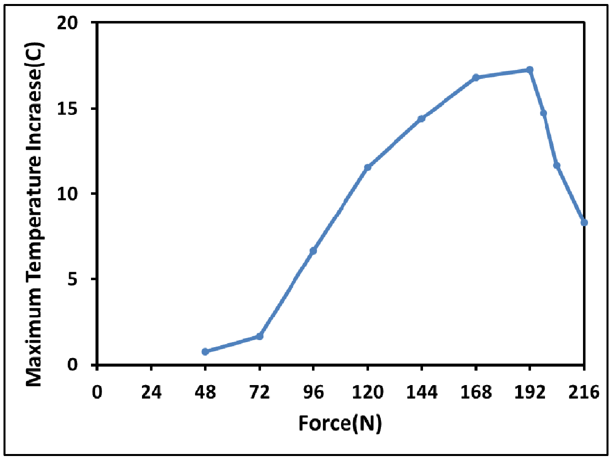

Figure 10. Maximum Temperature Increase of the Crack for Different Loading Forces

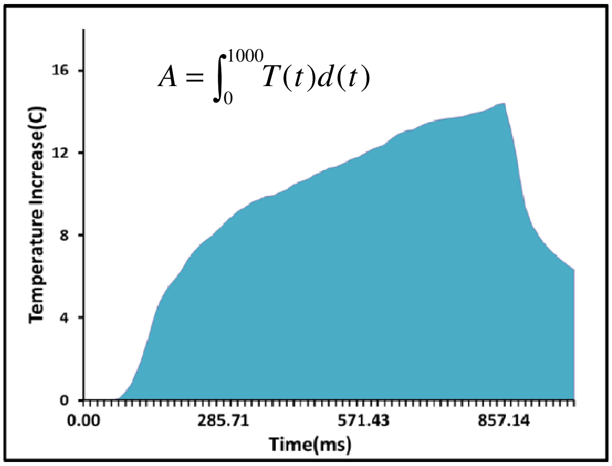

Figure 11. Schematic Showing the Calculated Method for the Area on the Temperature-Time Curve

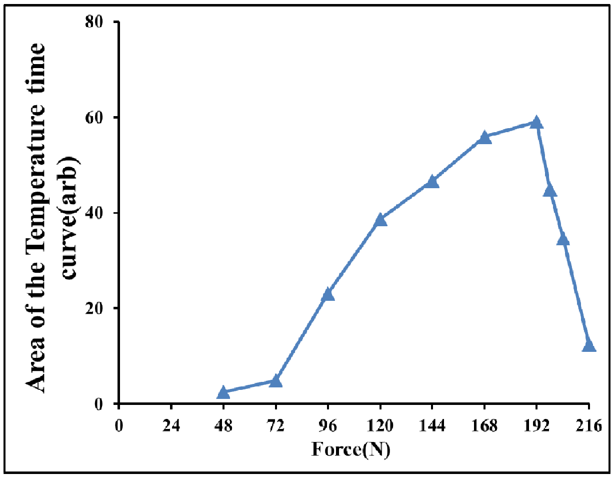

Figure 12. Comparison of the Area of the Temperature-Time Curve for Different Loading Forces

The ratio of "thermal energy" to "acoustic energy" is shown in Figure 13. The ratio curve is not flat, which means the "thermal energy" was not proportional to the "acoustic energy". In other words, the "thermal energy" did not increase linearly with the "acoustic energy" when loading force increased. The non-linear phenomenon is highly related to the status change of the coupling media at higher loading forces.

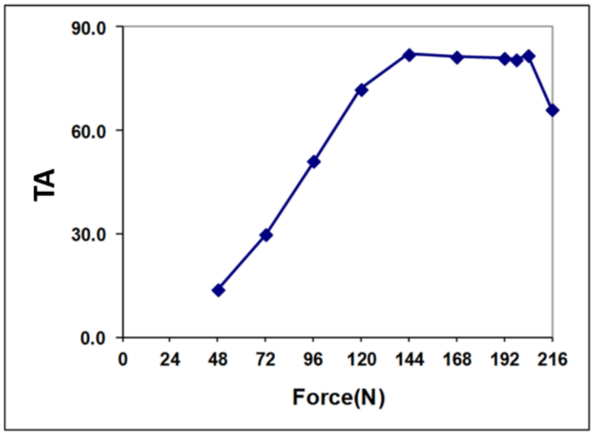

Figure 13. Ratio of "Thermal Energy" to "Acoustic Energy" at Different Loading Forces

Figure 14 shows the optical image of the duct tape as a result of each test at different loading forces. It clearly shows that as loading force increases, the duct tape is compressed; the residual shape of the coupling material differs from the initial stage.

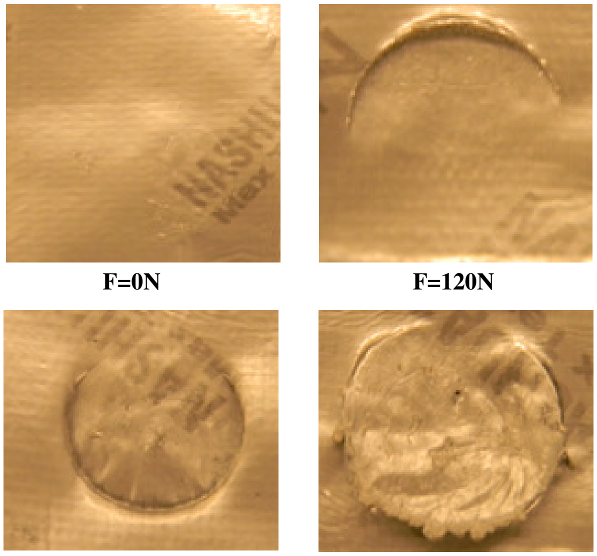

F=0N **F=120N**

F=198N **F=216N**

Figure 14. Optical Image of Duct Tape after each Test from Different Loading Forces

As higher loading forces were induced in the transducer tip, the higher output energy would melt the duct tape. The status change of the duct tape changed its properties, such as acoustic impedance and density, and then the acoustic transmission coefficient [21], [22] changed at higher forces. As far as how significant this change contributes to the vibration of the crack is an unknown factor. It can also be seen from this picture that, when the loading force was 198N and 216N, the duct tape melted due to the passing of higher energy transducers. As the loading force increased to 198N, the thickness of the coupling material was significantly reduced due to the tighter compression from the transducer tip. The contact zone thickness between transducer tip and Al bar was negligible. In this case, the transducer tip was loaded with a semi-rigid post. As far as the heating mechanism from the crack site at higher velocities, other unknown factors such as plastic deformation need to be investigated more. Such factors also contribute to the "thermal energy".

The power of the ultrasound can be expressed in Equation [23]:

$$P=F*V \tag{5}$$

Here, F is the loading force and V is the transducer velocity. According to the equation, the maximum trigger force that can be loaded onto the transducer tip is 220N. At or beyond such maximum force, the power required to properly operate the transducer is more than the unit's available power, at which point the transducer will stop. Correspondingly, the thickness change of the coupling materials is plotted in Figure 15. In this case, the importance of the coupling material is obvious [13]. This coupling material plays a role as damping source for the energy transmitted to the sample.

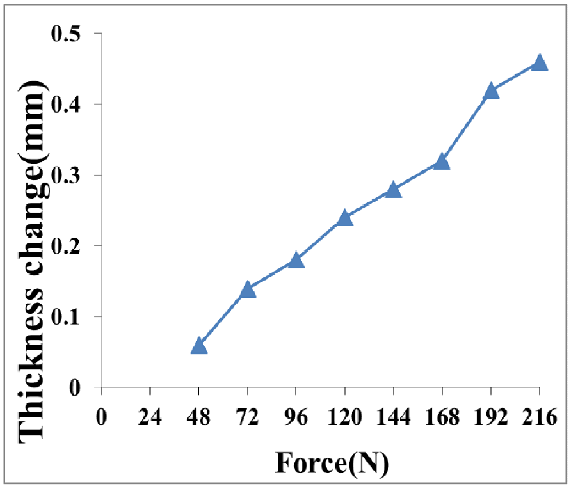

Figure 15. Thickness Change of 2LayerDT from Different Loading Forces

Figure 16 shows the correlation between the waveform and the temperature time plot for a loading force of 216N. In this case, the ultrasound pulse only shows a small portion of the input pulse length. One observation is that once overloading occurs, increasing additional forces will further reduce the pulse length output from the vibrometer. Another observation is that the spectrum of test is characterized of chaos.

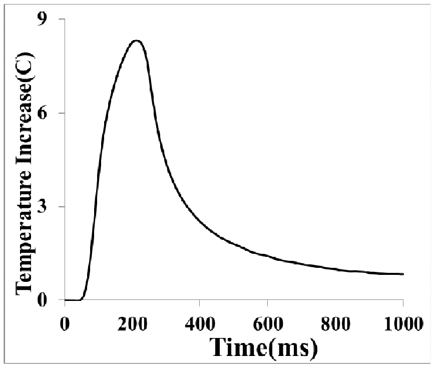

(a) Temperature-Time Plot at 216N

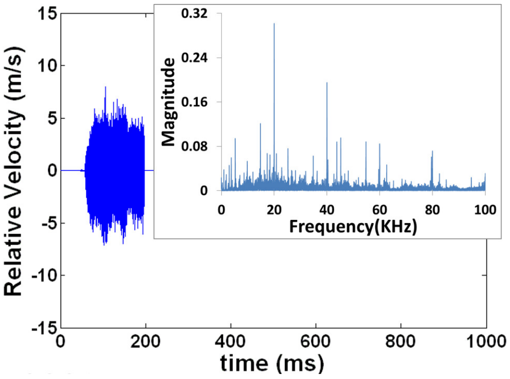

(b) Waveform and its Spectra at a Loading Force of 216N

Figure 16. Correlating Crack Vibration and Crack Heating via Waveform/Spectra and Temperature-Time Plot at 216N

Figure 17 gives another perspective view for the temperature time curve for different loading forces. These curves were separated into two phases, corresponding to phases I and II. The difference between these two phases is obvious; the reason behind it is that the speed at which the temperature increased varied with the time period when the ultrasound waves are transferred to the crack tip. At the same time, the slope of the curve was numerically estimated. It was shown that with an increase in the loading force, the slope will increase, which is also consistent with the energy calculation. The maximum temperature increase among the experiments was about 17°C. This temperature increase at room temperature did not have any effect on the mechanical properties of the sample, which has been shown in the handbook on aluminum alloys [24]. Since the time intervals between any experiments allowed the sample and the crack area to reach the equilibrium temperature of the lab conditions, there was no residual heat left for successive testing. As is shown in Figure 18, the initial thermal energy at the point of interest before each test was shown, the variations in the energy were negligible. Thus, the boundary conditions for friction heating for each test were the same. Therefore, there was no bias in the comparison of the temperature increase around the crack area for different loading forces.

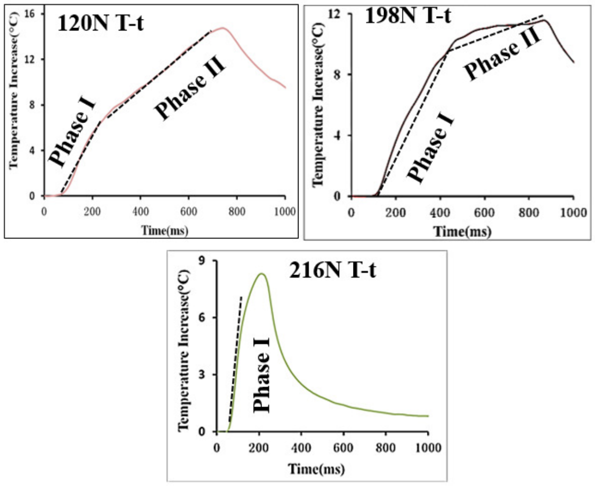

	Phase I	Phase II
120N	Y=0.0221x	Y=0.016x
198N	Y=0.0252x	Y=0.0241x
216N	Y=0.0416x	N/A

Figure 17. Numerical Regression Fitted Curve/Functions for Different Phases on Different Temperature-Time Curves on the Three Loads

Because of the chaotic acoustic behavior, a subtle change in an experiment can result in different vibration waveforms and their spectra. Therefore, no two repeated experiments have exactly the same data under acoustic chaotic conditions. However, by using the same controllable parameters and settings, these repeated experiments present very similar vibration waveforms and corresponding spectra, although the fraction of each frequency may vary slightly, and the magnitude of each frequency may vary a bit from test to test. One common characterization of each individual test was that the spectra always show the chaos frequency; and, the trend of the curve for either "acoustic energy" or "thermal energy" verse different loading forces was the same.

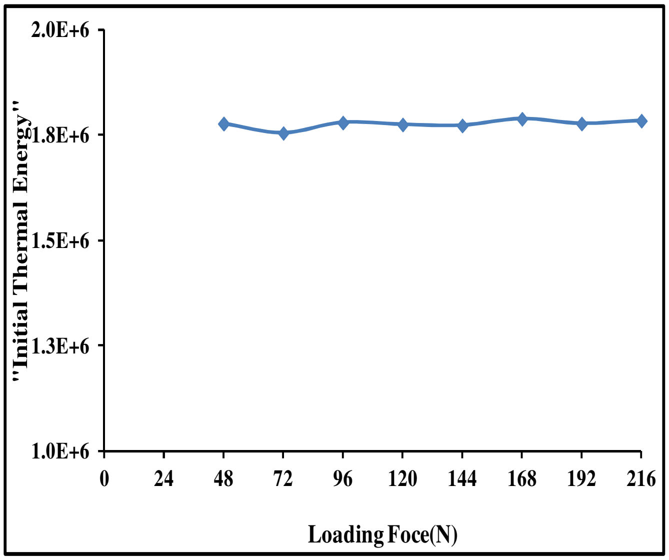

Figure 18. Initial "Thermal Energy" Calculated at Point of Interest from Crack Area at Different Loading Forces

Conclusion

The effect of loading force on the coupling between transducer and Al bar by using 2LayerDT as a coupling material under inspection in sonic IR imaging was shown. Chaos frequency for 2LayerDT can easily be obtained in 20k Hz systems, from the lowest force of 48N to the highest force at 216N. The amplitude of the vibration waveforms around the crack area increased with an increase in the loading forces by using 2LayerDT as a coupling material. The temperature changes in the crack increased when the loading force increased, and the amplitude of the vibration of the crack also increased when the loading forces increased. The higher loading forces produced higher energy to the crack site, which will easily brighten the crack. But there is a limitation in the loading forces for a 20 kHz system using 2LayerDT as a coupling material, which was 198N. Such transition forces are highly related to the maximum power capacity of the ultrasound transducer system. Beyond that force, it will not produce a full length of the vibration for predefined pulse lengths, which will not increase the temperature change in the crack site. This limitation can be a guide to the usage of 20 kHz transducers and 2LayerDT on Al bars.

Acknowledgements

This work was sponsored by Wayne State University.

References

[1] Favro, L., Han, X., Li, L., Ouyang, Z., Sun, G., Thomas, R., et al. (2001). Thermosonic imaging for NDE, *Review of progress in quantitative nondestructive evaluation*, *20*(2),478.

[2] Favro, L., Thomas, R., Han, X., Ouyang, Z., Newaz, G., et al. (2001).Sonic infrared imaging of fatigue cracks. *International Journal of Fatigue*, 23, 471-476.

[3] Yi, H., Peng-Cheng, M., Zhong-Ning, Z., Shu-Yi, Z., Li, S., Xiu-Ji, et al. (2003).The Ultrasonic Infrared Thermography and its Application in NDE. *Journal of Nanjing University (Natural Sciences)* 4, 014.

[4] Zhu, Y.-K., Tian, G.-Y., Lu, R.-S., & Zhang, H. (2011). A Review of Optical NDT Technologies. *Sensors*, 11, 7773-7798.

[5] Chen, C-H. (2007). *Ultrasonic and advanced methods for nondestructive testing and material characterization*. World Scientific.

[6] Han, X., Favro, L., Ouyang, Z., & Thomas, R. (2001). Thermosonics: detecting cracks and adhesion defects using ultrasonic excitation and infrared imaging. *The Journal of adhesion*, *76*, 151-162.

[7] Huang, S., Li, L., Yang, H., & Shi, K. (2001). In *NDE of composites delamination by infrared thermography*, NDE and Health Monitoring of Aerospace Materials and Composites II, 5046, (pp. 219-223).

[8] Li, G.-h., Wu, L.-x., Wu, M., & Qu, J.-x. (2004). Current status and applications of infrared thermography. *infrared and laser engineering*. *33*, 227-230.

[9] Mian, A., Han, X., Islam, S., & Newaz, G. (2004). Fatigue damage detection in graphite/epoxy composites using sonic infrared imaging technique. *Composites Science and Technology*, *64*, 657-666.

[10] Han, X., Lu, J., Islam, M.S., Li, W., Zeng, Z., Favro, et al. (2005). In *Sonic infrared imaging NDE, Proceedings of SPIE Smart Structures and Materials*, *5765*(4), 142-147.

[11] Choi, M., Park, J., Kim, W., & Kang, K. (2008). In *Detection of delamination defect inside timber by sonic IR, Proceedings. of SPIE*, *6939*(2), 268-272

[12] Song, Y., Godfrey, G., & Han, X. (2009). In What Role A Coupling Material Could Play In Sonic Ir Imaging, *AIP Conference Proceedings*, *1096*(1), 511.

[13] Han, X., Song, Y., & Godfrey, G. (2008). Investigation of non-linear effects of coupling materi-

als in sonic IR imaging, *The 15th International Symposium on: Smart Structures and Materials & Nondestructive Evaluation and Health Monitoring*, *6932* (3), 225-228.

[14] Song, Y., & Han, X. (2012). Further study of coupling materials on aluminum sample using sonic IR, *AIP Conference Proceedings*, *1403*(2), 546.

[15] Han, X., & Song, Y. (2013). Study the effect of engagement force of ultrasound transducer on crack detectability in sonic IR imaging, *AIP Conference Proceedings*, *1511*(1), 532.

[16] Gómez, T. E., & Montero, F. (2000). Bridging the gap of impedance mismatch between air and solid materials, *Proceedings of IEEE Ultrasonic Symposium,*.1072-1069 ,(6)1073

[17] Ke, W., Castaings, M., & Bacon, C. (2009).3 D finite element simulations of an air-coupled ultrasonic NDT system. *NDT & E International*, *42*, 524-533.

[18] Han, X., & Yu, R. (2007). Studying the effect of coupling materials in sonic IR imaging, *The 14th International Symposium on: Smart Structures and Materials & Nondestructive Evaluation and Health Monitoring*, *6529*(4), 869-972.

[19] Han, X., & He, Q. (2006). Developing thermal energy computing tools for sonic infrared imaging, *Proceedings of SPIE, Smart Structures and Materials, 6174*(3), 969-975

[20] Cohen, L. (1995).*Time-frequency analysis.* Prentice Hall PTR, New Jersey,

[21] Auld, B. A. (1973). *Acoustic fields and waves in solids*. Wiley New York:

[22] Krautkrämer, H., & Krautkrämer, J. (1990). *Ultrasonic testing of materials*. (4th ed.). Springer;

[23] Grewell, D. A. (1998). Welding system and method of setting welding machine parameters,US5772814 A,USPTO Office.

[24] Handbook, A. S. (1990). Aluminum and aluminum alloys. *ASM International*, *117*.

Biographies

YUYANG SONG is currently working at Toyota research institute of North America as a Research Scientist This research work is done during his PhD study at Wayne State University, where his research was mainly focus on nonlinear coupling effect of SonicIR system. His current research is also related with application of NDE technique at automotive industry, at the same time, he is also widely involved in lightweight material research at future mobility department at Toyota Technical center at Ann Arbor. Mr. Song may be reached at yysongenator@gmail.com or yuyang.song@tema.toyota.com

XIAOYAN HAN is Professor of electrical and computer engineering at Wayne State University. Her research area is nondestructive evaluation and material characterization. She is part of a team that is receiving the Airlines for America (A4A) Better Way Award for their work on Implementing Sonic IR on Critical Engine Components. Their WSU-patented technology uses sonic infrared imaging to detect flaws and cracks in critical airplane engine components. Prof Han can be reached at xhan@eng.wayne.edu

GROWTH AND PROPERTIES OF DIAMOND FILMS ON IRON-CATALYST COATED SUBSTRATES BY HFCVD

Parvaneh Azadfar, Science and Research Branch, I.A.U.; Mahmood Ghoranneviss, Science and Research Branch, I.A.U.;
Smohammad Elahi, Science and Research Branch, I.A.U.; Nazanin Farhadyar, Varamin-Pishva, I.A.U.

Abstract

In this study, diamond films were grown on Si and iron-coated Si wafers at different chamber pressures using pure ethanol vapor diluted in hydrogen by a Hot Filament Chemical Vapor Deposition (HFCVD) technique. To investigate the effect of catalyst and pressure on deposited diamond films, Raman and SEM techniques were used to characterize the properties of diamond films. Experimental results showed that diamond films with a higher intensity of diamond phase, smaller and more uniform crystalline sizes are able to grow on nanocatalyst layers. However, there was a significant decrease in growth rate of deposited films on the catalyst.

Introduction

Diamond films have a number of outstanding properties such as hardness, high propagation speed of acoustic waves, great thermal conductivity, chemical inertness, and high carrier mobility. Many researchers have tried to synthesize high quality, uniform diamond films with small crystal grains and high growth rates over large substrate areas [1-6].

The behavior of decreasing diamond crystallite size down to nanometer scales has been the subject of pioneering studies using the partial or complete replacement of hydrogen by argon. The presence of argon can influence the formation and excitation of plasma species through energy and charge transfer processes, as well as affect the density and energy distribution of free electrons in the discharge. In Ar rich plasma, the discharge resulted in an increase in the C_2 species. The existence of C_2 species is supposed to be responsible for a rise in the secondary nucleation rate of diamond in Ar rich plasma and, consequently, a reduction in the size of the grains, yet with more sp^2 bonds in the film composition [7-8].

There must also be a surface pre-treatment to enhance the nucleation density required for diamond film growth; for example, abrasive scratching with diamond powders or ultrasonication in diamond powder to bias enhanced nucleation [2, 7]. There have been many reports on the role played by the metal catalyst in carbon nanostructures—such as carbon nanotubes, carbon nanoparticles, and carbon nanofibers—that could be selectively synthesized using catalyst-coated substrates by HFCVD [9-12]. Following a search on the effect of catalytic decomposition of hydrocarbons by transition metal on diamond growth [6], the authors of this study chose to use iron as a catalyst on Si wafers in order to compare diamond films deposited on directed Si and Fe-coated Si substrates by the HFCVD technique.

Iron produced the highest density of carbon structure at any temperature between 580 ℃ to 1000 ℃. Hernadi et al. [12] tested an iron-based catalyst with different hydrocarbons on different supports and observed that iron presents the highest activity in the decomposition of different unsaturated compounds. In this current study, experimental results were reported for hot filament chemical vapor deposition of diamond films from ethanol vapor diluted in hydrogen. The effect of total gas pressure and different kinds of substrates on the grain size, quality, and growth rate of films was investigated using scanning electron microscopy (SEM) and Raman spectroscopy.

It is important to mention that common pretreatment methods were not used. It was verified that the use of iron as a catalyst causes more uniform and near two times smaller crystal grains than those grains grown on directed Si wafers. This procedure may provide a route to control the size of diamond crystals, leading to thick and smooth nanocrystalline diamond film.

Experimental Details

Four 1×1 cm^2 single-crystal p-type silicon substrates were cleaned with acetone, ethanol, and de-ionized water separately in an ultrasonic bath for 10 minutes. In order to assess the effect of the catalyst, the best combination of diamond film properties, small grain size, high structure quality, and growth rate, two Si substrates were covered by SiO_2 (70 nm) using an electron beam and then by iron as a catalyst (8 nm) using thermal evaporation.

A silicon oxide layer was interposed between the Si and Fe in order to prevent the iron diffusion into the Si bulk and undesired reactions between them [13]. For efficient growth of diamond, the etching process was done in 10 minutes in

Table 1. Experimental Deposition Conditions, Value of Crystal Size and Growth Rate

	Flow(sccm)	Catalyst	P(Torr)	T_S(∘C)	T_F(∘C)	t(min)	Crystal Size (nm)	Growth Rate (μm/h)
Si1	100	-	10	800	1800	90	1107-178	14
Fe1	100	+	10	800	1800	90	742	2.46
Si2	100	-	15	800	1800	90	364	1.4
Fe2	100	+	15	800	1800	90	190	0.86

order to change the morphology of the substrates in a working pressure of 10 Torr with hydrogen and flow rates of 100 sccm. Diamond films were deposited from a mixture of ethanol vapor (99.995% purity), 2% by volume, diluted in hydrogen on Si and Fe-coated Si wafers using a HFCVD reactor.

It is important to mention that for a more accurate study of the film properties of samples Si1 and Fe1 in a pressure 10 Torr, and Si2 and Fe2 in a pressure of 15 Torr, were grown together to keep experimental conditions similar, while other parameters were also kept constant, which are listed in Table 1. The surface morphology was observed by top view and cross-sectional images from the scanning electron microscope (KYKY EM-3200). The diamond and non-diamond phases in the grown films were examined by a micro-Raman spectrometer (Almega Thermo Nicolet) using an Nd:YLF laser (532 nm wavelength).

Results and Discussion

Raman Spectra of Diamond Films

Raman spectra of the samples are shown in Figure 1. In all spectra, an intense band at around 1332 cm^{-1} (diamond peak) can be observed, which is due to the sp^3 bonding in the film composition [14]. For each set of samples grown at constant pressure (see Table 1 and Figure 1), the diamond films which were grown on Fe-catalyst lead to more intense sp^3 peaks, which is indicative of the better structural quality of deposited diamonds on nanocatalyst versus deposited diamonds on directed Si substrates.

The peaks at 1450-1650 cm^{-1} (G peaks) are associated with sp^2 bonds and correspond to graphite or amorphous carbon [14]. Comparing peaks, the intensity of sp^2 bonds decreased from sample Si1 to Fe1 in Figures 1(a) and 1(b), which show that nano-Fe catalysts induced the deposition of diamond films with few non-diamond carbon phases. It is important to point out the peculiar ability of transition metals, such as iron, to link their catalytic activity for the decomposition of carbon compounds, their ability to form carbides, and the possibility for carbon to diffuse through and over the catalyst particles, leading to supersaturation of carbon in the metals. Also there are enhanced formations of H atoms by a catalytic dissociation of H_2 on nano-catalyst surfaces, which can subsequently activate the hydrogen abstraction reaction and saturate the dangling bonds on the diamond growing surfaces [6]. These can play an essential part in the initial stage of the growth process [12].

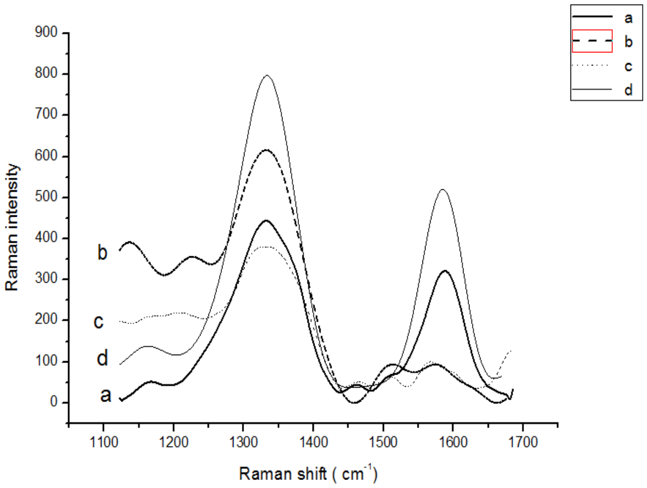

Figure 1. Raman Spectrum of Samples (a) Si1, (b) Fe1, (c) Si2, and (d) Fe2

The behavior of G peak intensity of Si2 in Figure 1c is the same as Fe1 in Figure 1(b); this indicates that diamond film was grown with more concentration of hydrogen atoms with a pressure of 15 Torr (Si2) than Fe1 (10 Torr and Fe-coated), which promotes more etching of sp^2 carbon phases. However, from Figure 1(d), it can be seen that the relative intensity of G peak increased in sample Fe2 (more pressure and Fe-coated).

The amorphous layer formed on the Fe surface may lead to speculation that it is the initial growing phase before a transformation from an amorphous phase to the crystalline diamond structures [6]; this conclusion can be confirmed by a very low growth rate of film in this condition obtained by an SEM analysis. Deposited films obtained in lower pressures, in Figures 1(a) and 1(b), have a higher intensity of diamond peaks than those in higher pressures as in Figures 1(c) and 1(d), as expected [1].

The better quality of the films obtained in lower pressures is due to a higher number of active sites available for diamond nucleation when lower pressure is kept inside the reactor. This may be assigned to the free pathway of radicals present in gas phase increases, which contributes to an increase in etching rates of free radicals followed by increasing the active sites on the substrate surface permitting the production of more of such radicals [1]. However, the concentration of hydrogen atoms was lower in the gas phase chemistry in low pressure, so it reduces the etching of sp^2 carbon phase (high intensity G peak in sample Si1). Figures 1(c) and 1(d) confirm that higher pressure values induce lower intensities of characteristic diamond peaks.

A feature appeared at about 1140 cm^{-1} (1136 cm^{-1} for sample Fe1 and 1120 cm^{-1} for sample Si2), which was attributed to the formation of transpolyacetylene around the surface of the diamond films [6]. It is important to point out that the formation of a transpolyacetylene phase in diamond films grown on nano-Fe catalysts (Fe1) is more than that for the transpolyacetylene phase in diamond film grown on sample Si2, which is not in agreement with results reported by Teng et al. [6].

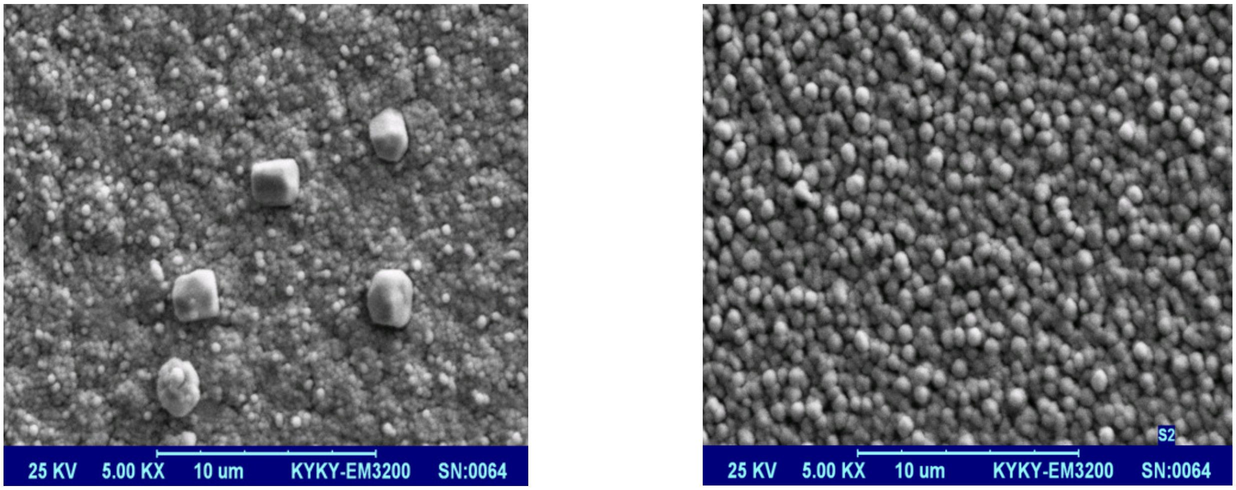

(a) Si1 **(b) Fe1**

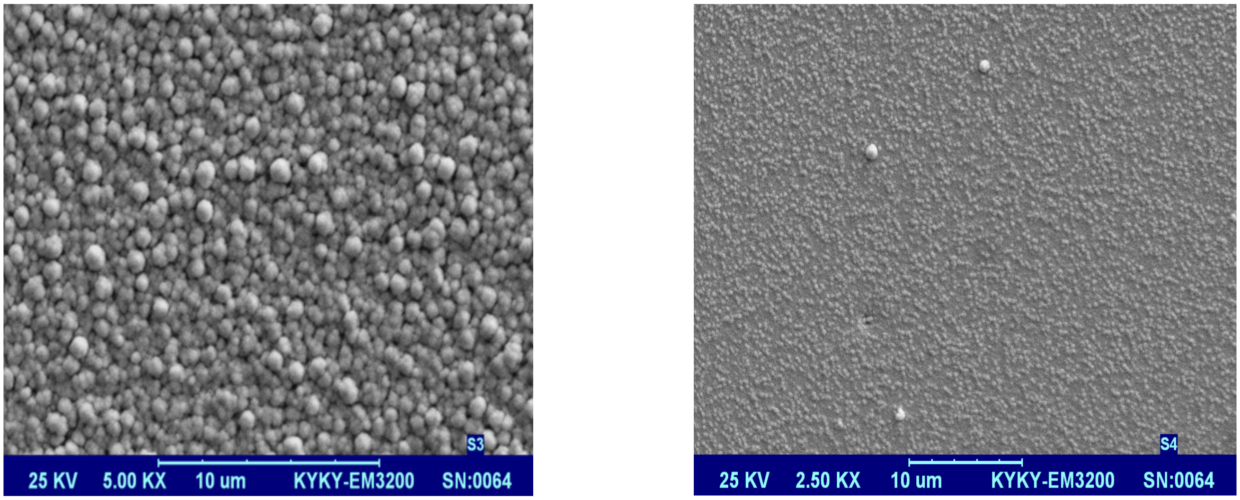

(c) Si2 **(d) Fe2**

Figure 2. SEM Micrographs of Diamond Films

SEM Studies of Diamond Films

SEM pictures of diamond films on Si and catalyst-coated substrates are presented in Figure 2; average crystalline sizes calculated by image analysis from SEM micrographs are listed in Table 1. It is clear that at constant pressures, crystalline size decreases from Si1 (where there are nonuniform crystals with 2 different sizes) to Fe1, and Si2 to Fe2, and reaches a more uniform and nanometer-sized scale. The formation of these uniform diamond crystals can possibly result from the high and isotropic nucleation, thereby yielding more diamond crystals on the Fe nanocatalyst [6] and raising the number of diamond phases. From Figure 2 (left to right), it is also possible to see that the rise in pressure induced a decrease in the size of crystals from micrometer on Si1 to about 364 nm on Si2, and 742 nm of Fe1 to 190 nm on Fe2.

In order to calculate the growth rate of the films, cross-sectional features of samples were obtained by SEM. A typical example is shown in Figure 3. The results are presented in Table 1. The decrease in growth rate and crystal size to the rising pressure may relate to the decrease of mean free path of radicals, as mentioned earlier, which decreases the concentration of radicals and dissociation of carbon and hydrogen molecules on the surface of the deposited film. Consequently, it decreases the formation of diamond crystals and film quality.

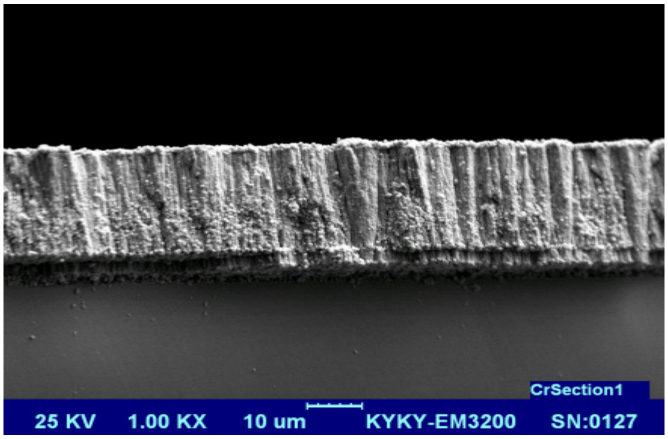

Figure 3. Typical Cross-Sectional SEM Image of Si1

There is a significant decrease in the growth rate of diamond films at a constant pressure on different substrates. For each set of samples with a pressure of 10 Torr, growth rate decreased from 14 µm/h for sample Si1 to 2.46 µm/h of sample Fe1, and 1.4 µm/h for sample Si2 to 0.86 µm/h for sample Fe2. This may be attributed to a large incubation period at the beginning of the growth period, which consisted of a radical adsorption and dissociation, carbon dissolution into catalysts, and carbon diffusion through catalyst particles [9]. Longer incubation periods could lead to a reduction in growth time for films grown on catalyst layers.

Conclusion

The structure and morphology of deposited diamond films using ethanol and hydrogen were demonstrated. No mechanical or other pretreatments were used to scratch or seed the substrates for creating nucleation sites. Interposing an 8 nm iron layer as a catalyst between Si wafers and diamond films resulted in more molecular decomposition by chemical interactions between the iron electrons and the carbon electrons, as well as low amorphous carbon and transpolyacetylene phases. Consequently, it is possible to grow diamond with smaller crystal sizes in the absence of re-nucleation processes by using nano-layer catalysts, which induces high initial ucleation required for high quality diamond growth.

References

[1] Braga, N. A., Cairo, C. A. A., Baldan, M. R., Trava-Airoldi, V. J., & Ferreira, N. G. (2011). Optimal parameters to produce high quality diamond films on 3D porous Titanium substrates. *Diamond & Related Materials*, *20*, 31-35.

[2] Williams, O. A. (2011). Nanocrystalline diamond. *Diamond & Related Materials*, *20*, 621-640.

[3] Sampaio, M. A., Peterlevitz, A. C., Ceragioli, H. J., Correa, W. L. A., Damiani, F., Chiquito, A. J. et al. (2010). Electrical properties of diamond films prepared from carbon disulfide and ethanol in hydrogen. *Vacuum*, *85*, 180-183.

[4] Barbosa, D. C., Barreto, P. R. P., Trava-Airoldi, V. J., & Corat, E. J. (2010). Growth and characterization of diamond micro and nano crystals obtained using different methane concentration in argon-rich gas mixture. *Diamond & Related Materials*, *19*, 768-771.

[5] You, M. S., Hong, F. C. N., Jeng, Y. R., & Huang, S. M. (2009). Low temperature growth of highly transparent nanocrystalline diamond films on quartz glass by hot filament chemical vapor deposition. *Diamond & Related Materials*, *18*, 155-159.

[6] Teng, C. C., Ku, F. C., Sung, C. M., Deng, J. P., Chien, S. F., Song, S. M. et al. (2010). Effect of Nano -Ni Catalyst on the Growth and Characterization of Diamond Films by HFCVD. *Journal of Nanomaterials*, Article ID 365614.

[7] Amaral, M., Silva, D. J., Fernandes, A. J. S., Costa, F. M., Oliveira, F. J., & Silva, R. F. (2009). Surface activation pre-treatment for NCD films grown by HFCVD. *Vacuum*, *83*, 1228-1232.

[8] Rakha, S. A., Xintai, Z., Zhu, D., & Guojun, Y. (2010). Effects of N_2 addition on nanocrystalline diamond films by HFCVD in Ar/CH_4 gas mixture. *Current Applied Physics*, *10*, 171-175.

[9] Hong, N. T., Koh, K. H., Tam, N. T. T., Minh, P. N., Khoi, P. H., & Lee, S. (2009). Combined model for growing mechanism of carbon nanotubes using HFCVD: effect of temperature and molecule gas diffusion. *Thin Solid Films*, *517*, 3562-3565.

[10] Lee, S., Choi, S., Park, K. H., Chae, K. W., Cho, J. B., Ahn, Y. et al. (2008). Hot-filament CVD synthesis and application of carbon nanostructures. *Thin Solid Films*, *516*, 700-705.

[11] Akbarzadeh Pasha, M., Ranjbar, M., Vesaghi, M. A., & Shafiekhani, A. (2010). The evolution of catalyst layer morphology and sub-surface growth of CNT over the hot filament grown Fe-Cr thin films. *Applied Surface Science*, *257*, 1511-1515.

[12] Dupuis, A. C. (2005). The catalyst in the CCVD of carbon nanotubes. *Progress in Materials Science*, *50*, 929-961.

[13] Dikonimos Makris, Th., Giorgi, R., Lisi, N., Pilloni, L., Salernitano, E., Sarto, F. et al. (2004). Carbon nanotubes growth by HFCVD: effect of the process parameters and catalyst preparation. *Diamond and Related Materials*, *13*, 305-310.

[14] Baranauskas, V., Ceragioli, H. J., Peterlevitz, A. C., Tosin, M. C., & Durrant, S. F. (2000). Effect of the addition of helium on the synthesis of diamond films. *Thin Solid Films*, *377*, 182-187.

Biographies

PARVANEH AZADFAR is currently a Ph.D. student at the Science and Research Branch I.A.U of Tehran. She earned her M.S. degree (Solid State, 2008) from Karaj Branch I.A.U. Her present research interests are in surface science, thin film and semiconductors. She can be reached at pazadfar@gmail.com

MAHMOOD GHORANNEVISS is a Professor of Plasma Physics at Science and Research Branch I.A.U of Tehran. He received his M.S. (Plasma Physics, 1980) and Ph.D. (Plasma Physics, 1983) from University of Poona, India. He is currently head of Plasma Physics Research Center. His interests are energy, atomic and molecular physics. He can be reached at ghoranneviss@pprc.srbiau.ac.ir

SMOHAMMAD ELAHI is an Associate Professor of Condensed Matter at Science and Research Branch I.A.U of Tehran. He earned his M.S. (Condensed Matter, 1975) and Ph.D. (Condensed Matter, 1979) from Brunel University, England. Dr. Elahi is currently teaching in Physics Department at Science and Research Branch I.A.U of Tehran. His interests are condensed matter and nano science. Dr. Elahi can be reached at smohammad-elahi@srbiau.ac.ir

NAZANIN FARHADYAR is an Assistant Professor of Inorganic Chemistry at Varamin-Pishva I.A.U. She earned her M.S. degree from North Tehran Branch I.A.U. (2004) f and Ph.D. (Inorganic Chemistry, 2009) from Science and Research Branch I.A.U of Tehran. Dr. Farhadyar is currently teaching in Chemistry Department of Varamin-Pishva I.A.U. Her interests are nanotechnology, nanomaterials, photocatalyst and drug delivery. Dr. Farhadyar may be reached at nfarhadyar@gmail.com

A NEW SEMI-ACTIVE SUSPENSION SYSTEM FOR VEHICLE APPLICATIONS

Yaswanth Siramdasu, Virginia Tech, Blacksburg; Saied Taheri, Virginia Tech

Abstract

A novel, double-damper-based suspension system with two dampers attached in parallel was developed in this study. The scope of potential improvements in ride control, without bottoming of suspension and deterioration of road-holding properties is presented here. A Lyapunov-based adaptive ride-control algorithm using a quarter-car vehicle model with single-damper and double-damper suspension was developed. The parameter adaptation laws were derived based on system dynamics and were selected to be sprung mass and tire stiffness. An ideal Skyhook-Groundhook 2 DOF suspension was used as the reference model. The simulation of no control, fully active control of a single-damper suspension, and semi-active control of a double-damper suspension was performed. The reduced RMS acceleration of sprung mass, due to fully active single-damper control, was almost identical to the semi-active double-damper control without deviation from suspension travel and road-holding properties of a normal suspension. This behavior resulted in reduced power consumption, complexity, and cost, while the system performed like a fully active suspension system.

Introduction

During the 1980s, replacement of passive suspensions with hydraulic-based active suspension systems was explored extensively. Although the potential improvements of ride comfort with active suspension is much more than passive suspension, several major disadvantages—such as high power consumption, unreliability, more complex and costly systems—placed the active suspension on the shelf. Semi-active suspension systems, on the other hand, seem to be the best compromise in terms of cost, reliability, and power consumption. In this case, the damper can only draw energy from the vehicle system by opposing the motion of the mass. The objective of this study was to achieve a ride performance equivalent to a fully active suspension system using a semi-active suspension. Furthermore, the suspension deflection and road-holding properties of such semi-active suspensions should not be deteriorated.

In this paper, a novel double-damper suspension is introduced in order to show that a simple design modification of the suspension can further improve the performance of the semi-active suspension. A single-damper in a typical suspension system was replaced with two separate dampers in parallel, as shown in Figure 1. The added advantage was clearly to increase the number of controllable dampers such that, during jounce or rebound, the respective damper associated with the sprung mass would resort to minimum damping without affecting the road-holding capability of the unsprung mass or unsprung mass resorting to minimum damping without affecting the vibration isolation of the sprung mass. Liu et al. [1] applied the concept of two controllable dampers to one DOF base excitation case. It was observed that the addition of controllable dampers in parallel with passive springs changes the equivalent stiffness of the springs, thereby controlling the stiffness of the system without physically varying spring stiffness.

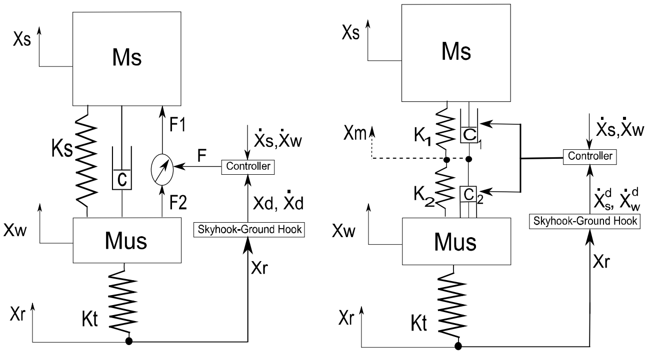

Figure 1. Schematic Diagram of Single- and Double-Damper Quarter-Car Models with Active and Semi-Active Controllers

With this background, two controllable semi-active dampers were used to improve the vibration characteristics of the vehicle. A Lyapunov-based adaptive control algorithm was developed and used for both active and semi-active damper control. The advantage of this method is computation simplicity, due to effective exploitation of system dynamics. Slotine and Weiping [2] used a similar methodology for control of robot manipulators, which they later modified for vehicle applications [3-5]. Looking at past studies, the skyhook model is considered the optimal control policy for vibration control of 1 DOF mass-spring-damper systems with base excitation [6]. The groundhook model is also considered as the optimal control policy for wheel hopping to increase road-holding capability [7].

A combination of the skyhook and groundhook models was used as the reference model in this current study. For evaluating the ride comfort of the human body, minimum RMS acceleration of the sprung mass was used as the performance criterion [7]. For semi-active control of a double-damper system, the control forces are first computed assuming a fully active system followed by the imposition of the constraints. Used in a semi-active mode, the system reduces energy consumption, complexity, and cost. The outcome of this study was a novel semi-active suspension system emulating an active suspension, which could overcome the primary hurdle of power consumption [8] and unreliability in implementation of active control.

Mathematical Modeling

As this study focused on the control of vertical vibration from the vehicle, the quarter-car model represents all of the important components which affect the vertical dynamics of vehicles in simplified form: sprung mass, unsprung mass, spring and damper as suspension, and a spring as the point contact tire model. The mathematical models used in this study were single-damper- and double-damper-based quarter-car models for evaluating performance analysis and control system design through an ideal skyhook-groundhook 2 DOF suspension with two dampers each attached to sprung mass and unsprung mass at one end and an inertial frame at the other end.

Quarter-Car Model with a Single Damper

The equations of motion of sprung (X_s) and unsprung masses (X_w) are given here in state space form, with the following assumptions: 1) The spring and damper are operating in a linear region; and, 2) Damping of the tire is assumed to be negligible when compared with that of suspension.

$$I\begin{bmatrix}\dot{X}_1\\ \dot{X}_2\\ \dot{X}_3\\ \dot{X}_4\end{bmatrix}+\begin{bmatrix}0 & -1 & 0 & 0\\ \frac{K_s}{M_s} & \frac{C_s}{M_s} & -\frac{K_s}{M_s} & -\frac{C_s}{M_s}\\ 0 & 0 & 0 & -1\\ -\frac{K_s}{M_{us}} & -\frac{C_s}{M_{us}} & \frac{K_s+K_t}{M_{us}} & \frac{C_s}{M_{us}}\end{bmatrix}\begin{bmatrix}X_1\\ X_2\\ X_3\\ X_4\end{bmatrix}+\begin{bmatrix}0\\ 0\\ 0\\ -\frac{K_tX_r}{M_{us}}\end{bmatrix}=F \quad (1)$$

where

$$\begin{bmatrix}X_1 & X_2 & X_3 & X_4\end{bmatrix}=\begin{bmatrix}X_s & \dot{X}_s & X_w & \dot{X}_w\end{bmatrix}$$

and

$$F=\begin{bmatrix}0 & F_1 & 0 & F_2\end{bmatrix}^T$$

Quarter-Car Model with a Double Damper

As shown in Figure 1, the equation of motion of the double-damper model represents additional displacement of points in-between two dampers (X_m) other than sprung (X_s) and unsprung masses (X_w). Solving for X_m by equating reaction forces in-between parallel dampers, the equations of motion are given as

$$\dot{X}_m(C_1+C_2)+X_m(K_1+K_2)=C_1\dot{X}_s+K_1X_s+C_2\dot{X}_w+K_2X_w \quad (2)$$

$$I\begin{bmatrix}\dot{X}_1\\ \dot{X}_2\\ \dot{X}_3\\ \dot{X}_4\end{bmatrix}+\begin{bmatrix}0 & -1 & 0 & 0\\ \frac{K_1}{M_s} & \frac{C_1}{M_s} & 0 & 0\\ 0 & 0 & 0 & -1\\ 0 & 0 & \frac{K_2+K_t}{M_{us}} & \frac{C_2}{M_{us}}\end{bmatrix}\begin{bmatrix}X_1\\ X_2\\ X_3\\ X_4\end{bmatrix}+\begin{bmatrix}0\\ A\\ 0\\ B-\frac{K_tX_r}{M_{us}}\end{bmatrix}=F \quad (3)$$

where,

$$A=-\frac{C_1}{M_s}\dot{X}_m-\frac{K_1}{M_s}X_m$$

and

$$B=-\frac{C_2}{M_{us}}\dot{X}_m-\frac{K_2}{M_{us}}X_m$$

C_1 and C_2 are the damping coefficients of two dampers in parallel. K_1 and K_2 are the stiffness of the upper and lower parts of the suspension spring; here, both are assumed equal to $2K_s$ so that equivalent stiffness is the same as the single-damper model.

Skyhook-Groundhook Reference Model

As shown in Figure 2, a 2 DOF skyhook and groundhook reference model is being used to obtain desired position and velocities for the control algorithm to follow. C_{sky} and C_G are selected appropriately to guarantee less vibration of sprung mass and less hopping of unsprung mass. Note that these values should be around actual controlling suspension parameters so that the desired values are within physical limits. The equation of motion of desired sprung and unsprung masses are given by Equation (4).

$$I\begin{bmatrix}\dot{X}_1^d\\ \dot{X}_2^d\\ \dot{X}_3^d\\ \dot{X}_4^d\end{bmatrix}+\begin{bmatrix}0 & -1 & 0 & 0\\ \frac{K_s}{M_s} & \frac{C_{sky}}{M_s} & -\frac{K_s}{M_s} & 0\\ 0 & 0 & 0 & -1\\ -\frac{K_s}{M_{us}} & 0 & \frac{K_s+K_t}{M_{us}} & \frac{C_G}{M_{us}}\end{bmatrix}\begin{bmatrix}X_1^d\\ X_2^d\\ X_3^d\\ X_4^d\end{bmatrix}+\begin{bmatrix}0\\ 0\\ 0\\ -\frac{K_tX_r}{M_{us}}\end{bmatrix}=0 \quad (4)$$

From the above equations, the motion of sprung mass is not affected by the groundhook damper and unsprung mass is not affected by the skyhook damper due to attachment of each damper to the inertial reference frame. This is the main reason for using the skyhook-groundhook model as an optimal control policy.

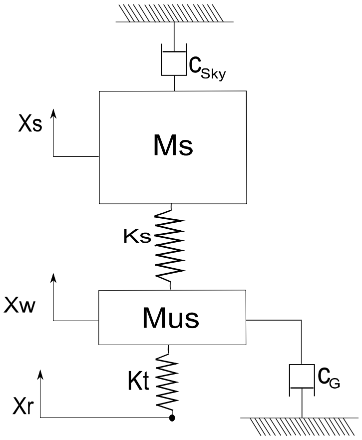

Figure 2. Schematic Diagram of the Skyhook-Groundhook Reference Model

Control Algorithm

General Formulation

A new Lyapunov-based adaptive control algorithm was developed for ride control. The algorithm consists of a proportional feedback section and a full dynamics feed forward section, which estimates unknown model parameters online. The advantage of this method is due to its computational simplicity, just like PID, and use of only a velocity sensor for each mass, thus reducing cost and computational power. Due to its simplicity and fast response, it is well suitable for practical implementation on a full vehicle model. The method requires the equations of motion of a dynamic system under consideration to be of the form

$$\mathbf{A}\dot{x}+\mathbf{B}x+C=F \tag{5}$$

Equations (1) and (3) are represented in the form of Equation (5), where $x=\begin{bmatrix}X_1 & X_2 & X_3 & X_4\end{bmatrix}^T$ and F is the control force output from the control algorithm. To derive the control algorithm and adaption law, a Lyapunov function was considered:

$$V(x,t)=\frac{1}{2}(\tilde{x}^T\mathbf{A}\tilde{x}+\tilde{p}^T\mathbf{\Gamma}\tilde{p})+\int\tilde{x}^T\mathbf{B}\tilde{x}\,dt \tag{6}$$

where, p is an n-dimensional vector containing n unknown model parameters and $\tilde{x}=x-x^d$ was the error in states and $\tilde{p}=\hat{p}-p$ was the parameter error between the estimated and nominal parameters, $\hat{p}$ and p, respectively. From Equation (6), the Lyapunov function is always positive definite, if the gain matrix $\mathbf{\Gamma}$ is positive definite; it was selected here as a positive diagonal matrix. If the derivative of $V(x,t)$ is negative definite then the system is asymptotically stable. Differentiating $V(x,t)$ yields

$$\dot{V}(x,t)=\frac{1}{2}(\dot{\tilde{x}}^T\mathbf{A}\tilde{x}+\tilde{x}^T\mathbf{A}\dot{\tilde{x}}+\dot{\tilde{p}}^T\mathbf{\Gamma}\tilde{p}+\tilde{p}^T\mathbf{\Gamma}\dot{\tilde{p}})+\tilde{x}^T\mathbf{B}\tilde{x} \tag{7}$$

Here, $\mathbf{A}$ and $\mathbf{\Gamma}$ are diagonal matrices and, thus, $\dot{\tilde{x}}^T\mathbf{A}\tilde{x}=\tilde{x}^T\mathbf{A}\dot{\tilde{x}}$ and $\dot{\tilde{p}}^T\mathbf{\Gamma}\tilde{p}=\tilde{p}^T\mathbf{\Gamma}\dot{\tilde{p}}$. Therefore Equation (7) is reduced to

$$\dot{V}(x,t)=\tilde{x}^T\mathbf{A}\dot{\tilde{x}}+\tilde{p}^T\mathbf{\Gamma}\dot{\tilde{p}}+\tilde{x}^T\mathbf{B}\tilde{x} \tag{8}$$

The term $\mathbf{A}\dot{\tilde{x}}$ can be expanded and, substituting Equation (5) into Equation (8), yields the following equation:

$$\dot{V}(x,t)=\tilde{x}^T[-\mathbf{B}x^d-C+F-\mathbf{A}\dot{x}^d]+\tilde{p}^T\mathbf{\Gamma}\dot{\tilde{p}} \tag{9}$$

The control law, as mentioned earlier, consists of a feedback section and a full dynamics feed forward section, and is defined as

$$F=\hat{\mathbf{A}}\dot{x}_d+\hat{\mathbf{B}}x_d+\hat{C}-K_p\tilde{x} \tag{10}$$

where, K_p is the positive definite proportional gain matrix; $\tilde{\mathbf{A}}=\hat{\mathbf{A}}-\mathbf{A},\tilde{\mathbf{B}}=\hat{\mathbf{B}}-\mathbf{B},\tilde{C}=\hat{C}-C$ represents error between the estimated ($\hat{\mathbf{A}},\hat{\mathbf{B}}$ and $\hat{C}$) and nominal model parameters. Substituting Equation (10) in Equation (9) yields

$$\dot{V}(x,t)=\tilde{x}^T[\tilde{\mathbf{A}}\dot{x}^d+\tilde{\mathbf{B}}x^d+\tilde{C}-K_p\tilde{x}]+\tilde{p}^T\mathbf{\Gamma}\dot{\tilde{p}} \tag{11}$$

To derive the adaption law, let H be defined as

$$H\tilde{p}=\tilde{\mathbf{A}}\dot{x}^d+\tilde{\mathbf{B}}x^d+\tilde{C} \tag{12}$$

Substituting Equation (12) into Equation (11) yields

$$\dot{V}(x,t)=\tilde{x}^T[H\tilde{p}-K_p\tilde{x}]+\tilde{p}^T\mathbf{\Gamma}\dot{\tilde{p}} \tag{13}$$

The product of $\tilde{x}^T H\tilde{p}$ is scalar and symmetric, therefore $\tilde{x}^T H\tilde{p}=\tilde{p}^T H^T\tilde{x}$ and Equation (13) is written as

$$\dot{V}(x,t)=-\tilde{x}^T K_p\tilde{x}+\tilde{p}^T[\mathbf{\Gamma}\dot{\tilde{p}}+H^T\tilde{x}] \tag{14}$$

From the above equation, it is clear that $\dot{V}(x,t)$ is negative definite if, $[\mathbf{\Gamma}\dot{\tilde{p}} + H^T\tilde{x}] = 0$ which is the adaptation law and given as

$$\dot{\hat{p}} = -\mathbf{\Gamma}^{-1}H^T\tilde{x} \tag{15}$$

Note that $\dot{\hat{p}} = \dot{\tilde{p}}$ because the nominal parameters $(\dot{p} = 0)$ are always constant. Therefore, the control law, Equation (10), and the adaption law, Equation (15), are globally asymptotically stable such that

$$\dot{V}(x,t) = -\tilde{x}^T K_p \tilde{x} \le 0 \tag{16}$$

Implementation using Dynamic Models

Uncertainty in some of the model parameters has relatively more significance on the performance of the controller than the other minor parameters. In order to ensure robustness, the parameters to be adapted have to be selected wisely. In this study, sprung mass and tire stiffness parameters were selected, $p = \left[\dfrac{1}{M_s}, K_t\right]^T$. The vertical load variation was more significant on rough roads and tire stiffness varied due to road undulations.

The desired values, displacement, and velocities of the sprung and unsprung masses were calculated from Equation (4). For calculation of control forces, Equation (10), the estimated parameters $\hat{\mathbf{A}}, \hat{\mathbf{B}}$ and $\hat{C}$ have to be calculated by solving Equation (12) for *H* and substituting it into Equation (15) in order to solve for $\hat{p}$.

Active Control of a Single-Damper Suspension

For determination of *H*, dynamic equations of the quarter-car model for a single-damper suspension, Equation (1), were used.

$$\tilde{\mathbf{A}} = 0$$

$$\tilde{\mathbf{B}} = \begin{bmatrix} 0 & 0 & 0 & 0 \\ K_s\tilde{p}_1 & C_s\tilde{p}_1 & -K_s\tilde{p}_1 & -C_s\tilde{p}_1 \\ 0 & 0 & 0 & 0 \\ 0 & 0 & \dfrac{\tilde{p}_2}{M_{us}} & 0 \end{bmatrix} \tag{17}$$

$$\tilde{C} = \begin{bmatrix} 0 & 0 & 0 & -\dfrac{\tilde{p}_2}{M_{us}}X_r \end{bmatrix}^T$$

where, $\tilde{p}_1 = \left[\dfrac{1}{\hat{M}_s} - \dfrac{1}{M_s}\right]$ and. $\tilde{p}_2 = \hat{K}_t - K_t$ Substituting in Equation (12) and solving for *H* yields

$$H = \begin{bmatrix} 0 & 0 \\ K_s(X_1^d - X_3^d) + C_s(X_2^d - X_4^d) & 0 \\ 0 & 0 \\ 0 & \dfrac{X_3^d - X_r}{M_{us}} \end{bmatrix} \tag{18}$$

Substituting Equation (18) into Equation (15) to solve for $\hat{p}$ by integration and substituting in Equation (10) yields

$$\begin{aligned} F_1 &= \dot{X}_2^d + K_s\hat{p}_1(X_1^d - X_3^d) + C_s\hat{p}_1(X_2^d - X_4^d) - K_{p2}(X_2 - X_2^d) \\ F_2 &= \dot{X}_4^d + \frac{K_s(X_3^d - X_1^d) - C_s(X_2^d - X_4^d) + \hat{p}_2(X_3^d - X_r)}{M_{us}} - K_{p4}(X_4 - X_4^d) \end{aligned} \tag{19}$$

where $F = [0\ F_1\ 0\ F_2]^{\mathrm{T}}$.

F_1 and F_2 are the control force outputs from the control algorithm which are applied to the fully active suspension actuator, as shown in Figure 1. From the above equations, the control algorithm uses only the error in velocities of the sprung and unsprung masses. Thus, for physical experimentation only, a velocity sensor for each mass is needed.

Semi-Active Control of a Double-Damper Suspension

Solving for *H* again for a double-damper case,

$$\tilde{\mathbf{A}} = 0$$

$$\tilde{\mathbf{B}} = \begin{bmatrix} 0 & 0 & 0 & 0 \\ K_1\tilde{p}_1 & C_1\tilde{p}_1 & 0 & 0 \\ 0 & 0 & 0 & 0 \\ 0 & 0 & \dfrac{\tilde{p}_2}{M_{us}} & 0 \end{bmatrix} \tag{20}$$

$$\tilde{C} = \begin{bmatrix} 0 \\ -(C_1\dot{X}_m + K_1X_m)\hat{p}_1 \\ 0 \\ -\dfrac{\tilde{p}_2}{M_{us}}X_r \end{bmatrix}$$

Substituting in Equation (12) and following the procedure used for a single-damper case yields

$$H = \begin{bmatrix} 0 & 0 \\ K_1(X_1^d - X_m) + C_1(X_2^d - \dot{X}_m) & 0 \\ 0 & 0 \\ 0 & \frac{X_3^d - X_r}{M_{us}} \end{bmatrix} \quad (21)$$

Solving for F_1 and F_2

$$F_1 = \dot{X}_2^d + (K_1X_1^d + C_1X_2^d - C_1\dot{X}_m - K_1X_m)\hat{p}_1 - K_{p2}(X_2 - X_2^d) \quad (22)$$

$$F_2 = \dot{X}_4^d + \frac{(K_2 + \hat{p}_2)X_3^d + C_2X_4^d - (C_2\dot{X}_m + K_2X_m + \hat{p}_2X_r)}{M_{us}} - K_{p4}(X_4 - X_4^d)$$

Being a semi-active suspension, these control forces have to satisfy two criteria; the minimum F_{min} and maximum forces F_{max} generated by the damper, and a no energy input (i.e., a force in the direction of motion of mass is not applied, and the damper can only oppose the motion of the mass).

The control forces are constrained using simple *if* logic, in -between F_{min} and F_{max}, based on physical limitations of the damper

$$F_{i,\min} \le F_i \le F_{i,\max} \quad , i = 1, 2 \quad (23)$$

$$F_{1,\min} = C_{1,\min}(X_2 - \dot{X}_m)\hat{p}_1, F_{1,\max} = C_{1,\max}(X_2 - \dot{X}_m)\hat{p}_1,$$

$$F_{2,\min} = \frac{C_{2,\min}(\dot{X}_m - X_4)}{M_{us}}, F_{2,\max} = \frac{C_{2,\max}(\dot{X}_m - X_4)}{M_{us}}$$

where $C_{1,max}$ and $C_{1,min}$ are the maximum and minimum allowable damping by the upper damper. $C_{2,max}$ and $C_{2,min}$ are maximum and minimum allowable damping by the lower damper. Note that the values of C_1 and C_2 in Equation (3) have to be non-zero; if not, the open-loop system will have poles at the limit of stability and the discretized state space model can become unstable. Therefore, non-zero positive nominal values were considered. At any time, total maximum and minimum damping available are $C_{i,max}+C_i$ and $C_{i,min}+C_i$, respectively.

After satisfying constraints in Equation (23), for constraining the forces such that no energy is introduced into damper, the following clipping method was used, such that if the control force F_1 or F_2 and relative deflection velocity $(X_2 - \dot{X}_m)$ or $(X_4 - \dot{X}_m)$ are of the same sign, then the control applies a minimum damping force.

$$F_1 = \begin{cases} F_1 & \text{if } (X_2 - \dot{X}_m)F_1 \le 0 \\ F_{1,\min} & \text{if } (X_2 - \dot{X}_m)F_1 > 0 \end{cases}$$

$$F_2 = \begin{cases} F_2 & \text{if } (X_4 - \dot{X}_m)F_2 \le 0 \\ F_{2,\min} & \text{if } (X_4 - \dot{X}_m)F_2 > 0 \end{cases} \quad (24)$$

Control Policy of Skyhook-Groundhook

A 2-state on/off control strategy that switches between high and low damping values was used in order to achieve less sprung mass displacement without deteriorating road-holding properties. The control law was based on sprung and unsprung mass velocities and suspension deflection velocity. The damping for both dampers was equal to zero when the sprung or usprung mass velocities and deflection velocity with respect to corresponding masses are in opposite directions [2].

$$C_{sky} = \begin{cases} C_{sky} & \text{if } (X_2 - X_4)X_2 \ge 0 \\ 0 & \text{if } (X_2 - X_4)X_2 < 0 \end{cases}$$

$$C_G = \begin{cases} C_G & \text{if } (X_4 - X_2)X_4 \ge 0 \\ 0 & \text{if } (X_4 - X_2)X_4 < 0 \end{cases} \quad (25)$$

Simulation

The values used for the simulation were M_s = 290 Kg, M_{us} = 59 Kg, K_s = 16812 N/m, K_t = 190 KN/m, $K_1 = K_2 = 2K_s$, C_s = 1000 N/m/s, C_1 = 100 N/m/s, C_2 = 50 N/m/s, $C_{1,max}$ = 5000 N/m/s, $C_{2,max}$ = 1500 N/m/s, $C_{1,min}$, $C_{2,min}$ = 0 N/m/s, C_{sky} = 1000 N/m/s, C_G = 750 N/m/s. The adaptive gain matrix was $\boldsymbol{\Gamma} = diag\begin{bmatrix}800 & 10^{-11}\end{bmatrix}^T$ and the propositional gain matrix was $K_p = diag\begin{bmatrix}0 & 80 & 0 & 80\end{bmatrix}^T$. The initial values of all state variables $\begin{bmatrix}X_s & \dot{X}_s & X_w & \dot{X}_w\end{bmatrix}^T$ were assumed to zero. The initial adaptable parameters were assumed to off by 10% and 5% of actual values: $\hat{M}_s = 1.1M_s$ and $\hat{K}_t = 1.05K_t$.

From the formulations of control algorithm, the computed control forces were applied to the equations of motion of single- [(Equation (1)] and double-damper [(Equation (3)] quarter-car models. The input road profile used in this study is as shown in Figure 3.

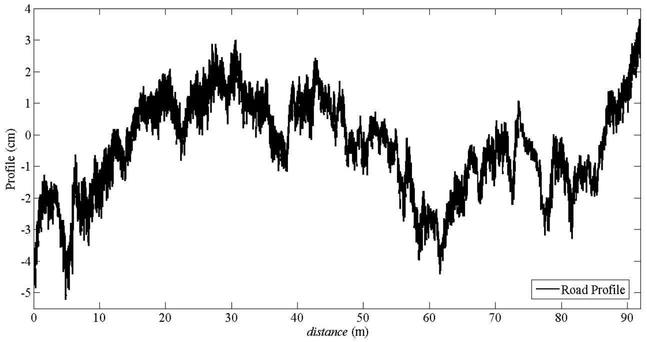

Figure 3. Road Profile Used in the Study

From Figure 3, the profile can be seen as being very rough with a maximum road displacement of -5.22 cm. For characterizing ride comfort, a simple criterion of reduced RMS acceleration of sprung mass was considered. Road-holding properties were characterized by tire deflection. $(X_3 - X_r)$ Suspension bottoming was characterized by suspension deflection,, $(X_1 - X_3)$ in the case of the double-damper model, and $(X_1 - X_m)$ and $(X_m - X_3)$ for the upper and lower dampers, respectively.

The simulations of no-control quarter-car model, active-controlled single-damper and semi-active-controlled double -damper models were performed, with respective RMS acceleration of sprung at different speeds using the input road profile in Figure 3 the results are computed and summarized in Table 1. Tire deflection and suspension deflection values were also calculated and are summarized in Table 2 for all three cases; no abnormal behavior of controlled suspensions from normal suspension was observed.

Table 1. RMS Acceleration of Sprung Mass (m^2/s) at Different Velocities (Kph)

Velocity (Kph)	**15**	**30**	**45**	**60**	**75**	**90**
No Control	0.887	1.003	1.179	1.481	1.666	1.807
Full Active	0.526	0.568	0.666	0.807	0.936	1.028
Semi Active	0.528	0.574	0.671	0.811	0.940	1.036

From Table 1, it can be seen that the RMS acceleration of active and semi-active suspensions are low compared to cases of no control. As noted earlier, and due to the use of double-damper-based suspension control, control of damping values of two dampers independently gives the advantage of increasing the performance of the controller, which is clearly evident at all the speeds. The RMS values of the fully active case were almost equal to the semi-active case at all speeds. Table 2 shows the maximum suspension deflection values for three cases. Although the values are 1 cm above the no-control case, they are within an acceptable range with a maximum deflection of 6.31 cm. For the double-damper case, the deflection of the upper and lower dampers was almost equal, thus guaranteeing the structural stability of the double-damper model. Table 3 shows the maximum tire deflection; note that all three cases had roughly the same values.

Table 3. Maximum Tire Deflection (cm) at Different Velocities (Kph)

Velocity (Kph)	**15**	**30**	**45**	**60**	**75**	**90**
No Control	4.12	4.34	4.57	4.69	4.69	4.71
Full Active	4.14	4.23	4.52	4.65	4.69	4.72
Semi Active	4.21	4.34	4.53	4.66	4.69	4.71

Figures 4 and 5 show the acceleration of the sprung mass at speeds of 30 Kph and 90 Kph. The Most important outcome was emulation of the semi-active suspension as the active suspension for both high and low speeds. Figure 6 shows the adaption of model parameters; the adaption of tire stiffness was fast and stayed around the nominal value, but the sprung mass adaption still required some time. This can be attributed to the fact that good tuning of adaptive gains is required for better adaption.

Figure 7 shows that the damping coefficients are within the saturation limits ($C_{1,max}$ = 5000 and $C_{2,max}$ = 1500) as imposed on each damper in Equation (23). Figure 8 shows the dissipative constraint on the semi-active dampers, based on damper velocity, as defined in Equation (24). One of the important observations is that the lower damper takes more force than the upper damper, which states that the unsprung mass experiences more velocity than sprung mass; thus, more vibration is taken by the lower damper. The saturation limit on the upper damper was greater than the lower damper, which was also evident from the slope of $F_{1,max}$ being greater than $F_{2,max}$.

Table 2. Maximum Suspension Deflection (cm) at Different Velocities (Kph)

Velocity (Kph)		**15**	**30**	**45**	**60**	**75**	**90**
No Control		5.6	5.55	5.29	5.01	4.95	4.91
Full Active		6.31	6.21	5.95	5.63	5.34	5.36
Semi Active	Damper1	3.13	3.09	2.94	2.78	2.64	2.62
	Damper2	3.14	3.11	2.96	2.8	2.65	2.63
	Total	6.2	6.2	5.9	5.58	5.29	5.24

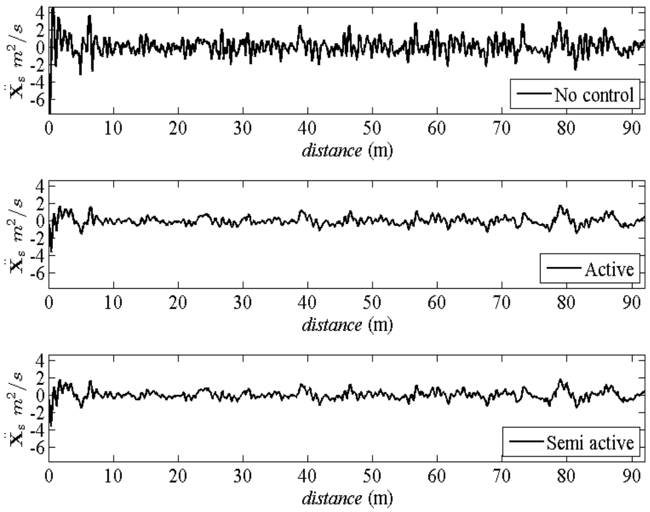

Figure 4. Acceleration of Sprung Mass at 30 Kph with No Control, Active Control, and Semi-Active Control

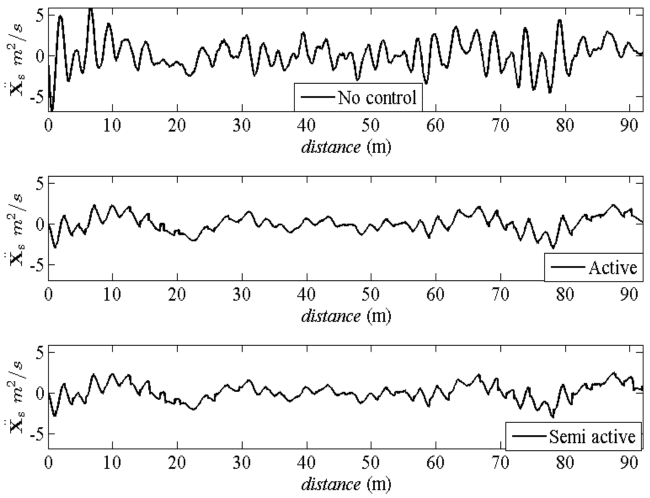

Figure 5. Acceleration of Sprung Mass at 90 Kph with No Control, Active Control, and Semi-Active Control

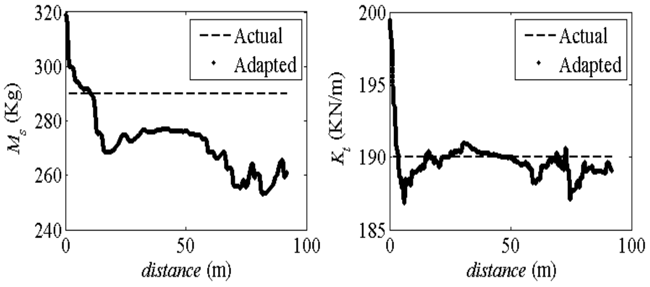

Figure 6. Adoption of Sprung Mass and Tire Stiffness at 90 Kph for Semi-Active Control

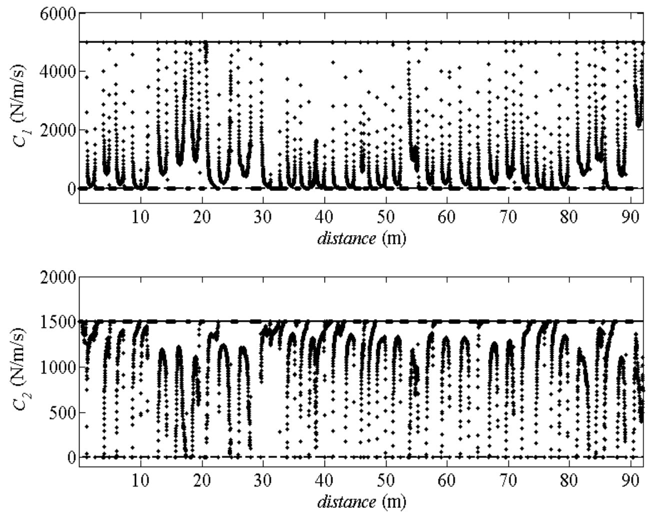

Figure 7. Damping Coefficients of Both Dampers within Maximum and Minimum Limits of the Damper at 90 Kph

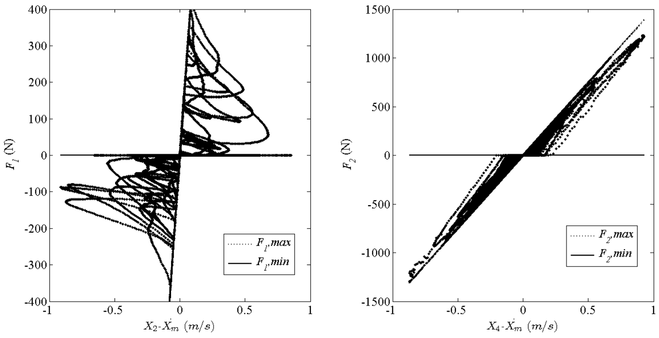

Figure 8. Dissipative Domain of Semi-Active Dampers

Conclusion

Application of double-damper-based suspension for ride control was studied. A Lyapunov-based adaptive controller was developed. The designed controller was used for the active control of single-damper and double-damper suspensions with random road inputs. The simulation results showed that the semi-active-based double-damper suspension can be a substitute for active suspensions. No abnormalities in suspension deflection and tire deflection from normal suspension were observed. Semi-active suspension results were shown to be constrained in saturation and energy limitation of the damper. This approach of ride control based on double-damper was shown to significantly improve ride performance of the vehicle at reduced power consumption, cost, and complexity, with more reliability.

References

[1] Liu, Y., Matsuhisa, H., & Utsuno, H. (2008). Semi-active vibration isolation system with variable stiffness and damping control. *Journal of Sound and Vibration*, *313*, 16–28.

[2] Slotine, E., & Weiping Li. (1987). On the adaptive control of robot manipulators. *The International Journal of Robotics Research*, *6*(3).

[3] Taheri, S. (1987). *An investigation of design of slip control braking systems integrated with four wheel steering*. Unpublished doctoral dissertation, Clemson University, Clemson, S.C.

[4] Tamaddoni, S. H., & Taheri, S. (2008). A New Control Algorithm for Vehicle Stability Control. *Proceedings of the 10th International Conference on Advanced Vehicle and Tire Technologies (AVTT), IDETC/CIE 2008-49304, August 3–6.* New York City, New York.

[5] Ding, N., & Taheri, S. (2010). An adaptive integrated algorithm for active front steering and direct yaw moment control based on direct Lyapunov method. *Vehicle System Dynamics*, *48*(10), 1193–1213.

[6] Karnopp, D. (1974). Vibration Control Using Semi-Active Force Generators. *Journal of Engineering for Industry*, *96*.

[7] Savaresi, M., Poussot-Vassal, C., Spelta, C., Sename, O., & Dugard, L. (2010). *Semi-Active suspension control design for vehicles*. (1st ed.). Amsterdam: Butterworth-Heinemann/Elsevier.

[8] Karnopp, D. (1992). Power requirements for vehicle suspension systems. *Vehicle System Dynamics: International Journal of Vehicle Mechanics and Mobility*, *21*.

Biographies

YASWANTH SIRAMDASU is graduated with a master degree from the University of Alabama in Huntsville in 2012. He is currently a Ph.D. student at Virginia Tech working in Center for Tire Research (CenTiRe). His research interests are vehicle dynamics and chassis control systems. Yaswanth Siramdasu may be reached at yaswanth@vt.edu.

SAIED TAHERI is an associate professor of mechanical engineering and the director of the Center for Tire Research (CenTiRe) at Virginia Tech. His research interests are tire and vehicle dynamics and control. Saied Taheri may be reached at staheri@vt.edu.

Nomenclature

Symbol	**Description**
M_s	Sprung mass
M_{us}	Unsprung mass
K_s	Stiffness of suspension spring
K_t	Stiffness of tire
K_1	Stiffness of upper Spring
K_2	Stiffness of lower Spring
C_s	Damping coefficient of damper
C_1	Damping coefficient of upper damper
C_2	Damping coefficient of lower damper
C_G	Damping coefficient of groundhook damper
C_{sky}	Damping coefficient of skyhook damper
$C_{1,\min}, C_{1,\max}$	Minimum and maximum damping coefficients of upper damper
$C_{2,\min}, C_{2,\max}$	Minimum and maximum damping coefficients of lower damper
X_s	Position of sprung mass
X_w	Position of unsprung mass
X_m	Position of point in between two dampers
X_r	Height of road profile
F_1	Force acting on sprung mass
F_2	Force acting on unsprung mass
$F_{1,\min}, F_{1,\max}$	Minimum and maximum force applicable by semi-active upper damper
$F_{2,\min}, F_{2,\max}$	Minimum and maximum force applicable by semi-active lower damper

MICROCONTROLLER-BASED EMBEDDED SYSTEM INTEGRATED INTO AN ULTRASONIC POSITION ESTIMATION SYSTEM

Sanjeevi Chitikeshi, Murray State University; Dustin Patton, Murray State University; Ajay Mahajan, The University of Akron

Abstract

In this paper, the authors present a microcontroller-based embedded system for accurately estimating the position of an ultrasonic transmitter by using the difference in the time of arrival (DTOA) of the signals at multiple receivers fixed in an inertial frame of reference. The ultrasonic transducers being used for this application had a narrow band with a peak resonant frequency around 40 kHz. The focus of this study was to use smart instrumentation to digitize the signals rather than separate A/D chips which then feed the digital data into a microcontroller for triangulating the transmitter position. To show proof of concept in one dimension (1D), two ultrasonic receivers were used to provide position estimations of single transmitters in 1D using the DTOA approach. It will be shown that this method is more robust, accurate, and ultimately more effective than the previously used method of using A/D converters and a microcontroller. This work has applications in robotics, virtual reality, real-time neurosurgery, and motion capture studies in ergonomics.

Introduction

Position estimation methods and equipment in 3 dimensions (3D) are used in a variety of applications such as the estimation of the position of space vehicles using star maps [1], GPS-based position estimation of cars [2], and the estimation of robotic end effectors using image analysis [3]. Typically, indoor systems have relied on image analysis techniques to triangulate the position of a point of interest using stereoscopic images. There have been other systems used in biomedical fields that have used eddy currents [4], infrared [5], and ultrasonic signals [6-10], but their applications have been limited.

Presented here are aspects of the development of a 3D position estimation system that uses ultrasonics. In particular, this paper focuses on the innovative use of embedded system technology to accurately and robustly determine the difference in the time of arrival of the ultrasonic signal at the various receivers fixed in an inertial frame of reference.

Figueroa and Mahajan [11] developed an ultrasonic 3D position estimation system that used the time of flights (TOFs) from a single transmitter to numerous receivers in order to triangulate the position of the transmitter. They used an analytical approach based on the Lagrange Multiplier Method for the constrained minimization problem to extract the optimal receiver configuration from the linear formulation. The system was designed for the robotics industry (i.e., to track the end-effector of a fixed robot or guide and navigate an autonomous mobile robot in an indoor environment). This is an important application for position estimation systems [12-15], and remains an active area of research. There are numerous 3D position estimation systems that use wave energy techniques.

Wave energy-based 3D position systems triangulate the position of the wave source using the actual time of flights (TOFs) to the various receivers. Low cost ultrasonic 3D position estimation systems have been developed that use actual TOFs from the transmitter to the receivers [16], [17]. The main disadvantage of using an actual time-of-flight method is that the transmitter and receivers always need to be synchronized, and it also limits the total work area, due to the cables from the transmitter. In contrast, the Difference in Time of Arrival (DTOA) method doesn't need synchronization between transmitter and receiver signals. Chitikeshi et al. [18], [19] used the DTOA method with neural networks and Kalman filter algorithms with manual data collection. Applying digital signal processing and Kalman filter algorithms for various control problems has been addressed in numerous papers and textbooks [20-22].

The presence of air turbulence and convection currents are the main components that limit the precise range measurements and have been studied using the stochastic method [23]. Figueroa and Mahajan [24] developed a system to address these aforementioned problems by using the speed of sound as an unknown variable in system formulation; hence, it was updated at each ranging operation. The problem was described by a set of linear equations presented in matrix form, and simply involved the solution of five (or more, depending on the number of receivers being used) simultaneous linear equations, thereby allowing for high update rates. There are two problems with this type of formulation. The first one deals with synchronizing the wave bursts from the transmitter so as to measure the TOFs to the receivers. This measured TOF incorporates delays from the electronic circuitry used to condition the signal at the receiver, delay inherent to the signal detection method to acknowledge reception of the pulses at the receivers, and the acousto-electromechanical delay associated with the transducers. All of these can be grouped together and called the system time delay that has to be subtracted from the measured TOFs to obtain the actual TOFs. Identification of this time delay term is the second problem.

Mahajan and Walworth [25] developed a formulation that takes the differences between the time of arrivals (TOAs) and the various receivers, which circumvents both of the problems mentioned above. First, one need not know when the pulse left the transmitter, since only the differences in the times of the received signals are recorded. Second, since the time delay term is the same for all receivers (this is an assumption based on using the same components for all of the receiver circuits), it automatically cancels out once the difference is taken for any two TOFs. Using the difference between the TOAs addresses both of the problems, but is sensitive to the location of the receivers and, hence, creates a need for a detailed analysis of the receiver configuration geometry.

System Formulation and Problem Definition

The 1D system consists of a single transmitter moving in a straight line, and two receivers, as shown in Figure 1. The DTOA between the two receivers is used to estimate the 1D distance of the transmitter to the nearest receiver. ‘T’ is the transmitter position that changes with time, and has coordinates (d, 0). Here, ‘d’ is the distance of the transmitter to the first receiver, R1; ‘a’ is the angle formed by the line that joins the two receivers with the horizontal; ‘z’ is the distance between the two receivers; and ‘DT_{12}’ is the difference in the time of flight between the transmitter and the two receivers.

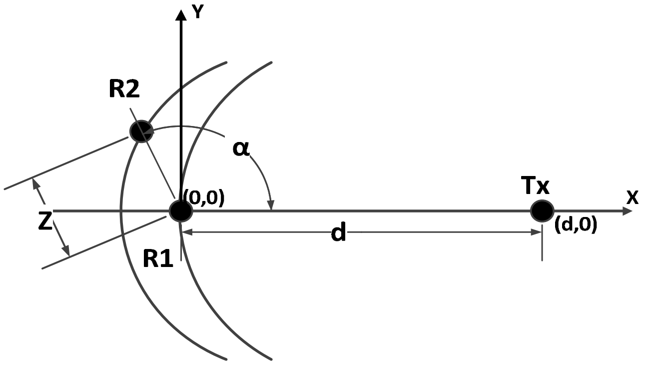

Figure 1. 1D System

The formulation for this 1D set-up is:

$$d = \frac{z^2 - c^2 \Delta T_{12}^2}{2(c\Delta T_{12} + z\cos\alpha)} \tag{1}$$

The 2D system is composed of a transmitter and five receivers in a single plane, as shown in Figure 2.

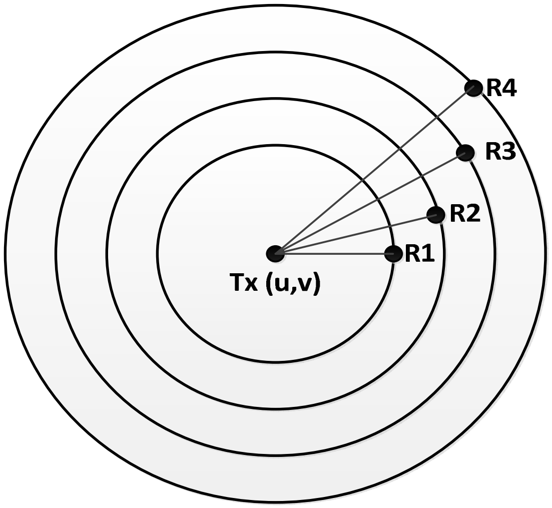

Figure 2. 2D System Setup

The transmitter is located at an unknown position (u, v). The receivers are randomly located at known positions: R1 (x_1, y_1), R2 (x_2, y_2), R3 (x_3, y_3), R4 (x_4, y_4), and R5 (x_5, y_5). The time of flight between the transmitter and any receiver is unknown, but the difference between times when the receivers sense the signals can be measured. In other words, if the transmitters sends a signal at time T=0, the receivers will sense the signals at the unknown times T_1, T_2, T_3, T_4 and T_5. The difference between the time of arrivals (DTOA) are then determined to be: $DT_{12} = T_2 - T_1$, $DT_{13} = T_3 - T_1$, $DT_{14} = T_4 - T_1$, and $DT_{15} = T_5 - T_1$. The formulation to estimate (u,v) is given in the matrix of Equation (2).

$$\begin{bmatrix} 2(x_1 - x_2) & 2(y_1 - y_2) & -2\Delta T_{12} & -2\Delta T_{12}^{\,2} \\ 2(x_1 - x_3) & 2(y_1 - y_3) & -2\Delta T_{13} & -2\Delta T_{13}^{\,2} \\ 2(x_1 - x_4) & 2(y_1 - y_4) & -2\Delta T_{14} & -2\Delta T_{14}^{\,2} \\ 2(x_1 - x_5) & 2(y_1 - y_5) & -2\Delta T_{15} & -2\Delta T_{15}^{\,2} \end{bmatrix} * \begin{bmatrix} \mu \\ \nu \\ cd \\ c^2 \end{bmatrix} = \begin{bmatrix} x_1^2 + y_1^2 - x_2^2 - y_2^2 \\ x_1^2 + y_1^2 - x_3^2 - y_3^2 \\ x_1^2 + y_1^2 - x_4^2 - y_4^2 \\ x_1^2 + y_1^2 - x_5^2 - y_5^2 \end{bmatrix} \tag{2}$$

The above formulation treats the speed of sound as a variable and estimates it along with the position of the transmitter. The above analysis can be extended to the 3D case that requires a minimum of six receivers. The aim is to estimate (u,v,w); refer to Equation (3),

$$A * \mu = B \tag{3}$$

where,

$$A = \begin{bmatrix} 2(x_1 - x_2) & 2(y_1 - y_2) & 2(z_1 - z_2) & -2\Delta T_{12} & -2\Delta T_{12}{}^2 \\ 2(x_1 - x_3) & 2(y_1 - y_3) & 2(z_1 - z_3) & -2\Delta T_{13} & -2\Delta T_{13}{}^2 \\ 2(x_1 - x_4) & 2(y_1 - y_4) & 2(z_1 - z_4) & -2\Delta T_{14} & -2\Delta T_{14}{}^2 \\ 2(x_1 - x_5) & 2(y_1 - y_5) & 2(z_1 - z_5) & -2\Delta T_{15} & -2\Delta T_{15}{}^2 \end{bmatrix}$$

$$\mu = \begin{bmatrix} u \\ v \\ w \\ cd \\ c^2 \end{bmatrix} \quad \text{and } B = \begin{bmatrix} x_1{}^2 + y_1{}^2 + z_1{}^2 - x_2{}^2 - y_2{}^2 - z_2{}^2 \\ x_1{}^2 + y_1{}^2 + z_1{}^2 - x_3{}^2 - y_3{}^2 - z_3{}^2 \\ x_1{}^2 + y_1{}^2 + z_1{}^2 - x_4{}^2 - y_4{}^2 - z_4{}^2 \\ x_1{}^2 + y_1{}^2 + z_1{}^2 - x_5{}^2 - y_5{}^2 - z_5{}^2 \end{bmatrix}$$

In Equation (3), matrices A and B are known and **u** is to be determined.

Figure 3(a) shows the system setup with 6 receivers but the system presented in this paper was composed of an ultrasonic transmitter and two receivers placed on an optic table to formulate a 1D system for proof of concept. The transmitter emits signals at a frequency of 40 kHz and 10 cycles per burst. The received signals were amplified and processed using a microcontroller-based embedded system. The DT's mentioned in the matrix formulation were the differences in time of arrivals at the various receivers. The setup, the oscilloscope window showing the signals and the DTs, are shown in Figures 3(a) and 3(b). The focus of this study was the mechanism for obtaining accurate values for the DTs.

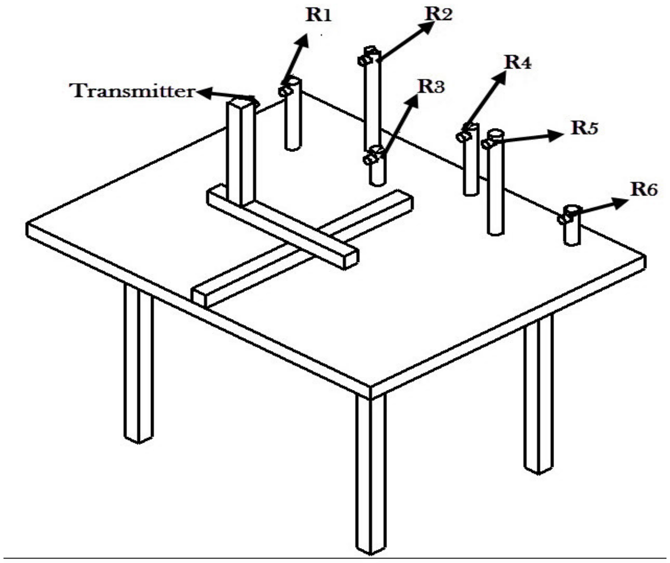

Figure 3(a). Multiple Receivers Setup

Several researchers have examined the parameters that affect accuracy in ultrasonic systems. They have discussed the effects of air turbulence, humidity and temperature dependence, misalignment between transducers, and time delay of an electromechanical nature. Due to these effects, ultrasonic ranging systems (URS) have been traditionally characterized by low accuracy, low reliability, and limited range. Ray and Mahajan [26] proposed a genetic algorithm-based approach for finding optimal receiver locations in 3D positioning systems to address some of these accuracy issues. A genetic algorithm is a very useful technique for finding local and global minima solutions for nonlinear systems in various engineering and business applications [27].

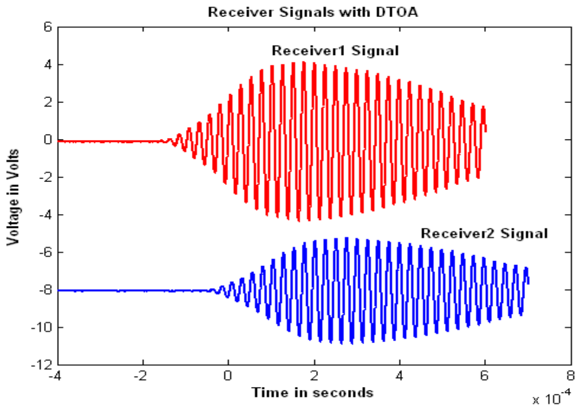

Figure 3(b). Receiver Signals with DTOA

Figures 4 and 5 [28] show affected receiver signals due to misalignment and non-equidistance problems. The overall signal amplitude produced by a transmitter-receiver pair decreases as the receiver moves away from the transmitter normal, keeping the transmitter-receiver distance constant, as shown by positions R_1 and R_2 in Figure 4. In addition, the overall signal amplitude decreases even further when the receivers do not face the transmitter (i.e., the receiver normal makes an angle with the line joining the transmitter and receiver). This is illustrated by considering the same positions R_1 and R_2, but when each is misaligned to R_3 and R_4, respectively.

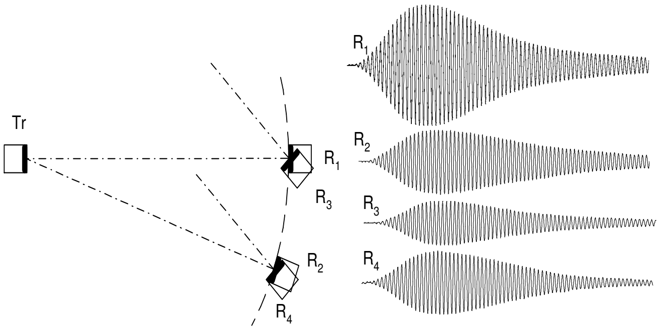

Figure 4. Signals from Misaligned Receivers

The overall signal amplitude produced by a transmitter-receiver pair also decreases as the receiver moves away from the transmitter, as shown in Figure 5. This is mainly due to the fact that the same energy from the transmitter is more spatially distributed as the receiver moves further away. Furthermore, the sound energy is also absorbed in the medium. The focus is to accurately find the time difference between the two receiver signals, say R1 and R2, shown in Figure 5. This is a different problem than finding the time between the transmitter and receiver signals, as is used in traditional triangulation schemes.

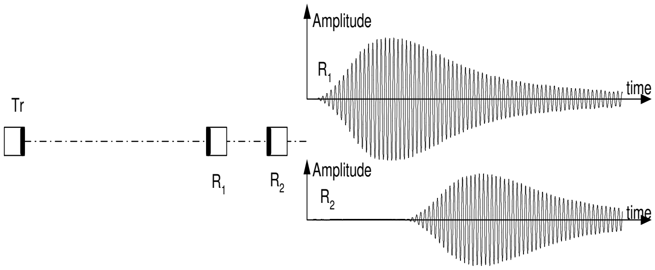

Figure 5. Signals from Non-Equidistant Receivers

Description of Hardware

Ultrasonic Transmitter

In this project, ultrasonic transducers with operating frequencies of 40 kHz and a bandwidth of 1 kHz were used. The beam angle of the transmitter was 60 degrees. The driving circuit generated a train of short-duration pulses at a specific repetition frequency. These are then converted into corresponding pulses of ultrasonic waves by a piezoelectric crystal acting as the transmitting transducer. The type, amplitude, and number of pulses of the transmitting signal affected the receiver response. The type of the signal affects the response mainly because of the energy content per cycle in the signal. The square wave has maximum energy followed by the sinusoidal wave. The higher amplitude and number of cycles mean more energy and, hence, a stronger response from the receiver. Number of cycles plays an important role, since too few cycles means that the receiver cannot be excited enough, and too many cycles means that the response will be saturated and it takes a longer time for the resonance to die out, hence the update rate decreases.

It was experimentally determined that 10 Vp-p and 10 cycles of square wave input excitation produced the right resonance amplitude in the work area of 100 cm. It was also observed that for 10 cycles of a 40 kHz square wave transmitting signal, the receiver response took 3 ms to completely die out; hence, at least 3 ms delay time is required between two consecutive burst of cycles, which limits the update rate. A digital generic 555 timer can be used to generate the 40 kHz burst cycles and a flag signal. The only disadvantage with this method is that in order to change the signal frequency or delay time, replacement of passive hardware components in the system (i.e., resistors and capacitors) is required. In contrast, software control is always better than hardware control, hence a microcontroller was used so that everything could be controlled in the firmware. The digital output from the microcontroller was 0V to 5V, but this voltage was not enough to drive the transmitter and it required a minimum of 10Vp-p for optimal results, as noted earlier. To convert the microcontroller output into these voltages, two commonly available circuits were tested. The overall hardware block diagram is shown in Figure 6.

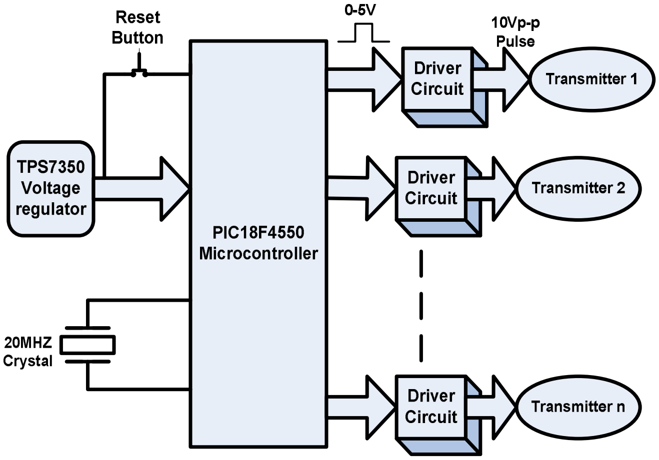

Figure 6. Block Diagram of the Transmitter Circuit

Receiver Circuit

This section describes the signal amplification circuits for ultrasonic receivers, the digital circuits for detecting the arrival of the signal, and the manner by which the microcontroller calculates the DTOA. The receiver circuit detects when the ultrasonic waveforms reach a particular transducer, which consists of a high-gain amplifier circuit and a threshold comparator. The performance of the receiver is measured by its sensitivity, which is the smallest signal that can be detected by the receiver. A signal is said to be detected if the amplified signal is greater than the largest voltage spike caused by noise at the amplifier's output. The noise voltage at a particular node is normally described by its root -mean-square value, Vn, which can be calculated as follows:

$$V_n = \sqrt{\int_0^\infty V_N^2(f) \bullet df} \tag{4}$$

where $V^2_N(f)$ is the noise power spectral density at the node. Typically, the largest spike caused by noise rarely exceeds six times V_n. Thus, if the amplified signal is greater than $6 \bullet V_n$, then the signal can be detected. Consequently, the receiver sensitivity at a frequency *f* can be defined as:

$$S(f) = \frac{6 \bullet V_n}{G(f)} \tag{5}$$

where *G(f)* is the gain of the amplifier at frequency *f*. In the following section, receiver circuits and techniques for achieving high sensitivities are described.

Receiver Amplifier

The receiver amplifier circuit shown in Figure 7 is comprised of two amplification stages. The first stage (consisting of OPA1, OPA2, R1, R2, and C1) provides a high-differential gain at signal frequencies around 40 kHz. The second stage (consisting of OPA3, R3, R4, C2, and C3) converts the differential signals from the first stage into a single-ended signal and amplifies them with a moderate gain. The final circuit output can swing from 0 to V_{DD}, and is centered at $V_{DD}/2$, which is the signal ground level generated by OPA4, R5, and C4.

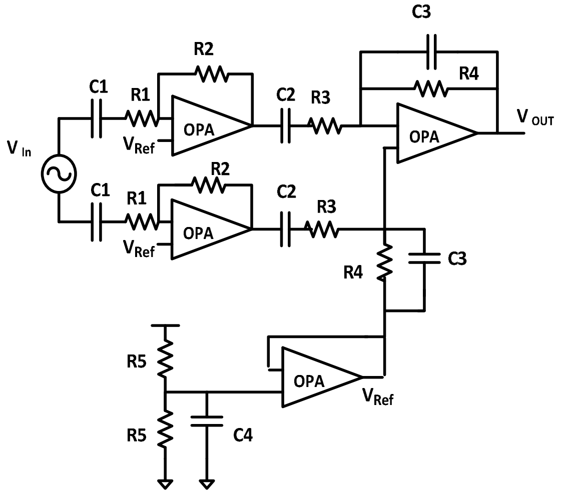

Figure 7. Schematic of the Receiver Amplifier

Signal Arrival Detection Circuit

Once the receiver signal is amplified, as discussed in the previous section, the signal is fed into the digital circuit to detect the starting point of the signal; hence, the arrival time DTOA values are calculated. The overall block diagram is shown in Figure 8.

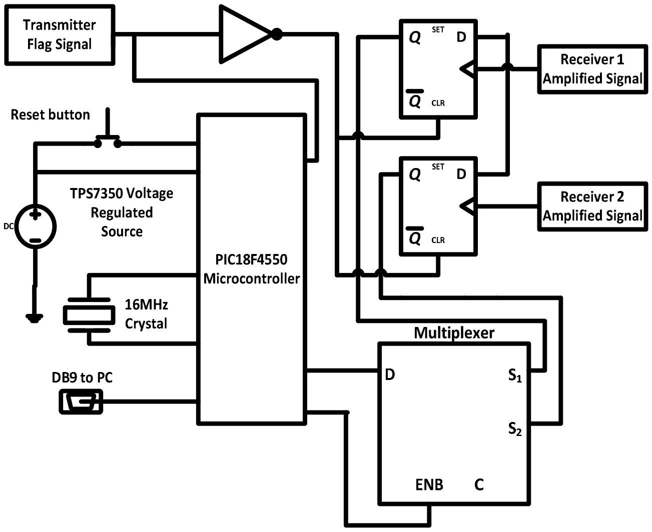

Figure 8. Block Diagram of the DTOA Calculation Circuit

To detect arriving receiver signals, a high-speed A/D converter can be used to capture the data then compared them with a reference signal. The required A/D has to have a very high sampling frequency of at least 80 kHz, according to the Nyquist sampling theorem, but at least 10 times higher than is required in practical applications (i.e., 400 kHz for 40 kHz receiver signal). The other requirement is that the A/D resolution has to be in the sub-millivolt range, which means more digital output bits. The PIC microcontroller has a built-in 10-bit, 3 kHz A/D converter, which is not suitable for this application; an external high-speed A/D is needed. Instead of using high-speed analog-to-digital converters, a comparator was used to detect the signal. To get amplification and comparator functionality, a basic electronic circuit was used in which an operational amplifier was configured as a comparator circuit. The operational amplifier amplifies the signal and gives the difference between two terminals at the output. At the negative input terminal, a potentiometer was connected by which the reference voltage could be changed. The positive input was connected to the amplified receiver analog signal. When the receiver signal amplitude goes above the reference voltage, the output goes to its saturation state (i.e., the output becomes the same as the power supply voltage of 5V). Conversely, when the analog amplitude goes below the reference voltage, the output goes to 0V. The operation is same as the comparator. However, because of inner circuit differences, a comparator cannot be used as an operational amplifier. In this study, the excitation voltage for the transmitter was between positive 9V and negative 9V, thus the amplified receiver signal was very strong in the work area of about 1 meter. It was also observed that a reference voltage between 2.8 and 3.1 volts gave the signal detection point with an error of 1 to 2 wavelengths.

Measuring the DTOA

The DTOA is the time difference between the arrival times of the same waveform at two receivers. In order to calculate these values in this study, a PIC18F4550 microcontroller was used. This microcontroller has two capture pins, which were configured to detect the rising edge of a signal. This microcontroller has three inner 16-bit timers/counters that are good enough for the 1D case. As shown in the block diagram of Figure (8), one capture pin was connected to the transmitter flag signal and the other one was connected to the comparator output. The signals coming out from the comparator circuit had the following problems.

- The amplified receiver signal had a small duration, 40 kHz signal at the start as soon as the transmitter was triggered. It was then picked up as the actual signal. Hence, the comparator was also giving a high output at the false section of the signal. This was not a comparator circuit problem as the comparator only compares the actual signal with the reference voltage. The problem was that there was a false echo at the beginning of the signal.
- Because of the noise level and fluctuations in the actual analog signal, the comparator output was not stable at the starting portion of the signal. If the starting portion is not stable, then the microcontroller cannot detect the correct rising edge; in other words, the correct arrival point of the signal.

To solve the first problem—to get rid of the false echo at the staring portion of the signal—two methods can be used. The first one is to use an analog switch that momentarily closes and opens when the actual signal has arrived. The main problem with this method is it requires precise control of the closing and opening time durations in the analog circuit, which could increase the noise and may also lead to some other problems since it directly works on the amplified signals from the receivers. The other method is to use digital gates on the comparator signals and get rid of the false echo. This method is easier and was the method selected to solve the problem. The second method was easy to implement and required a minimal addition of hardware and, more importantly, everything was controlled by the software.

First, the duration of the false echo signal was measured for the worst-case scenario (i.e., when the transmitter and receiver are very close to each other). It was observed that it came to about 600 µs and the comparator would have to wait this amount of time before producing the output signal. In this study, a digital AND gate was used, where one input of the gate was connected to the comparator output and the other input was connected to one of the digital output pins of the microcontroller. This digital pin was made a logical 0 until the duration of the echo signal, at which point it was made a logical high. Then, the output of the AND gate was connected to the next stage of the system; hence, the correct signal was obtained. Using a software-controlled microcontroller simplified the required changes in the system; for example, time duration for false echo. Figure 9 shows the receiver signal, the comparator output, and the digital AND gate output.

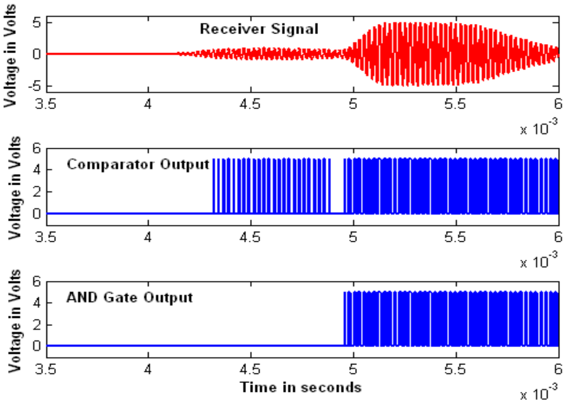

Figure 9. Comparator and Digital AND Gate Output Signals

The only limitation of this method is that the control system clearly has to be able to differentiate between the echo signal and actual receiver signal. If they are overlapping, then a fixed constant wait time value cannot be used for the comparator to wait. It was observed that a minimum distance of 25 cm should always be maintained between the transmitter and the receiver in order to distinguish between these two signals. Hence, the limitation of the system is that the minimum distance it can detect becomes 30 cm in a 1D case.

To solve the second problem, a D flip-flop was used. The comparator output was given to the clock input of the D flip-flop and the D input was connected to 5V. So, when the clock is high, the output is the same as the D input, and when the clock is zero, it holds the previous value of 5V. The D flip-flop must be cleared before it gets the next signal from the receiver. It is cleared by using the inverted form of the flag signal from the transmitter. Figure 10 shows these effects.

One of the hardware limitations of the PIC18F4550 microcontroller is it has only two capture and compare pins, hence a 2-1 multiplexer was used to connect the two D-flip flops and the transmitter flag signal. A 16-bit timer in the microcontroller starts timing with a time-base resolution of 1 us when a rising-edge transmitter flag reaches the first capture pin and is stopped when the rising-edge multiplexer output reaches the second capture pin. The ATOF is simply the timer value. This is the ATOF for the first receiver and transmitter. Once it is done, the multiplexer gets the control signal to connect to the second receiver. This time, the microcontroller measures the ATOF for the second receiver.

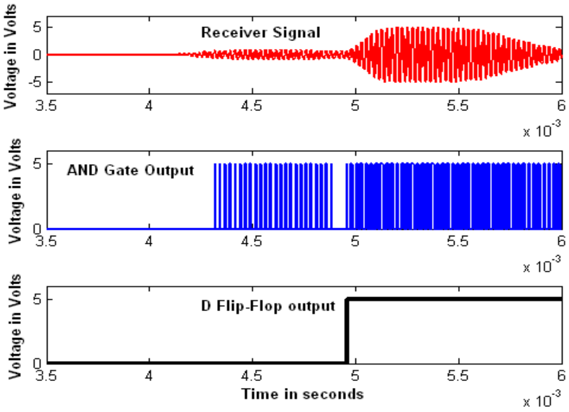

Figure 10. D-Flip-flop Output with a Clear Signal

There are two ways to measure DTOA values using this instrumentation. The first method is to disconnect the transmitter flag signal and connect the two D flip-flops' outputs at the same time to the two capture pins. The second method is to subtract the 2nd receiver's ATOF value from the 1st receiver's ATOF. In this study, the second method was chosen in order to simplify the software complexity. After these measurements were made, these values were sent to the PC through an RS-232 serial port for storage and graphical display purposes. The complete instrumentation gives the instantaneous transmitter position value; hence, it is called intelligent instrumentation.

Results and Discussions

In this study, a single transmitter was tracked in a 1D case using two receivers. The 1D system consisted of a single transmitter moving in a straight line, and one receiver (see Figure 1). The 1D system was set up on a table, as shown in Figure 11. Only the 1D case was considered here; that is, the transmitter was moved on a linear slide in one dimension and 2 receivers were fixed at known positions. Equation (1) shows 2 receivers that provide a single "d" position for a single transmitter. In this experiment, the two receivers were fixed in a straight line so that the angle value in Equation (1) became zero.

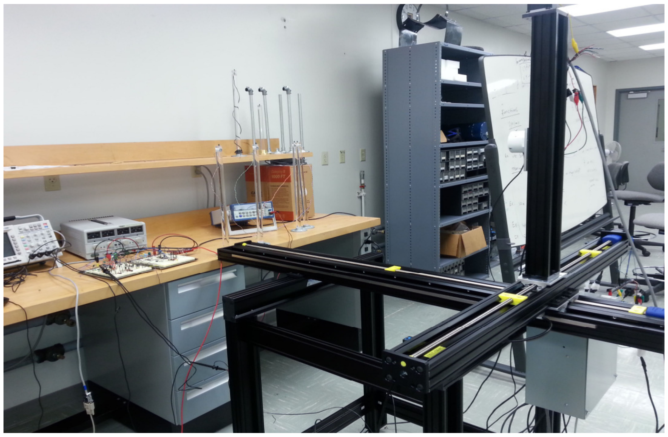

Figure 11. 1D System Setup on Linear Slides

Figures 12 and 13 show the difference in time of arrivals for different positions of the single transmitter.

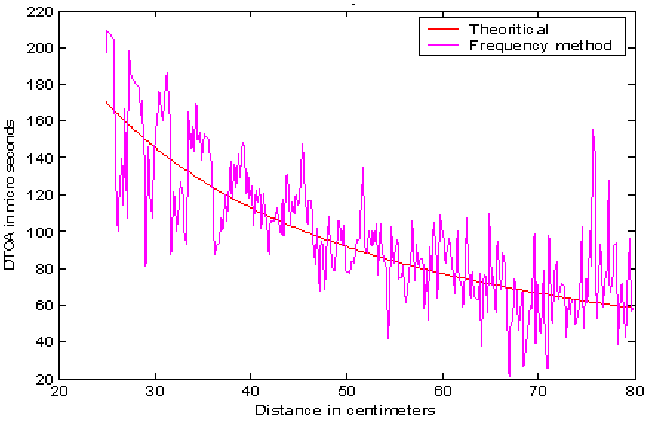

Figure 12. Theoretical and Experimental DTOA

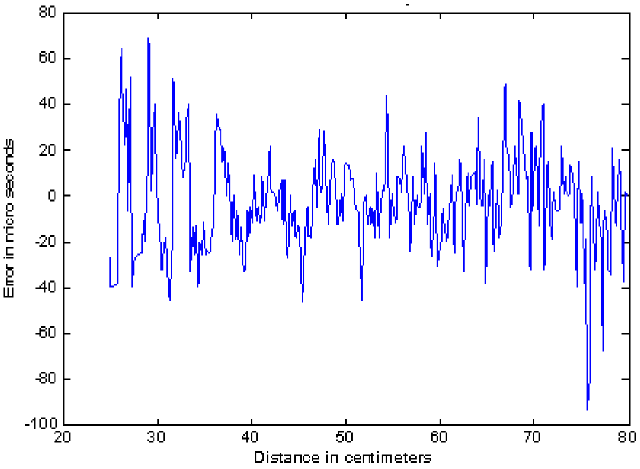

Figure 13. Error between Theoretical and Experimental DTOA

Table 1 shows the results for the experiment when the transmitter was moved on a linear slide in one dimension from 20-30 cm in order to simulate the operating distance in a typical neurosurgery application. The maximum absolute error was 0.11 cm (1.1 mm).

Table 1. Results of 1D Positioning System

d_{actual} (cm)	$d_{experimental}$ (cm)	Absolute error (cm)	Percentage error
5	5.08	0.08	1.6%
10	10.07	0.07	0.7%
15	14.91	0.09	0.6%
20	20.06	0.06	0.30%
25	24.89	0.11	0.44%
30	29,92	0.08	0.26%

The advantage of having the software-controlled microcontroller for data processing and estimating the position of the transmitter further reduced the error when the system was properly calibrated first. Table 1 shows the improved results.

Conclusion

The main objective of this study was the research and development of an ultrasonic positioning system that can be used in various applications such as neuronavigation systems and ergonomic application systems. The system would provide some distinct advantages over existing vision-based systems. Specifically, it could provide similar accuracy and increased robustness at a reduced cost, thereby making it the system of choice for all, or a slightly less accurate system, but increased robustness and reduced cost, thereby making it more attractive for applications in which the accuracies may be sufficient for effective surgical operations. The system may also be used as an adjunct with existing systems for increased robustness and effectiveness in real-time surgeries. The following tasks were completed in this study:

- A system formulation was developed for the use of the ultrasonic system.
- A circuit was developed on the transmitter side to trigger the transmitters with a series of 40 kHz pulses by using a PIC microcontroller.
- A preliminary 1D system was developed and extensively tested on the optic table to show proof of concept. A microcontroller-based, embedded system with smart instrumentation circuits was designed to measure the DTOA values that eliminated the A/D requirements, and lead to a more robust digital system.
- The system was then optimized at the hardware level.

References

[1] Image Guided Vision based Systems. (n.d). Retrieved February 10, 2003, from www.metronics.com.

[2] Hata, N., Takeyoshi, M. S., Iseki, H., & Takakura, K. (1997). Development of a Frameless and Armless Stereotactic Neuronavigation System with Ultrasonographic Registration. *Neurosurgery, 41*(3), 608-614.

[3] Reinhardt, H. F., & Zweifel, H. J. (1990). Interactive Sonar Operated Device for Stereotactic and Open Surgery. *Sterotact Funct Neurosurgery*, *54-55*, 393-397.

[4] Reinhardt, H. F., Horstmann, G. A., & Gratzl, O. (1993). Sonic Stereometry in Microsurgical Procedures for Deep-Seated Brain Tumors and Vascular Malformations. *Neurosurgery, 32,* 51-57.

[5] Barnett, G. H., Kormos, D. W., Steiner, C. P., & Weisenberger, J. (1993). Use of a Frameless, Armless Stereotactic Wand for Brain Tumor Localization with Two-Dimensionless and Three-Dimensionless Neuroimaging. *Neurosurgery, 33,* 674-678.

[6] Kato, A., Yoshimine, T., Hayakawa, T., Tomit, Y., Ikeda, T., Mitomo, M., et al. (1991). A Frameless, Armless Navigational System for Computer-Assisted Neurosurgery. *Neurosurgery, 74,* 845-849.

[7] Roberts, D. W., Strohbehn, J. W., Hatch, J. F., Murray, W., & Kettenberger, H. (1986). A Frameless Stereotactic Integration of Computerized Tomographic Imaging and Operating Microscope. *Neurosurgery, 65,* 545-549.

[8] Tan, K. K., Grzeszczuk, R., Levin, D. N., Pelizzari, C. A., Chen, G. T., Erickson, R. K., et al. (1993). A Frameless Stereotactic Approach to neurosurgical Plannong Based on Retrospective Patient-Image registration. *Neurosurgery, 79,* 296-303.

[9] Gronningsaeter, A., Kleven, A., Ommedal, S., Aarseth, T.E., Lie, T., Lindseth, F., et al. (2000). Sonowand, an Ultrasound-Based Neuronavogation System. *Neurosurgery, 47*, 1373-1380.

[10] Unsgaard, G., Ommedal, S., Muller, T., Gronningsaeter, A., & Hernes, T.A.N. (2002). Neuronavigation by Intraoperative Three-Dimensional Ultrasound: Initial Experience during Brain Tumor Resection. *Neurosurgery, 50,* 804-812.

[11] Figueroa, F., & Mahajan, A. (1994). A Robust Method to Determine the Coordinates of a Wave Source for 3-D Position Sensing. *ASME Journal of Dynamic Systems, Measurements, and Control*, *116,* 505-511.

[12] Milliken, R. J., & Zoller, C. J. (1978). Principle of Operation of NAVSTAR and System Characteristics. *Navigation, 25*(2), 95-106.

[13] Wells, D. (1989). *Guide to GPS Positioning.* Navtech Seminars and GPS Supply, Suite 610, 2775 S. Quincy St., Arlington, VA 22206, USA.

[14] Rathbone, R. R., Valley, R. A., & Kindlmann, P. J. (1986). Beacon-Referenced Dead Reckoning: A Versatile Guidance System. *Robotics Engineering*, *8* (12), 11-16.

[15] Miller, G. L., & Wagner, E. R. (1988). An optical Rangefinder for Autonomous Robot Cart Navigation. *Society of Photo-Optical Instrumentation Engineers, 852 - Mobile Robots II.*

[16] Hongo, T., Arakawa, H., Sugimoto, G., Tange, K., & Yamamoto, Y. (1985). *Proceedings of the IEEE/ SICE Inter. Conf. on Ind. Elec. and Control Instr., IECON '85*. San Francisco, CA.

[17] Aggarwal, J. K., & Nandhakumar, N. (1988). On the Computation of Motion from Sequence of Images - A Review. *Proceedings of IEEE*, *76*(8), 917-935.

[18] Chitiekshi, S., Akers, J., & Mahajan, A. (2004). An Intelligent Systems Approach for an Ultrasonic based Nueuronavigation System. *Proceedings of the ASME/ IMECE Inter.Conf. on Intelligent Control Systems, Paper # IMECE2004-59607,* (pp,1-9). Anaheim, CA.

[19] Chitiekshi, S., Akers, J., & Mahajan, A. (2007). An Iterative Kalman Filter for a 3D Ultrasonic Position Estimation System. *Proceedings of the ASME/ IMECE Inter.Conf. on Intelligent System, paper # IMECE2007-43490,* (pp 1-9). Seattle, Washington.

[20] Angelo, M. S. (1995). A Digital Signal Processing Technique for Compensating Ultrasonic Sensors. *IEEE Trans. Instrum. Meas.*, *44* (44), 869-874.

[21] Brown, R. G., & Hwang, Y. C. (1997). *Introduction to Random Signals and Applied Kalman Filtering*. John Wiley & Sons, Inc., New York.

[22] Mohinder, S. G., & Angus, P. A. (2001). *Kalman Filtering Theory and Practice Using Matlab*. John Wiley & Sons, Inc., New York.

[23] Wehn, H. W., & Belanger, P. R. (1997). Ultrasound-Based Robot Position Estimation. *IEEE Transactions on Robotics and Automation*, *13*(5), 682-692.

[24] Mahajan, A., & Figueroa, F. (1999). An Automatic Self Installation & Calibration Method for a 3D Position Sensing System using Ultrasonics. *Robotics and Autonomous Systems*, *28*(4), 281-294.

[25] Mahajan, A., & Walworth, M. (2001). 3D Position Sensing using the Difference in Time-of-Flights to Various Receivers from a Single Transmitter of Wave Energy. *IEEE Transactions on Robotics and Automation*, *17*(1)*,* 91-94.

[26] Ray, P. K., & Mahajan, A. (2002). A Genetic Algorithm-Based Approach to Calculate the Optimal Configuration of Ultrasonic Sensors in a 3D Position Estimation System. *Robotics and Autonomous Systems*, *1015,* 1-13.

[27] Haupt, R. L., & Haupt, S. E. (1998). *Practical Genetic Algorithms.* John Wiley & Sons, Inc.

[28] Unnikrishnan, N., Ray, P. K., Mahajan, A., & Chu, T. (2002). Accuracy Considerations in a 3D Ultrasonic Positioning System that uses the Difference in Time-of-Flights. *ASME Transactions on Dynamic Systems, Measurements, and Control*, *124*(4)*,* 688-693.

Biographies

SANJEEVI CHITIKESHI is an Assistant Professor in Industrial and Engineering Technology Department at Murray State University, Murray, KY. He earned both his Masters and Ph.D. in Electrical and Computer Engineering,) from Sothern Illinois University, Carbondale, IL, in 2004 and 2007 respectively. Dr. Chitikeshi is currently teaching at Murray State University in Electromechanical Engineering and Technology Program. His interests are in smart instrumentation and sensors, Electromechanical systems modeling, estimation and control, ultrasonic positioning system, mechatronics systems. Dr. Chitikeshi may be reached at schitikeshi@murraystate.edu.

DUSTIN PATTON is an undergraduate student in Electromechanical Engineering and Technology Program at Murray State University, Murray, KY. Mr. Patton may be reached at dpatton1@murraystate.edu

AJAY MAHAJAN is an Associate Dean for Research at The University of Akron, Akron, OH. He earned both his doctorate and master's degrees in mechanical engineering from Tulane University in New Orleans. He is president of Clipius Technologies, a company that produces concepts for novel products for applications in defense, aerospace and particularly, biomedical areas. Dr. Mahajan, is also a former professor of mechanical engineering at the Southern Illinois University Carbondale's Department of Mechanical Engineering and Energy Processes. Dr. Mahajan has more than 100 peer-reviewed journal publications and conference proceedings. Dr. Mahajan may be reached at majay@uakron.edu

TIME-INDEPENDENT REDUNDANCY IN SYSTEM RELIABILITY: A DUAL SYMMETRICAL APPROACH

Basile Panoutsopoulos, Central Connecticut State University

Abstract

Systems are made of subsystems and subsystems are made of components. Components and systems are connected in various ways, which can be reduced to basic series and parallel connections. Proper operation of a system requires its operation without fault. In this study, the reliability of these two basic connections, series and parallel, was determined for time independent redundancy. In addition, the reliability of two fully complex planar system connections, namely series/parallel and parallel/series, was determined by reducing them to simpler cases. Graphs of reliability for special cases are also presented here. The development of the subject follows the duality that naturally appears for complementary systems.

Introduction

The mathematical nature of the subject requires a mathematical approach to its development. The definitions of the various terms used in this study are presented first, followed by the examination of specific cases of interconnected components and systems.

Reliability is the probability that a device will function without failure over a specified time period and for predetermined amounts of usage [1].

Failure is the termination of the ability of an item to perform a required function [1].

A component or system will either operate properly or fail. Due to the dual nature of the phenomenon, the reliability or probability of success, p, and the unreliability or probability of failure, q, are related by [2]

$$p + q \equiv 1 \tag{1}$$

Redundancy is the introduction of auxiliary elements and components into a circuit, module, or system unit to perform the same functions as similar elements in such units for the purpose of improving their overall reliability in performance and safety [1].

System is a set of interconnected elements that achieve a given objective through the performance of a specified function [1].

A system fails if all alternative means of operation fail. The use of probability theory and part failure information form the basis in the overall analysis [2]. In this study, a dual algorithmic approach was followed. The importance of an algorithmic approach in engineering mathematics courses has been investigated elsewhere [3].

The redundancy of a system is time independent if the reliability of each one of the components is time independent; otherwise, it is time dependent. In this study, methods for predicting and evaluating the reliability of a system that consists of components with time independent reliability are presented. For this, the following approach will be pursued:

- Determination of paths for successful system operation through reliability block diagrams;
- Determination of a mathematical model for individual path reliability; and,
- Determination of a mathematical model for overall system reliability.

Subsystem is a portion of a system containing two or more integrated components which, while not completely performing the specific function of a system, may be isolated for design, testing, or maintenance [1].

Path is any continuous succession of branches traveled in the indicated branch directions [1].

Element is a product, subsystem, assembly, component, subcomponent, subassembly, or part of a physical or system architecture, specification tree, or system breakdown structure, including the system itself [1].

The effect of combining components in the basic configurations of series and parallel connections as well as their basic extension of series—parallel and parallel/series—was evaluated. It turns out that the development of the series/parallel topics follows a dual pattern because they are symmetrical. The equations are similar in both cases, as long as we consider the reliability for series connections and the failure for the parallel connections. Reliability and failure are complements of each other. The parallel/series and the series/parallel connections present the same symmetrical development when the general case and complementary special cases are considered.

Types of Redundancy

Redundancy is classified either as active or standby, based on the state of the redundant element [4].

Active redundancy is when all means for performing a given function are operating simultaneously [1].

Standby redundancy is when the alternative means for performing a given function are inoperative until needed [1]. If a system is in the standby state, it is necessary to have a means of detecting a failure in the primary element and switch in the redundant element.

Redundancy is realized by way of connecting either a component or a system or both. Typical means of duplicating either a component or system, or subsystem, is shown in Figure 1, and that of a system in Figure 2.

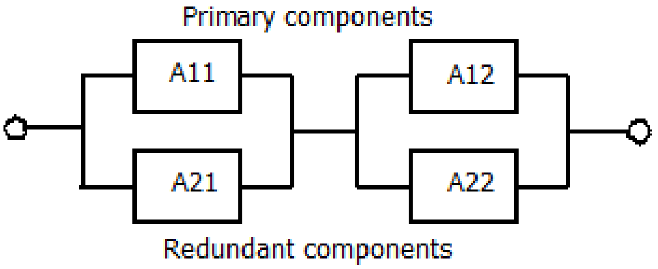

Figure 1. Redundancy Duplicating Components

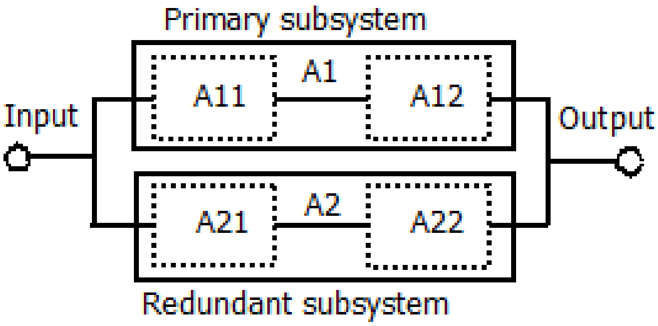

Figure 2. Redundancy Duplicating Subsystems and Systems

Evaluation of the Effect of Redundancy on the Performance of a System

The reliability of a number of basic standard redundant systems was determined and evaluated. In the modeling process, set theory was used, which applies easily to basic standard systems but becomes complicated for complex systems. The application of probability theory follows, based on set theory [2], [5]. The following assumptions are made:

- The failure of one unit is assumed to be statistically independent of the others. This is close to most practical cases and simplifies the calculations.
- The operation of a unit can be described as dual in nature, either success or failure.
- All elements in an operational signal path are continuously energized in the success state.
- Path failure of any type has no adverse effect on the operation of the remaining parallel paths.

The paths for successful operation of a system can be determined from the topology of the block diagram. The reliability of the system is determined by the path of the signal and the reliability of the components in the path. When an element ceases to function properly, the path containing that element is no longer available. Since redundancy implies more than one path for system success, reliability can alternatively be defined mathematically, as the probability that at least one path exists between a system's input and output [6].

Evaluation of Reliability in Series-Connected Components

A series system consists of N components or subsystems and is shown in Figure 3 [7], [9]. There is only one possible path for successful signal flow from the input to the output of the system.

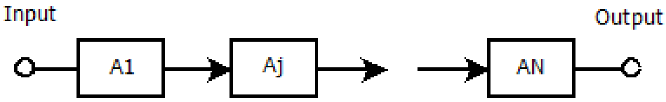

Figure 3. A Series System of N Components

The reliability of the system consisting of N components or N subsystems connected in series, R_S, is the probability of successful operation of the overall system. The functional operation of the whole system depends on the successful operation of each sub-unit; that is, $A_1 \wedge A_2 \wedge \cdots A_j \cdots \wedge A_N$.

All components must function properly for the system's proper operation. A component's failure results in total system failure. In general, [3]:

$$\begin{aligned} R_S &= P\left(A_1 \cap A_2 \cap \cdots \cap A_N\right) \\ &= P(A_1)P(A_2 / A_1)P(A_3 / A_1A_2)\cdots \\ &\quad P(A_N / A_1, \ldots A_{N-1}) \end{aligned} \tag{2}$$

where $P(A_N / A_1, \ldots A_{N-1})$ is the conditional probability. A_N is operational, given that $A_1, \ldots A_{N-1}$ are operational. Therefore, the failure of the system depends on the failure of its subsystems or components, as there are no other paths of signal flow. For many practical cases, the failure of one component is statistically independent of the others. The reliability of a system under this basic assumption of independent element failures and the necessity of successful operation of all components for the successful overall system operation is the probability of success of the overall system. Then, the reliability of the system is equal to the sum of the reliabilities of each one of its components. Mathematically, this statement is expressed as:

$$\begin{aligned} R_S &= P(A_1) \cdot P(A_2) \ldots P(A_j) \ldots P(A_N) = \prod_{j=1}^{N} P\left(A_j\right) \\ &= R_1 \cdot R_2 \ldots R_j \ldots R_N = \prod_{j=1}^{N} P\left(A_j\right) \\ &= p_1 \cdot p_2 \cdots p_j \cdots p_N = \prod_{j=1}^{N} p_j \end{aligned} \tag{3}$$

Special case: When all of the series-connected elements are identical, each with reliability p_j, and under the basic assumption of independent element failures, the reliability of the overall system consisting of N components connected in series is

$$\begin{aligned} R_S\big|_{R=R_j} &= \prod_{n=1}^{N} R_n = R^N \\ &= \prod_{n=1}^{N} p_n = p^N \end{aligned} \tag{4}$$

The reliability of a system with N series elements, each with a reliability or probability of success p, is plotted in Figure 4 [10]. It can be seen that the more the elements connected in series, the less the reliability of proper operation (i.e., the probability of a working path from the input to the output).

Evaluation of Reliability in Parallel-Connected Components

A parallel system consisting of M components is shown in Figure 5 [2], [9]. There is more than one possible path for successful signal flow from the input to the output of the system.

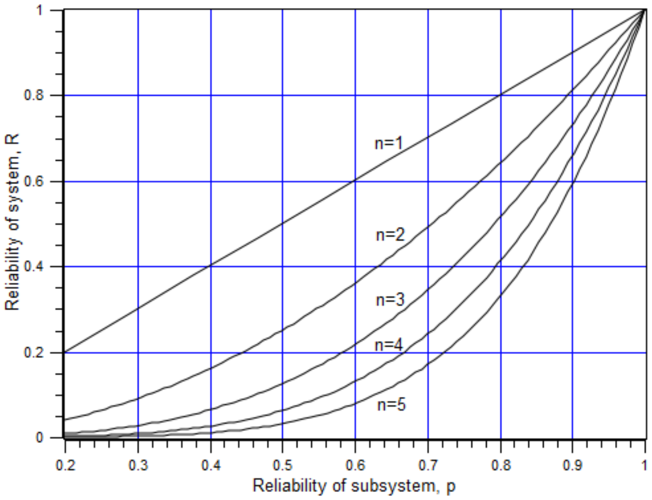

Figure 4. Reliability of Identical Subsystems Connected in Series [N represents the number of elements. The reliability of each element varies from 0.2 to 1.]

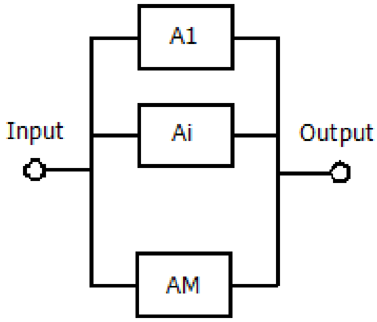

Figure 5. A Parallel System of M Components

The reliability, R_p, of the system consisting of M components or subsystems connected in parallel is the probability of successful operation of the overall system. The system will operate successfully if any sub-unit operates successfully; that is, $A_1 \vee A_2 \vee \cdots A_i \cdots \vee A_M$. The system will fail if all units fail. In general, failure of all components results in total system failure [5]. The reliability of such a system is

$$\begin{aligned} R_P &= P\left(A_1 \cup A_2 \cup \cdots \cup A_M\right) \\ &= P(A_1) + P(A_2) + \cdots + P(A_M) \\ &\quad -\left(P\left(A_1A_2\right) + P\left(A_1A_3\right) + \cdots + \underset{i \neq j}{P}\left(A_iA_j\right)\right) \\ &\quad +(-1)^{m-i} P\left(A_1A_2 \cdots A_M\right) \end{aligned} \tag{5}$$

This equation is complicated and difficult to solve. An alternative approach in order to simplify the operations is to use the dual of reliability or probability of success p, and the unreliability or probability of failure q. Thus, the probability of system failure is the intersection of the probability of unit failures. Mathematically, this is expressed as

$$\begin{aligned}\bar{R}_P &= P\left(\bar{A}_1 \cap \bar{A}_2 \cap \cdots \cap \bar{A}_M\right)\\ &= P(\bar{A}_1)\cdot P(\bar{A}_2/\bar{A}_1)\cdot P(\bar{A}_3/\bar{A}_1\bar{A}_2)\\ &\cdot P\left(\bar{A}_M/\bar{A}_1\bar{A}_2\cdots\bar{A}_{M-1}\right)\end{aligned} \tag{6}$$

where $P(\bar{A}_M / \bar{A}_1,\ldots A_{M-1})$ is the conditional probability that A_M failed, given that $A_1,\ldots A_{M-1}$ failed. Therefore, the failure of the system does not depend on the failure of one component as there are other paths for the signal to flow from the input to output. For many practical cases, the failure of one component is statistically independent of the failure of others. Then, the unreliability of the system is equal to the sum of unreliability of each one of the components. Mathematically, this statement is expressed as

$$\begin{aligned}\bar{R}_P &= P(\bar{A}_1)\cdot P(\bar{A}_2)\cdots P\left(\bar{A}_i\right)P(\bar{A}_M) = \prod_{i=1}^{M} P\left(\bar{A}_i\right)\\ &= \bar{R}_1\cdot\bar{R}_2\cdots\bar{R}_i\cdots\bar{R}_M = \prod_{i=1}^{M} q_i\\ &= q_1\cdot q_2\cdots q_i\cdots q_M = \prod_{i=1}^{M} q_i\end{aligned} \tag{7}$$

Since $p+q\equiv 1$, the reliability will be

$$\begin{aligned}R_P &= 1-\bar{R}_P\\ &= 1-\prod_{i=1}^{M} P\left(\bar{A}_i\right) = 1-\left[\prod_{i=1}^{M}\left(1-P\left(A_i\right)\right)\right]\\ &= 1-\prod_{i=1}^{M}\bar{R}_i = 1-\left[\prod_{i=1}^{M}\left(1-R_i\right)\right]\\ &= 1-\prod_{i=1}^{M} q_i = 1-\left[\prod_{i=1}^{M}\left(1-p_i\right)\right]\end{aligned} \tag{8}$$

The reliability of this M component connected in parallel under the basic assumption of independent element failures and the necessity of successful operation of at least one operational component for successful overall system operation is the probability of success of the overall system.

Special case: When all of the parallel-connected elements are identical, each with reliability p_m and under the basic assumption of independent element failures, the unreliability of the overall system consisting of M components connected in parallel is

$$\begin{aligned}\bar{R}_p\Big|_{\bar{R}=\bar{R}_i} &= \prod_{i=1}^{M}\bar{R}_i = \prod_{i=1}^{M}\left(1-R_i\right)\\ &= \bar{R}^M = \left(1-R_i\right)^M\\ &= q^M = \left(1-p\right)^M\end{aligned} \tag{9}$$

The reliability of the system will be

$$\begin{aligned}R_p\Big|_{R=\bar{R}_i} &= 1-\bar{R}_p\Big|_{\bar{R}=\bar{R}_i}\\ &= 1-\left(1-p\right)^M\end{aligned} \tag{10}$$

The reliability of a block with M parallel elements, each with reliability or probability of success p, is plotted in Figure 6. It can be seen that the more elements connected in parallel, the less the unreliability (the more the reliability) of proper operation (i.e., the probability of a working path from the input to the output).

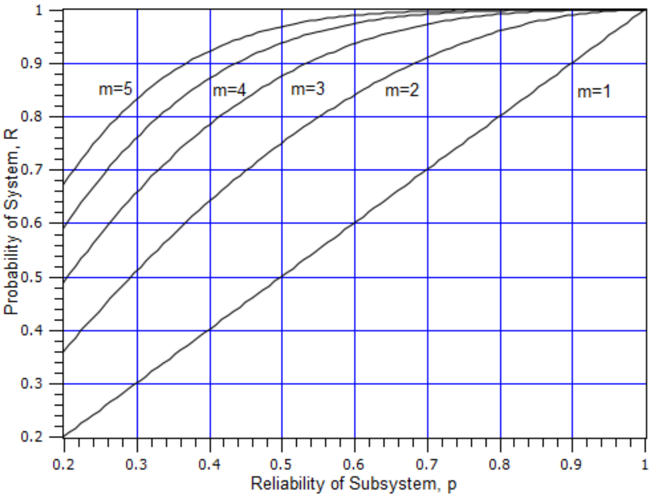

Figure 6. Reliability of Identical Components Connected in Parallel [M represents the number of elements. The reliability of each element varies from 0.2 to 1.]

A special case of two elements connected in parallel is considered next. There are two possible paths for successful system operation [11]. The signal flow is either path "In-A1 -Out" or "In-A2-Out" (see Figure 5). The two events are either mutually exclusive or the two events are not mutually exclusive for proper system operation. System of mutually exclusive events (Application of Multiplicative rule): The two components are independent. The only way the system can fail is through the failure of both elements. The probability that the system will fail is that both elements will fail and is the product of their unreliability.

$$\overline{R}_{2P} = q_1 q_2 \tag{11}$$

The reliability of the system is:

$$\begin{aligned} R_{2P} &= 1 - \overline{R}_{2P} \\ &= 1 - q_1 q_2 \end{aligned} \tag{12}$$

System of non-mutually exclusive events (Application of Additive Rule): The system operates successfully if at least A1 or A2 is operable. Because the events are not mutually exclusive, both elements are energized (i.e., both A1 and A2 can occur). The probability of proper system operation is

$$R_{2P} = p_1 + p_2 - p_1 p_2 \tag{13}$$

This is the additive rule for non-mutually exclusive events.

Evaluation of Reliability in Series/ Parallel-Connected Components

A complex system of a series of multiple parallel elements is shown in Figure 7 [6], [11]. The reliability of this system will be determined by reducing each of the parallel subsystems to an equivalent and then considering the resultant series system. Both the parallel and series connections of systems were considered in the previous sections.

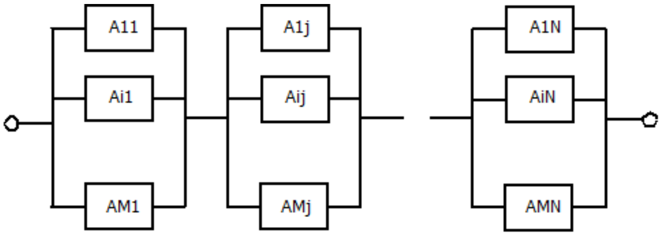

Figure 7. General Representation of a Series/Parallel System of Multiple Parallel Elements

The system has N parallel subsystems. Every parallel subsystem has M components. The reliability of the jth component out of the ith in the N parallel subsystem will be

$$R_j = 1 - \prod_{j=1}^{M} \left(1 - R_{i,j}\right) \tag{14}$$

This is Equation of the reliability of a system of parallel-connected components with proper indices for the system under consideration. The complex system consists of N such parallel subsystems. The overall reliability of the complex system with N series subsystems composed of M parallel components in each subsystem will be

$$\begin{aligned} R_{SP} &= \prod_{j=1}^{N} R_j \\ &= \prod_{j=1}^{N} \left[1 - \prod_{i=1}^{M} \left(1 - R_{i,j}\right) \right] \\ &= \prod_{j=1}^{N} \left(1 - q_{1j} \cdot q_{2j} \cdots q_{Mj}\right) \end{aligned} \tag{15}$$

This is the reliability of a system consisting of a series of N multiple parallel components. The probability of failure of the ith component in the jth unit is q_{in}. The overall operation reduces each one of the series-connected subsystems to an equivalent subsystem, A_{Mj}. The M parallel-connected subsystems in series are reduced to N series-connected subsystems, as shown in Figure 8.

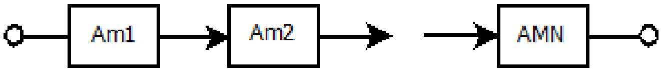

Figure 8. Equivalent Subsystem of a Series/Parallel Configuration

For the special case of a system with identical components in each parallel subsystem,

$$\begin{aligned} &A_{1j} = A_{ij} = \cdots = A_{Mj} \\ &R_j = R_{i1} = R_{i2} = R_{ij} = \cdots = R_{Mj} \end{aligned} \tag{16}$$

The reliability of the system is

$$\begin{aligned} R_{SP}\big|_{R_{i,j}=R_i} &= \prod_{j=1}^{N} R_j \\ &= \prod_{j=1}^{N} \left[1 - \prod_{i=1}^{M} (1 - R_i) \right] \\ &= \left[1 - \prod_{i=1}^{M} (1 - R_i) \right]^N \\ &= \left[1 - \prod_{i=1}^{M} q_i \right]^N = \left[1 - \prod_{i=1}^{M} (1 - p_i) \right]^N \end{aligned} \tag{17}$$

where q_i is the probability of failure or unreliability of the component in the ith unit. Furthermore, in the special case that all elements are identical with reliability $R_{i,j} = R = p$, then the overall system reliability is

$$\begin{aligned} R_{SP}\big|_{R_{i,j}=R} &= 1-\left[\prod_{i=1}^{M}(1-R)\right]^{N} \\ &= \left[1-(1-R)^{M}\right]^{N} \\ &= \left[1-(1-p)^{M}\right]^{N} \\ &= \left(1-q^{M}\right)^{N} \end{aligned} \tag{18}$$

The variation of reliability is shown in various graphs in Figure 9 and a 3-dimensional representation in Figure 10 for M=1-5, N=1-5 and p=0.2-0.8. For the practical case in which the probability of failure is small, the overall system reliability can be approximated by

$$R = 1 - Nq^{M} \tag{19}$$

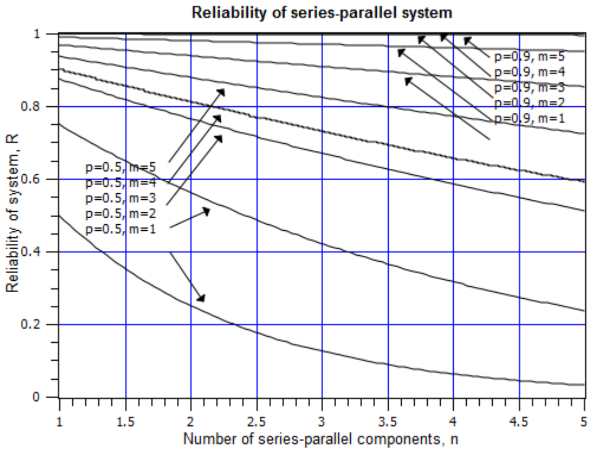

Figure 9. Evaluation of Reliability for Various Values: p, M, and N

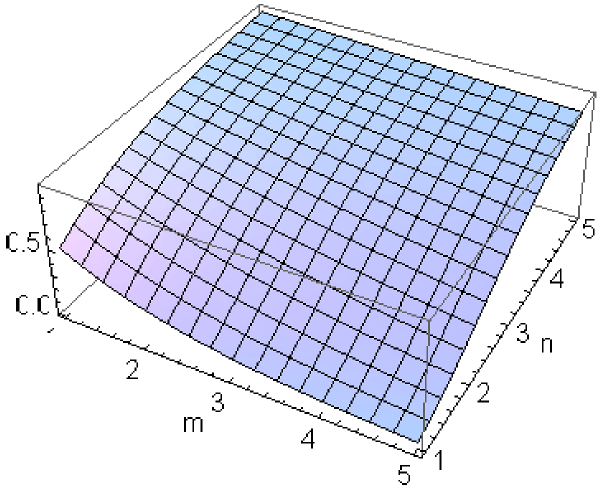

Figure 10. A 3-Dimensional Representation of the Reliability Dependence for a Series/Parallel System

Example: Evaluation of Redundancy in Series/Parallel-Connected Components for a Non-Symmetrical Configuration

The reliability of a system consisting of two series/parallel subsystems of components was examined and its reliability evaluated. The reliability of each component was assumed to be known. Then, the reliability of each subsystem was evaluated followed by the reliability of the whole system as the product of all parallel-connected subsystems [12], [13]. The two subsystems were connected in series. The first subsystem (A) consisted of two components (A_1, A_2) connected in parallel. The second subsystem (B) consisted of three components (B_1, B_2, B_3) in parallel (see Figure 11).

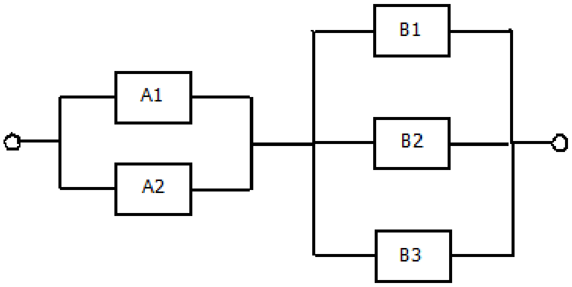

Figure 11. An Asymmetrical Series/Parallel System

For subsystem A to be operational, at least one of the two units, either A_1 or A_2, must be operational. The subsystem reliability is

$$\begin{aligned} R_A &= 1-\overline{R}_{A1}\overline{R}_{A2} \\ &= 1-(1-R_{A1})(1-R_{A2}) \end{aligned} \tag{20}$$

Similarly, for subsystem B to be operational, at least one of the three units, either B1 or B2, or B3 must be operational. The subsystem reliability is

$$\begin{aligned} R_B &= 1-\overline{R}_{B_1}\overline{R}_{B_2}\overline{R}_{B_3} \\ &= 1-\left(1-R_{B_1}\right)\left(1-R_{B_2}\right)\left(1-R_{B_3}\right) \end{aligned} \tag{21}$$

Since both subsystems are necessary for the successful operation of the system, the system's reliability will be

$$\begin{aligned} R &= R_A R_B \\ &= \left[1-(1-R_{A1})(-R_{A2})\right]\cdot \\ &\quad \left[1-\left(1-R_{B_1}\right)\left(1-R_{B_2}\right)\left(1-R_{B_3}\right)\right] \end{aligned} \tag{22}$$

The reliability of the system is a function of five variables.

Evaluation of Reliability in Parallel/ Series-Connected Components

A complex system of a parallel set of multiple series elements is shown in Figure 12 [5], [10]. The reliability of this system will be determined by reducing each one of the series subsystems to an equivalent and then considering the resultant parallel system. Both the series and the parallel connections of systems were considered in the previous sections.

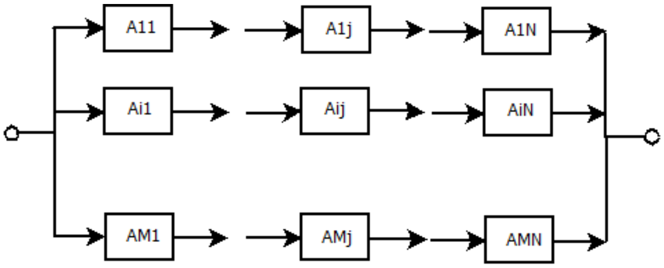

Figure 12. Generalized Parallel/Series Configuration of a System

The system has M series subsystems. Every series subsystem has N components. The reliability of the ith component out of the jth series of the M series subsystems is

$$R_i = \prod_{j=1}^{N} R_{i,j} \tag{23}$$

This is Equation of the reliability of a system of series-connected components with proper indices for the system under consideration. The complex system consists of M such series subsystems. The overall reliability of the complex system with M parallel subsystems of N series components each subsystem will be

$$\begin{aligned} R_{PS} &= 1-\prod_{i=1}^{M}(1-R_i) \\ &= \left[1-\prod_{i=1}^{M}\left(1-\prod_{j=1}^{N}R_{i,j}\right)\right] \\ &= 1-\prod_{i=1}^{M}(1-p_{i1}\cdot p_{i2}\cdots p_{iN}) \end{aligned} \tag{24}$$

where p_{ij} is the probability of success of the ith component in the jth unit. The overall operation reduces each one of the series-connected subsystems to an equivalent subsystem, A_{iN}. The N series-connected subsystems in parallel are reduced to M parallel-connected subsystems, as shown in Figure 13.

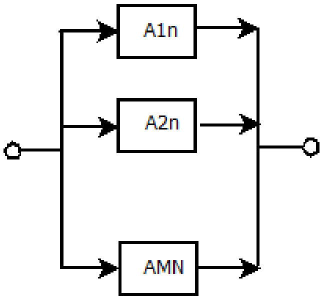

Figure 13. Equivalent Subsystem of a Parallel/Series Configuration

For the special case of a system with identical components in each series subsystem,

$$\begin{aligned} &A_{i1} = A_{ij} = \cdots = A_{iN} \\ &R_i = R_{i1} = R_{i2} = R_{ij} = \cdots = R_{Mj} \end{aligned} \tag{25}$$

And the reliability of the system simplifies to

$$\begin{aligned} R_{SP}\big|_{R_{i,j}=R_i} &= 1-\prod_{i=1}^{M}\left(1-\prod_{j=1}^{N}R_j\right) \\ &= \left(1-\prod_{j=1}^{N}R_j\right)^{M} \\ &= \left[1-\prod_{j=1}^{N}p_j\right]^{N} \end{aligned} \tag{26}$$

where p_j is the probability of success or reliability of the component in the ith unit. Furthermore, in the special case that all elements are identical with reliability $R_{i,j} = R = p$, then the overall system reliability is

$$\begin{aligned} R_{SP}\big|_{R_{i,j}=R} &= 1-\left[1-\prod_{j=1}^{N}R\right]^{M} \\ &= 1-\left[1-R^{N}\right]^{M} \\ &= 1-\left(1-p^{N}\right)^{M} \end{aligned} \tag{27}$$

The variation of reliability is shown in various graphs in Figure 14 and a 3-dimensional representation in Figure 15, for M=1-5, N=1-5 and p=0.2-0.8. Further investigation into applications of product development and design may enhance proposed approaches [14], [15].

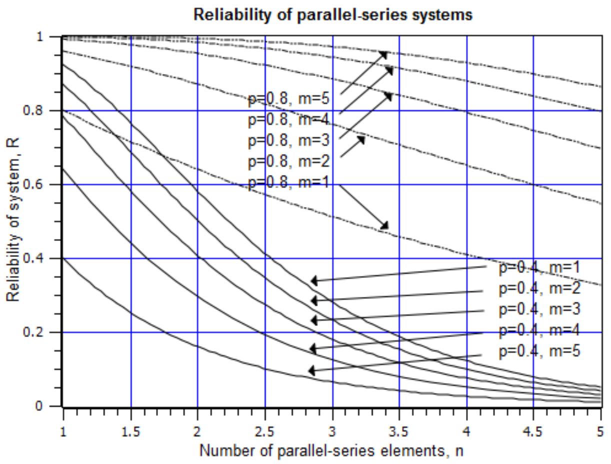

Figure 14. Evaluation of Reliability for Values p, M, and N

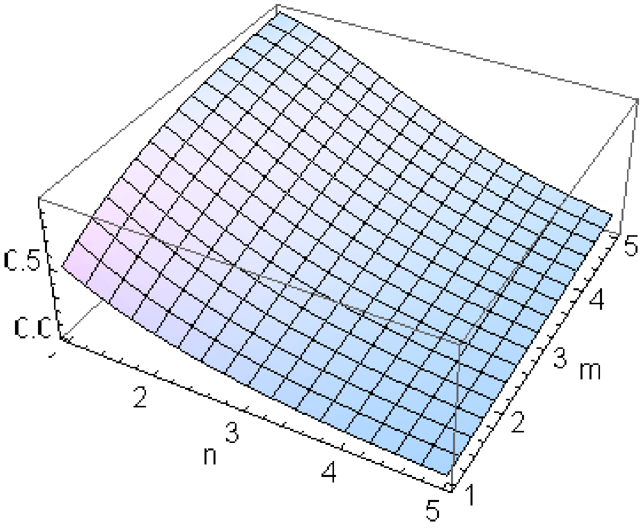

Figure 15. A 3-Dimensional Representation of the Reliability Dependence for a Parallel/Series System

Conclusion

A dual symmetrical approach to time independent redundancy in system reliability was developed. The classical and basic series and parallel connections present a dual parallel development when incorporating the reliability and unreliability concepts, respectively.

References

[1] IEEE. (1995). *The IEEE Standard Dictionary of Electrical and Electronic Terms.* Sixth Edition. IEEE, Inc.

[2] Papoulis, A., & Pillai, A. U. (2002). *Probability, Random Variables, and Stochastic Processes.* (4th ed.). McGraw-Hill.

[3] Siyambalapitiya, S. B. (2000). Importance of Algorithmic Approach for Engineering Mathematics Courses. *The Technology Interface*, *4*(1).

[4] Kleon, J. (1977) *A Redundancy Notebook.* Rome Air Development Center.

[5] Smith, D. J. (2011). *Reliability, Maintainability and Risk: Practical Methods for Engineers.* (8th ed.). Butterworth-Heinemann.

[6] Ireson, W., Coombs, C., & Moss, R. (1995). *Handbook of Reliability Engineering and Management.* (2nd ed.). McGraw-Hill Professional.

[7] Bozovsky, I. (2004). *Reliability Theory and Practice.* Dover.

[8] Frankel, E. G. (1988). *System Reliability and Risk Analysis.* Springer.

[9] MIL-HDBK-338B. (1988). *Military Handbook: Electronic Reliability Design Handbook.* Rome Air Development Center.

[10] Wolfram S. (1999). *The Mathematica Book.* (4th ed.). Cambridge University Press.

[11] Arsenault, J. E., & Roberts, J. A. (1983). *Reliability & Maintainability of Electronic Systems.* Computer Science Press.

[12] Lewis, E. E. (1995). *Introduction to Reliability Engineering.* (2nd ed.) Wiley.

[13] Billinton, R. & Allan, R. N. (1992). *Reliability Evaluation of Engineering Systems: Concepts and Techniques.* Springer.

[14] Hsiung, S., & Belliston, W. (spring, 2007). Applied Research on Product Development between the Engineering Technology Program and Industry Applications. *The Technology Interface.*

[15] Alavizadeh, A., & Jetley, S. (2010). Usage of Axiomatic Design Methodology in the US Industries. *International Journal of Modern Engineering, 10*(2)76.

Biography

BASILE PANOUTSOPOULOS holds a Ph.D. from the Graduate Center of the City University of New York, a ME in Electrical Engineering from The City College of the City University of New York, and a MS in Applied Mathematics and a BS in Electrical Engineering from New Jersey Institute of Technology. He is a Senior Member of IEEE. He joined the School of Engineering and Technology at Central Connecticut State University during the Fall semester 2010. Previously, he worked for eighteen years with the Naval Undersea Warfare Center, initially in New London, CT, and later in Newport, RI. His research interests are in Electromagnetics and Applications, Radio Frequency Telecommunications, Bioelectromagnetics, Energy Systems, Applied Mathematics, and Pedagogy. Dr. Panoutsopoulos may be reached at Basile.Panoutsopoulos@ieee.org

INSTRUCTIONS FOR AUTHORS: MANUSCRIPT REQUIREMENTS

The INTERNATIONAL JOURNAL OF MODERN ENGINEERING is an online/print publication, designed for Engineering, Engineering Technology, and Industrial Technology professionals. All submissions to this journal, submission of manuscripts, peer-reviews of submitted documents, requested editing changes, notification of acceptance or rejection, and final publication of accepted manuscripts will be handled electronically. The only exception is the submission of separate high-quality image files that are too large to send electronically.

All manuscript submissions must be prepared in Microsoft Word (.doc or .docx) and contain all figures, images and/or pictures embedded where you want them and appropriately captioned. Also, for all accepted manuscripts, each figure, image or picture that was imported into your Word document must be saved individually as a **300dpi or higher JPEG (.jpg)** file and submitted separately; your manuscript and figure numbers must be used in the title of the file (e.g., **M12-S-18 Figure 4**); that means one additional file for each image imported into your manuscript. These 300dpi images do NOT need to be embedded in your manuscript. For tables or graphs created directly in Word, you do not need to submit them as separate files.

Included below is a summary of the formatting instructions. You should, however, review the sample Word document of our website for details on how to correctly format your manuscript. The editorial staff reserves the right to edit and reformat any submitted document in order to meet publication standards of the journal.

The references included in the References section of your manuscript must follow APA-formatting guidelines. In order to help you, the sample Word document also includes numerous examples of how to format a variety of scenarios. Keep in mind that an incorrectly formatted manuscript will be returned to you, a delay that may cause it (if accepted) to be moved to a subsequent issue of the journal.

1. **Word Document Page Setup**: Two columns with ¼" spacing between columns; Top of page = ¾"; Bottom of page = 1" (from the top of the footer to bottom of page); Left margin = ¾"; Right margin = ¾".

2. **Paper Title**: Centered at the top of the first page with a 22-point Times New Roman (Bold), Small-Caps font.

3. **Page Breaks**: Do not use page breaks.

4. **Body Fonts**: Use 10-point Times New Roman (TNR) for body text throughout (1/8" paragraph indention); 9-point TNR for author names/affiliations under the paper title; 16-point TNR for major section titles; 14-point TNR for minor section titles; 9-point TNR BOLD for caption titles for tables and figures; other font sizes as noted in the sample document.

5. **In-text Referencing**: List and number each reference when referring to them in the body of your document (e.g., [1]). The first entry must be [1] followed by [2], [3], etc., continuing in numerical order to the final entry in your References section. Again, see the sample Word document for specifics. Do not use the End-Page Reference utility in Microsoft Word. You must manually place references in the body of the text.

6. **Tables and Figures**: Center all tables and figures. Captions for tables must be above the table, while captions for figures are below; all captions are left-justified.

7. **Page Limit**: Manuscripts should not be more than 15 pages (single-spaced, 2-column format).

8. **Page Numbering**: Do not use page numbers.

9. **Publication Charges:** Manuscripts accepted for publication are subject to mandatory publication charges.

10. **Copyright Agreement:** Review the **copyright transfer agreement**.

11. **Submissions:** All manuscripts and associated files must be submitted electronically; the only exception would be if you wish to submit a CD with the individual files for your high-quality images, as noted above.

MANUSCRIPTS should be submitted to Dr. Philip D. Weinsier, manuscript editor, at philipw@bgsu.edu along with a copy to editor@ijme.us.

FILES containing your high-quality images should ONLY be submitted to philipw@bgsu.edu.

CUTTING EDGE JOURNAL OF RESEARCH AND INNOVATION IN ENGINEERING

www.ijeri.org

Print ISSN: 2152-4157
Online ISSN: 2152-4165

www.iajc.org

INTERNATIONAL JOURNAL OF ENGINEERING RESEARCH AND INNOVATION

ABOUT IJERI:

- IJERI is the second official journal of the International Association of Journals and Conferences (IAJC).
- IJERI is a high-quality, independent journal steered by a distinguished board of directors and supported by an international review board representing many well-known universities, colleges, and corporations in the U.S. and abroad.
- IJERI has an impact factor of **1.58**, placing it among an elite group of most-cited engineering journals worldwide.

OTHER IAJC JOURNALS:

- The International Journal of Modern Engineering (IJME)
  For more information visit www.ijme.us
- The Technology Interface International Journal (TIIJ)
  For more information visit www.tiij.org

IJERI SUBMISSIONS:

- Manuscripts should be sent electronically to the manuscript editor, Dr. Philip Weinsier, at philipw@bgsu.edu.

  For submission guidelines visit
  www.ijeri.org/submissions

TO JOIN THE REVIEW BOARD:

- Contact the chair of the International Review Board, Dr. Philip Weinsier, at philipw@bgsu.edu.

  For more information visit
  www.ijeri.org/editorial

INDEXING ORGANIZATIONS:

- IJERI is currently indexed by 16 agencies. For a complete listing, please visit us at www.ijeri.org.

Contact us:

Mark Rajai, Ph.D.

Editor-in-Chief
California State University-Northridge
College of Engineering and Computer Science
Room: JD 4510
Northridge, CA 91330
Office: (818) 677-5003
Email: mrajai@csun.edu

www.tiij.org

www.ijme.us

The latest impact factor (IF) calculation (Google Scholar method) for IJME of 3.0 moves it even higher in its march towards the top 10 engineering journals.

IJME IS THE OFFICAL AND FLAGSHIP JOURNAL OF THE INTERNATIONAL ASSOCATION OF JOURNALS AND CONFERENCE (IAJC)
www.iajc.org

The International Journal of Modern Engineering (IJME) is a highly-selective, peer-reviewed journal covering topics that appeal to a broad readership of various branches of engineering and related technologies. IJME is steered by the IAJC distinguished board of directors and is supported by an international review board consisting of prominent individuals representing many well-known universities, colleges, and corporations in the United States and abroad.

IJME Contact Information

General questions or inquiries about sponsorship of the journal should be directed to:

Mark Rajai, Ph.D.
Editor-in-Chief
Office: (818) 677-5003
Email: editor@ijme.us
Department of Manufacturing Systems Engineering & Management
California State University-Northridge
18111 Nordhoff St.
Northridge, CA 91330